CPPM-T-2008-02

UNIVERSITÉ DE LA MÉDITERRANÉE
AIX-MARSEILLE II
FACULTÉ DES SCIENCES DE LUMINY
163, avenue de Luminy
13288, MARSEILLE cedex 09
FRANCE

THÈSE DE DOCTORAT

Spécialité : Physique Mathématique, Physique des Particules et Modélisation

présentée par

TRINH Thi Nguyet

en vue d'obtenir le grade de docteur de l'Université de la Méditerranée

Recherche de leptons excités sur le collisionneur HERA avec le détecteur H1

Soutenue le 22 mai 2008 devant le jury composé de :

Monsieur	**Boudjema Fawzi**	Rapporteur
Monsieur	**Kajfasz Eric**	Président
Madame	**Perez Emmanuelle**	Examinateur
Monsieur	**Sauvan Emmanuel**	Co-directeur de thèse
Monsieur	**Schwemling Philippe**	Rapporteur
Monsieur	**Vallée Claude**	Directeur de thèse

Remerciements

Trois années de thèse ne sont pas aussi longues qu'elle y paraissent. Voici le résultat de mes trois années de thèse, le début de ma carrière de recherche. Il est très dur (pour moi!).

J'ai eu vraiment de la chance de faire une thèse au Centre de Physique des Particules de Marseille. Je tiens tout d'abord à remercier le directeur du CPPM, Roy Aleksan et puis ensuite Eric Kajfasz pour m'avoir acceuilli au sein de ce laboratoire. Je remercie également Eric Kajfasz d'avoir accepté de faire partie de mon jury.

J'aimerais remercier Claude Vallée qui a accepté d'être mon directeur de thèse. Merci à sa gentillesse, ses encouragements et à sa relecture du manuscrit.

Merci du fond du coeur à mon co-directeur de thèse, Emmanuel Sauvan, qui m'a dirigé tout au long des recherches exposées dans cette thèse. Je n'aurais certainement pas eu ce jour sans son soutien sans réserves.

Je voulais remercier Fawzi Boudjema et Philippe Schwemling, qui ont accepté d'être les rapporteurs de mes travaux, pour la lecture du manuscrit et leurs commentaires qui ont enrichi ce manuscrit. J'aimerais remercier Emmanuelle Perez pour son aide pour développer le générateur ”H1NuStar” qui est un des travaux originaux de la recherche de neutrinos excités. Et merci mille fois à sa précieuse gentillesse. Je la remercie également d'avoir accepté de faire partie de mon jury.

Je tiens à remercier Cristi Diaconu pour son aide, qui a contribué à la progression de mes travaux, ainsi que les autres membres du groupe H1 en France.

Merci au professeur Le Trong Tuong, mon professeur de physique des particules quand j'étais encore à l'Ecole Normale supérieure de Hanoi, pour son aide et ses encouragements.

Merci à Roland Triay qui m'a apporté son soutien inconditionel au début de mon séjour en France et lors de mon arrivée.

Je voudrais remercier tous les thésards du CPPM. Merci pour votre sympathique et votre gentiless.

Merci à mes amis, Viet, Nguyet, Phuong, Hieu et amis vietnamiennes dans le campus de Luminy, qui m'encouragent sans cesse à croire en moi-même et à avancer sur le chemin que j'ai choisi.

Merci beaucoup à Thibault pour avoir corrigé ”mon français”. Merci beaucoup à sa patience et à gentilesse.

Finalement, merci à mes parents et à mon petit frère, merci à mes grand-parents. Quatre ans en France, loin du pays, suffisent largement pour que je comprenne que leur amour inconditionel est le plus pur et unique.

Aujourd'hui, j'ai eu ma thèse. Toutefois, elle n'est pas vraiment à moi : elle est à toutes celles et ceux qui, par leur propre exemple, m'ont appris à vivre comme je suis.

Contents

Introduction

Le Modèle Standard (MS) de la physique des particules fournit une description des constituants de la matière et des forces gouvernant leurs interactions. Le Modèle Standard représente une grande réussite théorique, et jusqu'à présent, aucune mesure expérimentale n'est en contradiction avec ses prédictions. Pourtant, il est attendu que le MS ne soit pas la théorie "finale" car de nombreuses questions fondamentales restent encore sans réponses.

La découverte de nouvelles interactions ou de particules au-delà du MS permetrait la confirmation ou le développement de nouvelles théories et menerait très certainement à une nouvelle conception de la nature. Le collisionneur électron-proton HERA avec une énergie disponible dans le centre-de-masse de $\sqrt{s} = 319$ GeV est intermédiaire entre les énergies maximales disponibles au LEP (environ 203 GeV) ou au Tevatron (1.9 TeV). HERA est évidemment une machine idéale pour la recherche de nouveaux états couplant directement aux leptons et aux quarks, comme les leptoquarks ou des quarks supersymétriques. Les recherches de fermions excités sont également intéressantes car les collisions *ep* présentent des états finaux d'interaction relativement propres et ces recherches peuvent y être réalisées jusqu'à une limite cinématique supérieure à celle du LEP.

Cette thèse présente une recherche de leptons excités de première génération en utilisant toutes les données enregistrées par le détecteur H1 à HERA, entre 1994 et mi-2007. Les données utilisées représentent une luminosité intégrée totale de 475 pb^{-1}.

Le premier chapitre résume notre compréhension actuelle du monde subatomique en présentant les aspects pertinents du Modèle Standard de la physique des particules. Ensuite, une brève description de la physique au-delà du MS et des tentatives théoriques pour son extension sera présentée. Les détails du cadre théorique utilisé pour l'interpétation des résultats de la présente analyse seront également donnés. Le chaptre 2 sera consacré à la description des principaux processus physique du MS et la production de leptons excités dans les interactions *ep* à HERA. L'appareillage expérimental et la reconstruction des événements dans le détecteur H1 seront présentés dans les chapitres 3 et 4. Les chapitres 5 et 6 décrivent les critères de sélection qui ont été développés pour distinger un signal potentiel de leptons excités des processus de bruit de fond du MS. Enfin, l'interprétation des résultats est discutée dans le chapitre 7, où des limites supérieures sur les paramètres principaux du modèle sont calculées. Les résultats de cette analyse sont comparés aux contraintes obtenues auprès d'autres expériences sur collisionneurs.

Introduction

The Standard Model (SM) of particle physics provides a description of the matter constituents and of the forces governing their behavior. The Standard Model has been exceptionally successful and there are currently no known strong violations of its predictions. However, it is expected that the SM will not be the final theory, as many questions have still no answers within the SM.

The discovery of new interactions or particles beyond the SM would certainly be welcome as they would lead to new theories and a new conception of nature. HERA is the only existing electron-proton collider. The HERA center-of-mass energy of up to $\sqrt{s} = 319$ GeV is intermediate between maximum energies available at LEP (up to about 203 GeV) and at the Tevatron (1.9 TeV). HERA is of course ideally suited to look for new states coupling directly to leptons and quarks, such as leptoquarks or some supersymmetric quarks. Searches for excited fermions are also particularly interesting as *ep* collisions lead to relatively clean interaction final states, and such searches can be performed up to the kinematic limit.

This thesis presents a search of the first generation of excited leptons using all data collected by the H1 detector in *ep* collisions from 1994 up to the end of HERA operation mid-2007. This corresponds to an integrated luminosity of 475 pb^{-1}.

The reminder of the first chapter summarizes our current understanding of the subatomic world, introducing the relevant aspects of the SM of particles physics. This is followed by a brief description of the physics beyond the SM with attempts to answer some problematic aspects of the SM. Details of the theoretical framework used to interpret results of the present analysis will be given. The main SM physics processes and the production of excited leptons in *ep* interactions at HERA are presented in chapter 2. The experimental apparatus and the reconstruction and measurement of events in the H1 detector are the topics of chapters 3 and 4. Chapters 5 and 6 describe the selection criteria, that were developed to discriminate potential signal of excited leptons from SM background processes. The interpretation of the results is discussed in chapter 7 and upper limits on the main parameters of the model are derived. Results from this analysis are also compared to present constraints obtained by other collider experiments.

Chapter 1

Theoretical overview

The Standard Model (SM) as the theory of elementary particles describes the elementary constituents of matter and forces governing their interactions. The success of the Standard Model, which provides answers to many fundamental questions, is indisputable. However, the Standard Model leaves few open questions which will be briefly discussed. The main properties of the SM and its deficiencies will be presented in the first section. In the second section, some of the possible theoretical extensions to the SM will be presented. The third section is devoted to the presentation of phenomenological models based on possible lepton compositeness which will be considered in this thesis.

1.1 The Standard Model

The Standard Model is a renormalizable gauge theory based on the $SU(3)_C \times SU(2)_L \times U(1)_Y$ group. The constituent particles of matter are organized into three families with a similar structure. This classification is related to the algebraical structure of the groups. Within the fermions representing matter particles, we can separate the leptons and the quarks. Leptons are grouped into three pairs (e, ν_e), (μ, ν_μ) and (τ, ν_τ), the first pair containing the electron and its associated neutrino. The quarks are also arranged in three generations (u, d), (c, s) and (t, b) and are the constituents of hadrons. Most known hadrons are the proton with an electric charge of $+1$ being composed of two u quarks and one d quark and the neutron composed by two d quarks and one u quark, with a null electric charge. Each of the six quarks exists in three colors (red, blue and green). Fundamental particles of matter are summarized in table 1.1.

These particles are subject to four types of interactions:

- *The gravitational interaction* acts on all massive particles and its strength is in general negligible at the energy of collider interactions.

- *The electromagnetic interaction* acts on only charged particles. It concerns e, μ and τ leptons having a charge of -1, the u, c and t quarks having a charge

Fermions	Generation			T	T^3	Q	Y
	1	2	3				
Leptons	$\begin{pmatrix} e \\ \nu_e \end{pmatrix}_L$	$\begin{pmatrix} \mu \\ \nu_\mu \end{pmatrix}_L$	$\begin{pmatrix} \tau \\ \nu_\tau \end{pmatrix}_L$	1/2	1/2 −1/2	−1 0	-1
	e_R	μ_R	τ_R	0	0	-1	-2
Quarks	$\begin{pmatrix} d \\ u \end{pmatrix}_L$	$\begin{pmatrix} s \\ c \end{pmatrix}_L$	$\begin{pmatrix} b \\ t \end{pmatrix}_L$	1/2	−1/2 1/2	−1/3 2/3	1/3
	d_R	s_R	b_R	0	0	-1/3	-2/3
	u_R	c_R	t_R	0	0	+2/3	+4/3

Table 1.1: Quantum numbers of leptons and quarks arranged in three generations where T, T^3, Q and Y are the weak isospin, third component of the isospin, the electric charge and the weak hypercharge.

of 2/3 and the b, s and d quarks with a charge of $-1/3$. This interaction does not affect neutrinos which have no electric charge.

- *The weak interaction* links particles of each pair, as for example the electron and its associated neutrino or the u quark to the d quark.
- *The strong interaction* acts on quarks and particles made of quarks, the hadrons.

The SM describes the electromagnetic, weak and strong interactions. The electromagnetic and weak interactions have been unified in the electroweak theory of Glashow-Salam-Weinberg [1] relying on the $SU(2)_L \times U(1)_Y$ gauge group. This is the group of transformations leaving invariant the Lagrangian of weak interactions. The Quantum Chromodynamic (QCD) describes the strong interactions within the $SU(3)_C$ gauge group. In a gauge theory, interactions are an automatic consequence of the existence of a symmetry associating different particles, as for example the three colors of a u quark or the electron-neutrino pair. This symmetry means that particles are in fact similar and can transform into each other. The interaction between matter particles are mediated by spin 1 gauge bosons:

- the photon, massless, for the electromagnetic interaction,
- the massive bosons $W^\pm$ and Z^0 for the weak interaction,
- eight massless gluons for the strong interaction.

Main properties of the bosons of the SM are summarized in table 1.2.

1.1.1 The strong interaction

Quarks belong to $SU(3)_C$ triplets and each quark flavor can carry three colors (red, blue and green). The leptons are, on the contrary, non-colored particles and behave as singlets under a $SU(3)_C$ transformation. Gluons belong to $SU(3)_C$ octets. Generators of $SU(3)_C$ transformations are the Gell-Mann matrices. Contrary to electromagnetic and weak interactions, the strength of the strong interaction increases with the distance. At small distances, quarks can be considered as free particles (this property is called asymptotic freedom). But when the distance between two quarks q_1 and q_2 increases, quark-antiquark pairs are created from vacuum such that q_1 and q_2 can not be observed individually but form non-colored objects, the hadrons. This is the confinement property.

Bosons	Spin	Q	Mass (GeV)
gluons $g_i (i = 1..8)$	1	0	0
photon γ	1	0	0
$W^\pm$	1	± 1	80.4
Z^0	1	0	91.2
Higgs H	0	0	> 114.4 at 95% CL

Table 1.2: Bosons of the Standard Model.

1.1.2 The electroweak interaction

Parity violation in the weak interactions implis that the components of right and left chiralities of the fermions be treated differently in the theory. Therefore, the left lepton components belong to isospin doublets of the $SU(2)_L$ group:

$$\psi_L = \begin{pmatrix} \nu_e \\ e \end{pmatrix}_L, \begin{pmatrix} \nu_\mu \\ \mu \end{pmatrix}_L, \begin{pmatrix} \nu_\tau \\ \tau \end{pmatrix}_L, \begin{pmatrix} u \\ d \end{pmatrix}_L, \begin{pmatrix} c \\ s \end{pmatrix}_L, \begin{pmatrix} t \\ b \end{pmatrix}_L \tag{1.1}$$

and the right components belong to singlets (a $SU(2)_L$ transformation leaving invariant the right components):

$$e_R, \mu_R, \tau_R, u_R, d_R, c_R, s_R, t_R, b_R \tag{1.2}$$

In the simplest version of the Standard Model the neutrinos are assumed to be massless in the SM and are represented only by states of left chirality. However, convincing evidences in favour of neutrino oscillations, driven by small neutrino masses and neutrino mixing, were obtained in diffrent solar, atmosphere and long-baseline neutrino experements [2]. Such small neutrino masses can be accounted for in the SM by a see-saw mecanism. The hypercharge Y is the generator of $U(1)$ transformations and the weak isospin $\vec{T} = \vec{\tau}/2$ is the generator of $SU(2)$ transformations, $\vec{\tau}$ being the Pauli matrices. The electric charge Q of a state is related to its hypercharge and to the third component of its weak isospin T_3 by $Q = T_3 + Y/2$.

The mass eigenstates of quarks are not the same as the weak interaction eigenstates. The weak interaction acts on $(u, d')_L, (c, s')_L$ and $(t, b')_L$ doublets, the d', s' and b' states being linear combinations of the d, s and b mass eigenstates. By convention, the quarks of charge 2/3 are not subject to the mixing. The relation between the mass eigenstates and the weak eigenstates is provided by the Cabibbo-Kobayashi-Maskawa matrix V:

$$\begin{pmatrix} d' \\ s' \\ b' \end{pmatrix} = V \begin{pmatrix} d \\ s \\ b \end{pmatrix} \tag{1.3}$$

This matrix is defined by three angles and one phase measuring the CP violation.

The coupling constants of the weak and electromagnetic interactions, g and g', respectively, are linked by the Weinberg angle θ_W: $\tan\theta_W = g'/g$. We should note that the unification of these two interactions is purely formal and the value of θ_W is not predicted by the theory but measured experimentally.

1.1.3 The generation of masses

As long as the $SU(2)_L \times U(1)_Y$ symmetry is exact, fermions are massless, as a mass term $\bar{\psi}\psi = \bar{\psi}_L \psi_R$ is not invariant under $SU(2)_L$. Similarly, at this stage, the part of the Lagrangian describing gauge bosons does not contain any mass term for these bosons. Masses in the SM are generated by the Higgs mechanism. We assume the existence of a $SU(2)_L$ doublet Φ of complex fields and a potential $V(\Phi)$. The potential is chosen such as at its minimum, the field Φ get a non-zero mean value in the vacuum ($v =< \Phi >\simeq 250$ GeV). The $SU(2)_L \times U(1)_Y$ symmetry is then spontaneously broken and particles acquire a mass via their interaction with the field Φ. The Higgs boson has not been observed yet.

1.2 Limits of the Standard Model

In general, from present experimental measurements, we may think that the SM describes well the physics of processes probed at the energies available at present large colliders (below 1 TeV). Great successes of the SM are the discovery, after the prediction of their existence by the SM, of the W and Z bosons in 1983 at CERN and of the top quark at the Tevatron in 1995. Up to now, all precision measurements confirm the predictions of the electroweak sector of the SM. Only the Higgs boson, which is one of the fundamental basis of the SM, has not been observed yet.

But this model has still many deficiencies and some of its properties are yet unexplained. We may then think that it is only an effective theory valid at "low energies" of a more fundamental theory.

The Standard Model has 19 free parameters, in addition to neutrino masses:

- 3 coupling constants g_s, g, g' or $\alpha, \theta_W, \Lambda_{QCD}$.
- 2 parameters of the Higgs potential v and λ, or m_{Z^0} and m_{Higgs}.
- 9 fermion masses: $m_e, m_\mu, m_\tau; m_u, m_c, m_t; m_d, m_s, m_b$.

- 3 mixing angles and 1 phase in the Kobayashi-Maskawa matrix.
- The vacuum parameter of QCD, θ_{QCD}.

This large number of parameters and the fact that their values have to be measured experimentally restrict the predictive potential of the SM. The existence of an underlying theory can therefore be assumed, to explain and relate together the values of these parameters.

There is no explanation for the existence of exactly three generations of fermions. The number of light neutrinos was constrained by LEP experiments to exactly 3, but nothing in the SM can justify this number. The electroweak interaction Lagrangian is simply constructed separately for each of the lepton and quark generations. There are no direct couplings between different lepton families while, intriguingly, three quark families (at least) are needed if quark mixing is to be the cause of all observed electroweak CP violation. The existence of the fermion generations could be hinting that more elementary constituents exist which form the known quarks and leptons.

Gravitation, one of the four fundamental forces, is still not included in the SM. Therefore, the SM can not describe processes at very high energies, where gravitational effects can not be neglected.

The SM does not provide particle candidates for dark matter. According to present cosmological observations, as only about 4% of the total energy density in the universe can be seen directly, the rest would be composed of dark matter ($\sim 22\%$) and dark energy (74%), both of unknown nature. The dark matter component is postulated to originate from new elementary particles, which can not be provided by the Standard Model.

A naturality problem results from the presence in the SM of one fundamental scalar field, the Higgs field. To avoid quadratic divergences in the mass of scalar particles, a renormalization should be applied. The threshold of this renormalization (the energy scale used to cut divergences) can be for example the Planck scale (10^{19} GeV), the energy scale where quantum mechanics conflicts with gravitation. But the difference between the electroweak energy scale, of the order of 100 GeV and set by masses of W and Z bosons, and the Planck scale is very large and not understood in the SM. This large difference imposes a precise and "un-natural" fine-tuning of the mass of the Higgs field at the Planck scale.

1.3 Beyond the Standard Model

Many theories exist, trying to provide answers to certain of the unanswered problems of the SM. In the following, some of them will be briefly presented.

1.3.1 Supersymmetry

Supersymmetry (SUSY) assumes an underlying symmetry relating fermions to bosons [3, 4]. In SUSY, the supersymmetric transformation Q transforms a bosonic state into a fermionic state and vice versa:

$$Q\ |\text{boson}>=|\text{fermion}> \qquad Q\ |\text{fermion}>=|\text{boson}>.$$

The operator Q has to satisfy the following commutation and anti-commutations relations stated by the Coleman-Mandula theorem [5]:

$$\begin{aligned} \left\{Q,Q^\dagger\right\} &= P^\mu, & (1.4)\\ \{Q,Q\} &= \left\{Q^\dagger,Q^\dagger\right\}=0, & (1.5)\\ [P^\mu,Q] &= \left[P^\mu,Q^\dagger\right]=0, & (1.6) \end{aligned}$$

where P^μ is the generator of space-time translations.

The representations of this super-algebra are called supermultiplets. The supermultiplets contain both fermionic and bosonic states called superpartners. In unbroken supersymmetry, particles of the same supermultiplet must have the same mass, the same electric charge, the same weak isospin and the same color. In addition the number of fermionic and bosonic degrees of freedom in a supermultiplet must be the same.

The simplest possibility for a supermultiplet satisfying the upper conditions is a so-called *chiral* or *matter* supermultiplet which is a combination of a two-component Weyl fermion and a complex scalar field. The next simplest supermultiplet so-called *gauge* supermultiplet containing a Weyl fermion and a spin 1 vector boson, which is massless before spontaneous symmetry breaking. A supersymmetric model with only gauge and chiral multiplets is called *N=1 supersymmetry.*

In the Minimal Supersymmetric Model (MSSM), each of the known fundamental particles must be arranged in either a chiral or gauge supermultiplet. The left-handed and right-handed SM fermions are Weyl fermions and are arranged in a chiral supermultiplet. Each fermion has its own complex scalar partner, called *sfermion* (*slepton* and *squark*). They are denoted with a tilde. The scalar Higgs boson must be a member of a chiral supermultiplet since it has a spin of 0. One Higgs chiral supermultiplet with $Y=\frac{1}{2}$, which gives masses to up-types quarks (u,c,t), called H_u, and one Higgs chiral supermultiplet with $Y=-\frac{1}{2}$, which gives masses to down-type quarks (d,s,b) and to charged leptons (e,μ,τ), called H_d, are introduced. The particle content of all chiral supermultiplets is given in table 1.3.

The vector bosons of the SM are members of a gauge supermultiplet. Their superpartners are called *gauginos.* The partner of the spin 1 $SU(3)_C$ gauge boson, the gluon is the gluino which has spin $\frac{1}{2}$. The $SU(2)_L \otimes U(1)_Y$ gauge bosons of the SM are $W^\pm$, W^0 and B^0. Their spin $\frac{1}{2}$ partners are called *wino* and *bino.* The particle content of all gauge supermultiplets is given in table 1.4 . As in the SM W^0 and B^0 gauge eigenstates mix to form mass eigenstates Z^0 and γ. The corresponding mixtures of $\widetilde{W}^0$ and $\widetilde{B}^0$ are called *zino* ($\widetilde{Z}^0$) and the *photino* ($\widetilde{\gamma}$).

Because of the electroweak symmetry breaking effects, the superpartners listed above are not necessary the mass eigenstates of the theory. Mixing can appear between electroweak gauginos and the higgsinos, and between the various squarks and sleptons and the Higgs scalars which have the same electric charge. The ($\widetilde{B}^0$, $\widetilde{W}^0$) mix with the two neutral higgsinos ($\widetilde{H}_u^0$, $\widetilde{H}_d^0$) to form four neutralinos. The charged *wino* $\widetilde{W}^+$ (resp. $\widetilde{W}^-$) mixes with the charged Higgsino $\widetilde{H}_u^+$ (resp. $\widetilde{H}_u^-$) to form the *chargino* $\widetilde{\chi}_i^+$ (resp. $\widetilde{\chi}_i^-$). Different arguments encourage the development of supersymmetry:

- The natural value of the Higgs mass of about $10^{14} - 10^{17}$ GeV is not around the electroweak scale as suggested by precise electroweak data. This hierarchy problem could be solved by the supersymmetric theory: in "low energy" SUSY theories, the effective scale of the spontaneous SUSY breaking is equal to the electroweak scale. It is therefore a way to resolve the hierarchy problem.

- The SUSY particles contribute to the different couplings of the strong, weak and electromagnetic interactions above the effective SUSY scale of about 1 TeV, which causes, via virtual effects of the extra SUSY particles in loops, a change in the slope in the evolution of the couplings where they could unify in the 10^{15} GeV region [6].

- If supersymmetry is embedded in a grand unified theory and the unifications of the coupling constants is assumed, it makes a very precise prediction of the electroweak mixing parameter $\sin^2\theta_W$ which has been measured at LEP at the per mill level. For example, the simplest $SU(5)$ GUT implies $\sin^2\theta_W = 0.375$ at the GUT scale [11], corresponding at low energies to $\sin^2\theta_W \sim 0.21$ in close agreement with experiment.

- In supersymmetric models the electroweak symmetry breaking may be a result of renormalization group evaluation.

- If supersymmetry is formulated as a local symmetry, it naturally incorporates gravity since a field of spin 2 must be introduced, which can be identified as the graviton.

Names		Spin 0	Spin 1/2
squarks, quarks	Q	$(\tilde{u}_L,\tilde{d}_L)$	(u_L,d_L)
(in 3 families)	U	$\tilde{u}_R^*$	$u_R^\dagger$
	D	$\tilde{d}_R^*$	$d_R^\dagger$
sleptons, leptons	L	$(\tilde{\nu},\tilde{e}_L)$	(ν,e_L)
(in 3 families)	E	$\tilde{e}_R^*$	$e_R^\dagger$
Higgs, Higgsinos	H_u	(H_u^+,H_u^0)	$(\tilde{H}_u^+,\tilde{H}_u^0)$
	H_d	(H_d^0,H_d^-)	$(\tilde{H}_d^0,\tilde{H}_d^-)$

Table 1.3: Chiral supermultiplets in the MSSM. The spin 0 fields are complex scalars, and the spin 1/2 fields are left-handed two-component Weyl fermions.

Names	Spin 1/2	Spin 1
gluino, gluon	$\tilde{g}$	g
winos, W bosons	$\tilde{W}^{\pm}$ $\tilde{W}^{0}$	$W^{\pm}$ W^{0}
bino, B bosons	$\tilde{B}^{0}$	B^{0}

Table 1.4: Gauge supermultiplets in the MSSM.

1.3.2 Extra-dimensions

We live in a 3− dimensional space but the existence of extra dimensions is not excluded, provided that these dimensions be compactified in order to explain their non-observation up to now [7]. In some models with a relatively large compactification volume, the large value of the Planck scale in 4 dimensions results from a geometrical effect. The fundamental Planck scale in the complete space would be of the order of magnitude as the electroweak scale, resolving the hierarchy problem between the two scales.

1.3.3 Grand unification

Looking at the success of the unification of the electromagnetic and weak interactions, we may think of the construction of a theory able to unify also electroweak and strong interactions. Using renormalization group equations, the coupling constants g, g' and α_S can be extrapolated up to high energies and we observe that all three constants reach a similar order of magnitude at an energy scale of $10^{15} - 10^{16}$ GeV. This suggests the existence of a higher unification level at high energy. The idea is then to try to build a new gauge theory with only one coupling constant and a larger gauge group, which can include $SU(3)_C \times SU(2) \times U(1)$. A first attempt was tried using the $SU(5)$ group [8] but it failed as this theory gives a proton life time lower than the measured value [9, 10]. Present attempts to construct a Grand Unification Theory (GUT) are based on the $SO(10)$ or E_6 groups. Some of the GUT theories also predict that around the unification energy, particles are not point-like but may be compared to vibrating strings. These theories are based on larger groups as $SO(32)$ or $E_8 \times E_8$ and often include the gravitation. They require a space with 11 dimensions. But such models are in general not testable at the energies presently available at large colliders.

1.3.4 Composite models

To solve the Standard Model problems, we may consider it as an effective theory based on another more fundamental model assuming that at least one of the SM particles may be composite and made of more fundamental objects [11]. We can distinguish three categories of theories depending on the attribution of the composite structure either to the Higgs boson, to the weak bosons or to the fermions.

1.3.4.1 Model with a composite Higgs: Technicolor

The Higgs boson of the SM can not solve alone the hierarchy problem due to divergence problems arising during the calculation of the masses of fundamental scalar particles. But a composite Higgs could bring a solution to this problem as it would not suffer from the same problems in calculations of the radiative corrections to particle masses. Similarly to mesons, initially supposed by Yukawa as being the mediators of the strong force and which are in fact composite particles of a quark-antiquark pair, the Higgs from *technicolor* models [12, 13] may be formed by a bound state of two fermions (a *technifermion*) in analogy with the Cooper pair explaining the supraconductivity. This model allows to solve the hierarchy problem but it is necessary to introduce new bosons called *extra technicolor bosons* to avoid that the technifermions acquire also a mass, leading to renormalisation problems.

1.3.4.2 Model with composite weak bosons

The weak force is of short range and is the only force whose vector bosons are massive. The mass of weak bosons requires the existence of a mechanism bringing them a mass. The Van der Waals force in atomic physics was also initially considered as a short range force before being explained as a manifestation of the electromagnetic force of infinite range. In the absence of observation of the Higgs boson, a new force of short distance, resulting itself from another force of infinite range, may solve certain problems of the SM. A theoretical model, where the weak bosons (W and Z) may be composite, was proposed by Suzuki [14]. Nevertheless, this model does not include parity violation and is hardly compatible with the precise electroweak measurements from LEP.

1.3.4.3 Model of composite fermions

The fermions of the Standard Model, including antiparticles, amount to some 48 particles. However, with their replication in three families of quarks and leptons, their similar couplings to the weak force and their charge, the existence of sub-structure of SM fermions may be imagined to reduce the number of fundamental objects. Such possible sub-constituents of quarks and leptons are called generically *preons* [11].

In the following, few composite models considering quarks and leptons as built from *preons* are briefly discussed.

Model of Haplons

The model of Haplons [15] introduces the existence of two fermions α and β and two scalars x and y whose properties are summarized in table 1.5. With the help of these four particles, called *Haplons*, all SM fermions and vector bosons can be generated, as indicated in table 1.6.

In this model, the photon, the gluons, n^2-1 hypergluons as well as the fermions (α and β) and the scalars (x and y) are fundamental particles, all others being composites. A new quantum number is introduced, the *Hypercolor H* and the model is then based on the $U(1)_{EM}\otimes SU(3)_C\otimes SU(n)_H$ group. In this theory, we have two distinct energy scales, the scale governing the known particles, Λ_{QCD} and its equivalent at the haplons scale, Λ_H.

Particles	Spin	Charge (e)	$SU(3)_C$	$SU(n)_H$
α	$\frac{1}{2}$	$-\frac{1}{2}$	3	n
β	$\frac{1}{2}$	$+\frac{1}{2}$	3	n
x	0	$-\frac{1}{6}$	3	$\bar{n}$
y	0	$+\frac{1}{2}$	$\bar{3}$	$\bar{n}$

Table 1.5: Quantum numbers of *Haplons*.

$\nu_e = (\bar{\alpha}\beta)_1$ $\quad$ $u = (\bar{\alpha}\bar{x})_3$

$e^- = (\bar{\beta}\bar{y})_1$ $\quad$ $d = (\bar{\beta}\bar{x})_3$

$W^+ = (\bar{\alpha}\beta)_1$ $\quad$ $W^- = (\bar{\beta}\alpha)_1$

$$Z^0 = \frac{1}{\sqrt{2}}(\bar{\beta}\beta + \bar{\alpha}\alpha)_1$$

(the index denote a singlet or a triplet color)

Table 1.6: Composition of some SM particles in the model of Haplons.

Model of Rishons

In the model of Rishons [16], the fermions and the intermediate vector bosons of the electroweak interaction (W and Z) are composites. They are made up of triplets of *Rishons*, the *Rishons* being some fermions called T and V. This theory uses also a new quantum number called *Hypercolor (H)* and the model is based on the $SU(3)_C\otimes SU(3)_H$ group. Two energy scales Λ_{QCD} and Λ_H associated to $SU(3)_C$ and $SU(3)_H$, respectively, are also introduced. The scale Λ_H is much larger than Λ_{QCD} to be in agreement with experimental data.

Particles	Spin	Charge (e)	$SU(3)_C$	$SU(3)_H$
T	$\frac{1}{2}$	$\frac{1}{3}$	3	3
V	$\frac{1}{2}$	0	$\bar{3}$	3

Table 1.7: Quantum numbers of *Rishons*.

The properties of the T and V fermions are summarized in table 1.7. By combining them, the usual SM fermions and the intermediate vector bosons of the electroweak interaction can be obtained, as presented in table 1.8. A very similar model was proposed by M. Shupe [17] under the name of the model of *quips*.

Other models of preons

Other models assuming the composite nature of fermions exist, with their advantages and their defects. They are mainly based on models listed above, bringing them some improvements. The majority of these models are presented in [11].

$\nu_e \sim (V\ V\ V)$	$u \sim (T\ T\ V)$
$e^- \sim (\bar{T}\ \bar{T}\ \bar{T})$	$d \sim (\bar{V}\ \bar{V}\ \bar{T})$

Table 1.8: Composition of some SM particles in the model of Rishons.

However, even if most of the compositeness models are able to resolve some of the SM deficiencies, none of these models is complete and the different approaches presented above are considered as prototypes. All are facing theoretical difficulties which can only be resolved by increasing the model complexity. For example, most models deal only with a single generation of particles. Another problem common to most models is the unwanted generation of unseen exotic particles. As none of these models is unominaly accepted, no "standard" definition of the composite dynamics exists. Therefore an effective approach describing the consequences of compositeness at actual collider energies should be used.

1.4 Phenomenological approaches to lepton compositeness

Since there exists no "standard" model for composites which can be used, a phenomenological approach describing the consequences of compositeness at current collider energies should be used. The existence of fermion substrutures would imply the possibility of different arrangements of the fermion subconstituents. The arrangement of lower energy would be the fundamental level of the particle, while other arrangements may lead to excited states. The observation of excited fermion states would therefore be an evidence of the existence of a fermion substructure.

1.4.1 Gauge mediated interaction

If we assume that the mass of fermion excited states are below the available center-of-mass energy of existing colliders, they may be directly produced, opening the possibility of a direct search. Their production would be followed immediately by their decay into usual SM particles, which could be detected in the final state. Interactions between excited and ordinary fermions may be mediated by gauge bosons, leading to their production from SM fermion collisions and their decay.

In the present study, we will assume that the excited leptons have spin $\frac{1}{2}$ and isospin $\frac{1}{2}$. Higher spin and isospin assignments have been discussed in [18]. Both left-handed and right-handed components of excited fermions form a weak isodoublet F_L^* and F_R^*. It is assumed that they acquire their masses prior to the $SU(2)\times U(1)$ breaking which allows to explain why fermion foundamental states are lighter than excited states. For example, in the case of first generation fermion, we have:

$$\begin{pmatrix} e \\ \nu_e \end{pmatrix}_L , \quad e_R \; ; \quad \begin{pmatrix} e^* \\ \nu_e^* \end{pmatrix}_L , \quad \begin{pmatrix} e^* \\ \nu_e^* \end{pmatrix}_R , \tag{1.7}$$

$$\begin{pmatrix} u \\ d \end{pmatrix}_L , \quad u_R \, , d_R ; \quad \begin{pmatrix} u^* \\ d^* \end{pmatrix}_L , \quad \begin{pmatrix} u^* \\ d^* \end{pmatrix}_R , \tag{1.8}$$

and similarly for the second and third generations.

In general and to be independent of any specific composite model, an effective Lagrangian is used, as introduced by Hagiwara, Komamiya and Zeppenfeld [19], to describe the magnetic transitions of excited fermions F^* to ordinary fermions F:

$$\mathcal{L}_{eff} = \sum_{V=W^\pm,\gamma,Z} \frac{e}{\Lambda} \bar{F^*} \sigma^{\mu\nu} (c_{VF^*F} - \gamma^5 \, d_{VF^*F}) F \, \partial_\mu V_\nu + h.c., \tag{1.9}$$

The parameter Λ has unit of energy and can be regarded as the compositeness scale. Parameters c_{VF^*F} and d_{VF^*F} are the couplings of the gauge fields to excited and ordinary leptons. These couplings have several experimental bounds, the most stringent being derived from $(g-2)$ measurements and from the absence of electric dipole moments for the electron and muon. To a high degree of accuracy $(g-2)$ measurements imply $|c_{VF^*F}| = |d_{VF^*F}|$ [20] and the absence of a dipole moment for electrons and muons requires that these coefficients are almost real if Λ is of the order of 1 TeV [21].

The couplings of the excited fermions to the gauge fields (γ, $W^\pm$ and Z) are vector-like. The excited fermion doublet is noted as $F^* = F^*_L + F^*_R$.

The Lagrangian describing the transition between excited and ordinary (left-handed) fermions should respect a chiral symmetry in order to protect the light leptons from radiatively acquiring a large anomalous magnetic moment. This means that only the right-handed component of the excited fermions takes part in the generalized magnetic de-excitation. Hence, the effective Lagrangian describing these transitions can be written:

$$\mathcal{L}_{gauge} = \frac{1}{2\Lambda} \bar{F^*_R} \, \sigma^{\mu\nu} \left[g \, f \frac{\vec{\tau}}{2} \vec{W_{\mu\nu}} + g' \, f' \, \frac{Y}{2} B_{\mu\nu} + g_s \, f_s \, \frac{\vec{\lambda}}{2} \vec{G_{\mu\nu}} \right] F_L \; + \; h.c., \tag{1.10}$$

where Y is the weak hypercharge, g_s, $g = \frac{e}{\sin\theta_W}$ and $g' = \frac{e}{\cos\theta_W}$ are the strong and electroweak gauge couplings, where e is the electric charge and θ_W is the weak mixing angle; $\vec{\lambda}$ and $\vec{\tau}$ are the Gell-Mann matrices and the Pauli matrices, respectively. $G_{\mu\nu}$, $W_{\mu\nu}$ and $B_{\mu\nu}$ are the field strengh tensors describing the gluon, the $SU(2)$, and the $U(1)$ gauge fields. f_s, f and f' are the coupling constants associated to each gauge field. They depend on the composite dynamics. As ν^* and e^* are expected not to have strong interactions, the present study is insensitive to f_s.

The relations between the f and f' parameters and the coupling constants in equation (1.10) are given by [19]:

$$c_{\gamma e^* e} = -\frac{1}{4} (f + f') \qquad c_{Z e^* e} = -\frac{1}{4} (f \cot\theta_W - f' \tan\theta_W) \, , \tag{1.11}$$

$$c_{\gamma \nu^* \nu} = \frac{1}{4} (f - f') \qquad c_{Z \nu^* \nu} = \frac{1}{4} (f \cot\theta_W + f' \tan\theta_W) \, , \tag{1.12}$$

$$c_{W^+ \nu^* e} = c_{W^- e^* \nu} \;\; = \;\; \frac{f}{2\sqrt{2} \, \sin\theta_W}, \tag{1.13}$$

$$|c_{VF^*F}| \;\; = \;\; |d_{VF^*F}| \tag{1.14}$$

By fixing the relations between f and f', it is possible to write the Lagrangian (1.10) as a function of only one parameter f/Λ.

1.4.2 Contact interactions

The existence of a substructure at an high energy scale Λ could also manifest itself at the lower energies available in present collider experiments by the presence of four-fermions contact interactions (CI), in analogy with Fermi's four-fermion CI model of the weak force.

The contact interaction model describes an interaction in which the *preons* interact with one another. So excited fermions may couple to ordinary quarks and leptons via CI. For energies below the compositeness scale Λ, such interactions can be described by an effective four-fermion Lagrangian [22]:

$$\mathcal{L}_{CI} = \frac{4\,\pi}{2\Lambda^2} j^\mu j_\mu \,, \tag{1.15}$$

where j_μ is the fermion current

$$j_\mu = \eta_L \bar{F}_L \gamma_\mu F_L + \eta'_L \bar{F^*}_L \gamma_\mu F^*_L + \eta"_L \bar{F^*}_L \gamma_\mu F_L + h.c. + (L \rightarrow R), \tag{1.16}$$

where F and F^* represent the SM and excited fermions, respectively. For simplicity, it is assumed in the following that Λ is the same parameter as in the gauge interaction Lagrangian (1.10). By convention, the η factors of left-handed currents are set to one, while the factors of right-handed currents are considered to be zero.

The diagrams in figure 1.1 show the possible four-fermions contact interactions between excited and standard fermions.

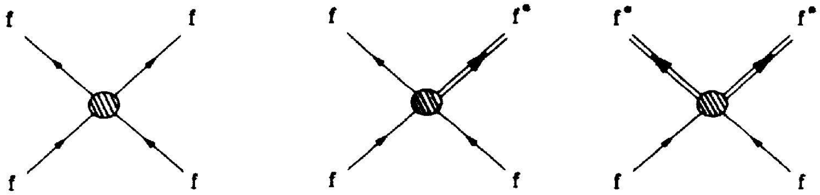

Figure 1.1: Diagram of contact interactions between standard (F) and excited (F^*) fermions.

Contact interactions may induce changes in the cross section of neutral current deep inelastic scattering $ep \rightarrow eX$. Searches of deviations from the SM cross section at the highest squared momentum transfers Q^2 in neutral current deep inelastic scattering processes have indirectly excluded values of Λ between 1.6 TeV and 5.5 TeV, depending on the chiral structure considered [23]. In ep collisions at HERA, contact interaction may also mediate the resonant production of excited fermions. In this thesis, the possibility of excited electron production and their decays by gauge and contact interactions together will be considered for the first time.

The production of excited neutrino via contact interactions is of lower interest. Indeed, non-standard contributions to CC DIS interactions and on a possible $e\nu qq'$ contact interaction are already strongly constrained by electroweak measurements. The constraints are provided by the measurement of the muon decay constant and by the observed unitarity of the Cabibbo-Kobayashi-Maskawa (CKM) matrix. A lower bound on the mass scale of lepton-quark CC contact interactions was derived to be $\Lambda_{CC}^{lq} > 5.8$ TeV [24]. Therefore, possible ν^* production by contact interactions will not be considered in this analysis.

Chapter 2

The Physics of *ep* interactions at HERA

In this chapter, a brief introduction to deep inelastic scattering processes at HERA, their kinematics, and their cross section is given. The main SM processes creating events with high transverse momentum particles in *ep* collisions are then described. In the third part, production mechanism for excited leptons are discussed. Finally, simulations used to simulate SM and excited lepton events are presented.

2.1 Deep inelastic scattering

Deep inelastic scattering (DIS) at HERA is the scattering of an electron on a proton where the electron has sufficient energy to interact with a charged constituent of the proton (quark) and, as a result, a multi-hadron final state is produced. Two deep inelastic electron-proton scattering processes are measured at HERA:

- Neutral current deep inelastic scattering (NC DIS) $ep{\rightarrow}eX$
- Charged current deep inelastic scattering (CC DIS) $ep{\rightarrow}\nu X$

where, the label X denotes all possible hadronic final states. The particles exchange between the electron and the quark in neutral current interactions are a photon (γ) or a Z boson. In charged current scattering processes, a charged $W^{\pm}$ boson is exchanged. The diagrams of NC and CC DIS processes are shown in figure 2.1.

A final state of NC DIS consists of a scattered electron and a jet coming from the stuck quark. Additional jets can be present in the final state due to radiations of hard gluons. At high Q^2 the scattered electron has typically a high transverse momentum and is isolated from the hadronic final state.

A final state of CC DIS consists of a jet and the scattered neutrino or anti-neutrino (ν, $\bar{\nu}$), but the neutrino is not detected and results in an apparent missing transverse momentum. However, the missing transverse momentum can be measured and is a typical signature of a charged current event. The production of two or more jets is possible in NC or CC DIS final state due to gluon radiation.

Figures 2.2, and 2.3 show event displays of a typical NC DIS and CC DIS events, respectively (see chapter 3 for a description of the detector components).

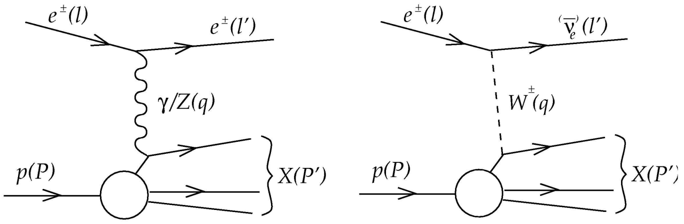

Figure 2.1: Diagrams of neutral (left) and charged (right) current deep inelastic scattering processes.

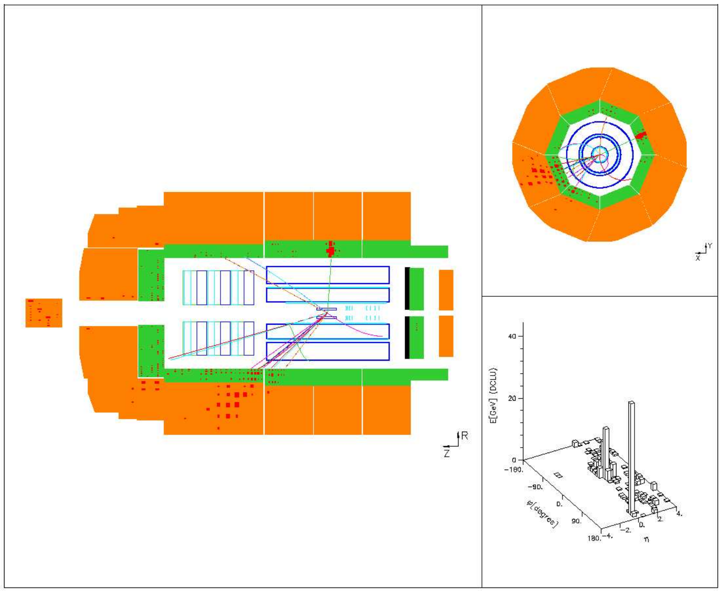

Figure 2.2: Display of a NC DIS event.

Kinematics of DIS Events:

The four-vectors of particles involved in the scattering processes of figure 2.1 are:

l - the four-vector of the incoming electron,
P - the four-vector of the incoming proton,
l' - the four-vector of the outgoing electron,
P' - the four-vector of the hadronic final state X,
$q = l - l'$ - the four-momentum carried by the exchanged boson.

Based on the four-vectors momenta of the incoming electron and proton, and of the final state lepton, the kinematics of the electron(positron)-proton scattering is determined at the lowest order by the following three Lorentz invariant variables:

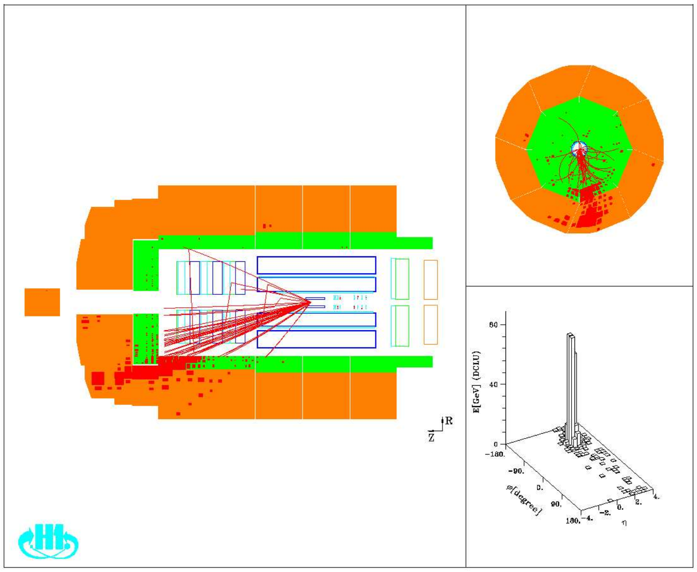

Figure 2.3: Display of a CC DIS event.

- the four-momentum transfer squared $q^2 = (l - l')^2$, q^2 is a measure of the virtuality of the exchanged boson, usually the positive quantity Q^2 is used:

$$Q^2 = -q^2 \, . \tag{2.1}$$

- the inelasticity y, which is the energy fraction lost by the incident electron in the proton rest frame:

$$y = \frac{P.\, q}{P.\, l} \, . \tag{2.2}$$

  In the rest frame of the proton, where $P = (M, 0, 0, 0)$, y is given by $(E_e^0 - E_e)/E_e^0$ with $E_e^0,\ E_e$, denoting the energies of the incoming electron(positron) and of the scattered lepton, as calculated from $P.\, q = P\,(l - l') = M\,(E_e^0 - E_e)$ and $P.\, l = M\ E_e^0$.

- the Bjorken scaling variable x:

$$x = \frac{Q^2}{2\,P.\, q} \, . \tag{2.3}$$

  In the "infinite momentum frame" (where the transverse momentum of the stuck quark can be neglected) x is the longitudinal proton momentum fraction carried by the stuck quark. This frame represents the basis idea of the Quark Parton Model (QPM), the assumption that the proton is made out of point-like constituents or "partons".

The three above variables are related to the square of the ep center-of-mass energy, $s = (P + l)^2 \approx 2\,P\,l = 4\,E_p\,E_e^0$, by $Q^2 = s\,x\,y$.

Unpolarised $e^{\pm}p$ DIS cross section:

The Born cross section for the deep inelastic ep scattering neutral current process is given by:

$$\frac{d^2\sigma_{NC}^{e\pm p}}{dx\,dQ^2} = \frac{2\,\pi\,\alpha^2}{x\,Q^4}\Phi_{NC}^{\pm}(x, Q^2)\ , \tag{2.4}$$

with

$$\Phi_{NC}^{\pm}(x, Q^2) = Y_+\ \tilde{F}_2^{\pm}(x, Q^2) - y^2\ \tilde{F}_L^{\pm}(x, Q^2) \mp \tilde{F}_3^{\pm}(x, Q^2)\ , \tag{2.5}$$

where $\alpha = e^2/4\pi$ is the fine structure constant. At leading order and by neglecting the contribution of the longitudinal structure function F_L and of $x\,F_3$, $\Phi_{NC}^{\pm}$ can be written as:

$$\begin{aligned}\Phi_{NC}^{\pm}(x, Q^2) &= Y_+\,x\left[\frac{4}{9}\left(u(x) + \bar{u}(x) + c(x) + \bar{c}(x)\right)\right.\\ &\quad\left. + \frac{1}{9}\left(d(x) + \bar{d}(x) + s(x) + \bar{s}(x) + b(x) + \bar{b}(x)\right)\right]\ ,\end{aligned} \tag{2.6}$$

where, $u(x),\ \bar{u}(x),\ c(x),\ \bar{c}(x),\ b(x),\ \bar{b}(x),\ s(x),\ \bar{s}(x)$ are the quarks and anti-quarks densities.

The charged current cross section can be written as:

$$\frac{d^2\sigma_{CC}^{e\pm p}}{dx\,dQ^2} = \frac{G_F^2}{2\pi x}\left[\frac{M_W^2}{Q^2 + M_W^2}\right]^2 \Phi_{CC}^{\pm}(x, Q^2). \tag{2.7}$$

We see that the CC DIS cross section has a structure similar to the NC DIS cross section (see equation (2.4)), the only difference is that the fine structure constant α is replaced by the Fermi coupling constant G_F and the photon propagator term $1/Q^4$ is replaced by the corresponding W propagator. Therefore, the CC DIS cross section is much smaller than the NC DIS cross section. In the quark parton model, the term $\Phi_{CC}^{\pm}$ can be expressed via quark and anti-quark densities as:

$$e^+ :\ \Phi_{CC}^{+}(x, Q^2) = x\left[(\bar{u}(x) + \bar{c}(x)) + (1 - y)^2(d(x) + s(x))\right]\ , \tag{2.8}$$

$$e^- :\ \Phi_{CC}^{-}(x, Q^2) = x\left[(u(x) + c(x)) + (1 - y)^2(\bar{d}(x) + \bar{s}(x))\right]\ . \tag{2.9}$$

From equations (2.8) and (2.9), for an incident positron emitting a W^+ boson, the cross section is sensitive to d quarks and u anti-quarks, and for an incident electron the cross section is sensitive to u quarks and d anti-quarks. CC DIS interactions can therefore distinguish flavors, which is not possible for photon exchange in NC DIS interaction. As the proton is composed of two u and one d valence quarks, the CC DIS cross section is much larger in e^-p collisions than in e^+p collisions. This is illustrated in figure 2.4.

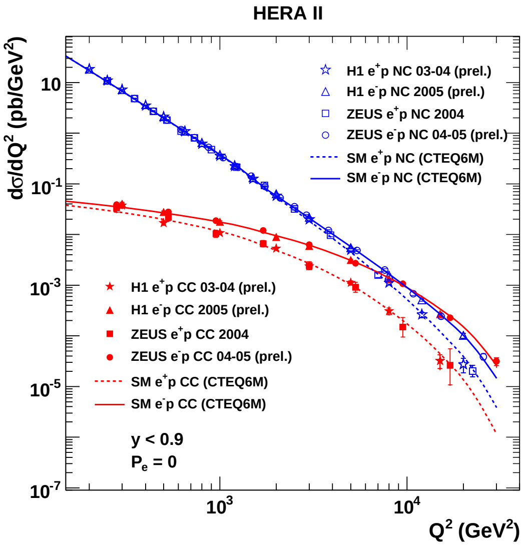

Figure 2.4: Cross section of unpolarized NC (open symbols) and CC (solid symbols) DIS processes as a function of Q^2, measured with the H1 and ZEUS detectors for the $2003-2004$ e^+p and 2005 e^-p data. The results are compared to the Standard Model expectation determined from the CTEQ6M proton density functions. This figure is taken from [26].

DIS cross section with polarized leptons:

During the HERA-II running period the lepton beam was longitudinally polarized (see section 3.1.2). If the longitudinal polarization (P_e) of the lepton beam is considered, the cross section of CC DIS processes now becomes:

$$\frac{d^2\sigma_{CC}^{e\pm p}}{dx\, dQ^2} = (1 \pm P_e)\,\frac{G_F^2}{2\pi x}\left[\frac{M_W^2}{Q^2+M_W^2}\right]^2 \Phi_{CC}^{\pm}(x,Q^2)\,. \tag{2.10}$$

Figure 2.5 presents the evolution of the total CC DIS cross section as a function of the polarization for e^+p and e^-p collision modes.

The polarized NC DIS cross section can be written as:

$$\frac{d^2\sigma_{NC}^{e\pm p}}{dx\, dQ^2} = \frac{2\,\pi\,\alpha^2}{x\,Q^4}\left[\Phi_{NC}^{\pm}(x,Q^2) + P_e\,\Phi_{NCpol}^{\pm}(x,Q^2)\right]\ , \tag{2.11}$$

where $\Phi_{NCpol}^{\pm}(x,Q^2)$ is similar to $\Phi_{NC}^{\pm}(x,Q^2)$ but involves quark densities and fermion axial and vertor couplings. Unlike for CC DIS, the NC DIS cross section is influenced by the lepton polarization only at high Q^2. More details can be found in [27].

2.2 Photoproduction

Photoproduction (γp) is a process where a quasi-real photon, emitted by the incident electron, interacts with the proton. The cross section of events with photon exchange depends on the four-momentum transfer as $1/Q^4$ (see equation (2.4)). Therefore, photoproduction is the dominant process as $Q^2 \rightarrow 0$ (events with Q^2 greater than a few GeV^2 are considered as NC DIS events). The photon can fluctuate into virtual pairs of charged leptons or quarks for a short time according to the quantum uncertainty principle. For photons of high energy the quark-antiquark pair can develop into a quark-gluon cascade leading to a complicated partonic object with the

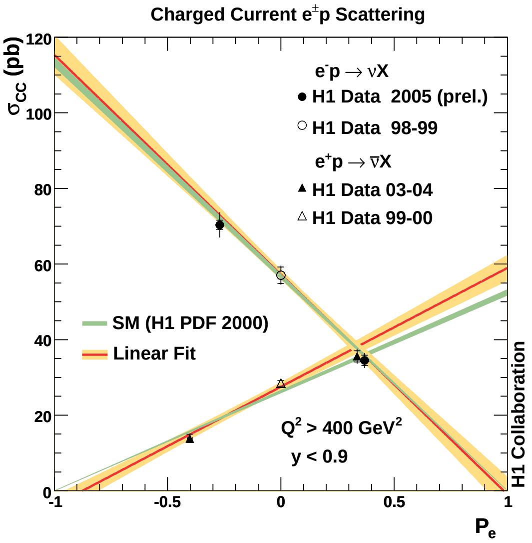

Figure 2.5: Dependence of the $e^{\pm}p$ CC DIS cross section with the lepton beam polarization P_e. This figure is taken from [28].

same quantum numbers as the photon. We distinguish two types of photoproduction processes according to the fluctuation of the photon. In the direct process, the exchanged photon couples directly to the quarks of the proton. In the resolved process, the photon fluctuates into a hadronic state and a parton of the photon enters the hard interaction, and in this case there is a photon remnant which is not participating in the hard interaction similar to the case of the electron(positron)-proton interaction. Two examples of photoproduction processes are shown in figure 2.6. The hadronic final state in the photoproduction process consists of at least two jets. Figure 2.7 shows a display of a photoproduction event.

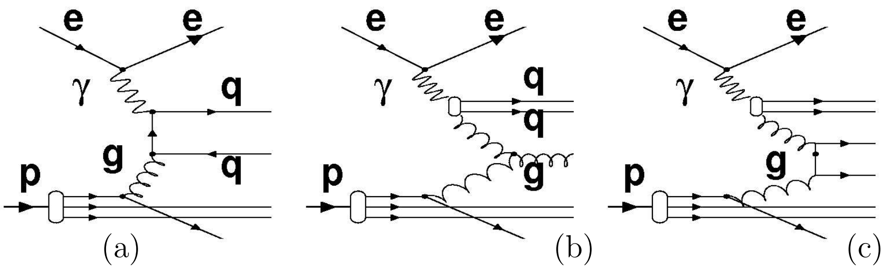

(a) (b) (c)

Figure 2.6: Diagrams for direct (a) and resolved (b,c) photoproduction processes.

2.3 QED compton

The final state of QED Compton processes, which is illustrated in figure 2.8, consists of the scattered electron and a radiated photon. The interaction can be elastic ($ep \rightarrow ep\gamma$) or inelastic ($ep \rightarrow eX\gamma$). These processes are also known as wide angle bremsstrahlung. An example of elastic QED Compton event is shown in figure 2.9.

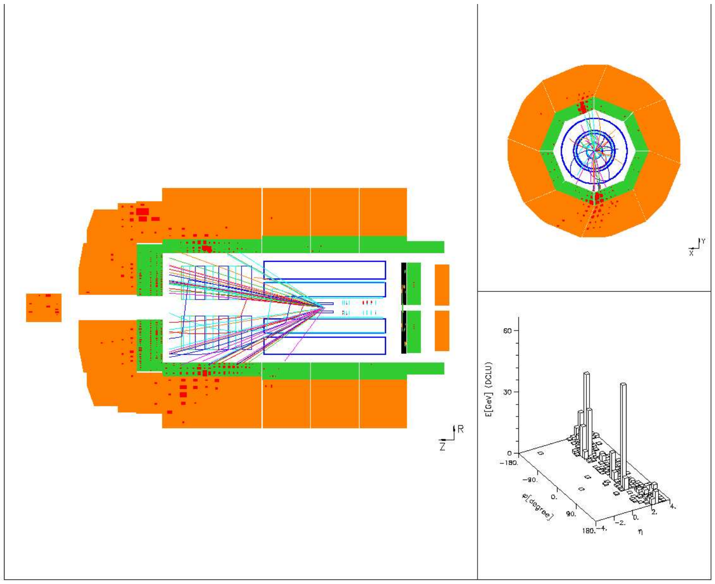

Figure 2.7: Display of a photoproduction event with two jets.

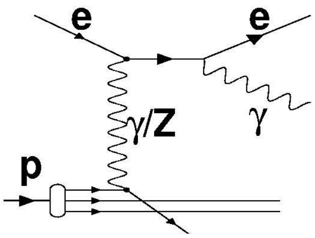

Figure 2.8: Diagram of the QED Compton diffusion.

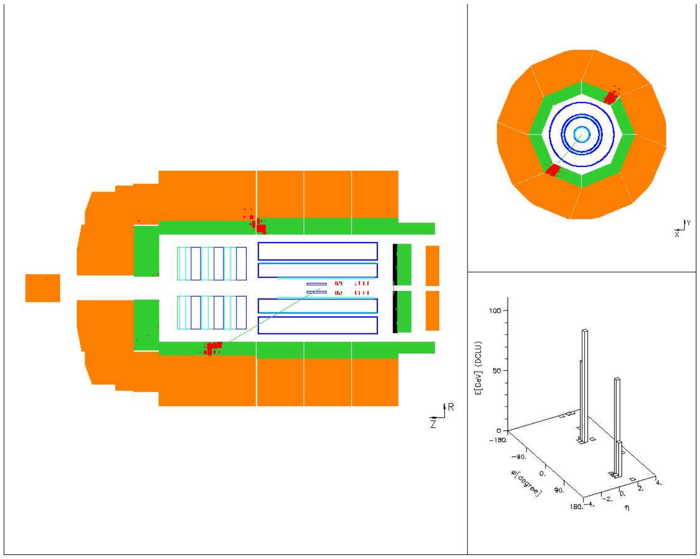

Figure 2.9: Display of a QED Compton event.

2.4 Lepton-Pair production

Pairs of leptons, $ep \rightarrow e\,X\,l^+\,l^-$, are dominantly produced at HERA by photon-photon interactions, one photon being radiated by the incident electron and the second by the proton. Figure 2.10 shows an example of the diagram of this process. The final state of this process consists of up to three leptons with a possible hadronic final state depending on the inelasticity of the interaction. Figure 2.11 shows a display of an electron pair event.

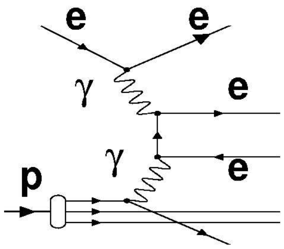

Figure 2.10: Diagram of lepton pair production at HERA.

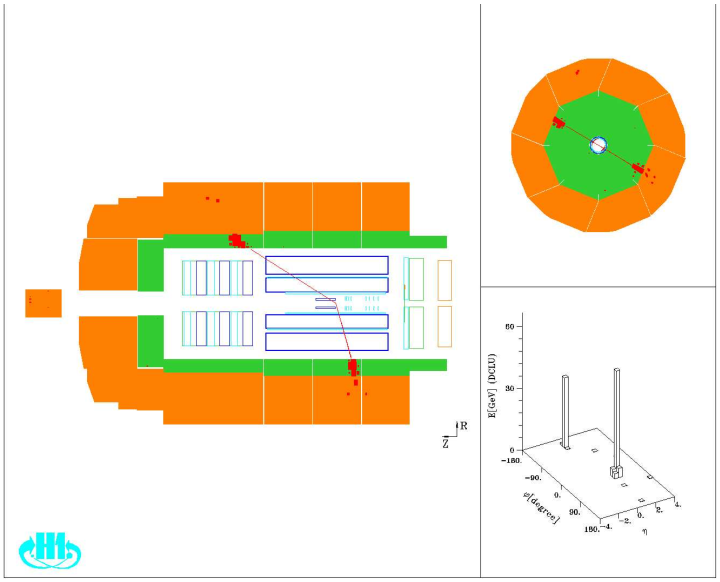

Figure 2.11: Display of an electron pair event.

2.5 W production

Another rare process is real $W^{\pm}$ production. The corresponding diagram is shown in figure 2.12. The $W^{\pm}$ is produced in $ep \rightarrow eWX$ or $ep \rightarrow \nu WX$ reactions. Figure 2.13 shows an example of a W production event with subsequent leptonic decay.

Some of the processes represented above occur often at HERA while others are observed only rarely. Table 2.1 gives a comparison of typical cross section of physics processes described above.

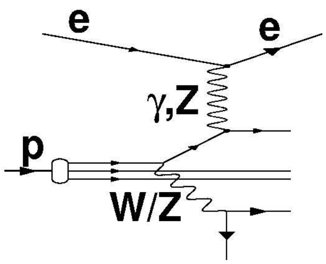

Figure 2.12: Main diagram of real $W^{\pm}$ production.

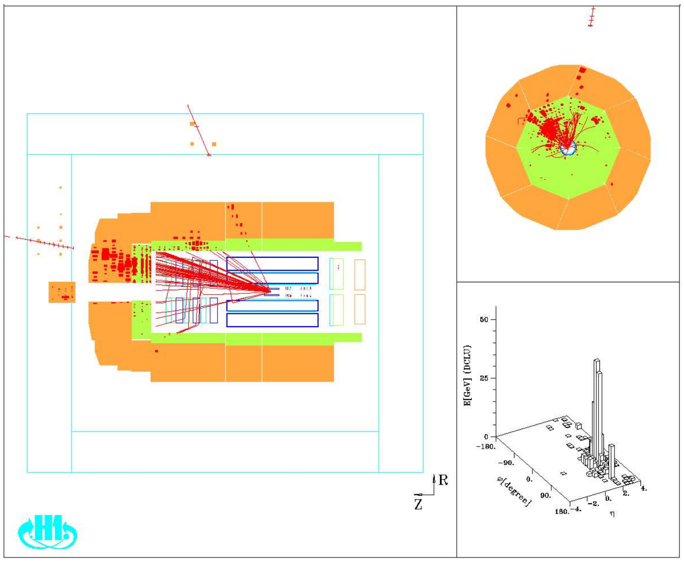

Figure 2.13: Display of a W event, with the W decaying into a neutrino and a muon.

Process	Restriction	Typical cross section (pb)
NC DIS	$Q^2 > 100$ GeV	7600
NC DIS	$Q^2 > 1000$ GeV	270
CC DIS	$Q^2 > 100$ GeV (e^+p)	35
CC DIS	$Q^2 > 100$ GeV (e^-p)	70
Photoproduction	Direct, $\hat{P}_T > 6$ GeV	14300
Photoproduction	Resolved, $\hat{P}_T > 6$ GeV	66400
QED Compton	Elastic	100
QED Compton	Quasi-elastic	60
QED Compton	Inelastic	90
Lepton Pair	Elastic	10
Lepton Pair	Inelastic	25
W production	Leptonic decay	0.05

Table 2.1: Typical cross sections of physics processes observed at HERA, predicted by the SM.

2.6 Production of excited leptons in *ep* collisions

In this section, we will first discuss the production and decay modes of excited leptons in *ep* collisions via a gauge mediated interaction. The cross section of excited electron production and their decay modes via contact interaction will then be presented.

2.6.1 Excited leptons production and decays via gauge interactions

The HERA *ep* collider is well suited to search for excited electrons and neutrinos. In *ep* collisions, the magnetic type coupling of electrons to first generation excited leptons allows the single production of excited electron e^* through $t-$channel γ or Z boson exchange and of excited neutrino ν^* via $t-$channel W boson exchange. Excited quarks may also be produced via $t-$channel exchange of a gauge boson (γ or Z, the contribution of W is negligible). Produced excited fermions will then decay into ordinary fermions plus a gauge boson. Figure 2.14 presents the diagrams of e^* (a) and ν^* (b) production in *ep* collisions and of possible subsequent decays.

In this section, the production cross section of excited leptons in *ep* collisions are detailed. Different approaches have to be followed for the calculation, depending on the photon virtuality Q^2 and on the mass W of the hadronic final state. A decomposition in three different regions for deep inelastic, elastic and quasi-elastic *ep* interactions is used:

- elastic region, i.e. elastic scattering off the proton: $W^2 = m_p^2$ with no restriction on Q^2 apart kinematical constraints.
- quasi-elastic region: $Q^2 < Q_0^2$, $W^2 > (m_p + m_\pi)^2$.
- deep-inelastic region: $Q^2 > Q_0^2$, $W^2 > (m_p + m_\pi)^2$.

The separation between the quasi-elastic and deep-inelastic regions is done depending on Q^2 by a threshold value Q_0^2, chosen here to be equal to 5 GeV^2.

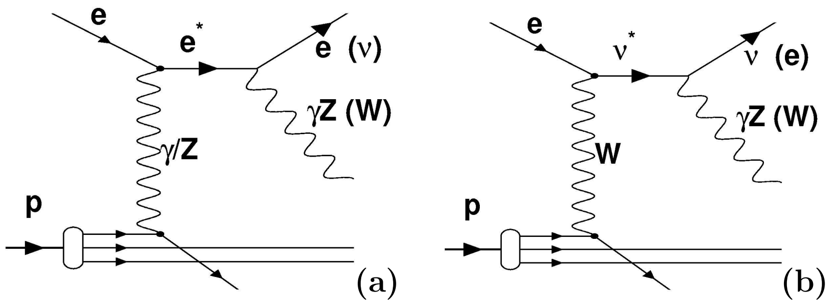

Figure 2.14: Diagrams of the production of excited electrons (a) and excited neutrinos (b).

The deep-inelastic total cross section for the process $ep{\rightarrow}F^*X$ is given by:

$$\sigma(ep{\rightarrow}F^*X) = \int_{\widehat{s}_{min}/s}^{1} dx \int_{Q_0^2}^{sx-m_{F^*}^2} dQ^2 \sum_q q(x,Q^2) \frac{d\widehat{\sigma}}{dQ^2}(eq{\rightarrow}F^*q'; \hat{s}=sx), \tag{2.12}$$

with $\widehat{s}_{min} = m_{F^*}^2 + Q_0^2$. It is a convolution of the effective quark distribution $q(x,Q^2)$ in the proton and the differential cross section which is expressed as:

$$\begin{aligned} \frac{d\widehat{\sigma}}{dQ^2}(eq{\rightarrow}F^*q') = \frac{2\,\pi\,\alpha^2}{\widehat{s}^2\,\Lambda^2}\,Q^2 \sum_{VV'} \Big\{ \Big[2\widehat{s}^2 - (Q^2+m_{F^*}^2)(2\widehat{s}-m_{F^*}^2)\Big]\ A_4^{VV'} \\ \pm\, m_{F^*}^2\, \left(2\,\widehat{s} - Q^2 - m_{F^*}^2\right)\, A_5^{VV'} \Big\}\, D_V(t)\, D_{V'}(t)^*, \end{aligned} \tag{2.13}$$

where $\widehat{s} = xs$ and $Q^2 = -t$. V, V' are the gauge bosons. The plus and minus signs are for scattering off quarks and anti-quarks, respectively. The coefficients $A_4^{VV'}$ and $A_5^{VV'}$ are the couplings between the gauge bosons and the leptons:

$$A_4^{VV'} \;=\; (a_{Vq'q}\, a_{V'q'q}^* + b_{Vq'q}\, b_{V'q'q}^*)(c_{VF^*e}\, c_{V'F^*e}^* + d_{VF^*e}\, d_{V'F^*e}^*), \tag{2.14}$$

$$A_5^{VV'} \;=\; (a_{Vq'q}\, b_{V'q'q}^* + b_{Vq'q}\, a_{V'q'q}^*)(c_{VF^*e}\, d_{V'F^*e}^* + d_{VF^*e}\, c_{V'F^*e}^*), \tag{2.15}$$

and $D_V(q^2) = [q^2 - m_V^2 + i\, m_V\, \Gamma_V\, \theta(q^2)]^{-1}$ is the gauge boson propagator factor, with $\theta(q^2)$ the Heaviside function and Γ_V the width of gauge bosons. The couplings c_{VF^*e} and d_{VF^*e} are defined in the section 1.4.1 and the $a_{Vq'q}$ and $b_{Vq'q}$ are the SM couplings of fermions with gauge bosons.

For ν^* production, as the only contribution comes from $t-$channel W exchange, most of the cross section comes from high Q^2 interactions, $Q^2 \geq 5$ GeV^2. On the contrary, for e^* production, the contribution at lower Q^2 (elastic and quasi-elastic) plays an important role and must be included.

In the elastic and quasi-elastic regions, the parton model is not valid and the electromagnetic proton structure functions $F_1(x,Q^2)$ and $F_2(x,Q^2)$ are used. Using these functions, the differential cross section is expressed as:

$$\begin{aligned} \frac{d^2\widehat{\sigma}}{dW^2 dQ^2} \;=\; & \frac{\pi\,\alpha^2}{\Lambda^2}\, \frac{|c_{\gamma e^* e}|^2 + |d_{\gamma e^* e}|^2}{(s-m_p^2)^2\, Q^4} \\ & \times \Big\{ 2\, F_1(x,Q^2)\, (2m_{F^*}^2 - Q^2)\, (m_{F^*}^2 + Q^2) + F_2(x,Q^2) \\ & \times \left[\frac{4\,(s-m_p^2)^2\, Q^2}{W^2+Q^2-m_p^2} - (m_{F^*}^2 + Q^2) \right. \\ & \left. \times \left(4\,s - W^2 - Q^2 - 3\,m_p^2 + \frac{4\,m_p^2\, m_{F^*}^2}{W^2+Q^2-m_p^2} \right) \right] \Big\}. \end{aligned} \tag{2.16}$$

The calculation for the elastic contribution uses the elastic form factors:

$$\begin{aligned} F_1(x,Q^2)|_{elas} \;&=\; \delta(W^2-m_p^2)\frac{Q^2}{2} G_M^2(Q^2), \\ F_2(x,Q^2)|_{elas} \;&=\; \delta(W^2-m_p^2){\times}Q^2 \left[G_E^2(Q^2) + \frac{Q^2}{4m_p^2} G_M^2(Q^2) \right] \left(1 + \frac{Q^2}{4m_p^2} \right)^{-1}, \end{aligned} \tag{2.17}$$

with G_E and G_M being taken from dipole fits of the electric and magnetic form factors of the proton:

$$G_E(Q^2) \approx G_M(Q^2)/2.79 \approx [1 + Q^2/0.71 \text{ GeV}^2]^{-2}. \tag{2.18}$$

For the quasi-elastic contribution, the electromagnetic structure function $F_1(x, Q^2)$ and $F_2(x, Q^2)$ are taken from an analytical parametrization of the resonance structure of the proton at low Q^2 [29].

Figure 2.15 shows separately the different contributions to the total e^* production cross section from the three kinematic regions, calculated using $Q_0^2 = 5$ GeV^2. At $M_{e^*} = 100$ GeV, the contribution of the elastic process to the total cross section is of the order of 40% and reaches 50% at 250 GeV.

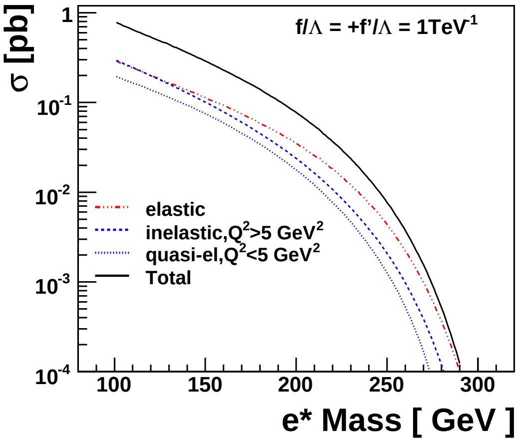

Figure 2.15: Production cross section for e^* from the three kinematic regions: elastic, quasi-elastic and inelastic. The total e^* cross section is also shown (plain-black curve). These results are obtained with the assumptions $f = +f'$, $Q_0^2 = 5$ GeV^2 and $\Lambda = 1$ TeV.

Excited neutrinos are produced by a $t-$channel exchange of a W boson, similarly to charged currents. The incident lepton charge influences the charge of the W boson emitted by the lepton and thus the flavour of the scattered quark. The ν^* production cross section therefore depends on the u and d valence quarks and sea quarks distributions. This cross section is also influenced by a term $Y_\pm = 1 \pm (1-y)^2$, corresponding to the helicity dependence of the electroweak interaction. It is much larger in e^-p collisions where the u valence quark of the proton intervenes (to conserve the charge, the quark must loose one charge unit so that the incident electron can gain one and becomes a neutral neutrino) than in e^+p collisions where the d valence quark interact mainly. For example, the cross section to produce a ν^* of mass $M_{\nu^*} = 250$ GeV is 3.33×10^{-4} pb in e^-p collisions, compared to 1.16×10^{-6} pb in e^+p collisions (for $f = -f'$, $\Lambda = 1$ TeV). Nevertheless, the ν^* production cross section remains smaller than e^* production cross section, coming mainly from the exchange of a photon at much lower Q^2. In figure 2.16 the total ν^* production cross section in ep collisions at a center-of-mass energy of 319 GeV is compared to the e^* production cross section with the assumption $f = +f'$. The ν^* production cross section is clearly one order of magnitude smaller than the e^* production cross section in the accessible mass range.

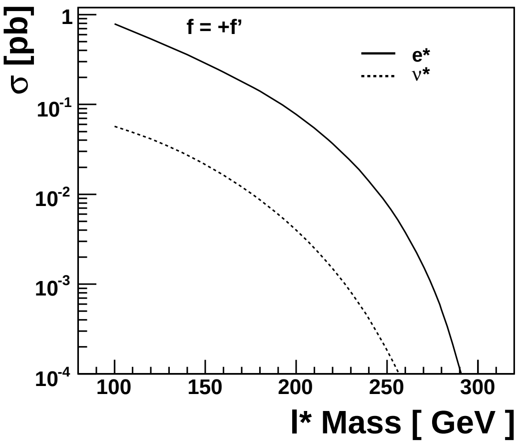

Figure 2.16: Total ν^* production cross section compared to e^* production cross section with the assumptions $f = +f'$ and $\Lambda = 1$ TeV.

In addition, similarly to CC DIS, the effect of longitudinal polarization of the incident electron beam to ν^* production cross section will be introduced through:

$$\sigma^{\nu^*}_{pol} = (1 \pm P_e)\, \sigma^{\nu^*}_{unpol}\,. \tag{2.19}$$

For the present analysis the periods with left and right-handed beams are combined and the e^-p data sample used in the ν^* search has a residual polarisation of 5% left-handed.

Excited leptons decay modes

The decay width of excited fermions into a V boson $f^* \to f\ V$ is proportional to $\frac{m^3_{F^*}}{\Lambda^2}$ and can be written in terms of the c_{VF^*F} and d_{VF^*F} couplings, the fine structure constant $\alpha = e^2/4\pi$, and the compositeness scale Λ [29]:

$$\Gamma(F^* \to FV) = \frac{\alpha}{4} \frac{m^3_{F^*}}{\Lambda^2}\, c^2_{VF^*F} \left(1 - \frac{m^2_V}{m^2_{F^*}}\right)^2 \left(1 + \frac{m^2_V}{2\, m^2_{F^*}}\right)\,, \tag{2.20}$$

where m_V is the mass of the V boson.

According to the Lagrangian (1.10), excited electrons have three possible decays: $e^* \to e\gamma$ (radiative decay), $e^* \to \nu W$ and $e^* \to eZ$. The Z and W bosons can subsequently decay to hadrons or leptons. Similarly, excited neutrinos have three possible gauge decays: $\nu^* \to \nu\gamma$ (radiative decay), $\nu^* \to \nu Z$ and $\nu^* \to eW$.

The branching ratio of a specific gauge decay channel is defined as:

$$BR(F^* \to F\, V) = \frac{\Gamma(F^* \to FV)}{\sum_{V=\gamma,Z,W} \Gamma(F^* \to FV)}. \tag{2.21}$$

Relative branching ratios between the three different decay modes of an F^* can be fixed by assuming fixed numerical relations between f and f' and they are independent of Λ. As m_{F^*} increases, the relative branching ratios of the three decay channels become constant as shown in figure 2.17 for excited electrons and in figure 2.18 for excited neutrinos. Assuming a relationship between f and f' allows also to express the excited lepton production cross section as a function of only two parameters, the ratio f/Λ and the mass m_{F^*}. Two conventional assumptions are used: $f = -f'$ and $f = +f'$.

According to the relations between f and f' introduced in equations (1.11), (1.12) and (1.13), the e^* production cross section in the assumption $f = -f'$ (meaning $c_{e^*e\gamma} = 0$) becomes much smaller than for $f = +f'$ ($\sigma^{e^*}_{(f=-f')}$~7.8×10^{-6} pb, $\sigma^{e^*}_{(f=+f')}$~7.1×10^{-3} pb for an e^* mass of 250 GeV). Therefore, only the case $f = +f'$ will be studied for e^* production. In the case of ν^* production, the coupling $c_{W\nu^*e}$ is independent of the relation between f and f' and both relationships $f = -f'$ and $f = +f'$ are considered. However, the electromagnetic decay of excited neutrinos is forbidden under the assumption $f = +f'$. Figure 2.19 presents the relative branching ratios for excited electron and excited neutrino decays as a function of ratio f/f'. We can see that the electromagnetic coupling of e^* and ν^* vanishes if $f = -f'$ and $f = +f'$, respectively.

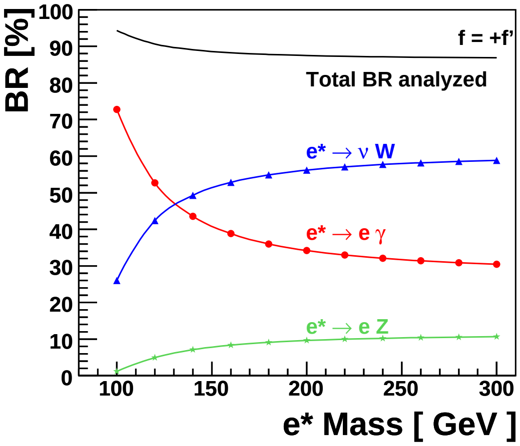

Figure 2.17: Relative branching ratio (BR) of e^* decay channels as a function of the e^* mass for $f = +f'$. The black curve represents the total branching ratio accessed in this analysis.

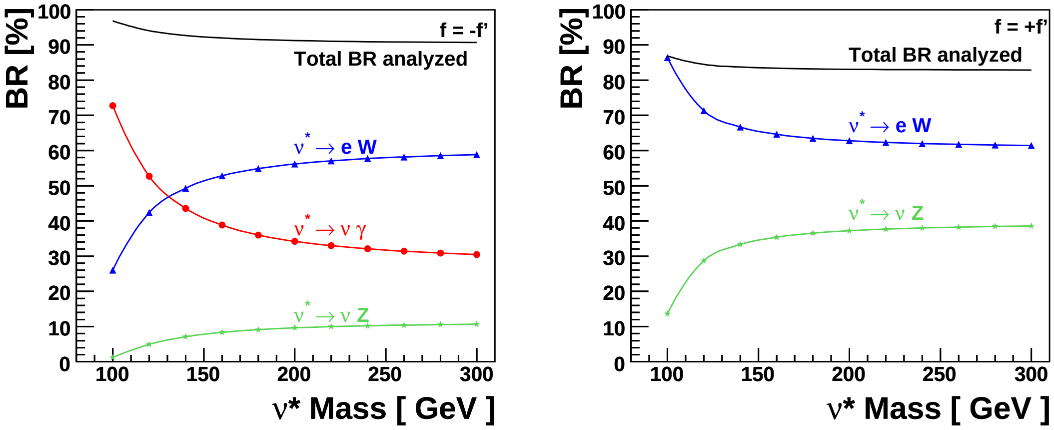

Figure 2.18: Relative branching ratio of ν^* decay channels as a function of the ν^* mass for $f = -f'$ (left) and $f = +f'$ (right). The black curve represents the total branching ratio accessed in this analysis.

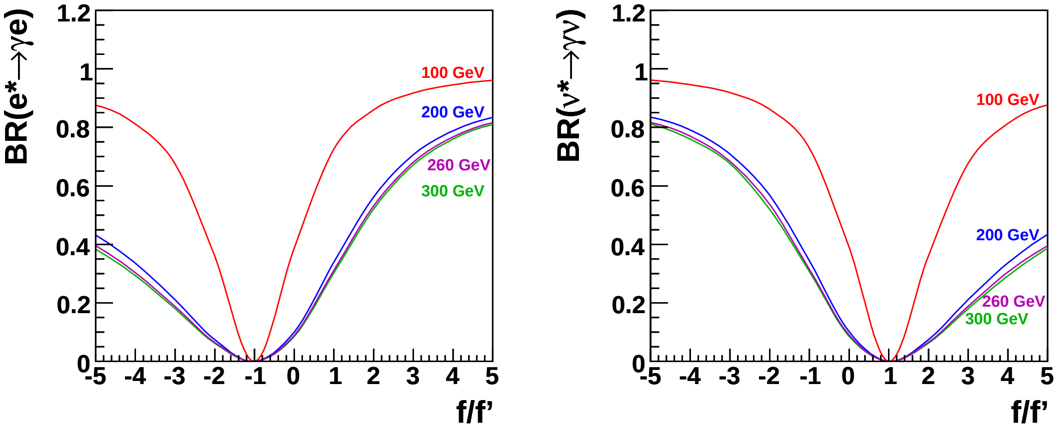

Figure 2.19: Electromagnetic branching ratio of excited electrons (left) and excited neutrinos (right) for different values of f, f' and for excited lepton masses of 100, 200, 260 and 300 GeV.

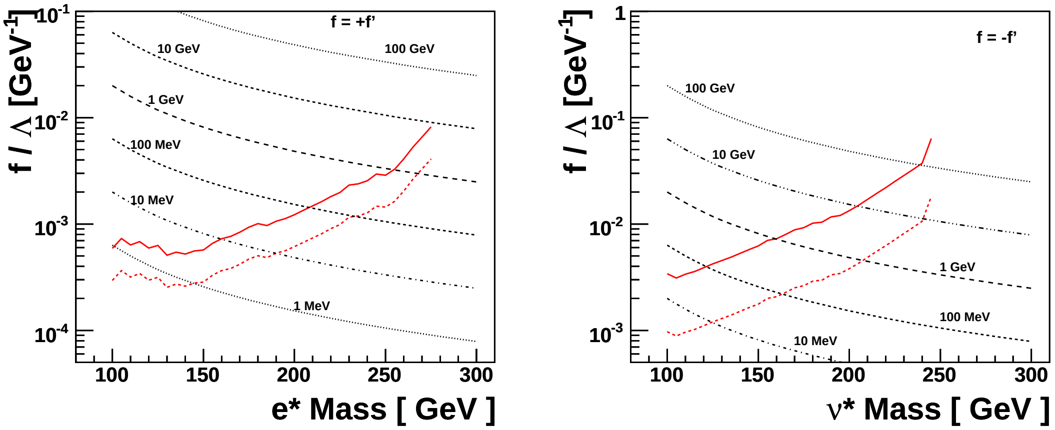

Figure 2.20: Decay width of excited electron (left) and excited neutrino (right) as a function of their mass and of the coupling constant f/Λ. For each case, the HERA-I limit is shown by the red plain curve. The red dashed curve corresponds to the extrapolated limit expected with the additional luminosity of this analysis.

In figure 2.20, the evolution of the total decay widths of e^* (left) and ν^* (right) as calculated from equation (2.20), is presented as a function of f/Λ and of the mass of the excited lepton. The limits obtained in previous ν^* and e^* H1 searches are also displayed, as well as the limits we expect to obtain in this analysis using new additional data. In the case of ν^* with a mass below 230 GeV, the decay width remains smaller than the detector resolution for f/Λ value expected to be probed, thus the narrow width approximation (NWA) is applicable. The NWA uses the assumption that the production $ep \rightarrow l^* X$ and the decay $l^* \rightarrow lV$ of a particle factorize. However, in the high mass region ($M_{\nu^*} > 230$ GeV), the ν^* decay widths can reach a few hundred GeV, much larger than the detector resolution (~ 10 GeV). The production and the decay of the ν^* should therefore be considered together ($ep \rightarrow lVX$). A dedicated Monte Carlo program has been developed for this purpose in this analysis. It will be used to calculate the ν^* production cross section and to simulate ν^* events (see section 2.7.2.2). In the case of e^* with masses below 290 GeV, we can see that the NWA assumption is valid for all f/Λ values relevant to this analysis, since the natural width of the e^* is in that case of the order of the experimental resolution or smaller.

2.6.2 Excited electrons production cross section and their decays via CI

As seen in section 1.4.2, resonant production in *ep* collision and decays of excited leptons may also be induced by new contact interactions. Therefore, the possibility of e^* production by gauge and contact interactions together will also be studied in this thesis.

The parton cross section of excited electron production via contact interaction can be expressed as [30]:

$$\frac{d\hat{\sigma}^{CI}}{d\hat{s}\,dt} = \left(\frac{8\,\pi}{\Lambda^2}\right)^2 \left(\eta^2_{L,e}\left[\hat{s}\,(\hat{s}-m^2_{F^*})\,\eta^2_{L,q} + (\hat{s}+t)\,(\hat{s}+t-m^2_{F^*})\,\eta^2_{R,q}\right]\right.$$
$$\left. +\eta^2_{R,e}\left[\hat{s}\,(\hat{s}-m^2_{F^*})\,\eta^2_{R,q} + (\hat{s}+t)\,(\hat{s}+t-m^2_{F^*})\,\eta^2_{L,q}\right]\right). \qquad (2.22)$$

If gauge (GM) and contact (CI) interactions are considered together, the total e^* production cross section σ^{CI+GM} is the sum of pure GM and CI cross section and of the interference between the two processes:

$$\sigma^{CI+GM} = \sigma^{GM} + \sigma^{CI} + \sigma^{interf}, \qquad (2.23)$$

where σ^{interf} is the interference term between the gauge and contact interactions, σ^{CI} and σ^{GM} are the CI and GM cross sections, respectively.

The differential cross section of the interference term σ^{interf} can be written as [30]:

$$\begin{aligned}\frac{d\hat{\sigma}^{interf}}{d\hat{s}\;dt} &= \left(\frac{32\pi}{\Lambda^3}\right)\left(\frac{\mathrm{A}^L_{e^*\gamma}}{t}\,m_{F^*}\,t\,\eta_{e,L}\left[-(\hat{s}+t-m^2_{F^*})\,\mathrm{A}^R_{q\gamma}\,\eta_{q,R} + \hat{s}\,\mathrm{A}^L_{q\gamma}\,\eta_{q,L}\right]\right. \\ &\left. + \frac{\mathrm{A}^L_{e^*Z}}{(t-m^2_Z)}\,m_{F^*}\,t\,\eta_{e,L}\left[-(\hat{s}+t-m^2_{F^*})\,\mathrm{A}^R_{qZ}\,\eta_{q,R} + \hat{s}\,\mathrm{A}^L_{qZ}\,\eta_{q,L}\right]\right)\,,\end{aligned} \qquad (2.24)$$

where q are the u or d valence quarks, the coefficients $\mathrm{A}^L_{e^*\gamma}$, $\mathrm{A}^L_{e^*Z}$, $\mathrm{A}^{L,R}_{q\gamma}$ and $\mathrm{A}^{L,R}_{qZ}$ are defined as:

$$\begin{aligned}\mathrm{A}^L_{e^*\gamma} &= -\frac{1}{2}\,e\,(f+f')\,, \\ \mathrm{A}^L_{e^*Z} &= \frac{e}{\sin\theta_W\cos\theta_W}\left[-\frac{1}{2}\left(f\,\cos^2\theta_W - f'\,\sin^2\theta_W\right)\right],\end{aligned}$$

for $q = u$:

$$\begin{aligned}
\mathrm{A}^{L}_{u\gamma} &= \mathrm{A}^{R}_{u\gamma} \;=\; \frac{2}{3}\,e, \\
\mathrm{A}^{L}_{uZ} &= \frac{e}{\sin\theta_W \cos\theta_W}\left[\frac{1}{2}-\frac{2}{3}\sin^2\theta_W\right];\; \mathrm{A}^{R}_{uZ} = \frac{e}{\sin\theta_W \cos\theta_W}\left[-\frac{2}{3}\sin^2\theta_W\right],
\end{aligned}$$

for $q = d$:

$$\begin{aligned}
\mathrm{A}^{L}_{d\gamma} &= \mathrm{A}^{R}_{d\gamma} \;=\; -\frac{1}{3}\,e\,, \\
\mathrm{A}^{L}_{dZ} &= \frac{e}{\sin\theta_W \cos\theta_W}\left[-\frac{1}{2}+\frac{1}{3}\sin^2\theta_W\right];\; \mathrm{A}^{R}_{dZ} = \frac{e}{\sin\theta_W \cos\theta_W}\left[\frac{1}{3}\sin^2\theta_W\right],
\end{aligned}$$

where e is the electromagnetic coupling ($e^2 = 4\,\pi\alpha$).

The parameter Λ is assumed to be the same in gauge and contact interaction Lagrangians of equations (1.10) and (1.15), respectively. For simplicity, we will assume that the relative strength of gauge and contact interactions are fixed by setting the parameters f and f' of the gauge interaction to one. The η factors of left-handed currents are also set to one, while the factors of right-handed currents are considered to be zero. Thus, the parton cross sections for the contact and interference terms can be written as:

$$\frac{d\hat{\sigma}^{CI}}{d\hat{s}\,dt} = \left(\frac{8\,\pi}{\Lambda^2}\right)^2 \hat{s}^2 \left(1 - \frac{m^2_{F^*}}{\hat{s}}\right), \tag{2.25}$$

$$\frac{d\hat{\sigma}^{interf}}{d\hat{s}\,dt} = \frac{32\,\pi}{\Lambda^2}\,\hat{s}\,m_{F^*}\left[\mathrm{A}^{L}_{e^*\gamma}\,\mathrm{A}^{L}_{q\gamma} + \mathrm{A}^{L}_{e^*Z}\,\mathrm{A}^{L}_{qZ}\,\frac{t}{t-m^2_Z}\right]. \tag{2.26}$$

Figure 2.21 presents the comparison of the e^* production cross sections via gauge interactions only and via GM and CI together, as a function of the e^* mass and for different compositeness scales. We can observe that the ratio of the contact and gauge cross sections decreases as Λ or m_{e^*} increases. We can also note that the interference term leads to a reduction of the cross section. As an example, for $m_{e^*} = 150$ GeV and $\Lambda = 1$ TeV, the ratio $\sigma_{CI+GM}/\sigma_{GM}$ is equal to 8.4, but it reduces to 1.3 for $\Lambda = 4$ TeV.

Via contact interaction, the excited electron can decay into an electron and a pair of the SM fermions $e^* \rightarrow e + f'\bar{f}'$, with $f'\bar{f}' = (q\bar{q}, e\bar{e}, \mu\bar{\mu}, \nu\bar{\nu}, \tau\bar{\tau})$. The width of e^* decays mediated by contact interactions is given by [22]:

$$\Gamma(e^* \rightarrow e + f'\bar{f}') = \frac{m_{F^*}}{96\,\pi}\left(\frac{m_{F^*}}{\Lambda}\right)^4 N'_c\,S', \tag{2.27}$$

where, $N'_c = 3$ or 1 is the number of colors of the SM fermion f', and S' is an additional combinatorial factor:

- $S' = 1$ for $f \neq f'$,

- $S' = \frac{4}{3}$ for $f = f'$ and quarks,

- $S' = 2$ for $f = f'$ and leptons.

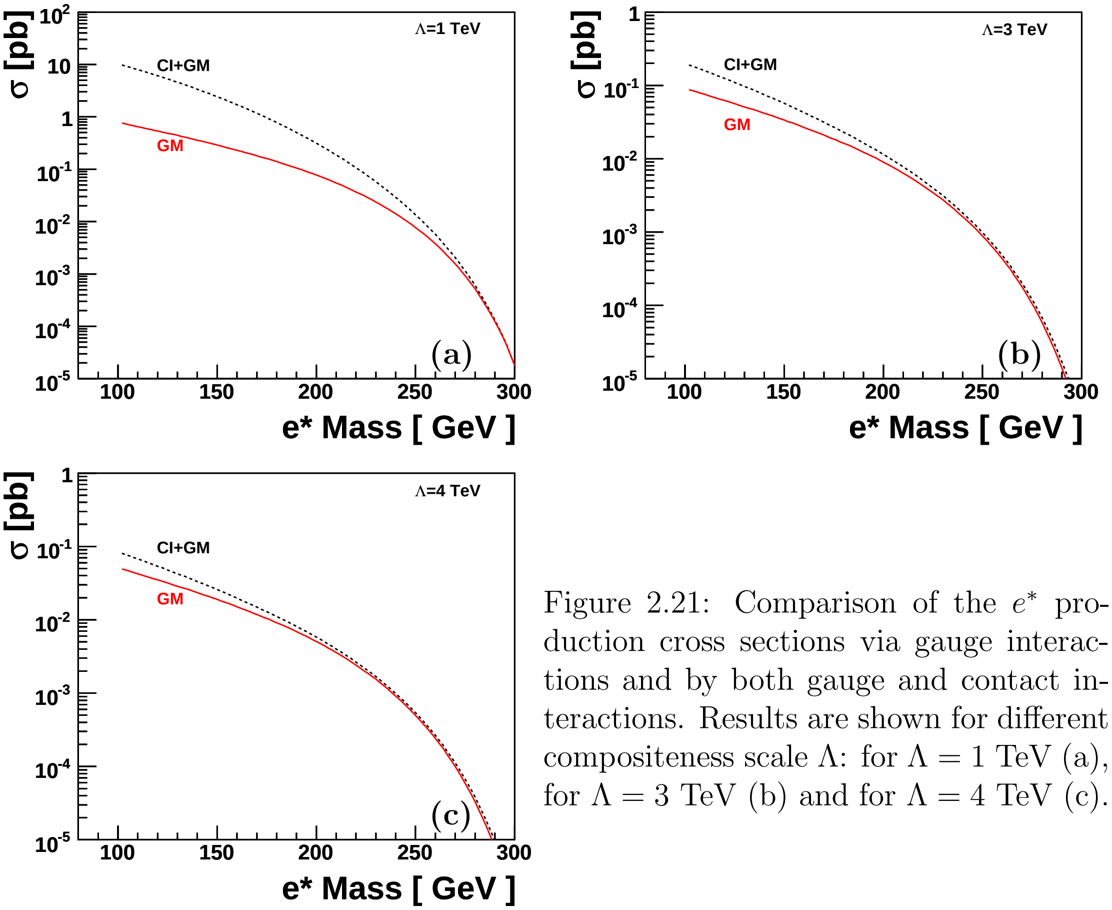

Figure 2.21: Comparison of the e^* production cross sections via gauge interactions and by both gauge and contact interactions. Results are shown for different compositeness scale Λ: for $\Lambda = 1$ TeV (a), for $\Lambda = 3$ TeV (b) and for $\Lambda = 4$ TeV (c).

So the partial width of decay via contact interactions is proportional to $\frac{m_{F*}^5}{\Lambda^4}$, while as presented in section (2.6.1) the partial width of decays via gauge interactions varies as $\frac{m_{F*}^3}{\Lambda^2}$. Therefore, the relative importance of the decay mediated by CI on the total decay width will be suppressed by a factor $\frac{m_{F*}^2}{\Lambda^2}$. Figure 2.22 shows the relative branching ratios (BR) of e^* decays via contact and gauge interactions as a function of the e^* mass. In the mass range accessed at HERA, e^* decays are dominated by gauge decays, provided that Λ is large enough. For example, for $\Lambda = 3$ TeV, contact interaction decays contribute to maximum 12% of all possible decays. Therefore, only gauge decays will be looked for in the present e^* search.

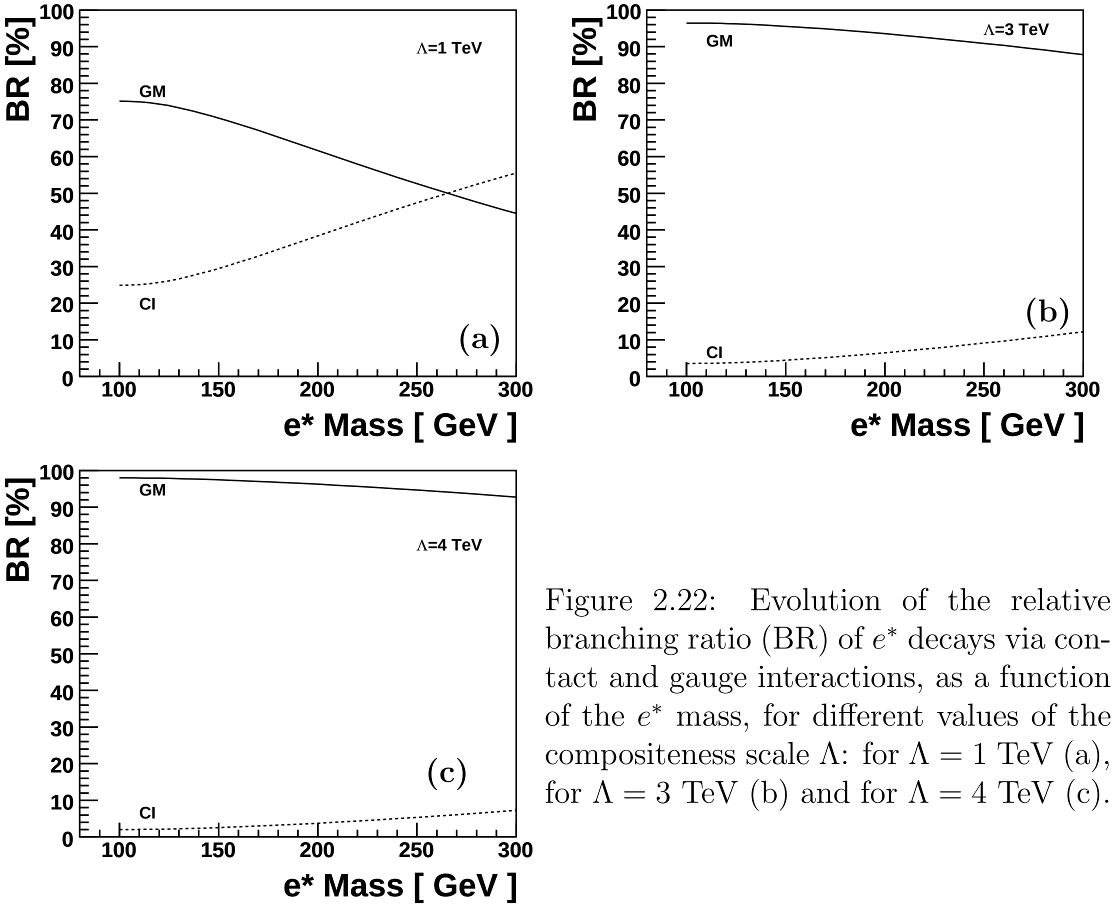

Figure 2.22: Evolution of the relative branching ratio (BR) of e^* decays via contact and gauge interactions, as a function of the e^* mass, for different values of the compositeness scale Λ: for $\Lambda = 1$ TeV (a), for $\Lambda = 3$ TeV (b) and for $\Lambda = 4$ TeV (c).

2.7 Simulations of physics processes

Simulation of physics events in the detector is done using Monte Carlo[1] programs, a traditional technique in physics. The format of a Monte Carlo event is in any point similar to a real data event if the "true" quantities of the generated event are not known. Monte Carlo is a very powerful tool to simulate the different effects of the detector response. The generation of an event is performed in three distinct steps. First of all, the physics process is generated by a program which calculates the hard interaction cross section (matrix element). The QED radiative effects arising from real photon emission from both the incoming and outgoing electrons are simulated using the HERACLES program. For QCD corrections, two models are used: the parton shower model MEPS (Matrix Element and Parton Showers) or the Color Dipole Model (CDM). Then the hadronisation of the particles is simulated. In general, the Lund string model is used for this step. It describes the fragmentation using a model of color strings.

The response of the detector is simulated by the H1SIM [53] program, based

---

[1] The name was originally used in the Manhattan Project at Los Alamos in the 1940's and was suggested by the gambling casinos in Monte Carlo, Monaco as a suitable name to describe the random number method used in numerical integrations [31].

on the GEANT3 [54] simulation program. H1SIM can be used either in a detailed simulation model, including all interactions of the particles with the detector, or in a simplified mode (H1FAST) which is faster and uses parameterizations to describe particle showers. The simulated events are then reconstructed by H1REC exactly in the same way as real data events. The simulation and the reconstruction of a H1 event in the HERA-II configuration takes of the order of 20 seconds, depending on the computer and the complexity of the event.

2.7.1 Simulation of Standard Model processes

As discussed in section 2.6.1, the production and decay of ν^* or e^* may lead to a large variety of possible final states, depending on the hadronic or leptonic decays of the W and Z bosons. As the majority of these possible final states will be studied, an accurate simulation of main possible SM processes is needed.

The background expectation from a NC DIS process is calculated using the event generator RAPGAP [32] in which the hard sub-process is generated according to the cross section obtained from the CTEQ5L [33] parametrization for the parton density functions (PDFs). The first order QED corrections are based on the HERACLES program [34] and QCD radiations are included via first order QCD matrix elements and parton showers (MEPS). The prediction of NC DIS processes with two or more high transverse momentum jets is scaled by a factor of 1.2 to normalize this leading order Monte Carlo simulation to next-to-leading order QCD calculations [35]. An error of 20% on the simulation of NC DIS processes with at least two high transverse momentum jets in the event final state is considered to account for the uncertainty on higher order QCD corrections.

The background expectation from CC DIS processes is calculated using the LEPTO program [36] interfaced to HERACLES via DJANGOH [37]. First order leptonic QED radiative corrections are taken into account by HERACLES. The H1PDF2000 [38] proton PDFs is used. The QCD radiation for CC DIS events is modelled with the colour-dipole model (CDM) [39] using the ARIADNE program [40]. In this thesis, the model uncertainty attributed to the simulation of CC DIS events with at least two high P_T jets is 20%. An uncertainty of 30% on the simulation of radiative CC DIS events is considered to account for the lack of QED radiation from the quark line in the DJANGOH generator. This uncertainty is estimated in the specific phase space of the analysis by a comparison of the DJANGOH result to the calculated cross section for the $e^-p\rightarrow\nu_e\gamma X$ process [41].

To simulate the direct and resolved photoproduction of jets and prompt photoproduction, the PYTHIA 6.1 event generator [42] is used. The simulation is based on Born level hard scattering matrix elements with radiative QED corrections. As for NC DIS processes, a factor of 1.2 is applied to γp events with at least two high P_T jets. An error of 20% on the simulation of photoproduction processes with at least two high P_T jets is also considered, to account for the uncertainty on higher order QCD corrections.

The simulation of elastic and quasi-elastic QED Compton scattering, the WABGEN [43] generator is employed. The error on the elastic QED Compton cross section is conservatively estimated to be 5%. Inelastic QED Compton events are included in the NC DIS simulations using RAPGAP. An error of 10% on the cross section of the process is considered, mainly coming from the uncertainty on the PDFs.

Contributions from W production or multi-lepton events are also considered. Multi-lepton events are simulated using the GRAPE [44] event generator. GRAPE is based on a full calculation of all electroweak diagrams taking into account intermediate photons and final state interferences. All three lepton generations are considered. Finally, W bosons events are simulated using the EPVEC [45] event generator. The uncertainty attributed to the simulation of lepton pairs production is 3%, as studied in [46]. Previous studies have shown that the cross section of the process $ep \rightarrow eW^{\pm}X$ is known to 15% [47].

Table 2.2 summarizes the amount of generated events for each SM process mentioned above.

2.7.2 Signal Monte Carlo Samples

Here we introduce the Monte Carlo generators used for ν^* and e^* production cross section calculations and for the simulation of signal events used to determine the efficiency of final selections.

2.7.2.1 e^* signal Monte Carlo

The COMPOS [48] generator is used for the calculation of the e^* production cross section and the simulation of signal events. It is based on the cross section formula given in section 2.6.1 for gauge interactions. Cross section formula for contact interaction production and for the interference between contact and gauge interactions are given in section 2.6.2 and have also been incorporated into COMPOS. Only gauge decay channels are simulated. Samples of excited electron events are generated for e^* masses up to 290 GeV. For e^* masses up to 290 GeV, the narrow width approximation is assumed. Initial state radiation of a photon from the incident electron is included using the Weizsäcker-Williams approximation [50]. The proton parton densities are taken from the CTEQ5L [33] parametrisation and are evaluated at the scale $\sqrt{Q^2}$. The hadronisation is performed by the Lund string fragmentation as implemented in PYTHIA [42].

For the e^* decay, the angular distribution of the outgoing lepton with respect to the incoming lepton in the e^* rest frame is given by:

$$\frac{1}{\Gamma}\frac{d\Gamma}{d\cos\theta^*} = \frac{1+\cos\theta^* + \frac{k}{2}(1-\cos\theta^*)}{2+k}\,, \tag{2.28}$$

where θ^* is the angle of the outgoing lepton in the e^* rest frame and $k = m_V^2/m_{F*}^2$ $(V = \gamma,\ Z,\ W)$.

Process(es)	Generator	Phase Space	Subprocess	$\mathcal{L}_{\text{MC}}/\mathcal{L}_{\text{data}}$
Photoproduction	PYTHIA61	$\hat{P}_T > 10$ GeV		2.74
		$\hat{P}_T > 15$ GeV		19
		$\hat{P}_T > 25$ GeV		183
		$\hat{P}_T > 40$ GeV		360
		$\hat{P}_T > 75$ GeV		2554
		$\hat{P}_T > 95$ GeV		50995
Prompt Photon	PYTHIA61	$\hat{P}_T > 10$ GeV		54.4
		$\hat{P}_T > 20$ GeV		602
		$\hat{P}_T > 40$ GeV		21787
NC DIS	RAPGAP	$Q^2 > 100$ GeV^2		6.7
		$Q^2 > 400$ GeV^2		42
		$Q^2 > 1000$ GeV^2		58
		$Q^2 > 2500$ GeV^2		89
		$Q^2 > 5000$ GeV^2		192
		$Q^2 > 10000$ GeV^2		603
		$Q^2 > 20000$ GeV^2		4470
CC DIS	DJANGO	$Q^2 > 100$ GeV^2		192
		$Q^2 > 10000$ GeV^2		1252
Lepton Pair Production	GRAPE		e-e	1953
			μ-μ	814
			τ-τ	1085
QED Compton	WABGEN	$M_{e\gamma} > 10$ GeV		11.6
		$M_{e\gamma} > 50$ GeV		416
		$M_{e\gamma} > 100$ GeV		6273
W Production	EPVEC			1085

Table 2.2: List of the different MC sets used in this analysis. The ratio of the amount of generated luminosity to the data luminosity is indicated in the right column.

The theoretical uncertainty on the e^* production cross section is dominated by the uncertainty on the scale at which the proton parton densities are evaluated. It is estimated by varying this scale from $\sqrt{Q^2}/2$ to $2\sqrt{Q^2}$. This resulting uncertainty depends on the e^* mass and is 10% at $M_{e^*} = 100$ GeV increasing to 15% at $M_{e^*} \sim 300$ GeV.

2.7.2.2 ν^* signal Monte Carlo

As mentioned in section 2.6.1, the decay width of the excited neutrino can reach, for a part of the accessible mass range, a few hundred GeV. The narrow width approximation can not be used for the simulation of ν^* events. To deal with this problem a new generator, called H1NuStar, was developed in collaboration with E. Perez. It is used to calculate production cross sections and to generate events with masses up to the kinematic limit and for all three electroweak decay channels.

In the H1NuStar generator the full cross section for ν^* production and decays is evaluated with CompHEP [52] using the Lagrangian (1.10). The parton distribution set CTEQ5L is used and they are evaluated at the scale $\sqrt{Q^2}$. The generator is interfaced to PYTHIA 6.1 [42], to perform the fragmentation, the hadronization and to include the QCD radiation, in the parton shower approach. Initial state radiation of a photon from the incident electron is included using the Weizsäcker-Williams approximation.

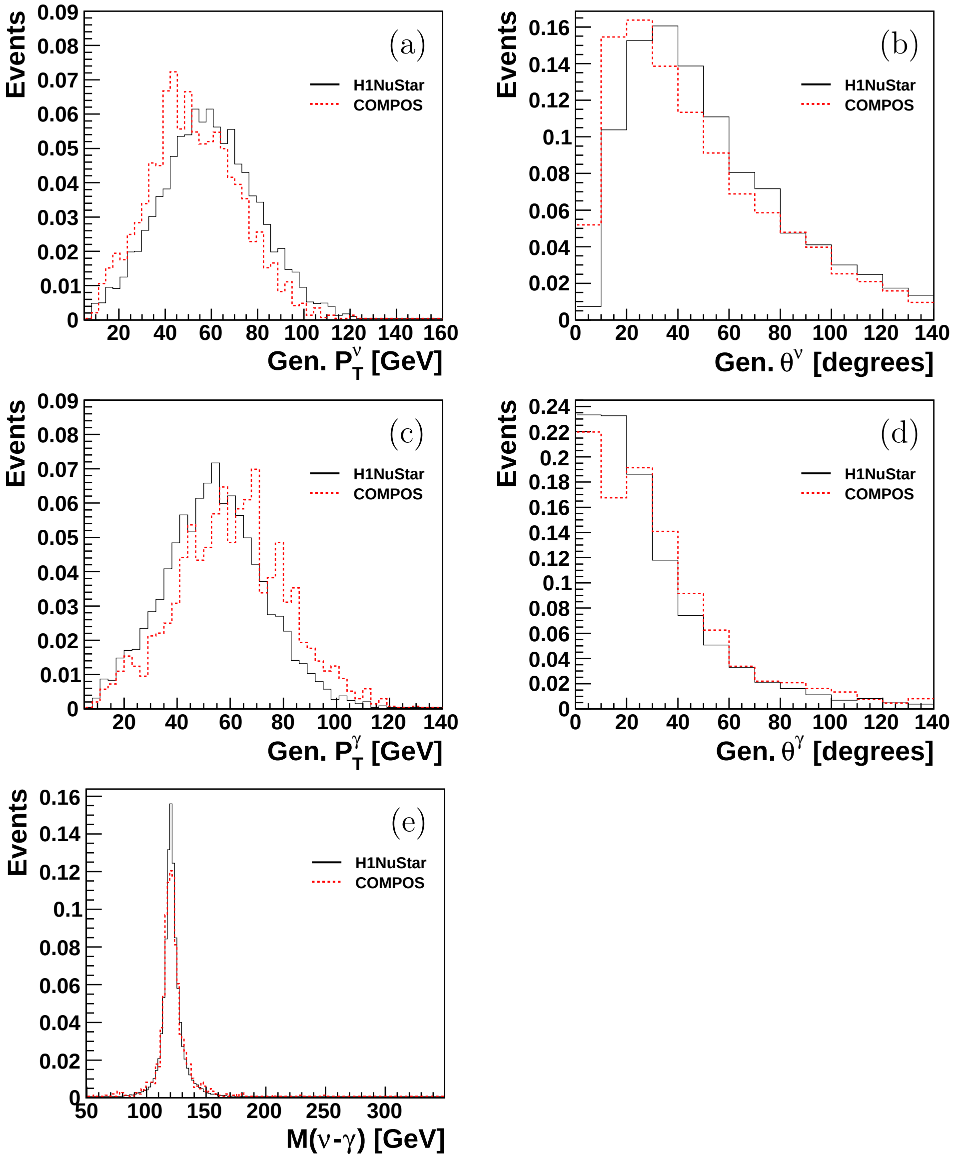

Figure 2.23: Distribution of kinematic variables of the generated neutrino (a, b) and the generated photon (c, d) and of the reconstructed ν^* invariant mass (e) obtained with the H1NuStar and COMPOS generators, for the $\nu^* \to \nu\gamma$ decay channel, with $M_{\nu^*} = 120$ GeV and $\Lambda = 1$ TeV.

The compatibility between the results of H1NuStar and COMPOS was verified for ν^* masses below 230 GeV and $\Lambda = 1$ TeV, a region where the narrow width approximation used in COMPOS is valid. This comparison is shown in figure 2.23 for the $\nu^* \rightarrow \nu\gamma$ decay channel, where the distributions of kinematic variables of the generated neutrino and photon are presented. Distributions obtained by H1NuStar and COMPOS are found to be in good agreement.

The theoretical uncertainty on the ν^* production cross section is dominated by the uncertainty on the scale at which the proton parton densities are evaluated. It is estimated by varying this scale from $\sqrt{Q^2}/2$ to $2\sqrt{Q^2}$. The resulting uncertainty depends on the ν^* mass and is 10% at $M_{\nu^*} = 100$ GeV increasing to 30% at $M_{\nu^*} \sim 300$ GeV.

Chapter 3

Experimental Environment

The HERA (Hadron Elektron Ring Anlage) is the only *ep* collider built in the world. Two multi-purpose detectors were designed and built, one of their major task being the study of the proton structure. In this chapter, a description of the HERA accelerator and of the H1 detector, used to record all data analyzed in this thesis, is presented.

3.1 The HERA accelerator

The HERA accelerator is located at the DESY facility in Hamburg, Germany. It started in 1992 and ended its operation in July 2007. Figure 3.1 shows a schematic view of HERA and of its preaccelerators. It has a circumference of 6.3 km and consists of two independent accelerators for electrons or positrons and protons. Since 1992, HERA produced collisions between electrons or positrons and protons. Electrons are accelerated up to energies of 27.6 GeV and protons up to energies of 920 GeV (820 GeV before 1998), yielding a center-of-mass energy of about $\sqrt{s} = \sim$319 GeV in the two interaction regions where the H1 and ZEUS detectors are located. The preaccelerators PETRA, DESY II and DESY III provide before their injection into HERA electrons at an energy of 12 GeV and protons at an energy of 40 GeV. The electrons and protons in the beam are collected into "bunches" before being accelerated to design energies. The beams are organised in up to 220 particle bunches, crossing each other every 96 ns. Figure 3.2 presents the kinematic range of HERA in the (x, Q^2) plane, which extends by more than two orders of magnitude the range accessible in fixed target experiments.

3.1.1 The installed experiments at HERA

Four experiments were installed at HERA. The collisions between the two beams are realized in the North and South Halls, where the H1 and ZEUS experiments are located. In the East Hall the HERMES experiment is installed since 1995. It is a spectrometer type experiment which uses a beam of longitudinally polarized electrons colliding with a target of polarized gas (H_2, He, D) to study the spin structure of the nucleon. In the West Hall, the HERA-B experiment is installed. It

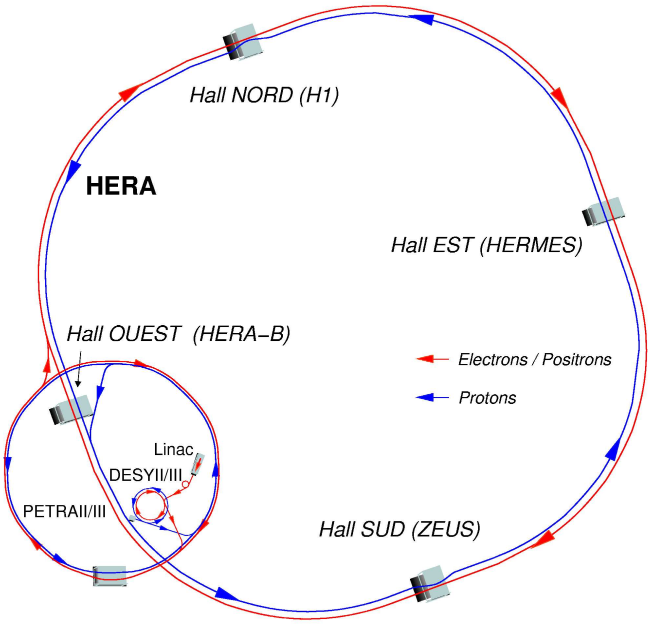

Figure 3.1: Schematic view of the HERA collider and its injectors.

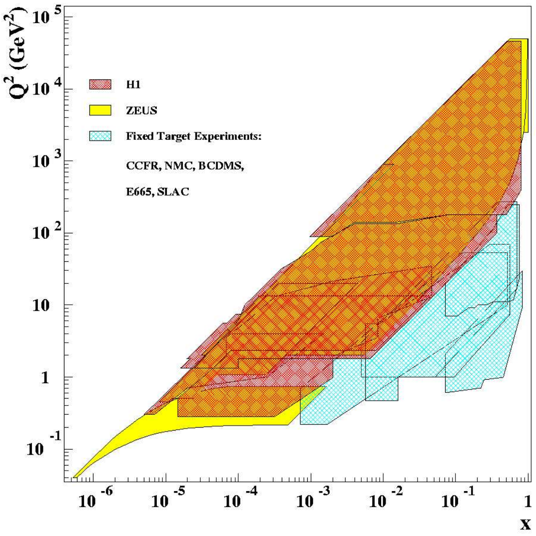

Figure 3.2: The HERA coverage of the kinematic plane (x, Q^2) compared to previous fixed target experiments. Fixed target regions are only located at large x and small Q^2 with just a small overlap with H1 and ZEUS.

was built to investigate charge-parity (CP) violation in $\bar{B}^0\,B^0$ pairs formed by the interaction of the proton beam halo with nucleons of a tungsten wire target.

3.1.2 The transition HERA-I to HERA-II

The life of HERA can be divided into two periods, before and after the luminosity upgrade, the HERA-I period from 1994 to 2000 and the HERA-II period from 2003 to 2007. During the shutdown (lasting from the years 2001 to 2002), two major improvements have been achieved.

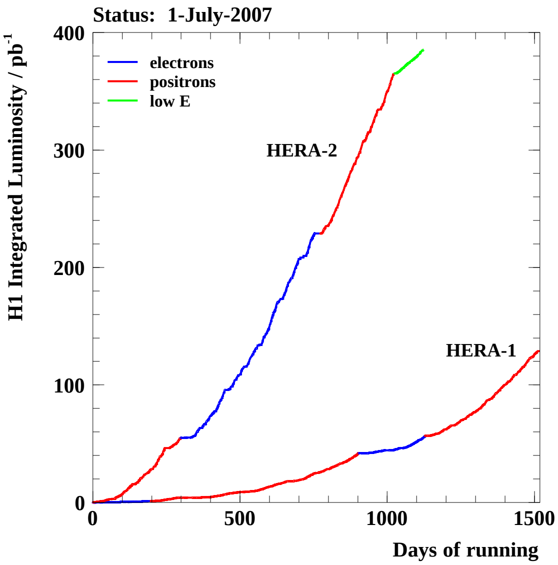

Figure 3.3: Luminosity collected by the H1 detector as a function of the days of running during the HERA-I and HERA-II running periods.

The luminosity was increased by installing focusing quadrupoles close to the interaction points within H1 and ZEUS. The instantaneous luminosity is defined as:

$$\mathcal{L} = \frac{f\ N_e\ N_p}{4\ \pi\ \sigma_x\ \sigma_y}\ \left[\frac{1}{\mathrm{cm}^2\ \mathrm{s}}\right]\ , \tag{3.1}$$

where N_e and N_p is the number of e and p particles per bunch, f is the bunch crossing frequency, σ_x and σ_y are transverse sizes of the beam. Figure 3.3 presents the integrated luminosity collected by H1 during HERA running. From this figure we can see that the installation of the focusing system improved the instantaneous luminosity by a factor of about three. During the last three months of HERA running, data were taken with a lower energy of the proton beam (460 and 575 GeV instead of 920 GeV). These data allowed a direct measurement of the longitudinal struture function of the proton which is related to the gluon content of the proton. These low energy data are not used in this thesis.

The second new feature at HERA-II is the possibility to longitudinally polarize the electron beam. The longitudinal electron beam polarization is achieved by installing spin rotators around the interaction regions in the HERA ring. Figure 3.4 presents a schematic representation of the HERA ring after the upgrade with installed spin rotators. The longitudinal polarization P_e of the electron beam is defined as:

$$P_e = \frac{(N_R - N_L)}{(N_R + N_L)}\ , \tag{3.2}$$

where $N_R,\ N_L$ are the fractions of right and left-handed electrons. The magnitude of the polarization generally increases with the beam lifetime and the helicity is flipped every few weeks to get equivalent amount of data with positive and negative polarization values. During the HERA-II running period, the electron beam was longitudinally polarised, at a level of typically 35%. For the present analysis the periods with left-handed and right-handed beams are combined.

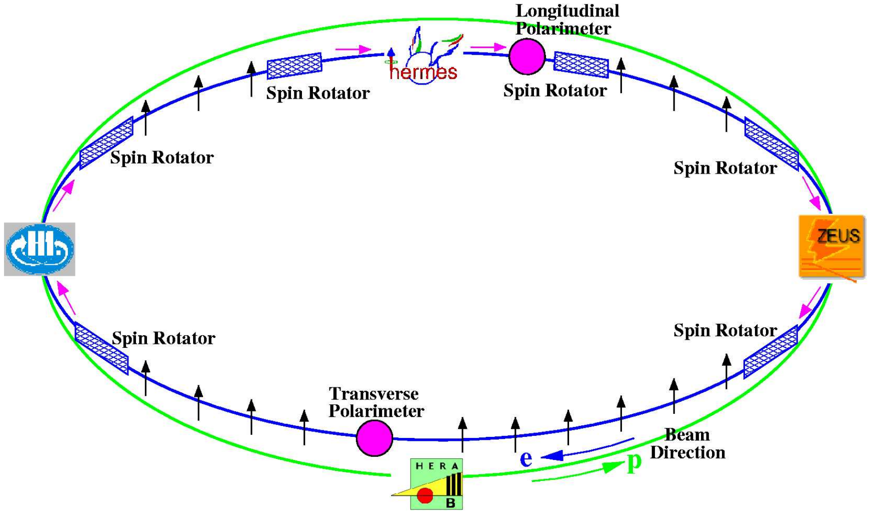

Figure 3.4: Schematic view of the HERA collider during the HERA-II running period with the TPol and LPol polarimeters and the spin rotators before and after H1, ZEUS and HERMES experiments. The arrows indicate the orientation of the electron polarization at each point around the ring.

3.2 The H1 detector

The H1 detector [55] is a 4π multi-purpose detector which was designed to study *ep* collisions. A drawing of the H1 detector is shown in figure 3.5, such as it was for the phase HERA-I. The nominal interaction point is the origin of the H1 coordinate system. The electron and proton beam energies are substantially different, the detector is therefore better instrumented in the proton outgoing direction, which by convention defines the positive z direction of the H1 coordinate system. The components of the detector located on the positive side from the interaction point are referred to as "forward". Similarly, the negative side is referred to as "backward". The region around the interaction point is called the "central" part of the apparatus.

The H1 detector is composed of central and forward tracking chambers surrounded by electromagnetic and hadronic calorimeters: the Liquid Argon (LAr) calorimeter in the central and forward regions and a Lead-Fibre calorimeter (SpaCal) in the backward region. A super-conducting coil surrounding the LAr calorimeter is used to produce an uniform magnetic field of 1.16 T, needed for the momentum measurements of tracks. The iron return yoke surrounding the whole detector contains several layers of streamer tubes. They are used to detect muons and to measure hadronic shower tails. In the forward direction, the measurement of muons is performed by drift chambers operated in a toroidal magnetic field. In the following sections, the most important parts of the H1 detector components are briefly described.

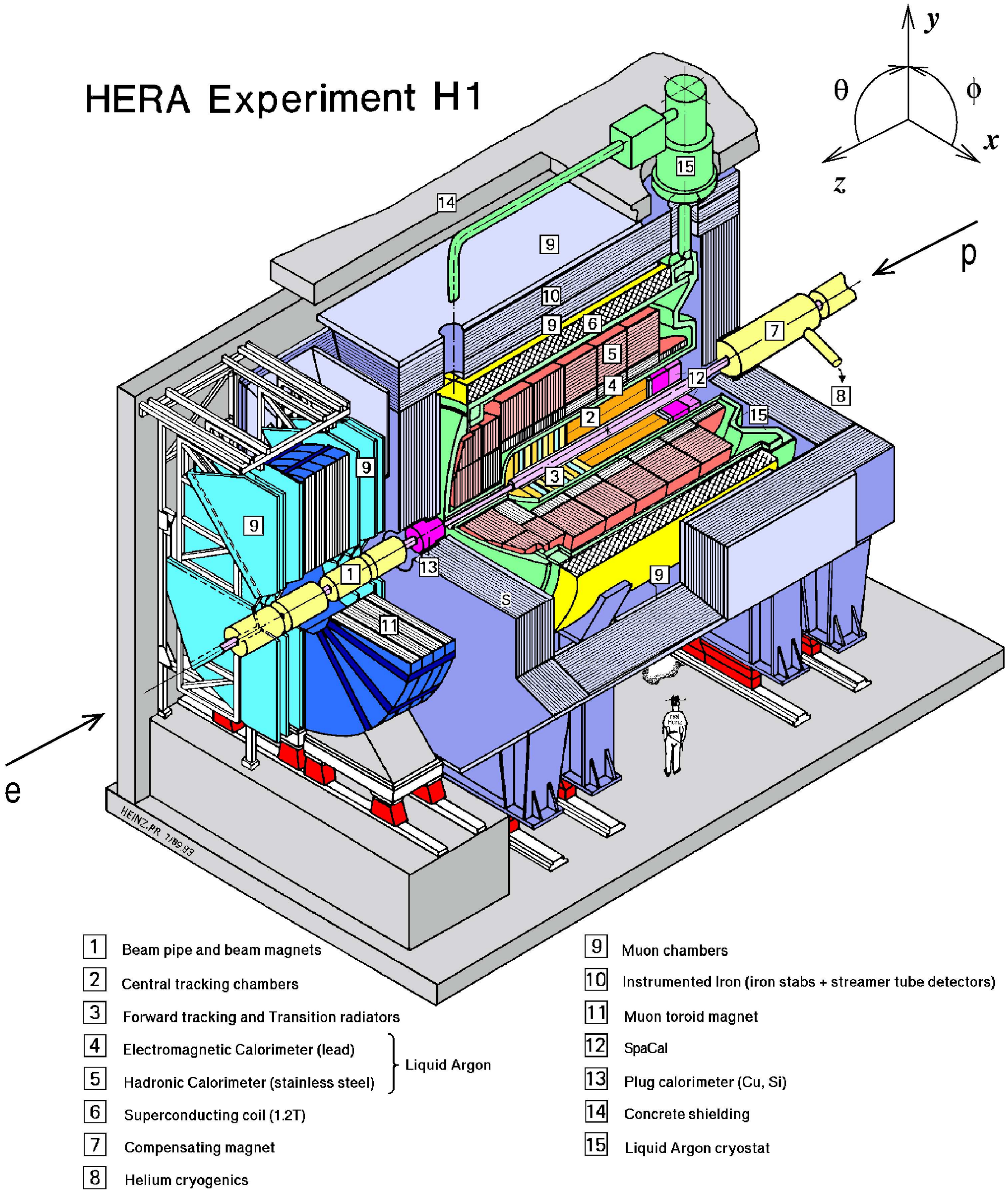

Figure 3.5: Schematic view of the H1 detector.

3.2.1 The calorimeters

Calorimeters are used to measure electromagnetic and hadronic energies, as well as in the identification of electrons, muons, neutral particles and in the reconstruction of the hadronic final state.

3.2.1.1 The Liquid Argon Calorimeter

The Liquid Argon Calorimeter [56] covers the central and forward part of the H1 detector within the angular range $4° < \theta < 154°$. The LAr calorimeter is the main detector component used to measure the energy of electromagnetic and hadronic showers. The characteristics of the LAr calorimeter are a high stability, ease of calibration, a fine segmentation offering a good e/π separation and homogeneity of the response. This allows a very good resolution on the measured energy and on the position of the scattered electron, as well as a good resolution on the hadronic energy measurement. The LAr calorimeter consists of an inner electromagnetic part (EMC) and an outer hadronic part (HAC). The HAC covers the angular range $4° < \theta < 135°$ while EMC has an extended coverage in the backward direction up to $\theta = 154°$. The LAr calorimeter is made of different "wheels" as can be seen in the schematic longitudinal view presented in figure 3.6 (a):

- Backward Barrel Electromagnetic calorimeter (BEE)
- Central Barrel calorimeter modules (CB1, CB2, CB3)
- Forward Barrel calorimeter modules (FB1, FB2)
- Outer and Inner Forward calorimeters (OF, IF)

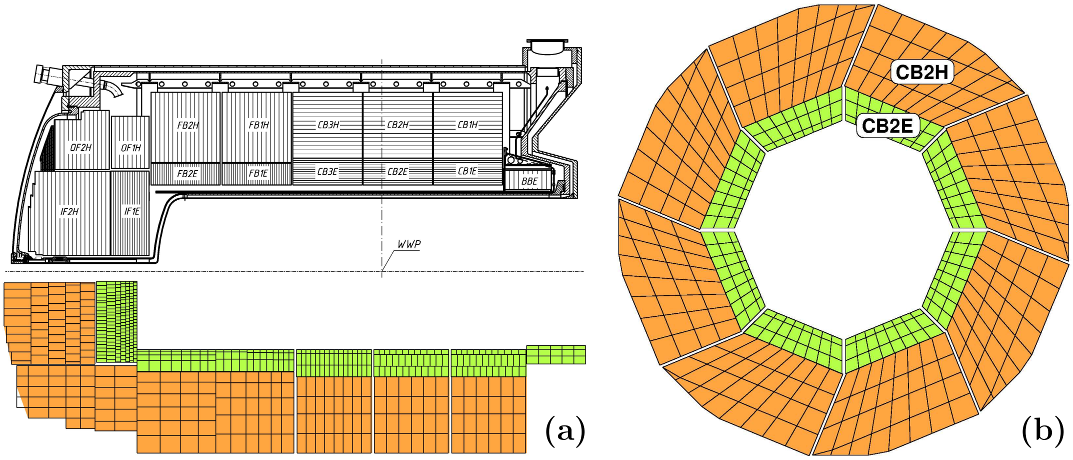

Figure 3.6: Longitudinal (a) and transverse (b) views of the Liquid Argon calorimeter.

All wheels, apart the BBE and the OF, have an electromagnetic and a hadronic section. The BBE has only an electromagnetic section, and the OF only an hadronic section. Each wheel is further divided in azimuthal angle, ϕ, into octants as shown in figure 3.6 (b).

In order to ensure a good spatial resolution, both electromagnetic and hadronic parts of the LAr calorimeter are highly segmented, resulting in a total of 45000 read-out cells. Because electromagnetic showers are more compact than hadronic ones, the electromagnetic section has a four-fold higher segmentation than the hadronic section. The segmentation is finer in the forward part than in the central part, in terms of Molière radius, cells are equivalent to 2.5 R_M in the backward part and to 1.0 R_M in the forward part. Figure 3.7 illustrates the granularity of the segmentation and the reconstruction of electron showers. In the electromagnetic part, the cells are made up alternatively of lead layers and Liquid Argon layers each being 2.4 mm of thick. In the hadron part two Liquid Argon layers of 2.4 mm alternate between iron layers of 1.9 cm. There are from three to six layers of cells in the electromagnetic part and four to six in the hadronic section.

Test beam measurements were done to measure the energy resolution of the LAr calorimeter. The EMC has an energy resolution for electrons of:

$$\frac{\sigma_E}{E} = \frac{(11.5 \pm 0.5)\%}{\sqrt{E/\mathrm{GeV}}} \oplus (1.0 \pm 0.1)\% \,. \tag{3.3}$$

The energy resolution for hadrons in the HAC is:

$$\frac{\sigma_E}{E} = \frac{(50.7 \pm 0.7)\%}{\sqrt{E/\mathrm{GeV}}} \oplus (1.6 \pm 0.1)\% \,. \tag{3.4}$$

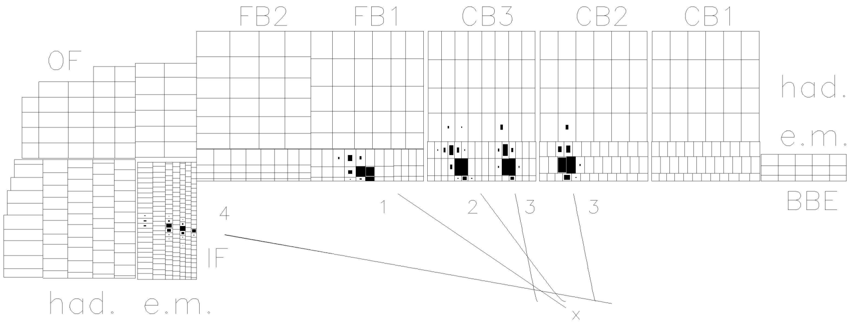

Figure 3.7: Wheels and cells of the LAr calorimeter with examples of electromagnetic showers.

3.2.1.2 The spaghetti calorimeter

At the beginning of H1 running, an electromagnetic lead scintillator sandwich calorimeter (BEMC) was installed in the backward region of the H1 detector. It provided a coverage in squared four-momentum transfer of $5 < Q^2 < 100$ GeV^2. To improve the acceptance towards lower Q^2 and thereby to allow access to the proton structure function at low x, the BEMC was replaced during the winter shutdown of $1994 - 1995$ by a spaghetti calorimeter (SpaCal). Figure 3.8 shows the calorimeter as it was used during the HERA-I running period. With this upgrade, the angular coverage was extended down to the beam pipe from $151° < \theta < 176°$ for the BEMC to $153° < \theta < 177.5°$ for the Spacal. This allows to access Q^2 values down to $\sim$2 GeV^2 and x values down to 10^{-5}. In comparison with the BEMC, the Spacal detector has also a much better granularity and an improved electromagnetic and hadronic energy resolution.

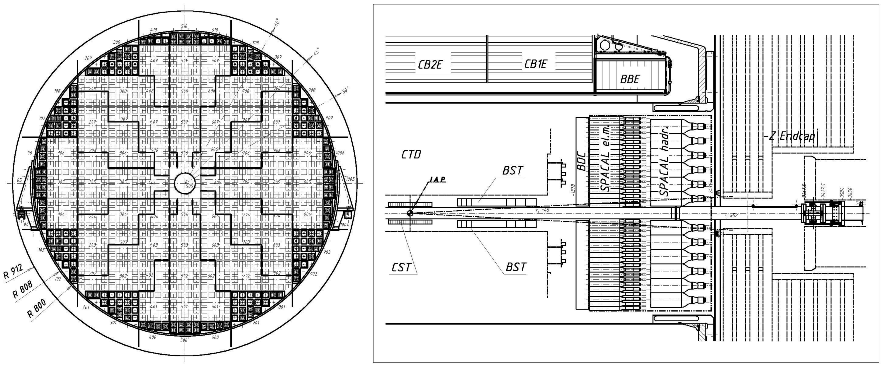

Figure 3.8: Transverse (left) and longitudinal views of the SpaCal.

The SpaCal is divided into an electromagnetic and a hadronic sections, as the LAr calorimeter, but is mainly used to measure electrons scattered at low backward angles. Both parts consist of lead absorbers, combined with scintillating fibers. Charged particle showers in the absorber create scintillation in the fibres. This light is collected and read out by photomultiplier tubes. The SpaCal has a time resolution of the order of 1 ns, providing also a time-of-flight information used for background rejection at the first level of the trigger system.

The electromagnetic part of the SpaCal has a fine granularity, providing a spatial resolution of few millimeters. Test beam measurements were performed in order to measure the energy resolution of the electromagnetic section of the Spacal:

$$\frac{\sigma_E}{E} = \frac{(7.1 \pm 0.2)\%}{\sqrt{E/\mathrm{GeV}}} \oplus (1.0 \pm 0.1)\%\,, \tag{3.5}$$

and for the hadronic part:

$$\frac{\sigma_E}{E} = \frac{(56.0 \pm 3.0)\%}{\sqrt{E/\mathrm{GeV}}} \oplus 7\%\,. \tag{3.6}$$

A good resolution on the measurement of the energy and polar angle of the scattered lepton are fundamental for a precise measurement of Q^2 and y using the electron method as described in chapter 4. The fine granularity of the electromagnetic section gives a polar angle resolution of $\sigma_\theta = 2$ mrad.

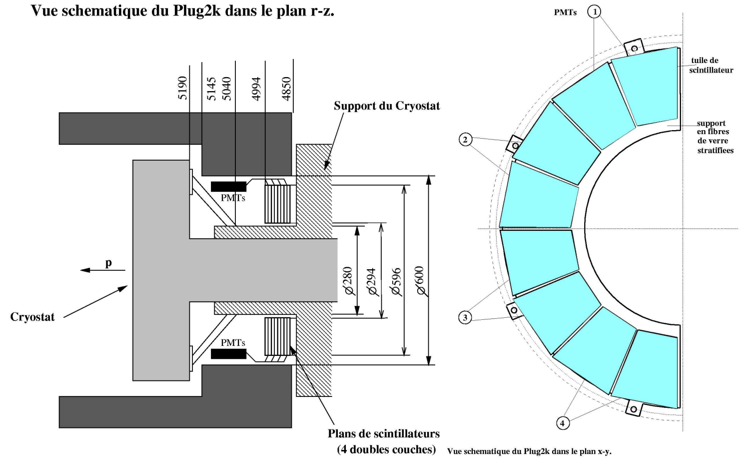

Figure 3.9: On the left side, a longitudinal view of the Plug2k. On the right side, haft-transverse view of scintillator tiles.

3.2.1.3 The plug calorimeter

The HERA-I Plug calorimeter was designed to cover the acceptance gap between the forward part of the LAr and the beam pipe, to complete the energy flow measurement. The angular opening of the PLUG is $0.3° < \theta < 3.3°$. With the introduction of the GO magnet in HERA-II, the Plug was replaced by the Plug2k, smaller and resistant to radiations. The Plug2k consists of 16 plastic scintillators, tiles 4 cm thick, coupled two by two with photomultipliers. The Plug2k has then eight layers in ϕ and covers the angular range $1.9° < \theta < 3.2°$. The Plug2k is presented in figure 3.9.

3.2.1.4 The tail catcher

In order to measure the hadronic energy leakage out of the LAr and SpaCal, eleven of the sixteen limited streamer tube layers of the instrumented iron are equipped in addition with readout electrodes. This part of the calorimeter system is named Tail Catcher (TC). The energy resolution of this calorimeter is:

$$\frac{\sigma_E}{E} \approx \frac{100\%}{\sqrt{E(\mathrm{GeV})}}\,. \tag{3.7}$$

3.2.2 The tracking system

The goal of the tracking system is to provide a precise measurement of momentum and angles of charged particles as well as fast trigger signals. The trajectories of particles are derived from signals of different sub-detectors. The momentum is obtained from the curvature of the track in the magnetic field of the superconducting solenoid magnet. The H1 tracking system consists of different tracking devices with different detector technologies. A side view of the tracking system is displayed in figure 3.10.

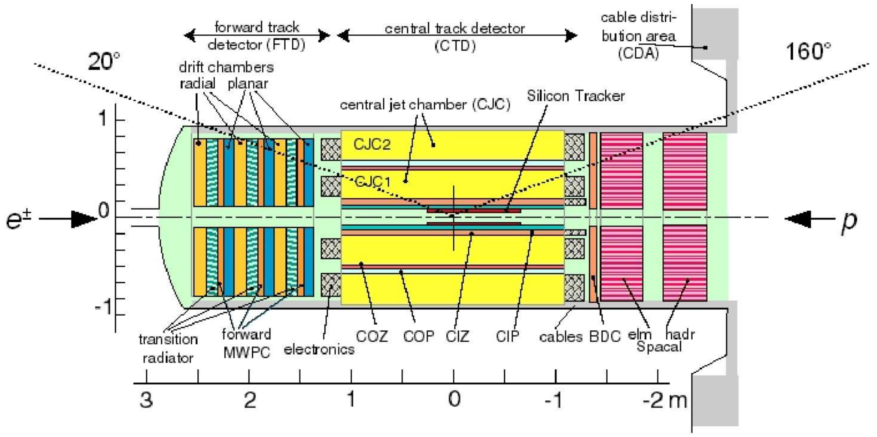

Figure 3.10: Side view of the H1 tracking system.

3.2.2.1 The central tracking detector

The central tracking detector shown in figure 3.11 consists of two central jet chambers (CJC1 and CJC2), two central $z-$drift chambers, the inner one (CIZ) and the outer one (COZ), the central silicon tracker (CST), used to measure starting point of tracks with a very good spatial resolution, and two proportional chambers, an inner one (CIP) and an outer one (COP).

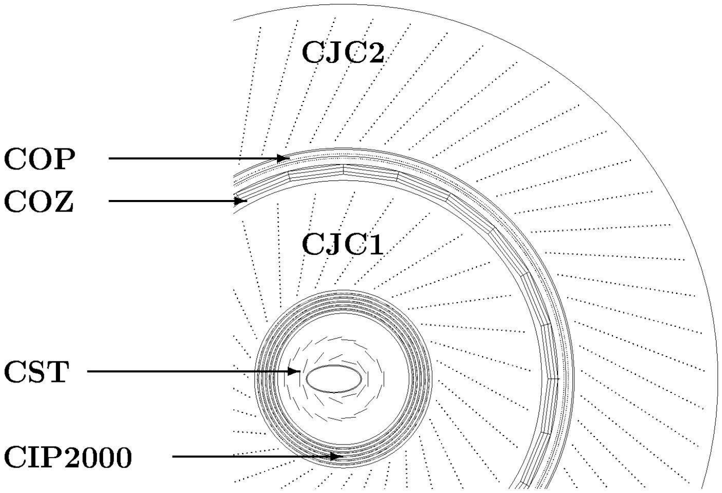

Figure 3.11: Radial view of the central tracking system.

The Central Jet Chamber (CJC)

The central jet chambers, CJC1 and CJC2, are about 2 m long with a width of 25 cm and 30 cm, respectively. The chamber closest to the beam pipe is CJC1 which covers the polar angle range $11^\circ < \theta < 169^\circ$ and consists of 30 cells with 24 sense wires for each of them. The outer jet chamber, CJC2, covers the polar angle range $26^\circ < \theta < 154^\circ$ and comprises 60 cells with 32 sense wires for each of them. The sense wires are parallel to the beam axis to allow a precise measurement of trajectories in the $r\phi$ plane. The drift cells have an angle of about 30° with respect to the radial direction. This ensures that particles from the interaction vertex pass through more than one drift cell. This solves drift ambiguities caused by mirror track segments. In addition, the tilt makes the electrons created from the particle ionisation to drift approximately perpendicularly to the direction of flight of the particle. This almost cancels the effect of magnetic field which causes that the drift direction of the electrons and the direction of the electric field are different, the so-called Lorentz angle. The spatial resolution in the $r\phi$ plane is about 170 μm and about 22 mm in z. The z resolution is worse since the z position is determined by charge division. The energy loss dE/dx is measured with a typical resolution of 10% and the precision on the momentum measurement is:

$$\frac{\sigma_{P_T}}{P_T\ (\mathrm{GeV})} = 5.10^{-3} \oplus 0.015\,. \tag{3.8}$$

The CJCs can provide an average time measurement of the events t^0_{CJC} with a resolution of the order of 1 ns. The average time of the CJC is used to distinguish events in time with the bunches crossing. The t^0_{CJC} is measured in "ticks", 500 ticks corresponding to 96 ns (one bunch crossing).

The Outer z Drift Chamber (COZ)

The outer $z-$chamber (COZ) shown in figure 3.12, is a drift chamber with a thickness of 0.015 X_0, and with wires perpendicular to the z-direction. It covers an angular range of $25^\circ < \theta < 165^\circ$. The COZ is installed between the two CJCs. The COZ informations are used to improve the track momentum measurement. The resolution on z is about 350 μm

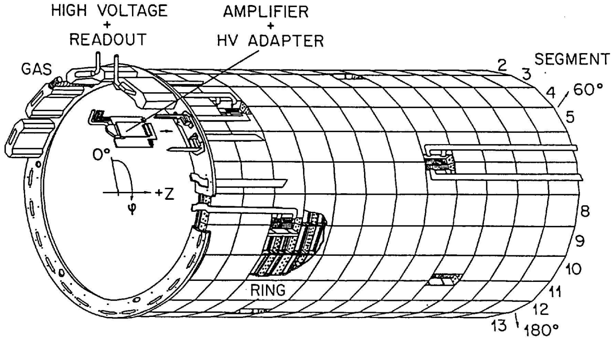

Figure 3.12: Schematic view of the COZ chamber.

The Silicon Tracker Detector (CST)

The central silicon tracker detector (CST) presented in figure 3.13, is a semiconductor detector installed close to the beam pipe. The CST was installed partially in 1996 and completed in 1997. The CST was adjusted to the new HERA beam tube in 2001 and covers the polar angle range $30° < \theta < 150°$. The CST consists of two cylindrical layers of silicon sensors. The inner radius is 5.57 cm, the outer radius 9.7 cm and the total length 44.2 cm. Its inner layer is made out of 12 ladders arranged around the z axis. Each ladder consists of 6 silicon sensors in the z direction with read-out electronics at both ends. The outer layer has 20 ladders.

The CST aims to obtain a very precise measurement of tracks close to their origin. It is used for the reconstruction of secondary vertices and the tagging of heavy mesons containing a b or c quark. It is the closest detector to the interaction point. A charged particle passing through the CST will produce $electron - hole$ pairs in the $p - n$ junction of the silicon. The electrons and the holes are drifted to the inner or outer side of the sensors due to the voltage applied between the two surfaces. Strips are mounted on the surface of the sensors, for the read-out of the deposited charge. The strips are perpendicular to each other, making possible the measurement of the $r\phi$ coordinate as well as the z coordinate. The resolution achieved is about 12 μm in the plane $r\phi$ and 22 μm for z-resolution. The resolution on the event $z-$vertex position is about 0.09 cm without the CST and 0.02 cm with the CST.

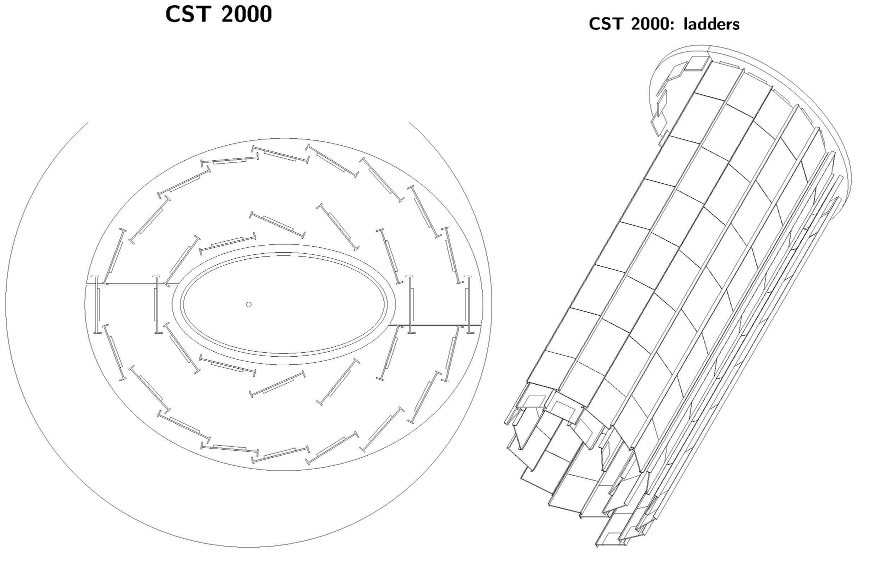

Figure 3.13: Transverse (left) and tridimentional (right) views of the CST.

The Proportional Central Chamber (CIP2k)

The central inner proportional chamber (CIP2k) is located between the CJC1 and the CST. The CIP2k is used in HERA-II, replacing the CIZ and the older CIP. The CIP2k is a multiwire proportional chamber consisting of 5 cylindrical layers which are 120-fold segmented in z and 16-fold in azimuthal angle ϕ. The spatial resolution of the CIP2k in z is about 1.5 cm. Since the chambers are about 2 m long, the CIP2k has a much larger polar angle acceptance than the HERA-I CIP. This allows to reject proton induced background with a true or apparent vertex position outside the H1 detector from −150 to −200 cm (see figure 3.14). The decision is based on track segments reconstructed using the five layers of the CIP2k as depicted in figure 3.14.

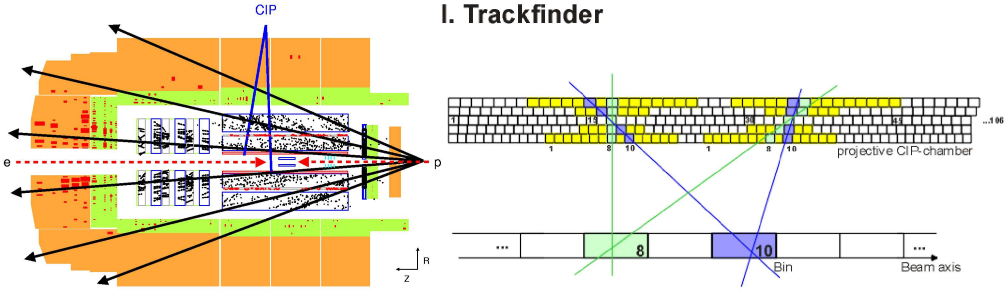

Figure 3.14: On the left side, view of an event resulting from a proton-collimator collision. On the right side, principle of the vertex finding algorithm of the CIP2k chamber.

The Outer z Proportional Chamber (COP)

The outer proportional chamber (COP) is located between the COZ and the CJC2 and has a radius of 50 cm. The COP and the CIP are used in combination with the FWPC to provide a fast information about the z-vertex position which is used in the first level of the trigger system.

3.2.2.2 The forward tracking detectors

The forward tracking detector (FTD) measures the tracks in the forward region $5^\circ < \theta < 25^\circ$. This detector has been deeply modified between HERA-I and HERA-II. The HERA-I detector has a track identification efficiency below 50% for high multiplicity events. The FTD used for HERA-II is made of three so-called ”super modules”. The modules are almost identical and consist of three ”planar dift” chambers. The HERA-II version is presented in figure 3.15. The goal of the FTD is to have a momentum resolution of $\sigma_P/P < 0.003$ and an angular track resolution of $\sigma_{\theta,\phi} < 1$ mrad. The forward silicon tracker (FST) is a semiconductor detector covering a polar angle range $8^\circ < \theta < 16^\circ$. It has been seriously damaged in 2004, then repaired and re-installed end of 2005.

3.2.2.3 The backward tracking detectors

In the backward region the tracks are measured by the backward silicon tracker detector (BST), a drift chamber (BDC) in HERA-I and a proportional chamber (BPC) in HERA-II. The BPC is mounted between the central tracking detector and the SpaCal and its angular coverage in θ is $155^\circ < \theta < 170^\circ$. The BST measures the tracks in the polar angle range $163^\circ < \theta < 174^\circ$. The combination of the BST and the BPC allows to obtain a resolution on the electron polar angle of $\Delta\theta \approx 0.5$ mrad.

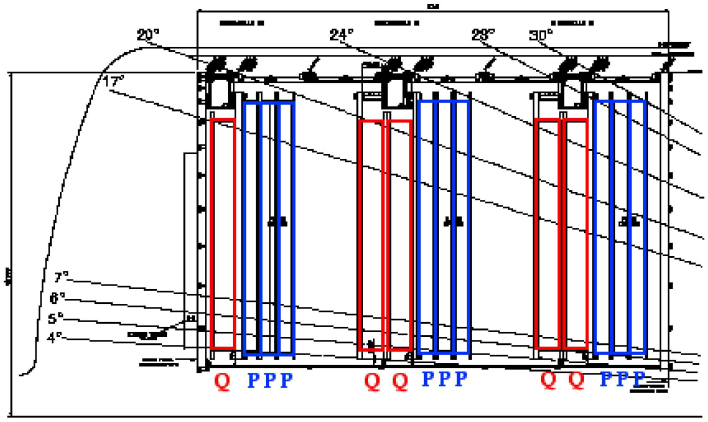

Figure 3.15: The $r-z$ view of the forward tracking detector used by H1 for HERA-II.

3.2.3 The muon system

The muon system is made of two sub-detectors covering the central region (CMD) and the forward region (FMD).

3.2.3.1 The central muon detector

The CMD consists of limited streamer tubes (LST) installed in the slits of the iron return yoke of the solenoid. The goal of the CMD is to detect muons and also tails of hadronic showers (same technology as used by the Tail Catcher) in the region $4^\circ < \theta < 172^\circ$. The CMD is divided into four regions: the forward and the backward barrel covering the range $33^\circ < \theta < 137^\circ$, and the forward and the backward end-cap in the angular ranges $6^\circ < \theta < 33^\circ$ and $137^\circ < \theta < 172^\circ$, respectively. Each of these parts of the CMD is made up of 16 modules. Each module consists of 10 iron plates with a thickness of 7.5 cm in the radial direction for the cental barrel and in the $z-$direction for the end-cap region. In front of and behind the instrumented iron, muon boxes are installed, each of them with three LST layers. These muon boxes are used to improve the muon track measurement. This detection system allows to reconstruct muon momenta between 1.5 GeV and 170 GeV with a high efficiency. The resolution for the strips hits is about $\sigma_{strip} = 10-15$ mm. The barrel polar angule resolution is $\sigma_\theta = 15$ mrad and $\sigma_\phi = 10$ mrad. The track segments found are fitted using a straight line, and the curvature is obtained by connecting several track segments. The track reconstruction is completed by the inclusion of the strip information and taking into account energy losses of at least 80 MeV. Possible variations of the magnetic field are also taken into account.

3.2.3.2 The forward muon detector

The FMD is a spectrometer consisting of a toroidal magnet with two layers of drift chambers at both sides. The goal of the FMD is to measure forward muons of high energy between 3 and 17 degrees. This detector can measure muon momenta between 5 GeV and 200 GeV. The momentum resolution is about 24% for a 5 GeV and deteriorates to 36% for a 200 GeV momentum muon. Muons with a momentum below 5 GeV are measured in the forward tracking detector.

3.2.4 The Time-of-Flight system

The time of flight system (ToF) consists of scintillators located at both ends of the detector down to the beam pipe. These scintillators are used to reject the beam induced background arriving out-of-time in the H1 detector. There are several ToF counters. The forward ToF (FToF) is located at z position of ≈ 7 m. The plug ToF (PToF) is installed in the Plug region at $z \approx 5.3$ m. The backward ToF (BToF) is located at $z \approx -3.3$ m. In addition, there are scintillator walls, so-called "veto wall" systems, the outer and the inner veto walls. The outer veto wall is located at $z \approx -6.5$ m. The inner veto wall is located at $z \approx -8.1$ m. The area covered by the inner veto wall is the near beam area 100×90 cm^2, down to a radius of 11 cm. A background event is rejected if it arrives out of time with respect to the bunch crossing or if the determined $z-$position of the ep interaction point is not in the allowed region. The configuration of the different ToFs is shown in figure 3.16.

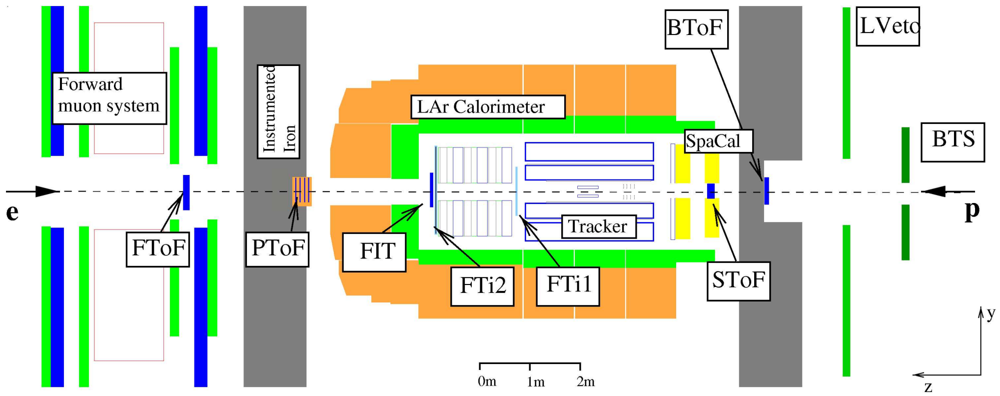

Figure 3.16: The longitudinal view of the different systems used to measure the time of flight.

3.2.5 The luminosity system

The integrated luminosity $\mathcal{L} = \int \mathcal{L}dt$ is the ratio of the number of events N and of the cross section of the reaction $\mathcal{L} = N/\sigma$. It is necessary to know the number N for the measurement of a cross section and in a reverse way the precise knowledge of the cross section of specific processes will allow to measure the luminosity. So far the best method for luminosity measurement at HERA used by both H1 and ZEUS experiments is based on the Bethe-Heitler (BH) reaction: $ep \rightarrow e\gamma p$, which has a theoretical uncertainty of 0.5%. Since the BH cross section is large ($\sim$170 mb), event samples with a large statistic can be obtained, and the luminosity can be calculated from the event rate, taking into account the detector acceptance. A general view of the luminosity system is shown in figure 3.17. It consists of two small electromagnetic calorimeters, the electron tagger (ET) and the photon detector (PD), located in the HERA tunnel at $z-$positions of -6 m and -104 m, respectively. The ET consists of 7 × 7 cells covering a total area of 154×154 mm^2. The angular acceptance of the ETAG is about 5 mrad. The PD consists of 5 × 5 cells covering a total area of 100×100 mm^2. The photon leaves the proton beam pipe through a window in the horizontal plane, where the beam pipe bands upwards, and hit the PD. The angular acceptance of the PD amounts to about 0.45 mrad. Two methods are used to measure the luminosity at HERA. One "coincidence" method which is used online by the H1 Luminosity Monitor and which requires the simultaneous detection of the e and the γ in the final state. Another "single photon" method is used for offline luminosity measurement and counts the number of events N with the photon energy above a certain threshold. In the HERA-II setup of the luminosity system, the rate of photons with an energy greater than 10 GeV is measured in the photon detector. The systematic uncertainty on the luminosity measurement is dominated by the geometric acceptance of the photon detector. Only the single-photon method was used for luminosity measurements in HERA-II.

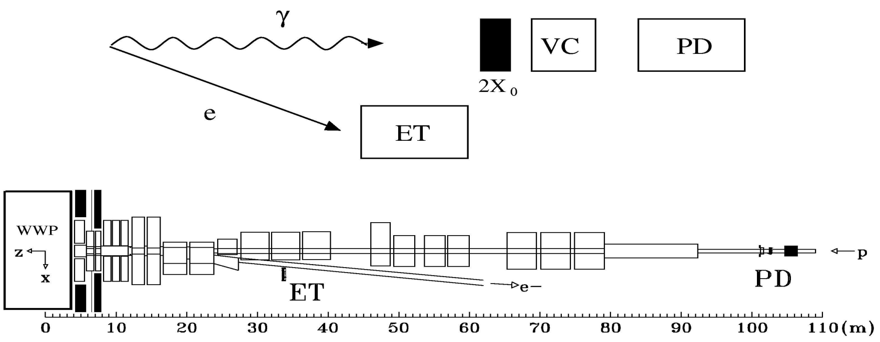

Figure 3.17: On the top, schematic principal of the luminosity measurement of a BH event with the simultaneous detection in the photon detector and in the electron tagger. At the bottom, schematic view of the luminometer and the location of the ET and the PD in the HERA-I configuration.

3.3 The H1 trigger and data acquisition

Due to the low cross section of ep interactions, the rate of real physics events is small compared to the high rate of background events. The low number of residual gas molecules, mainly hydrogen and carbon monoxide, with a pressure in the vacuum tube of 10^{-9} mbar, generates collisions with the proton beam at a frequency of a few kHz. Moreover, the frequency of the collisions between the proton beam and the various collimators of the machine is a few tens of kHz. In comparison, the typical frequency (under good luminosity conditions) of ep physics events is about a few ten of Hz. The table 3.1 shows the different orders of magnitude of the frequency of background events and of few physics processes. The frequency of background events being of 50 kHz, it is not possible to record all events because writing on tape is only done at a frequency of 10 Hz.

proton-gas interactions	50	kHz
cosmic muons	700	Hz
photoproduction	1000	Hz
low Q^2 NC DIS	2.2	Hz
high Q^2 NC DIS	1.4	min^{-1}
CC DIS $P_T > 25$ GeV	3	h^{-1}
W production	0.5	day^{-1}

Table 3.1: Event rates for a luminosity of $\mathcal{L} = 1.5{\times}10^{31}$ cm^{-2} s^{-1}.

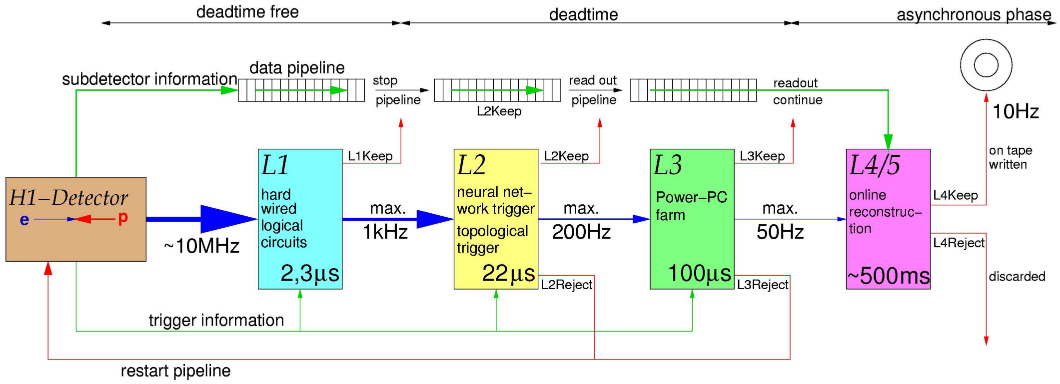

Figure 3.18: The structure of the H1 Trigger system.

The aim of the H1 Trigger System is a fast and efficient separation of real physics events from the dominating background and a proper recording of interacting *ep* collision events within the limited H1 bandwidth. This must be done in order to minimize the dead-time during which the system can not record events, by example during the reading of the different sub-systems. The H1 trigger system allows to reduce the event rate from 50 kHz to 10 Hz with a mean dead-time of $\sim$10%. For these purposes, the trigger system consists of four separate levels, each consecutively filtering incoming data and making more and more complex decisions. Filtered data from one level are sent to the next level until a manageable rate for the H1 data acquisition is reached at the final level. Each level is described in the following sub-sections. In section 4.2 the specific trigger requirements relevant to this analysis are summarized and their efficiency are studied.

3.3.1 The first trigger level (L1)

The first trigger level (L1) uses up to 256 trigger elements (TE) for the whole H1 detector. The trigger elements are logical variables combined to form sub-triggers (ST). Up to 128 of these ST conditions can be processed.

The decision to keep or reject an event at the first trigger level (L1) is based on the information arriving from all sub-detectors in the form of trigger elements. The trigger elements from the sub-detectors are passed in dead time free pipelines (the pipelines length varies between 27 and 35 BC's depending on the subdetector) to the Central Trigger Logic (CTL). The CTL coordinates and synchronises the data stream from all subdetectors, combines these trigger elements into so-called subtriggers and makes a decision to keep the event ("L1keep") if at least one subtrigger is set [1]. If the event was kept, the pipelines are stopped and the "dead time" (time when the detector cannot continue to take data) starts.

3.3.2 The second trigger level (L2)

Three trigger systems, the Neutral Network Trigger (L2NN) [58], the Topological Trigger (L2TT) [59] and for HERA-II a Fast Track Trigger (FTT), form the second trigger level. At level 2, the full L1 information from all subdetectors is available. Since the time in which the L2 decision has to be taken is 20 μs, there is enough time to exploit correlations between different subdetectors.

The L2NN system consists of 13 independent neural networks, each of them can have up to 64 input neurons, 64 hidden and 1 output neuron. Each network is trained to recognize a specific physics channel, making use of its specific pattern in the detector. The L2TT searches for spatial correlations in the level 1 trigger signals, using a 16×16 binned representation of the detector in the $\theta - \phi$ polar-azimuthal angle space.

The L2 trigger starts the readout for the full detector by the data acquisition systems.

3.3.3 The third trigger level (L3)

The third trigger level was not used during the HERA-I period and neither during the HERA-II period around the end of 2005. Its purpose is to contradict quickly the decision of the L2 within 100 μs, and thus to stop readout. This new trigger level uses the level 2 FTT information to compute invariant masses.

3.3.4 The fourth/fifth trigger level (L4/L5)

The L4/L5 trigger level makes the event reconstruction from the complete readout of the event information (the readout starts with the "L2 keep" signal). Event parameters (tracks, clusters, vertex, time of the interaction) are reconstructed by the H1 software reconstruction algorithm (H1REC). This reconstruction is done by a farm of tens of PCs and takes ∼100 ms. The L4/L5 reduces the event rate from ∼40 Hz to ∼15 Hz for the writting on tape. The events are classified into different physics classes by L4 filters [60] (or rejected if they do not fit in any of the existing classes), and are written to tape.

---

[1] Some subtriggers may have a prescale p which means that this trigger will be ignored by the CTL until it has been set p times.

Chapter 4

Reconstruction of events with the H1 detector

In this chapter, the whole data set recorded by H1 during HERA running and used in this analysis is presented. Initial selection requirements used to extract a clean data sample of *ep* collision events are briefly introduced. This data preselection is used for all analyzed channels in this thesis. Criteria used to remove non-*ep* background events such as beam halo and cosmic muon events are presented. The next important topic covered concerns the trigger used in this analysis. An introduction to these triggers and a discussion of their efficiency are presented. The reconstruction and identification of particles with the H1 detector are then discussed and the definition of the main kinematic variables used in this analysis is presented. Finally, tests of the energy calibration for electrons and hadrons are presented and the associated systematical errors are disccused.

4.1 Selection of a clean data sample

4.1.1 Data sets

All high energy data sets from HERA-I and HERA-II running periods and corresponding to a total integrated luminosity of 475 pb^{-1} are analyzed. The data were recorded in distinct running periods, which are listed in table 4.1. The complete HERA e^-p data sample corresponding to an integrated luminosity of 184 pb^{-1} was recorded during the years $1998-1999$, 2005 and 2006. The complete HERA e^+p data of 291 pb^{-1} are collected during the years $1994-1997$, $1999-2000$, $2003-2004$ and $2006-2007$. In total, the present analysis uses a data sample larger by factors four and ten compared to the previous published results for the e^* and ν^* searches, respectively.

4.1.2 Technical requirements

Each HERA *fill* of colliding protons and electrons is recorded by H1 in a series of data taking *runs*. Detector conditions may vary during runs and luminosity fills, so

Period	Years	Collisions	E_p	$\mathcal{L}$ (pb^{-1})
HERA-I	1994 – 1997	e^+p	820 GeV	35
	1998 – 1999	e^-p	920 GeV	14
	1999 – 2000	e^+p	920 GeV	68
HERA-II	2003 – 2004	e^+p	920 GeV	52
	2005	e^-p	920 GeV	112
	2006	e^-p	920 GeV	58
	2006 – 2007	e^+p	920 GeV	136
Total (e^-p)				184
Total (e^+p)				291
Total ($e^\pm p$)				475

Table 4.1: Details of the different data sets analyzed in this thesis. In the e^* search, all $e^\pm p$ data sets of 475 pb^{-1} are used. In the ν^* search, only e^-p data sets of 184 pb^{-1} are used.

a *good run* selection is performed on all of the recorded data used in this analysis. This selection is based mainly on high voltage (HV) conditions of certain detectors essential for the analysis. The high voltages of the central jet chambers CJC1, CJC2 and of the central proportional chamber CIP2000, must be at their nominal values. The LAr and SpaCal calorimeters must also be operational, as well as the ToF and Lumi systems.

4.1.3 Non-*ep* background suppression

In order to reduce non-*ep* physics background, a set of offline background finders has been developed [61]. These finders aim at detecting events originating from cosmics and from beam-halo muons. They can create electromagnetic showers being misidentified as an electron. Furthermore, a muon itself or some secondary particle from shower can produce a track in the tracking system leading to the reconstruction of a vertex. An example of a cosmic event within H1 is shown in figure 4.1. Such muon induced background can be identified using special topological background finding algorithms:

- HALAR: halo finder based on Liquid Argon information only.
- HAMULAR: halo finder correlating energy deposits in the Barrel Liquid Argon and in the Backward Iron Endcap.
- HAMUMU: halo finder correlating the Forward Iron Endcap with the Backward Iron Endcap.
- HASPALAR: halo finder correlating Liquid Argon Calorimeter with the SPACAL detector.

- HAMUIF: halo finder correlating the Inner Forward Liquid Argon deposits with the Backward Iron Endcap.
- COSMUMU: cosmic finder based on Muon Detectors only.
- COSMULAR: cosmic finder correlating the Muon Detectors and the Liquid Argon Calorimeter.
- COSTALAR: cosmic finder correlating the Tail-Catcher and the Liquid Argon Calorimeter.
- COSTRACK: cosmic finder based on CJC information only.
- COSLAR: cosmic finder based on Liquid Argon information only.

A complete description of the 10 finders is available in [61, 62].

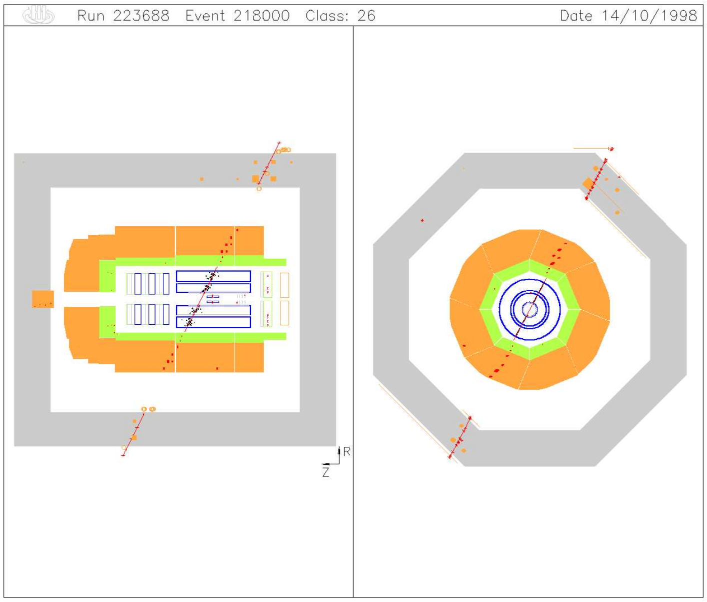

Figure 4.1: A cosmic event within the H1 detector.

In order to reject cosmic background, an additional requirement on the timing of the CJC can be used. The CJC track reconstruction software provides an event T_0 based on the drift time information of the different tracks with a resolution of about 1 ns. This time stamp is required to be within ±4.8 ns around the nominal time of a bunch crossing (BC) as given by the HERA clock ($T_0^{\mathrm{CJC}} - T_{\mathrm{BC}} < 4.8$ ns). More than 99.9% of the *ep* events are within this time window. On the other hand cosmic background events are asynchronous to the HERA clock. This cut only applies to data because non-*ep* physics is not modelled in the Monte Carlo.

Beam-gas and beam-wall interactions are suppressed by requiring that the $z-$vertex of the event lies within ±35 cm around the nominal position of the interaction vertex. Finally, all events in the final analysis selections have been visually scanned and the remaining non$-ep$ background events have been removed.

4.2 Events triggering

As described in section 3.3, the trigger system separates real physics events from background events. This section outlines the main triggers used to select events containing an high energy electron (photon) or an undetected neutrino by the presence of missing transverse energy. An introduction to these triggers, also used to select NC DIS and CC DIS events, and a discussion of their efficiency are presented in the following section.

4.2.1 NC DIS subtriggers

The triggering of NC DIS events is based on the detection of a high energy deposit in the LAr calorimeter. Two trigger elements `LAr_electron1` and `LAr_electron2` are based on this condition. These trigger elements are combined with timing informations from the LAr calorimeter (`LAr_T0`) or from the central proportional chamber (`CIP_T0`) to form the subtriggers ST67 and ST75. The definitions of these subtriggers and of their triggers elements are listed in table 4.2. All the subtriggers have veto conditions which are used to reject beam-wall and beam-gas backgrounds.

The majority of NC DIS events are triggered by the ST67. In the HERA-I period the ST67 was defined as:

- 1994 - 1995: ST67 = `LAr_electron2` && (`Ray_T0` || `LAr_T0`)
- 1996 - 2000: ST67 = `LAr_electron1` && (`Ray_T0` || `LAr_T0`)

During the detector upgrade, the central and forward proportional chambers timing trigger element (`Ray_T0`) was replaced by the central inner proportional chamber trigger element (`CIP_T0`) for the HERA-II running periods (2003 – 2007):

- 2003-2006 (before run 483314):
  ST67 = `LAr_electron1` && (`CIP_T0` || `LAr_T0`)

The ST67 was finally changed by adding the veto conditions (`CIP_mul` && !`Mu_BIEC`) to physics triggers for the periods 2006 (since run 490493) and 2007, due to different beam related background conditions.

- 2006 (since run 490493)-2007:
  ST67 = `LAr_electron1` && (`CIP_T0` || `LAr_T0`)) && (`CIP_mul` && !`Mu_BIEC`)

The subtriggers ST71 and ST75 are used to select mainly events with an electron of lower energy ($E_e < 10$ GeV). The subtrigger ST77 is also interesting as some of the veto options applied to other subtriggers are not applied in this subtrigger. The most important trigger element in ST67 is the LAr energy condition. For electrons with an energy $E_e > 10$ GeV, the LAr_electron1 trigger element is almost fully efficient [26]. The regions in the LAr where this is not the case are excluded. In this analysis, the selected electron will always have an energy above 10 GeV. Therefore, the main sources of inefficiency of ST67 will arise from timing or veto conditions.

The control of the inefficiency associated to these conditions will thus be discussed and few examples of the verifications performed will be given. The efficiency of a trigger element TE, or of a combination of trigger elements, can be calculated as:

$$\epsilon_{TE} = \frac{\text{number of events triggered by MT and TE}}{\text{number of events triggered by MT}}\,, \tag{4.1}$$

where MT is a set of monitor triggers which are chosen to be independent of the trigger element we want to test. The selection of monitor triggers used for different trigger elements is given in table 4.3.

Timing conditions of ST67:

The `T0` trigger elements allow the bunch crossing of the interaction to be determined. Three different trigger `T0` requirements are combined with the electron requirement to form the subtriggers: the LAr calorimeter time measurement `LAr_T0` and the central (or central inner) and forward proportional chambers timing `Ray_T0` or `CIP_T0`. The efficiency of the `LAr_T0` and `CIP_T0` TE depends on the electron energy, the $z-$impact of the electron at the LAr surface, z_e, and y_h of the event measured using the hadronic system (see section 4.4.3) as can be seen in figure 4.2. The efficiency of the `LAr_T0` TE decreases at high y_h since this corresponds also to low E_e. The efficiency of the `CIP_T0` TE varies as a function of E_e, z_e, y_h and is around 99%. The combined efficiency of the two timing conditions is obtained from the individual efficiencies via the formula:

$$\epsilon(\texttt{LAr\_T0}||\texttt{CIP\_T0}) = \epsilon(\texttt{LAr\_T0}) + [1-\epsilon(\texttt{LAr\_T0})].\epsilon(\texttt{CIP\_T0})\,, \tag{4.2}$$

under the assumption that `LAr_T0` and `CIP_T0` are independent of each other. The combined efficiency is close to 99.9% in most of the measured variable range as shown in figure 4.2.

Veto conditions:

Veto conditions are applied to a large number of subtriggers. They mainly reject the background from beam-gas and beam-wall interactions. The typical inefficiency of the ToF vetoes is ∼0.5% and depends on the run conditions. The CIP is also able to veto background coming from interations in the collimators located in the beam pipe on the basis of the $z-$vertex origin of the tracks. The typical inefficiency of the CIP vetoes is ∼0.3%. However, a new veto condition based on the background muon detector (`CIP_mul` || (`!Mu_BIEC`)) has been added to ST67 for the periods 2006 and 2007. Their efficiency as a function of $\log_{10}(y_h)$, E_e and the polar angle of the scattered electron θ_e is presented in the figures 4.3 and 4.4. They are close to 100%.

<table>
<tr><th>Subtrigger</th><th>Definition</th></tr>
<tr><td>ST66</td><td>LAr_IF>1 && LAr_Etmiss>2
&& (CIP_T0 || (LAr_T0 && (!CIP_T0_nextbc)))</td></tr>
<tr><td>ST67</td><td>LAr_electron1 && (CIP_T0 || LAr_T0))
&& (CIP_mul>0 || !Mu_BIEC)</td></tr>
<tr><td>ST71</td><td>CIP_sig>1 && (CIP_T0 && (CIP_sig>0))</td></tr>
<tr><td>ST75</td><td>LAr_electron2 && (CIP_T0 && (CIP_sig>0))</td></tr>
<tr><td>ST77</td><td>LAr_Etmiss && (CIP_T0 && (CIP_sig>0))</td></tr>
</table>

Trigger Element	Description
LAr_T0	timing of the LAr calorimeter signals compatible with the nominal bunch crossing
LAr_Etmiss	vector sum of transverse energies in the LAr calorimeter 'trigger towers' above a threshold value
LAr_electron1	energy in a local region of LAr calorimeter (trigger tower) above a threshold value of 5 GeV
LAr_electron2	energy in a trigger tower above a threshold value of 7.5 GeV
LAr_BR	local coincidence between MWPC 'rays' and calorimeter 'towers'
LAr_FB, LAr_CB and LAr_IF	sum over all energies of BT lying in FB, CB and IF
Ray_T0	track multiplicity in the central and forward regions
CIP_T0	at least one central track
CIP_T0_nextbc	at least one track in next BC (background veto, shortened)
CIP_T0_mul	CIP multiplicity (number of tracks within the CIP acceptance)
CIP_sig	significance of central peak in zvtx histogram
Mu_BIEC	muon in backward inner endcap

Table 4.2: Definition of subtriggers (first table) and main trigger elements (second table) used in this analysis. The symbols && and || denote the logical AND and OR operations, respectively.

Trigger elements	Monitor triggers
LAr_electron1	ST75
LAr_T0	ST67 && (CIP_T0)
Ray_T0	ST67 && (LAr_T0)
CIP_T0	ST67 && (LAr_T0)
CIP_mul	ST67 && !(Mu_BIEC)
!(Mu_BIEC)	ST67 && (CIP_mul)

Table 4.3: NC DIS trigger elements and corresponding monitor triggers.

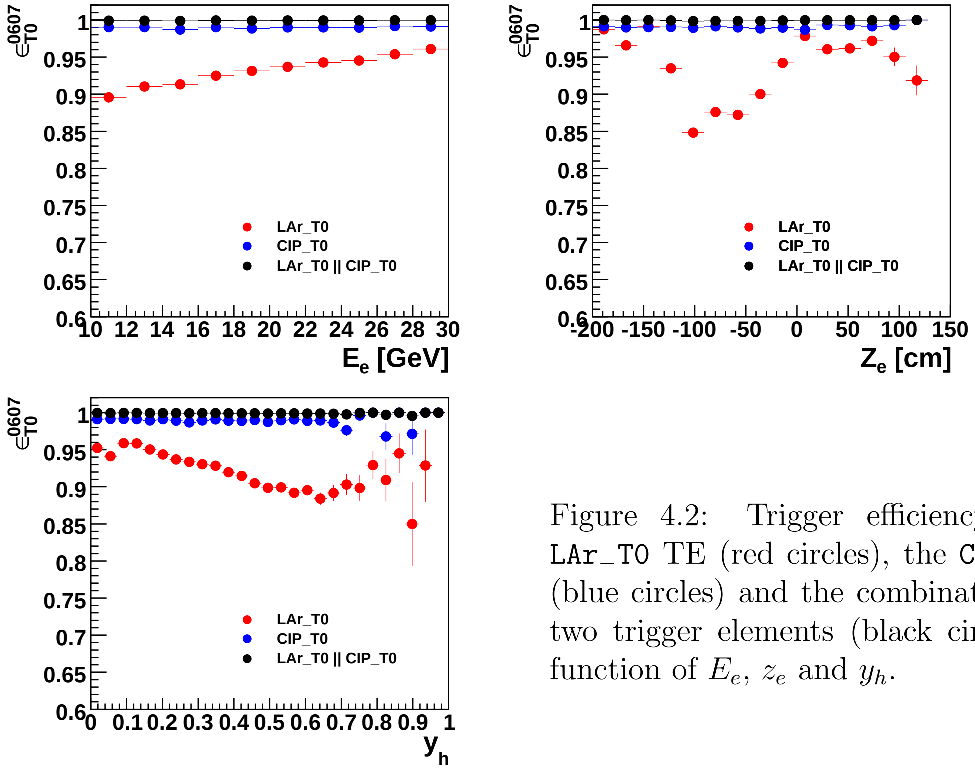

Figure 4.2: Trigger efficiency for the `LAr_T0` TE (red circles), the `CIP_T0` TE (blue circles) and the combination of the two trigger elements (black circles) as a function of E_e, z_e and y_h.

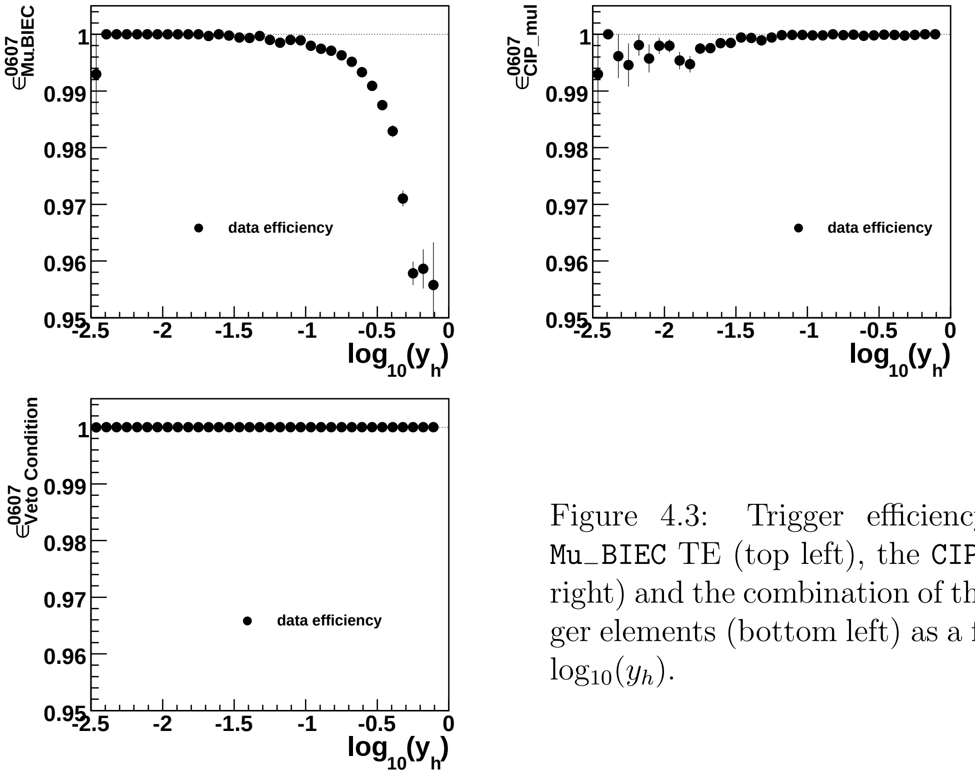

Figure 4.3: Trigger efficiency for the `Mu_BIEC` TE (top left), the `CIP_mul` (top right) and the combination of the two trigger elements (bottom left) as a function of $\log_{10}(y_h)$.

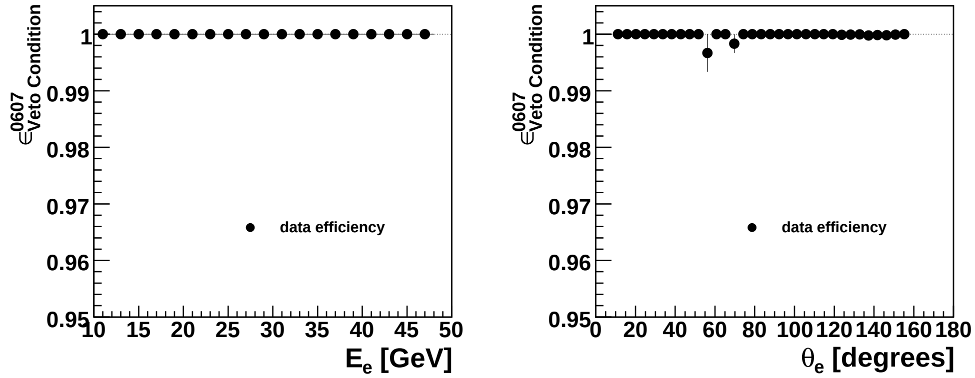

Figure 4.4: Trigger efficiency for the combination `CIP_mul||!Mu_BIEC` as a function of E_e (left) and θ_e (right).

4.2.2 CC DIS subtriggers

The triggering of CC DIS events is based on the detection of missing transverse energy in the LAr calorimeter. The corresponding trigger element (`LAr_Etmiss`) is combined with the timing information (`LAr_T0` and `CIP_T0`) from the LAr and from the tracking chambers to form the subtriggers ST66 and ST77. To further improve the trigger efficiency of CC DIS events, events triggered by the NC trigger ST67 are also accepted.

The efficiency of these CC DIS triggers can not be determined using true CC DIS events due to their low statistics. In Monte Carlo simulations the trigger response of these elements is also not correctly described and can not be used to determine the efficiency of CC DIS triggers. Therefore the technique of *Pseudo*-CC data events was introduced. For the production of *Pseudo*-CC events, real NC data events are selected and all informations related to the scattered electron are removed for all subdetectors and all triggers. That way modified NC DIS events mimic true CC DIS events. The full reconstruction and trigger filtering is then applied to these *Pseudo*-CC events. To ensure that the x and Q^2 spectra of CC DIS events are correctly reproduced, the *Pseudo*-CC events are reweighted with respect to the CC DIS spectra with the weight:

$$\omega(x, Q^2) = \frac{d^2\sigma_{CC}/dxdQ^2}{d^2\sigma_{NC}/dxdQ^2}\,, \tag{4.3}$$

where $d^2\sigma_{CC}/dxdQ^2$ and $d^2\sigma_{NC}/dxdQ^2$ are the CC and NC DIS differential cross sections, respectively. After this reweighting, the *Pseudo*-CC events can be used to measure the efficiency of CC triggers.

Under the assumption that the hadronic final state is similar for NC and CC DIS events, the *Pseudo*-CC events are indistinguishable from CC DIS events. Since for $Q^2 \leq 10000$ GeV^2 the NC DIS cross section is significantly higher than the CC DIS cross section, the statistic of *Pseudo*-CC events exceeds that of CC DIS events.

The efficiency of the subtrigger ϵ^{ST}_{trigg} can be calculated as follows:

$$\epsilon^{ST}_{trigg} = \frac{N^{ST}_{sel}}{N^{tot}_{sel}}\,, \tag{4.4}$$

where N^{tot}_{sel} is the total number of events and N^{ST}_{sel}, the number of events triggered by the subtrigger ST.

Examples of total trigger efficiencies in different running periods, are shown as a function of the missing transverse momentum, P_T^{calo}, and of the polar angle of the hadronic final state, γ^h in figure 4.5.

There is no large difference depending on the running period. The efficiency of the (ST66||ST67||ST77) combination increases from 40% at P_T^{calo} of 12 GeV to more than 95% for P_T^{calo} larger than 30 GeV. As the trigger efficiency is not described by the simulation, the inefficiency measured using *Pseudo*-CC events is applied to MC events.

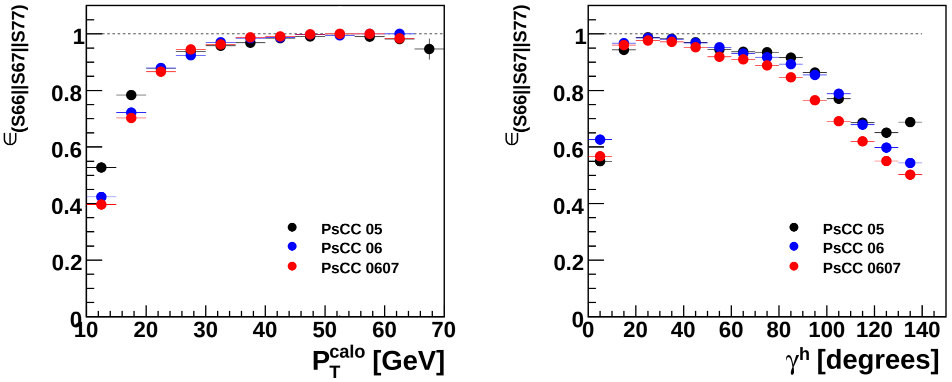

Figure 4.5: Trigger efficiencies as a function of P_T^{calo} and γ^h for different periods: 2005, 2006 and the fall of 2006 up to mid-2007.

4.3 Identification of particles

The final state reconstruction begins with tracks measured in the tracking detectors and clusters of calorimetric energy deposits in the calorimeters. Electromagnetic particles (electron and photon) and muons are then identified. The identification of electrons or photons relies on the measurement of a compact and isolated electromagnetic shower in the LAr calorimeter. The muon identification is based on a track in the inner tracking systems associated with signals in the muon detectors. Calorimeter energy deposits and tracks not previously identified as electron, photon or muon candidates are used to form combined cluster-track objects, from which the hadronic energy is reconstructed. Finally, jets are reconstructed from all hadronic final state particles.

4.3.1 Cluster and tracks

Clusters are reconstructed from neighboring calorimeter cells with an energy significantly above the noise threshold of ∼300 MeV. Cells not associated to clusters are suppressed to reduce noise. Clusters are defined to be electromagnetic or hadronic, depending in which region of the LAr calorimeter they are found.

Tracks must satisfy certain quality criteria as defined in [63]. Figure 4.6 presents the different types of tracks. These tracks are from the central and forward tracking detectors and are classified in three categories: Central (C), Combined (K) and Forward (F). The tracks can be from a primary vertex or from a secondary vertex.

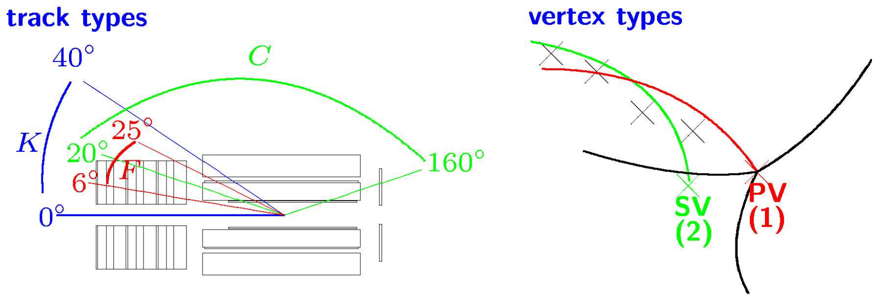

Figure 4.6: Different types of tracks depending on the polar angle range and the different possible vertex hypothesis for a single track.

For the track reconstruction, multiple fits and tracking detector combinations are used:

- Non-vertex-fitted tracks are stored in the DTNV bank. These tracks can be short, making the momentum measurement and even the direction uncertain.

- Vertex-fitted tracks are stored in the DTRA bank. These are reconstructed from DTNV tracks after a common fit to the event vertex.

- Good quality tracks are selected from vertex-fitted tracks. Tracks are of good quality if they satisfy the quality requirements presented in [64, 65]:

  - $P_T > 70$ MeV,
  - $|\mathrm{DCA}|.\sin\theta \leq 2$ cm,
  - $R_{start} \leq 50$ cm,
  - $R_{length} \geq 10$ cm for $\theta \leq 150°$ and
  - $R_{length} \geq 5$ cm for $\theta > 150°$

  where P_T is the transverse momentum of the track, θ the polar angle, DCA the distance of closest approach to the vertex in the transverse plane, R_{start} the track start radius from the nominal vertex position and R_{length} the length of the measured track segment in the transverse plane.

4.3.2 Electron and photon identification

Electromagnetic particles (electron and photon) are both defined as a compact and isolated electromagnetic shower in the LAr calorimeter.

Electromagnetic clusters are identified in the present analysis using the electron finder QESCAT, whose characteristics are described in details in [66]. Electrons are reconstructed starting from clusters in the calorimeter. First calorimetric clusters with at least 2 GeV and more than 50% of their energy in the electromagnetic part of the calorimeter are preselected. Neighbour clusters are grouped together if they are in the electron envelop. The envelop is defined by a cone with an opening angle of 7.5° and centered on the barycenter of the most energetic cluster. Then the resulting total cluster candidate has to satisfy the following criteria:

- a transverse momentum $P_T^e > 3$ GeV
- a total energy $E^e > 5$ GeV
- a number of calorimeter cells associated to the cluster greater than three to avoid to select a single "hot" calorimeter cell, produced by noise in the readout electronic.

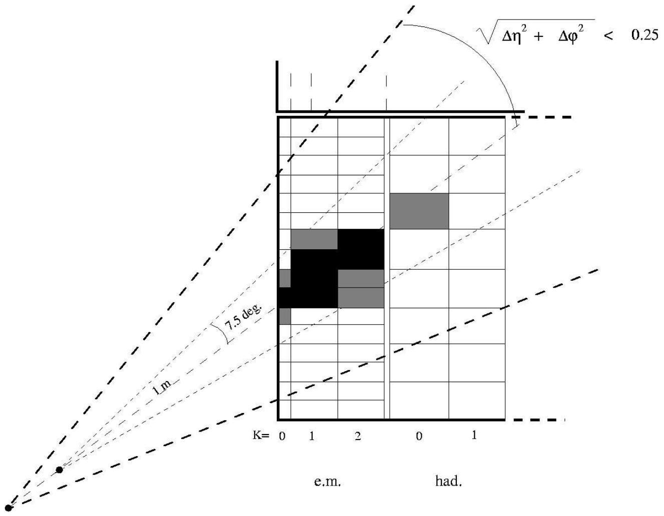

Figure 4.7: Schematic view of an electromagnetic cluster in the LAr, of the electron identification envelope and of the isolation cone.

In order to discriminate electrons or photons from hadronic particles, several conditions are applied on topological estimator variables used to characterize the electromagnetic shower. The most important estimators are described below:

- Electromagnetic fraction: EAEM. In order to reject pions which almost do not interact in the electromagnetic section, we define EAEM = E_{em}/E_{tot} where E_{em} is the energy deposited in the electromagnetic part of the calorimeter and E_{tot} is the total energy of the cluster. Only cells having a positive energy are considered. This fraction is close to one for electrons, except in the crack regions of the LAr (see section 3.2.1.1) where the electron deposits its energy in the first hadronic layer.

- Transverse radius: σ_R. The transverse size of an electromagnetic shower is of the order of the Molière radius R_M, which is smaller than the Interaction length λ_I. We calculate $\sigma_r = \sqrt{< r^2 > - < r >^2}$ where r^n are the moments of order n of transverse distances (r_i) of cells to the axis of the shower. These moments can be written as $< r^n >= w^{-1} \sum \omega_i \, r_i^n$ with $w_i = E_i/V_i$ and $w = \sum \omega_i$. V_i and E_i are respectively the moments volumes and the energies of the cells. For electrons, this radius is small.

- Energy fraction in the "Hot" core: EAHN $= E^N_{Hot}/E_{em}$ where E^N_{Hot} is the energy of the N most energetic neighboring cells. N is defined according to the cluster position in the LAr calorimeter: $N = 4$ for BBE, CB1 and CB2, $N = 8$ for CB3, FB1 and FB2 and $N = 12$ for IF. This fraction is required to be greater than 0.4 in the forward region and 0.8 in the backward region.

- Isolation criteria: EAIF. To estimate the isolation of the candidate cluster, we define EAIF= E_{tot}/E_{iso} where E_{iso} is the energy in an isolated cone of radius $R = 0.25$ in the $\eta - \phi$ plane and E_{tot} is the total energy of the cluster. A cluster is identified as an electron if EAHN$>$ 0.98 or EAHN$>$ 0.95 and $E^{had}_{iso} <$ 300 MeV where E^{had}_{iso} is the hadronic energy in the isolation cone.

After these criteria, identified electromagnetic clusters are required to be isolated against hadrons. The energy not associated to the electromagnetic cluster, in an isolation cone of radius $R = 0.5$ in the $(\eta - \phi)$ plane around the barycenter of the electromagnetic cluster is required to be less than 3% of the electron energy. Figure 4.7 shows a schematic view of a cluster in the LAr and the definition of the electron envelop and of the isolation cone.

The finding efficiency for electromagnetic clusters is close to 100% [26].

In a second step, track informations can be used to make the distinction between electrons and photons. Depending on the topology of the studied final state, this distinction may be applied to reduce the probability of misidentification or may not be used if a higher selection efficiency is needed. An electron is identified by requiring the presence of a track with a distance of closest approach (DCA) to the electromagnetic cluster below 12 cm. This track-matching requirement will be applied only in the central region ($\theta^e > 35°$) because the forward tracking detector has a lower track detection efficiency than the central tracker.

The photon identification relies also on the measurement of an electromagnetic shower and the same calorimeter isolation criteria against hadrons as for the electron are applied. In addition, to distinguish photons from electrons, vetoes on any charged track pointing to the electromagnetic cluster are applied. No track with a distance of closest approach (DCA) to the cluster below 24 cm or within $R < 0.5$ should be present. In the central region ($\theta^\gamma > 20°$), no well measured track with a DCA to the electromagnetic cluster below 12 cm should be present. Dead material of the tracking detectors may lead to the conversion of photons, tracks are then associated to the electromagnetic cluster, inducing inefficiency on the identification of photons.

Elastic QED Compton events can be used to estimate the inefficiency induced by the track vetoes. Elastic QED Compton events are selected from an event sample satisfying the following requirements:

- one electron with a transverse momentum $P_T^e > 10$ GeV, and a good track associated,
- an additional electromagnetic cluster with $P_T > 5$ GeV,
- they are detected in the central region $20° < \theta < 150°$,
- the longitudinal energy balance (see section 4.4.4) is required to be $E - P_z > 45$ GeV,
- the total hadronic energy E_h is required to be below 5 GeV and no signal should be present in the forward muon detectors (elasticity requirements),
- no track requirements for the second electromagnetic cluster.

The measured efficiency of photon identification is shown in figure 4.8. In the central region ($20° < \theta^\gamma < 150°$), where track vetoes are applied, the efficiency is ∼90%. The identification efficiency in the forward region is 100%, as no track vetoes are applied here. The agreement between the data and the MC simulation is better than 10%.

The polar angle of electrons or photons is measured from the barycenter of the electromagnetic cluster. It is know with a precision of 3 mrad, mainly dominated by the precision of the alignment of the LAr calorimeter with the tracking systems.

4.3.3 Muon identification

Muon candidates are identified by their characteristic signature in the LAr calorimeter, the instrumented iron surrounding the LAr calorimeter and some energy deposits in the central muon detector or by a track in the forward muon detector. The muon momentum is determined from the track curvature in the toroidal or solenoidal magnetic fields.

The muon identification starts by the presence of a good quality track in the inner tracking system. This track is required to be associated to a track in the forward muon detector or to a track or energy deposits in the central muon detector. The quality of the muon identification is categorized by a series of decreasing quality criteria (grades ranging from 1 to 5), related to the amount of detector informations available. Best quality muons are graded as grade ”1” or grade ”2”. They have an iron track associated to a central track within a distance of 0.5 unit in the $(\eta - \phi)$ plane. Grade ”3” muons have no iron track information and are based on a central

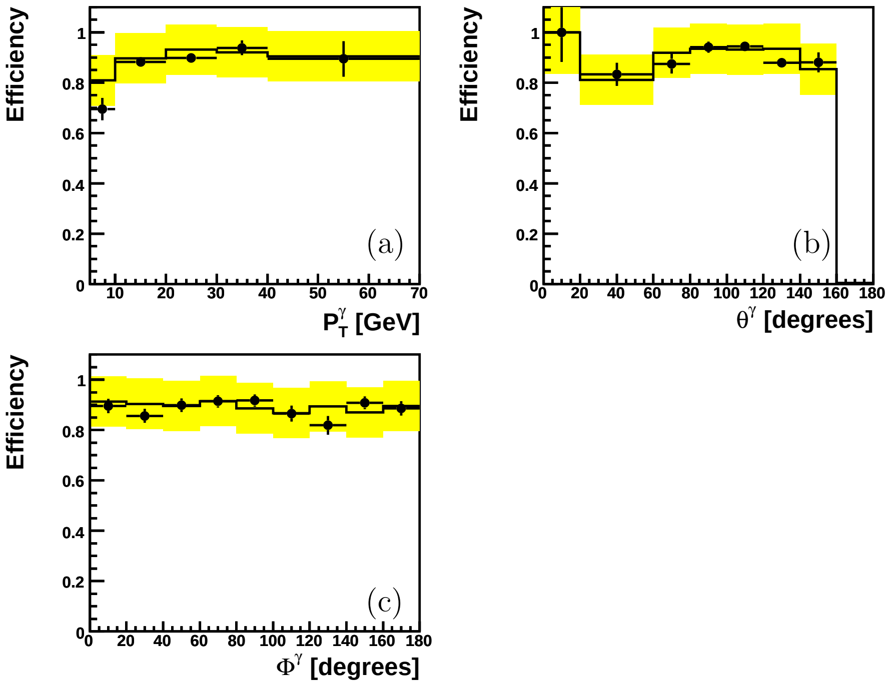

Figure 4.8: Photon identification efficiency as a function of the transverse momentum P_T^γ (a), the polar angle θ^γ (b) and the azimuthal angle Φ^γ (c) of the photon. The data are represented by the black dots and the MC simulation by the histogram. The yellow band represents the 10% systematic error on the MC simulation.

track associated to calorimetric energy in the iron. Only muons of grades ”1”, ”2” and ”3” are used in this analysis.

The muons should be isolated from any other energy deposit in the LAr calorimeter. A muon candidate should have no more than 5 GeV of deposited energy in a cylinder, centred on the muon track direction, of radius 25 cm and 50 cm in the electromagnetic and hadronic sections of the LAr calorimeter, respectively. Misidentified hadrons are almost completely suppressed by requiring that the muon candidate is separated from the closest jet with $P_T > 2.5$ GeV by $R > 1$ in the $(\eta - \phi)$ plane. The efficiency to identify muons is greater than 90% [67].

4.3.4 Hadronic final state reconstruction

The algorithm used to reconstruct the hadronic final state is based on a combination of informations from tracks and calorimetric clusters. The most precise information from the tracker or from the calorimeter is selected to improve the resolution of the hadronic energy reconstruction. In the combination, the algorithm takes care to avoid double counting of energy.

Hadronic final state identification starts with selected tracks and calorimeter clusters not yet identified as isolated electron or muons. The definition of hadronic final state particle candidates starts by assuming that every track originates from a pion. The track measurement is compared to the calorimetric energy behind the track and the most precise information is used to define the four-vector of the corresponding hadronic final state particle.

The relative error on the track energy E_{track} is compared to the expected relative LAr resolution by the condition:

$$\frac{\sigma_{E_{track}}}{E_{track}} < \frac{0.5}{\sqrt{E_{track}}} \,. \tag{4.5}$$

If this condition is satisfied, the calorimetric energy in a cone behind the track impact position is associated to the tracks and the track measurement is used to define the hadronic particle four-vector. In case the condition is not full-filled, the calorimetric energy measurement is preferred and used to define the four-vector of the hadronic particle. In the central region, the track energy can be more precise than the calorimeter energy up to 25 GeV. In this region, typically 60% of the total hadronic transverse momentum is measured from track information.

After all tracks have been associated to clusters, defining all charged hadronic final state particles, the residual clusters are considered to be neutral hadronic final state particles.

4.3.5 Jets identification

Jets are reconstructed from hadronic final state particles using an inclusive $k_\perp$ algorithm [68, 69]. The algorithm depends on a parameter R, which is chosen to be of the order of one. This parameter is comparable to the cone size parameter in a cone algorithm. The algorithm was coded with a recombination scheme balanced by the transverse momentum. The jet finder identifies jets with a minimum transverse momentum of 2.5 GeV.

The jet selection efficiency is close to 100%.

The error on the measurement of jet polar angles was determined using NC DIS events by comparing the polar angle of jet with the scattering polar angle of the struck quark, as deduced from the electron kinematic [70]. The uncertainy on the polar angle of jets was estimated to be 10 mrad.

4.4 Reconstruction of event kinematic variables

The different methods used in *ep* collisions for the reconstruction of main kinematic variables characterising an event are presented. First, the electron and double angle methods used for the kinematic reconstruction of NC DIS events are discussed. Then the hadron method, the only method available to reconstruct kinematic variables for CC DIS events, is presented. These methods are used for the electron and hadronic energy calibrations.

4.4.1 The electron method

The kinematic variables of an event are reconstructed in the electron method [71] using the energy E_e and the polar angle θ^e of the scattered electron:

$$Q_e^2 = 4E_e^0\ E_e\ \cos^2\frac{\theta^e}{2}, \quad x_e = \frac{E_e\ E_e^0 \cos^2\frac{\theta^e}{2}}{E_p\ (E_e^0 - E_e\ \sin^2\frac{\theta^e}{2})}, \quad y_e = 1 - \frac{E_e}{2E_e^0}(1-\cos\theta^e)\,, \tag{4.6}$$

where E_e^0 is the energy of the incident electron beam. The resolutions in x and Q^2 as a function of the energy and polar angle of the scattered electron are given by:

$$\frac{dx_e}{x_e} = \frac{1}{y}\frac{dE_e}{E_e} + \tan\frac{\theta^e}{2}(x\frac{E_p}{E_e^0} - 1)d\theta^e, \qquad \frac{dQ_e^2}{Q_e^2} = \frac{dE_e}{E_e} - \tan\frac{\theta^e}{2}d\theta^e\,. \tag{4.7}$$

Due to the $1/y$ dependence of $\frac{dx_e}{x_e}$ the resolution in x is sufficiently good only at high y. However, the Q^2 resolution is very good over the full kinematic range.

4.4.2 The double angle method

An alternative method which may be used for the reconstruction of kinematic variables in NC DIS events is the Double Angle method (DA method) [71]. In this case only the polar angle of the scattered electron (θ^e) and of the hadronic final state γ^h are used:

$$y_{DA} = \frac{\sin\theta^e.(1-\cos\gamma^h)}{\sin\gamma^h + \sin\theta^e - \sin(\theta^e + \gamma^h)}\,, \tag{4.8}$$

$$Q_{DA}^2 = \frac{4.E_e^{0^2}.\ \sin\gamma^h(1+\cos\theta^e)}{\sin\gamma^h + \sin\theta^e - \sin(\theta^e + \gamma^h)}\,, \tag{4.9}$$

and $x_{DA} = Q_{DA}^2/(s.\ y_{DA})$.

The hadronic polar angle γ^h is given by:

$$\tan\left(\frac{\gamma^h}{2}\right) = \frac{\sum E_h - P_{z,h}}{P_T^h}. \tag{4.10}$$

The electron transverse momentum calculated using the double angle method (P_T^{DA}) is then given by:

$$P_T^{DA} = \frac{2E_e^0}{\tan\frac{\gamma^h}{2} + \tan\frac{\theta^e}{2}}. \tag{4.11}$$

This method is particularly useful for the calibration of the calorimeters since it is to first order independent of the calorimeter energy. The energy of the scattered electron determined using the DA method is given by:

$$E_{DA} = \frac{2E_e^0\ \sin\gamma^h}{\sin\gamma^h + \sin\theta^e - \sin(\gamma^h + \theta^e)}. \tag{4.12}$$

4.4.3 The hadron method

For the hadronic final state, the transverse momentum P_T^h and the inclusive hadronic angle γ^h are defined by:

$$P_T^h = \sqrt{(\sum_h P_{x,h})^2 + (\sum_h P_{y,h})^2}, \quad \tan\gamma^h = \frac{\sum E_h - P_{z,h}}{P_T^h}, \tag{4.13}$$

where the sum run over all particles in the hadronic final state.

Using the method called hadron method, introduced by Jacquet-Blondel [72], the kinematic variables can be determined as follows:

$$y_h = \frac{\sum E_h - P_{z,h}}{2E_e^0}, \quad Q_h^2 = \frac{{P_T^h}^2}{1 - y_h}, \quad x_h = \frac{Q_h^2}{s\ y_h}. \tag{4.14}$$

4.4.4 Definition of other kinematic variables

The missing transverse momentum P_T^{miss}:

The missing transverse momentum in an event, P_T^{miss}, is calculated using the vector sum of all particles identified in the detector and taking the transverse component of this quantity. A large P_T^{miss} in an event is the signature of the emission of a neutrino, which can not be detected. Its transverse momentum should balance the calculated P_T of all detected particles.

The longitudinal energy balance $E - P_z$:

The longitudinal energy balance of an event, $E - P_z$, is calculated by a sum over all particles in the event, of their energy minus their momentum along the z-direction:

$$E - P_z = \sum_i (E_i - P_{z,i}). \tag{4.15}$$

If all final state particles are detected, energy conservation implies that $E - P_z$ be equal to twice the electron beam energy:

$$E - P_z = E_p + E_e^0 - P_{z,p} - P_{z,e} = 2\ E_e^0 \approx 55.2 \text{ GeV}, \tag{4.16}$$

with $P_{z,p} = E_p$ and $P_{z,e} = -E_e^0$.

This variable allows to distinguish events in which the final state is completely reconstructed in the detector, from events where particles have left the detector un-observed or where a neutrino has been emitted.

Figure 4.9 shows the distributions of $E - P_z$ for NC DIS and for CC DIS events. In NC DIS events, $E - P_z$ is peaked around 55 GeV, while in CC DIS events $E - P_z$ is below 55 GeV.

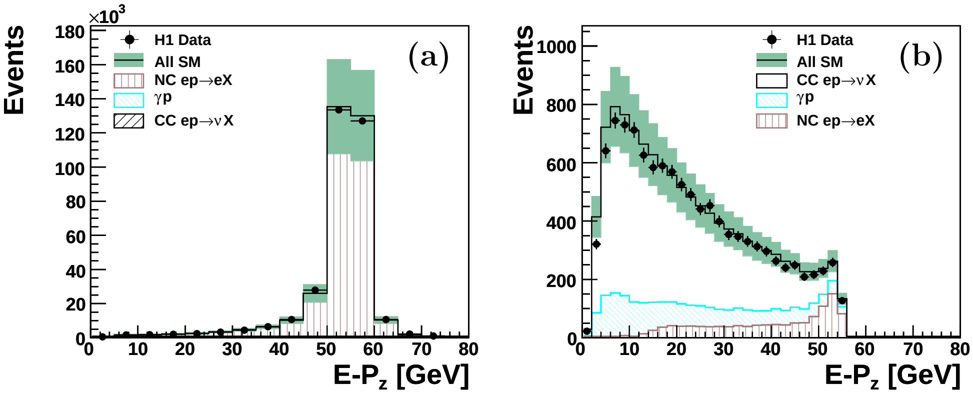

Figure 4.9: Distribution of the longitudinal energy balance $E-P_z$ for NC DIS events (a) which peaks at 55 GeV, on the contrary to CC DIS events (b).

The variable V_{ap}/V_p:

This variable is used to discriminate events with a true undetected neutrino and events where the missing transverse energy is created from energy leakage or mismeasurement. This variable corresponds to the ratio between the projections of the energy quantities parallel (V_p) and anti-parallel (V_{ap}) to the direction of the missing transverse energy.

The variables V_p and V_{ap} are defined as:

$$V_{ap} = -\sum \frac{\vec{P}_T^h . \vec{P}_T^{ap}}{P_T^h} \qquad for \quad \vec{P}_T^h . \vec{P}_T^{ap} < 0, \tag{4.17}$$

$$V_p = \sum \frac{\vec{P}_T^h . \vec{P}_T^p}{P_T^h} \qquad for \quad \vec{P}_T^h . \vec{P}_T^p > 0, \tag{4.18}$$

where $\vec{P}_T^p$ and $\vec{P}_T^{ap}$ are the transverse momentum vector parallel and anti-parallel to the transverse vector sum $\vec{P}_T^h$ formed by all detected particles. A schematic view of the definition of the two parallel and anti-parallel hemispheres is displayed in figure 4.10.

Events with a large missing transverse momentum, as CC DIS events, would typically have very different V_{ap} and V_p components leading to $V_{ap}/V_p \simeq 0$. In photoproduction events or NC DIS events with balanced transverse momentum vectors, $V_{ap}/V_p \simeq 1$. Figures 4.11(a) and (b) present the distribution of the V_{ap}/V_p variable in CC and NC DIS events, respectively.

The D_{jet} and D_{track}: Isolation criteria

To ensure a clean identification of leptons, minimal isolation distances to other objects, as tracks or jets, in the $(\eta - \phi)$ plane are often required. For example, the distance D_{jet} from the lepton track to the axis of the closest jet in the plane $(\eta - \phi)$ is defined as:

$$D_{jet} = \sqrt{(\Delta\eta_{track-jet})^2 + (\Delta\phi_{track-jet})^2}. \tag{4.19}$$

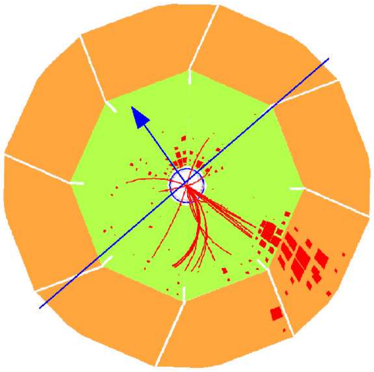

Figure 4.10: Radial view of a typical charged current event. The line shown is perpendicular to the axis of the transverse vector sum of the all detected particles ($\vec{P}_T^h$) and divide the detector in two hemispheres, visualizing the large transverse imbalance in the charged current event. All measured final state momentum is in one hemisphere, since the ν is not detected on the opposite side.

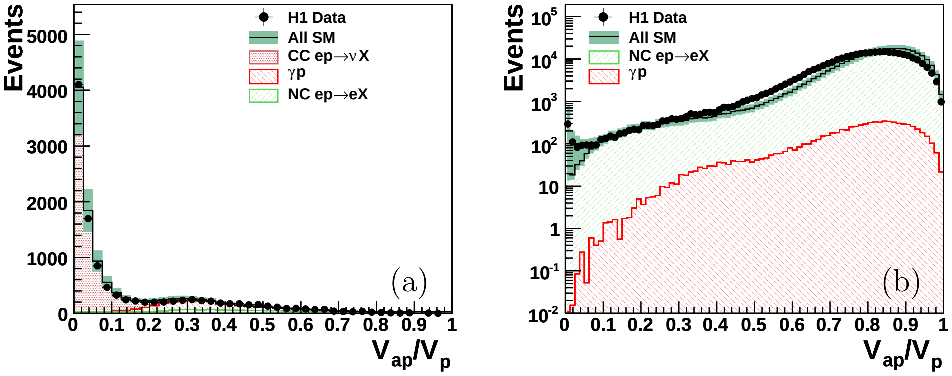

Figure 4.11: Distribution of the variable V_{ap}/V_p for CC DIS events (a) and for NC DIS events (b).

A similar definition is used for D_{track}, the distance from the nearest good track to the identified lepton in the plane $(\eta - \phi)$.

In the selection cuts of this analysis, the identified lepton is called "isolated lepton" if it is separated from jets, and from track by a minimum distances of $D_{jet} > 0.5$ and $D_{track} > 0.5$, respectively.

The variable ξ^e:

The variable ξ^e can be defined for any electromagnetic cluster as:

$$\xi^e = E_e \cos^2(\theta^e/2), \tag{4.20}$$

where E_e and θ^e are the energy and polar angle of the electromagnetic cluster, respectively. This variable is proportional to the four-momentum transfer squared Q_e^2 for NC DIS events. If the electromagnetic cluster is not the scattered electron of a NC DIS event or the radiative photon from a CC DIS event, but coming from the de-excitation of a massive particle, then high values of ξ^e are expected since the decay products are boosted in forward direction.

4.4.5 Reconstructed masses

In this section, we explain the methods use to reconstructed the mass of excited leptons l^* (ν^* and e^*) from their decay products. The l^* mass can be reconstructed from the four-vectors of the lepton l (l is an electron or a neutrino) and the V gauge boson ($V = \gamma, Z$ or W) by using energy and momentum conservation laws. The invariant mass of the excited lepton, M_{l^*}, is defined as:

$$M_{l^*}^2 = (E^l + E^V)^2 - (p^l + p^V)^2 \,. \tag{4.21}$$

where: $E^{l\,(V)}$ and $p^{l\,(V)}$ are the energy and momentum components of the lepton (l) and boson (V) four-vector. They are denoted as:

$$\begin{aligned} \mathbf{P}^l &= (E^l, p^l) = (E^l, p^l_x, p^l_y, p^l_z)\,, && (4.22)\\ \mathbf{P}^V &= (E^V, p^V) = (E^V, p^V_x, p^V_y, p^V_z)\,. && (4.23) \end{aligned}$$

In the final state of $\nu^*\rightarrow\nu\gamma$, $\nu^*\rightarrow\nu Z$ and $e^*\rightarrow\nu W$, at least one unobserved neutrino is present. The four-vector of the neutrino candidate is reconstructed assuming transverse momentum and $E - P_z$ conservations, and that all the missing transverse momentum of the event P_T^{miss} originates from a single neutrino.

The x and y components of neutrino four-vector are defined as $p_x^\nu = P_x^{miss}$ and $p_y^\nu = P_y^{miss}$, respectively. The energy and longitudinal momentum of the neutrino, determined by energy-momentum conservation, are:

$$\begin{aligned} P_\nu^z &= \frac{(P_T^{miss})^2 + (55.2 - (E - P_z))^2}{2\,(55.2 - (E - P_z))}, && (4.24)\\ E_\nu &= \sqrt{(p_x^\nu)^2 + (p_y^\nu)^2 + (p_z^\nu)^2}. && (4.25) \end{aligned}$$

In the case of hadronic decay of Z or W gauge bosons ($\nu^*\rightarrow\nu Z_{\hookrightarrow qq}$, $\nu^*\rightarrow eW_{\hookrightarrow qq}$ or $e^*\rightarrow eZ_{\hookrightarrow qq}$, $e^*\rightarrow\nu W_{\hookrightarrow qq}$), the invariant mass of the boson V is reconstructed from the four-vector of a pair of jets associated to its decay. Among all jets in the event, the pair of jets whose invariant mass is closest to the Z or W gauge boson mass is chosen and attributed to a possible decay of a Z or W boson.

To improve further the resolution on the l^* reconstructed mass, an additional correction on the sum of the four-vectors of the two jets associated to a boson decay is applied. The sum four-vector, corresponding to the four-vector of the boson candidate, is scaled such that its mass is set equal to the nominal boson mass.

A similar method is applied to reconstruct the l^* mass in the case of leptonic decays of the Z or W bosons.

If two neutrinos are expected in the final state, as in the $e^*\rightarrow\nu W_{\hookrightarrow e\nu}$ or $e^*\rightarrow eZ_{\hookrightarrow\nu\nu}$ decays, only one neutrino four-vector can be reconstructed from the P_T^{miss} observed in the data. This creates a shift of 20% to 30% on the mean value of the reconstructed e^* mass compared to the true one, as well as a broading of the reconstructed mass distribution.

4.5 Energy calibrations

4.5.1 Electron energy calibration

Calibration method:

For the electron calibration, NC DIS events are used and the cluster energy using the LAr calorimeter is compared to the electron energy calculated in the DA method. To ensure a sufficient precision of the DA method, only the following part of the phase space is used:

- $y < 0.3$ (0.5) for $z_{impact} < 20$ cm ($20 < z_{impact} < 100$ cm) ensures a precise reconstruction of E_{DA},
- $\gamma^h > 8°$ requires that the hadronic final state be well contained in the detector and therefore well measured,
- $44 < E - P_z < 66$ GeV reduces the influence of radiative effects on the DA reconstruction,
- $0.5 < P_T^h/P_T^e < 1.5$ ensures a good reconstruction of the hadronic final state.

Then we adjust the global response of each octant of each wheel of the calorimeter. In the forward region of the calorimeter this method is limited by the low statistic available. The BBE region is also difficult to calibrate because of important energy losses.

In the different regions of the LAr calorimeter, the measured energy of the electron cluster E_e is compared to the energy deduced from the double angle method, E_{DA}, by constructing the energy balance distribution E_e/E_{DA}. Figure 4.12 shows an example of the evolution of the mean value of $E_{bal} = E_e/E_{DA}$ distributions for the BBE, CB1 and CB2 octants before and after calibration. The calibration factor f_{cal} is determined from the E_e/E_{DA} distribution as $f_{cal} = 1/ < E_e/E_{DA} >$. In order to reduce the influence of tails in the distributions only events with $0.8 < E_e/E_{DA} < 1.2$ are considered for the mean value calculation. More details about the method can be found in [26, 73].

In the following, the results obtained from the tests of this calibration procedure are presented. NC DIS or elastic QED Compton event can be used to verify the precision of the calibration, but here only results using an NC DIS event sample are shown. The electron energy calibration has been tested for all running periods.

Only clean NC DIS events with only one reconstructed electron are selected. The NC DIS events used for the calibration are selected by the following requirements:

- good general quality of events (HV, vertex, *etc*),
- only one electron,
- $E_{DA} > 11$ GeV, $y_{DA} < 0.9$,

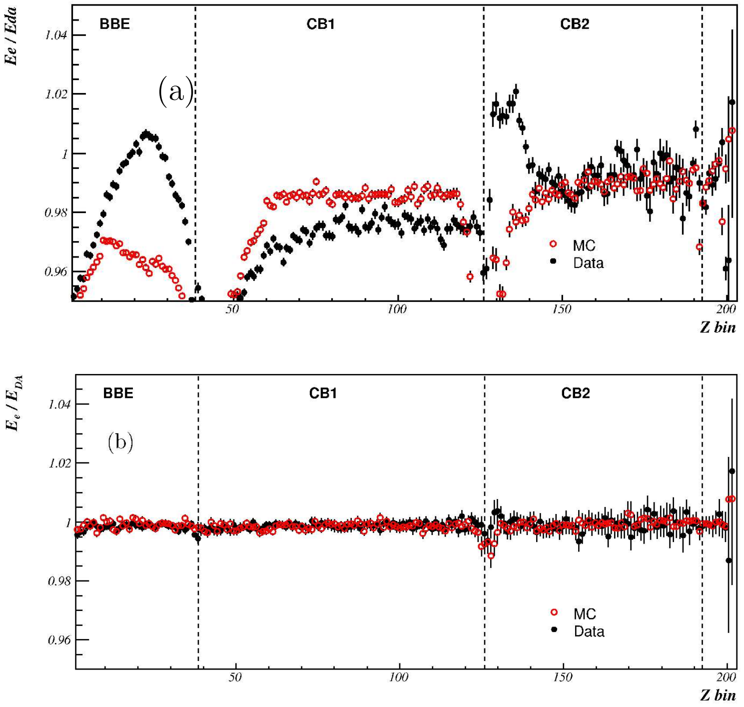

Figure 4.12: Evolution of the mean values of energy balance distributions E_e/E_{DA} as a function of the $z-$impact of the electron on the LAr surface before (a) and after (b) calibration. These figures are taken from [26].

- $|z_{vtx}| < 35$ cm,

- other selection cuts as used to select the calibration event sample.

Results:

Distributions of the energy balance $E_{bal} = E_e/E_{DA}$ are built for several bins in E_{DA} and θ^e or in $z-$impact. In each region, the mean value of the E_{bal} distribution is determined using a Gaussian adjustment to the central part of these distributions. Figure 4.13 illustrates the mean values of the energy balance E_{bal} distributions and of the ratio $E_{bal}(Data/MC)$ of the E_{bal} distributions mean values measured for data and MC events, as a function of θ^e in the forward region of the detector. The data are well described by the MC simulation within ±2% which is taken to be the systematic error on the electron energy measurement in the forward region. Figure 4.14 shows the mean values of E_{bal} distributions for data and for MC events, and their ratio $E_{bal}(Data/MC)$, as a function of the $z-$impact z_e of the electron on the LAr surface. We observe also a good agreement between the data and the MC within 0.7% in the central region, increasing to 2% in the forward region. These values are also taken as systematic errors on the electron energy measurement in the central region.

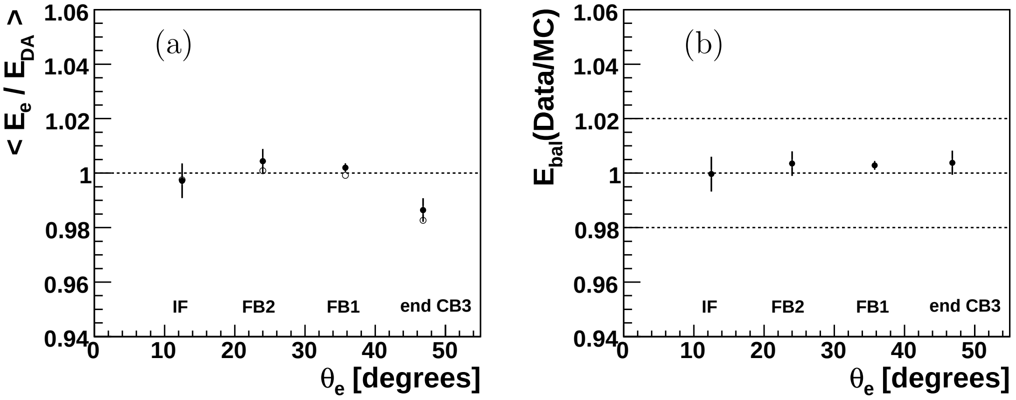

Figure 4.13: Results obtained using all data combined for the electron energy measurement in the forward region of the detector, for inclusive NC DIS events. The mean value of $E_{bal} = E_e/E_{DA}$ distributions (a) as a function of θ^e is shown. The open points are for the MC simulation and the closed points for the data. The ratio of the data and MC mean values of figure (a), $E_{bal}(data/MC)$ is presented in figure (b) as a function of θ^e. The dashed lines represent the uncertainty on the electron energy calibration of 2% considered in the forward region.

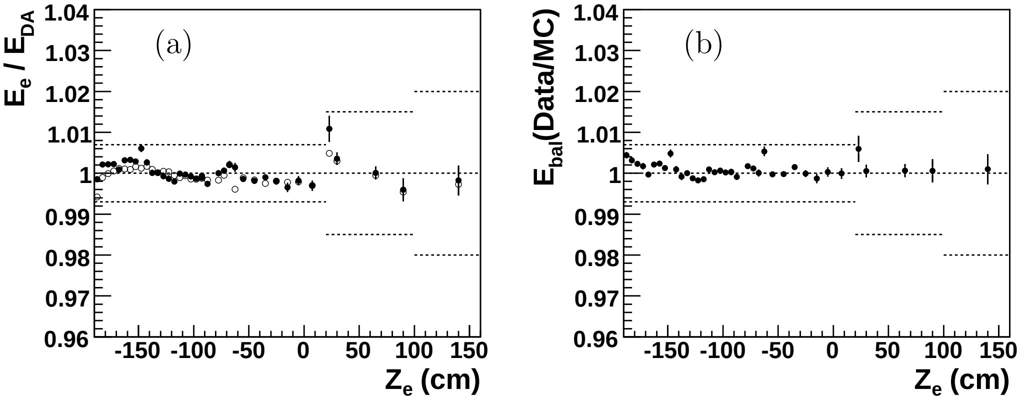

Figure 4.14: Results obtained using all data combined for the electron energy measurement in the central region of the detector. The absolute values of $E_{bal} = E_e/E_{DA}$ (a) and $E_{bal}(data)/E_{bal}(MC)$ (b) as a function of $z-$impact of e impact are presented. The dashed lines present the uncertainty on the electron energy calibration varying from 0.7% to 2% in the central region.

4.5.2 Hadronic energy calibration

Calibration method:

For the calibration of hadronic energies, kinematic quantities determined using the double angle method are also used as a reference. The goal of the calibration procedure is to achieve simultaneously a good absolute calibration of jet energies as well as a relative agreement between data and Monte Carlo. The absolute calibration is necessary to correctly determine the invariant mass of particles decaying into jets, which is of prime importance for searches. The relative agreement between data and MC is important to correctly compare observations and predictions.

The ratio of the hadronic transverse momentum P_T^h and the double angle transverse momentum P_T^{DA} is used in the calibration and is called P_T^{bal}:

$$P_T^{bal} = \frac{P_T^h}{P_T^{DA}} \tag{4.26}$$

The calibration is applied to jets. A specific sample of high Q^2 NC DIS events with only one reconstructed jet and suppressed initial state radiations is selected. The calibration factor $C(\theta, P_T^{DA})$ is determined as a function of the P_T^{DA} of the event, for different polar angle regions of the detector as defined in figure 4.15. In each θ region and in each P_T^{DA} bin, the factor $C(\theta, P_T^{DA})$ is determined by comparing the measured transverse momentum of the jet to the P_T^{DA} of the event.

The calibrations are applied only to the energy fraction of the uncalibrated jet four-vectors measured with clusters. The energy fraction of jets measured with tracks is already calibrated during their reconstruction and is left untouched.

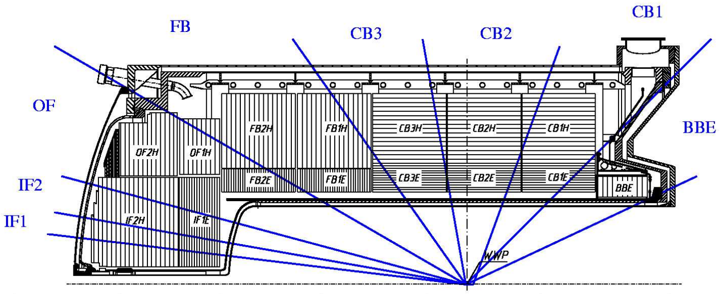

IF1	IF2	OF	FB	CB3	CB2	CB1	BBE
7°-10°	10°-15°	15°-30°	30°-55°	55°-80°	80°-110°	110°-135°	135°-155°

Figure 4.15: The different areas of the LAr calorimeter used for the hadronic calibration.

Test of hadronic calibration using NC DIS events:

To verify the precision of the calibration procedure, a specific NC DIS event sample is selected by the following requirements:

- good general quality events (high voltage, vertex, etc)
- $Q^2 \geq 100$ GeV^2,
- one electron with $P_T^e \geq 10$ GeV,
- $P_T^h / P_T^e > 0.35$,
- $E - P_z > 42$ GeV, to reduce effect of initial state radiations and to ensure that the double angle momentum is correctly measured,

- $\theta^{jet} > 7^\circ$, to ensure that all jets in the events are contained in the acceptance of the calorimeter. This allows to test also the absolute energy calibration.

Samples containing exactly one jet, two jets and three jets will also be separated. Samples with two or three several jets are completely independent from the events used for the calibration and therefore allows a good test of the method. In addition, as in the search for excited leptons we will be interested in events containing two or more jets, it is important to determine the precision of the hadronic calibration in such specific event samples.

One jet check sample:

First the checks with one jet sample are performed on both data and NC DIS Monte Carlo events. All H1 data are combined. The mean values of the $P_T^{bal} = P_T^h/P_T^{DA}$ distributions as a function of P_T^{da} and θ_h^e are presented in figure 4.16. The hadronic inclusive polar angle calculated with the scattered electron variable θ_h^e is defined as:

$$\tan(\theta_h^e/2) = (2\ E_e^0 - (E_e - P_z^e))/P_T^e \tag{4.27}$$

Values are presented before and after the application of the hadronic calibration. After calibration, the data are well described by the MC simulation within ±2%. The absolute energy scale is also correct to 2%, after calibration.

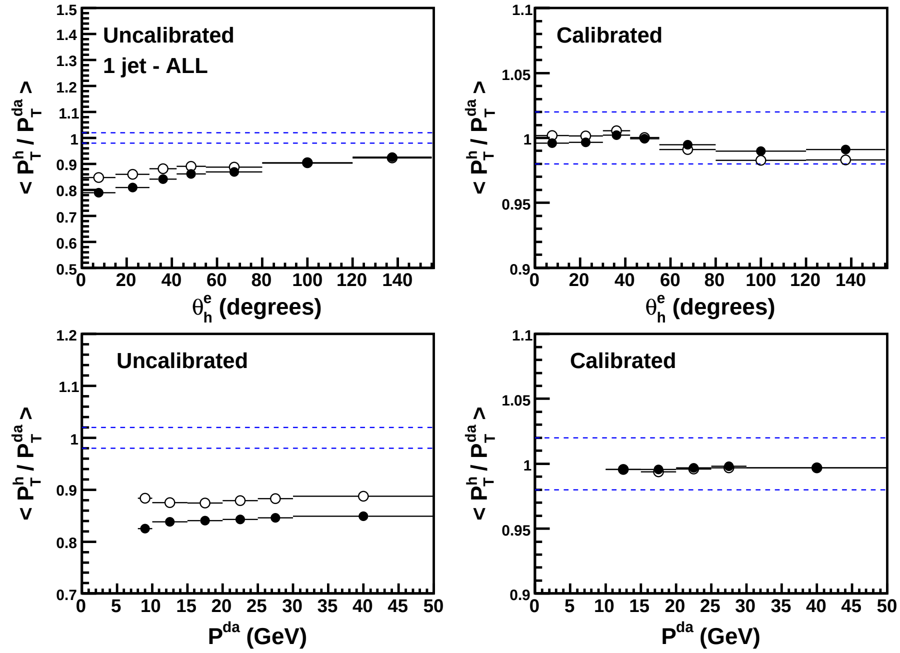

Figure 4.16: The ratio $P_T^{bal} = P_T^h/P_T^{da}$ as a function of θ_h^e (on the first line) and P_T^{da} (on the second line) for one jet event sample, before (left) and after (right) calibrations for all H1 data combined. The opened points are for the MC simulation and the black points for the data. The dashed lines represent the uncertainty on the jet calibration of ±2%.

Two and three jets check samples:

Same tests with the two and three jets event samples are also performed. The mean values of the $P_T^{bal} = P_T^h/P_T^{da}$ distributions as a function of P_T^{da} and θ_h^e are presented in figures 4.17 and 4.18, for the two and three jets check samples, respectively. Again, we observe a good agreement between data and MC simulation within ±2%, after calibration and in both samples.

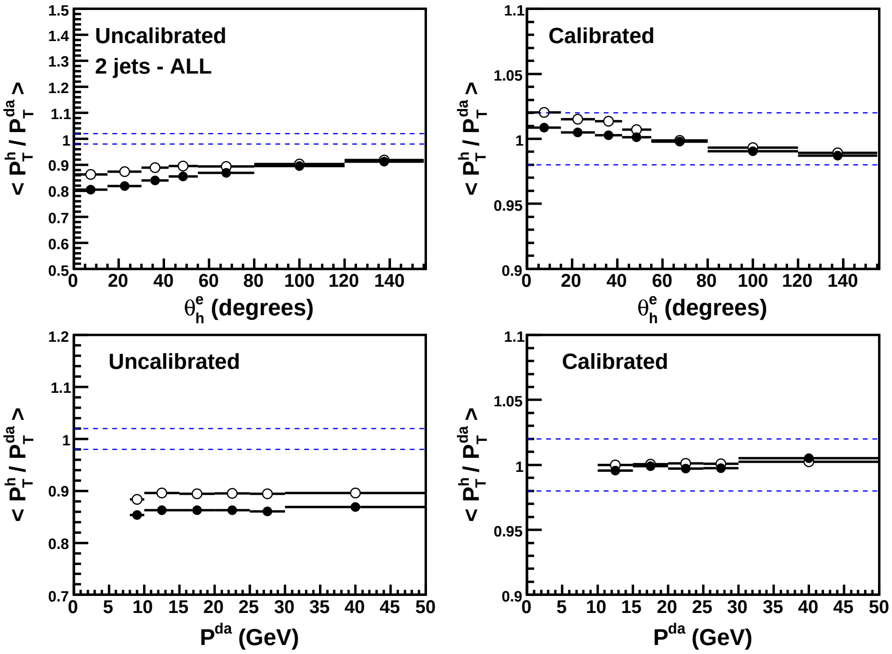

Figure 4.17: Distributions of $P_T^{bal} = P_T^h/P_T^{da}$ as a function of θ_h^e (on the first line) and P_T^{da} (on the second line) for two jets event sample, before (left) and after (right) calibrations for all data combined.

Summary:

Electron and hadronic calibrations have been determined and cross checked for all HERA data. The data are well described by the MC simulation within the systematic uncertainties. We quote a systematic uncertainty varying from 0.7% to 2% for the central region and of ±2% for the forward region of the detector on the electron energy measurement. The hadronic energy scale is known to 2%.

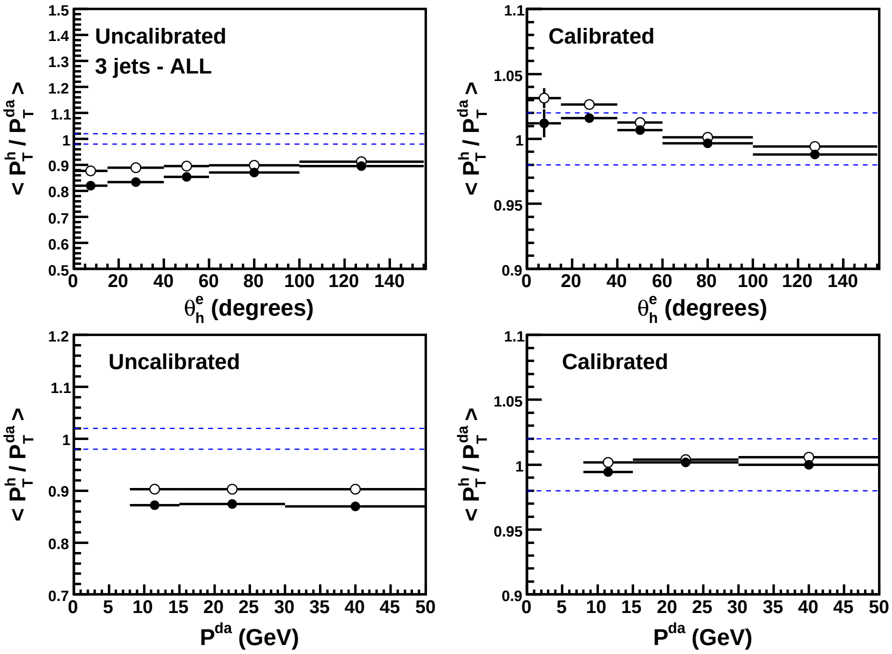

Figure 4.18: Distributions of $P_T^{bal} = P_T^h / P_T^{DA}$ as a function of P_T^{DA} (on the first line) and θ_h^e (on the second line) for three jets event sample, before (left) and after (right) calibrations for all data combined.

Chapter 5

Search for excited electrons

As discussed in section 2.6, excited electrons could be produced in $e^{\pm}p$ collisions at HERA via $t-$channel γ or Z bosons exchange. Details of the search for excited electrons using H1 data will be presented in this chapter. Excited electrons are searched for in the following decay channels: $e^* \to e\gamma$, $e^* \to eZ$, $e^* {\to} \nu W$. Almost all final states resulting from the decay of W and Z bosons are taken into account: hadronic decays of Z and Was well as leptonic decays of the Z boson into either electrons (e), muons (μ) or neutrinos (ν) and the leptonic decay of the W boson into an electron and a neutrino. All event final state topologies used in this analysis are summarized in table 5.1. The signatures we will search for as well as the main background sources from the SM are indicated for each channel. The full $e^{\pm}p$ data sample collected by the H1 experiment during the whole HERA operation from 1994 to mid-2007, corresponding to an integrated luminosity of 475 pb^{-1}, is used.

Channel	Signature	SM background
$e^*{\to}e\gamma$	electron + photon	QED Compton, NC DIS
$e^*{\to}eZ_{\hookrightarrow q\bar{q}}$	electron + 2 jets	NC DIS + 2 jets
$e^*{\to}\nu W_{\hookrightarrow q\bar{q}}$	P_T^{miss} + 2 jets	CC DIS + 2 jets
$e^*{\to}\nu W_{\hookrightarrow e\nu}$	electron + P_T^{miss}	CC DIS, W production
$e^*{\to}eZ_{\hookrightarrow \nu\nu}$	electron + P_T^{miss}	CC DIS, W production
$e^*{\to}eZ_{\hookrightarrow ee}$	3 electrons	$\gamma\gamma \to ll$
$e^*{\to}eZ_{\hookrightarrow \mu\mu}$	electron + 2 muons	$\gamma\gamma \to ll$

Table 5.1: Summary of event final states resulting from ν^* electroweak decays and used in this analysis. The associated signature and SM background sources are indicated.

5.1 The $e^* \rightarrow e\gamma$ decay channel

The $e^* \rightarrow e\gamma$ decay mode is the key channel to search for excited electron because it provides a very clear signature and this decay mode has a large branching ratio (only the case $f = +f'$ will be considered for the e^* search, see section 2.6.1). An example of an e^* Monte Carlo event in this decay channel is shown in figure 5.1. The signature of this channel consists of two isolated electromagnetic clusters in the LAr calorimeter, one being an electron and the second a photon. The distinction between the electron and the photon can be done by the presence of a track pointing to the electron cluster. However, in this decay channel this distinction will not be applied in order to maximise the detection efficiency. Indeed, electron and photon from the decay of a high mass e^* will be boosted in the forward region, where the material density is high and the tracking device is of poor quality for high P_T tracks. As discussed in chapter 2, since about half of the e^* production cross section is expected in the elastic channel, the analysis is separated into two parts. The first channel, called "elastic" is dedicated to the search for e^* produced elastically or quasi-elastically, the second channel, called "inelastic", concerns the search for inelastic e^* production.

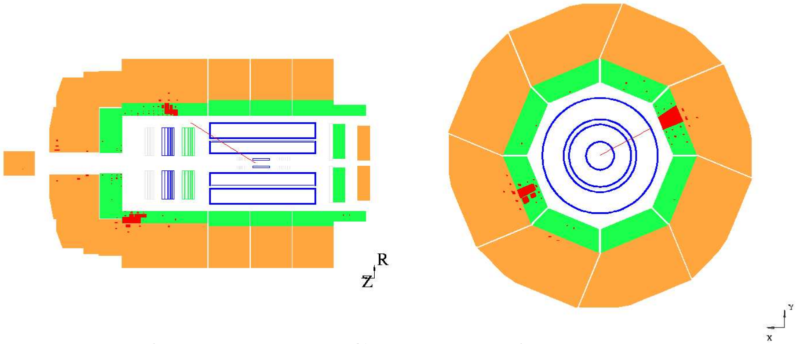

Figure 5.1: Example of an e^* Monte Carlo event for the $e^* \rightarrow e\gamma$ decay channel, in the longitudinal (left) and transverse (right) plane.

In the following, we start by discussing the main sources of SM backgrounds in this channel. Background contributions may arise either from SM processes having the same final state as $e^* \rightarrow e\gamma$ decays or by fake identification of final state particles.

- Elastic QED Compton ($e\gamma$) processes: the final state of this SM process is an electron and a photon, exactly what we look for in the elastic part of this search channel ($e \rightarrow e^*p \rightarrow e\gamma p$). Elastic QED Compton events are the largest source of background at low invariant masses of the $e\gamma$ system.
- NC DIS processes: NC DIS events or inelastic QED Compton events with a final or an initial photon radiation or a high energy π^0 in a jet are the main source of background in the inelastic part of this channel ($e \rightarrow e^*X \rightarrow e\gamma X$).
- Lepton pairs $\gamma\gamma \rightarrow l^+l^-$ processes: if the lepton pair in the final state is e^+e^-, the event may look like an $e\gamma$ candidate because no separation between electrons and photons is performed in this search.

Event Selection:

The main SM background processes in this radiative decay channel have been briefly discussed. The goal of the selection procedure is to identify a set of variables and of discriminating conditions able to minimize the contribution of SM events while retaining a high efficiency for potential signal events. We will therefore proceed step by step to try to reduce SM contributions. In the first selection step, we will verify that the data are well described by the MC simulations, to be sure that our simulation of background processes and of the detector response is accurate enough and within the systematic errors.

The requirements at each selection step in this decay channel are summarized in the table 5.2. As above mentioned, no distinction between photons and electrons is done here. Hence, the analysis starts from candidate events satisfying the following conditions:

- the presence of at least two isolated electromagnetic clusters is required,
- the transverse momenta ($P_T^{e,\gamma}$) of the two electromagnetic clusters are required to be larger than 20 and 15 GeV, respectively. They are detected in the polar angle range $5^\circ < \theta^{e,\gamma} < 130^\circ$.

Distributions of the transverse momentum and polar angle of the two electromagnetic clusters and their invariant mass after these requirements are shown in figure 5.2. The data are well described by the SM expectation which arises mainly from NC DIS and elastic QED Compton events (see table 5.2).

Step	Selection criteria
1	$N_e \geq 2$: $P_T^{e,\gamma} > 20, 15$ GeV, $5^\circ < \theta^{e,\gamma} < 130^\circ$
2	$E^e + E^\gamma > 110$ GeV
3	$P_T^e + P_T^\gamma > 75$ GeV
Elastic sample	$E_h < 5$ GeV
Inelastic sample	$E_h > 5$ GeV

Step	Data	MC	NC DIS	$\gamma\gamma \rightarrow l^+l^-$	eγ	Other SM
1	1516	1749 ± 131	949	107	689	4.2
2	239	247 ± 22	161	27	57	2.4
3	107	114 ± 11	63	6.4	44	0.46
Elastic	42	48 ± 4	3.5	3.4	41	0
Inelastic	65	65 ± 8	59	2.8	2.7	0.5

Table 5.2: In the first table, summary of the selection criteria used in the $e^* \rightarrow e\gamma$ decay channel. In the second table, observed and predicted event yields at each step of the selection of the $e^* \rightarrow e\gamma$ decay channel. The errors on the prediction include model uncertainties and experimental systematic errors added in quadrature.

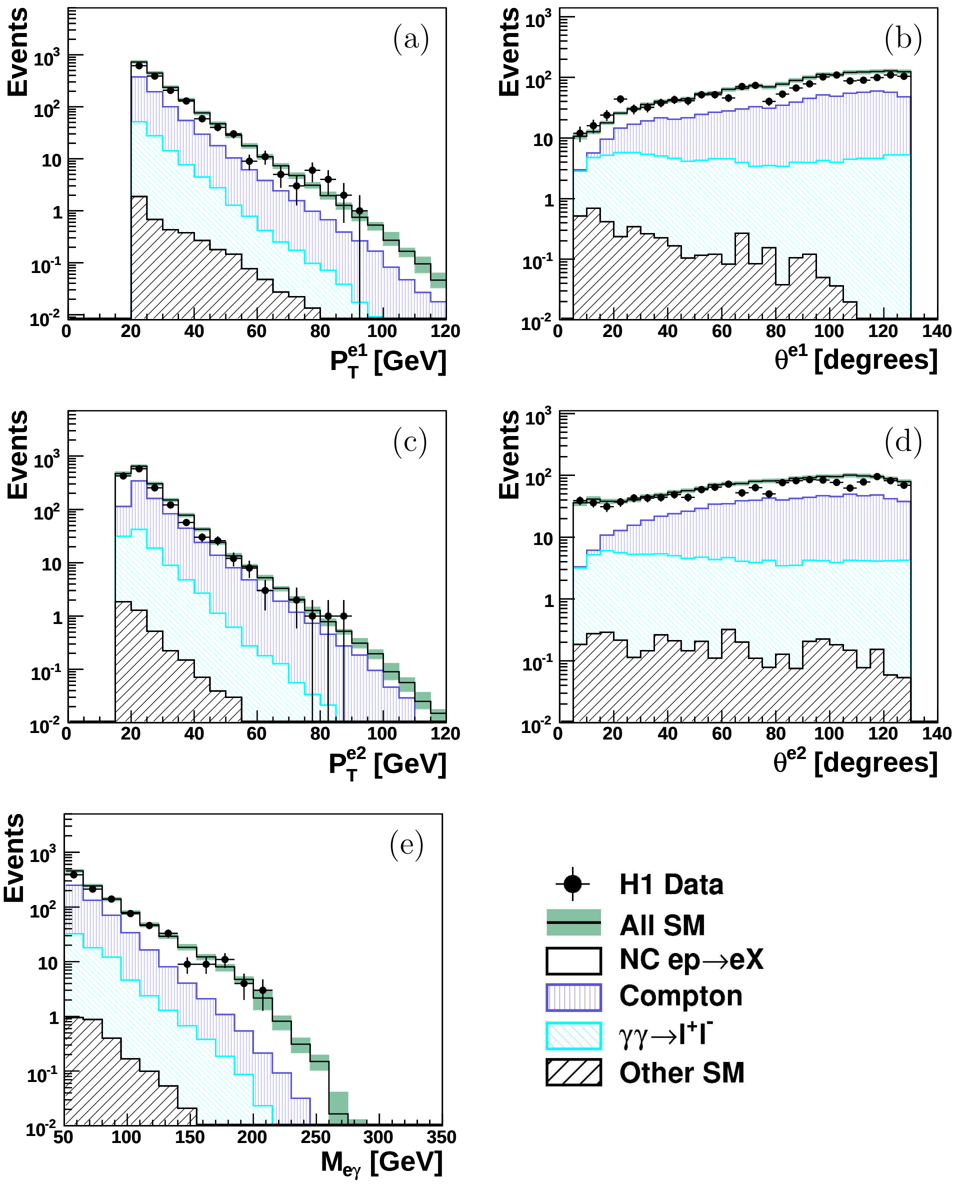

Figure 5.2: Transverse momentum (a,c) and polar angle (b,d) distributions of the two electrons and their invariant mass distribution (e) passing the requirements at the first selection step in the $e^* \to e\gamma$ decay channel.

In a next selection step, the aim is to suppress the SM background arising from the two main sources: NC DIS and elastic QED Compton processes. For the elastic QED Compton process, the cross section of $e\gamma$ events is much larger at low invariant mass of the $e\gamma$ system. As it can be seen in figure 5.3, $e\gamma$ events from SM background processes are therefore concentrated at low values of the sum of the energies of the two electromagnetic clusters $E^e + E^\gamma$. On the opposite, e^* decays lead to high $e\gamma$ invariant masses and large values of $E^e + E^\gamma$. To suppress the SM background it is thus required that $E^e + E^\gamma > 110$ GeV. This cut value is adjusted to keep a high selection efficiency for e^* with masses above 120 GeV. The main source of background

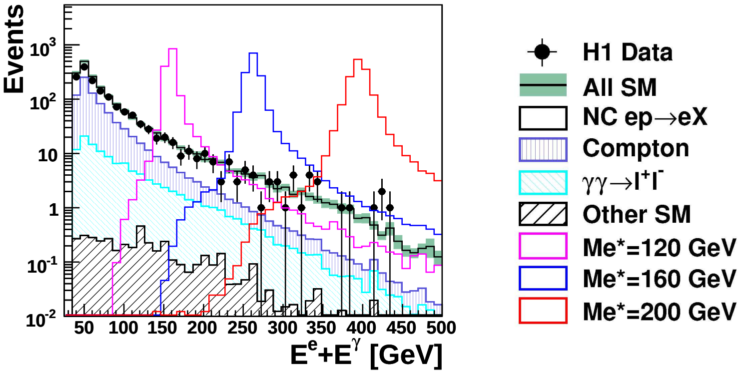

Figure 5.3: Distribution of the sum of the energies of the two electrons at the first selection step of the $e\gamma$ resonance search.

from elastic QED Compton events is strongly suppressed and the background from NC DIS events is now larger than that of elastic QED Compton (see table 5.2).

Figure 5.4 presents the distribution of the sum of the energies $E^e + E^\gamma$ and of the sum of the transverse momenta $P_T^e + P_T^\gamma$ of the two electromagnetic clusters for events selected in the second step. The contribution of elastic QED Compton and NC DIS events is mainly in the region $110 < E^e + E^\gamma < 200$ GeV. These background events are further suppressed by rejecting events with $P_T^e + P_T^\gamma < 75$ GeV. This cut on the sum $P_T^e + P_T^\gamma$ removes a large part of NC DIS events. After the first three selection steps, 107 candidate events are found in the data, in good agreement with the SM expectation of 114 ± 11 events, which is still dominated by elastic QED Compton and NC DIS events.

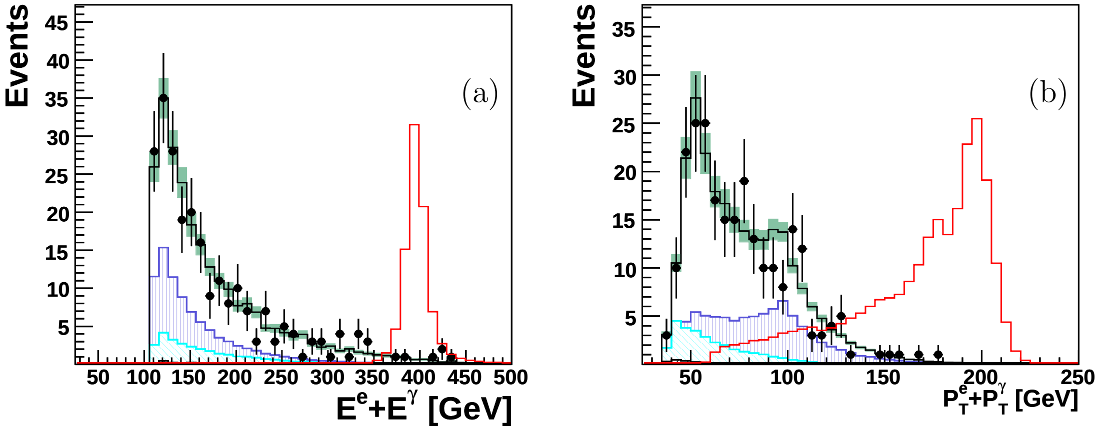

Figure 5.4: Distribution of the sum of the energies (a) and of the sum of the transverse momenta (b) of the two electromagnetic clusters in the second selection step of the $e\gamma$ resonance search. The red curves correspond to e^* events with a mass of 200 GeV.

About half of the e^* production cross section is expected in the elastic channel. SM background for elastic $ep \rightarrow e\gamma p$ events arise from elastic QED Compton processes and is concentrated at low $e\gamma$ invariant mass. On the opposite NC DIS events exhibit larger $e\gamma$ invariant masses. The search for e^* is thus separated into two elastic and inelastic parts in order to improve its sensitivity. In the elastic part only the two electromagnetic clusters should be present in the final state, with no other signals in the calorimeter. Events are required to have a total hadronic energy E_h lower than 5 GeV (see figure 5.5). This cut suppresses the NC DIS background. 42 elastic events are found, compared to an expected SM contribution of 48 ± 4 events, in which 41 events arise from elastic QED Compton processes. In the inelastic part, events with E_h larger than 5 GeV are selected. This cut suppresses the elastic QED Compton background. 65 inelastic events are selected, the SM background is of 65 ± 8 events, in which 59 events arise from NC DIS processes.

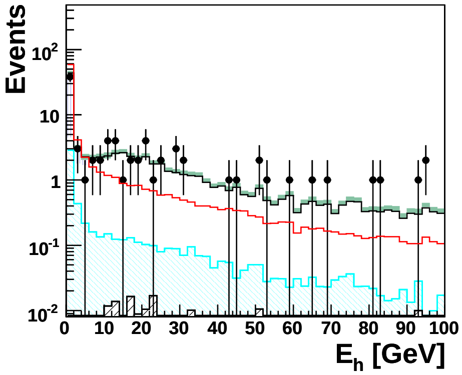

Figure 5.5: Distribution of the total hadronic energy E_h at the third selection step of the $e\gamma$ resonance search.

Figures 5.6 and 5.7 show the distributions of the kinematic variables of the two electromagnetic clusters and their invariant mass, in the elastic and inelastic channels, respectively. In both channels, the distributions of data events are well described by the SM background. The observed and expected event yields in each selection step are summarized in table 5.2. No deviation from the SM expectation is found in this channel. The efficiency for selecting the signal varies from 60% for an e^* mass of 120 GeV to 70% for an e^* mass of 260 GeV. The experimental resolution on the reconstructed e^* mass distributions varies between 3 GeV and 6 GeV for a generated e^* mass between 100 GeV and 290 GeV.

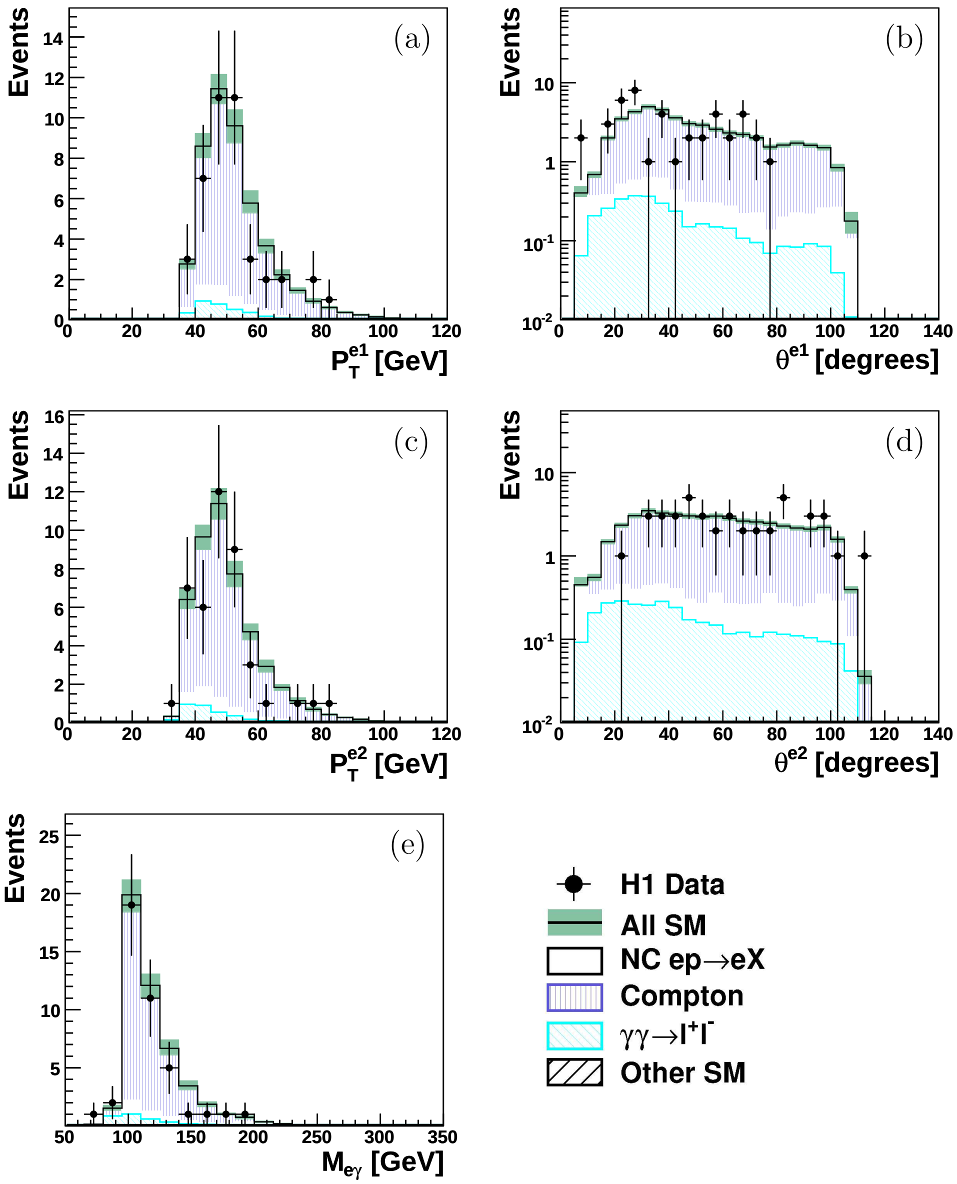

Figure 5.6: Transverse momentum (a,c) and polar angle (b,d) distributions of the two selected electromagnetic clusters, and their invariant mass distribution (e) after passing all selection criteria in the elastic channel $ep \rightarrow e^{*}p$.

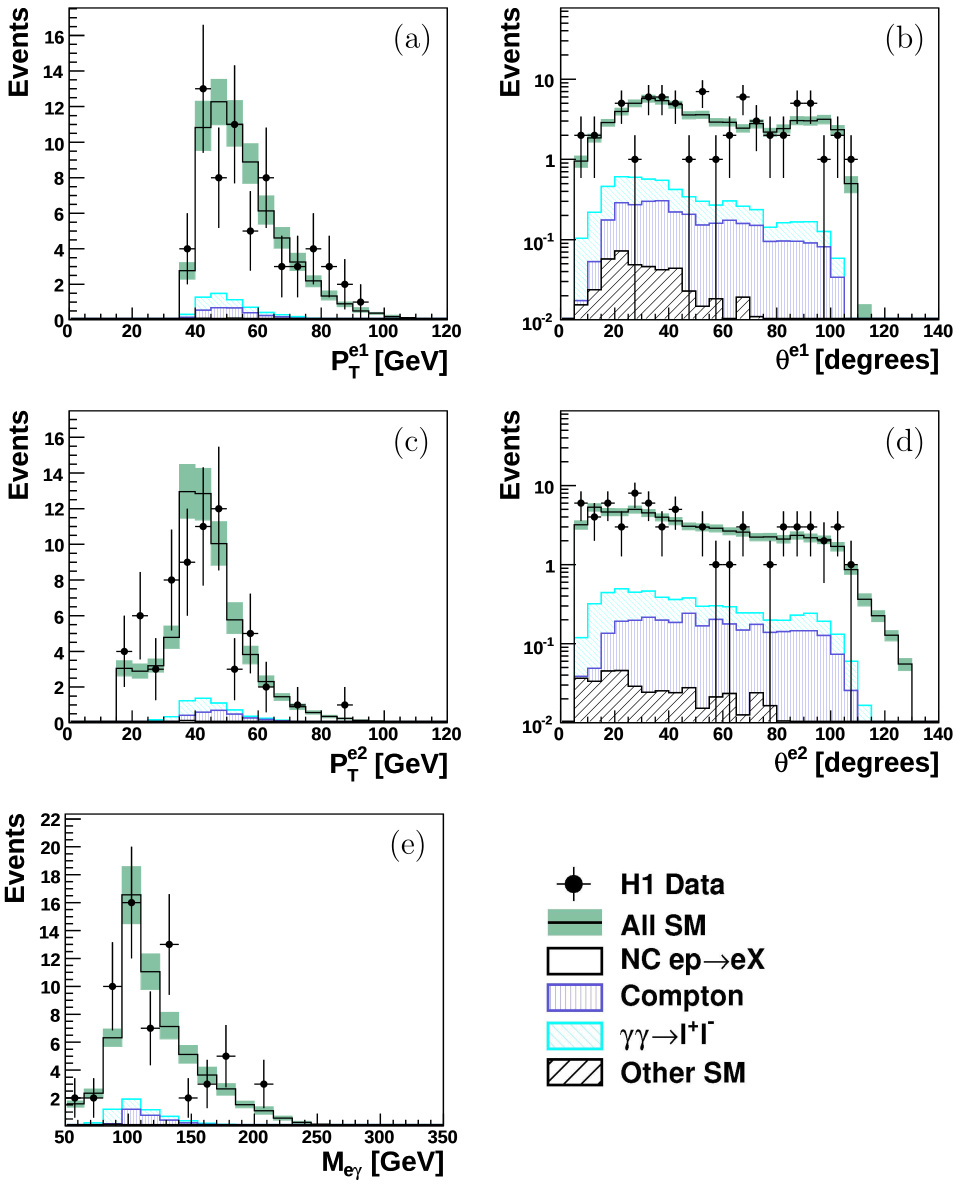

Figure 5.7: Transverse momentum (a,c) and polar angle (b,d) distributions of the two selected electromagnetic clusters, and their invariant mass distribution (e) after passing all selection criteria in the inelastic channel: $ep \to e^* X$.

5.2 The $e^* \to eZ_{\hookrightarrow qq}$ decay channel

The $e^* \to eZ_{\hookrightarrow qq}$ decay channel is characterized by an electron and at least two jets of high transverse momenta in the final state. Figure 5.8 shows an example of an e^* Monte Carlo event in this decay channel.

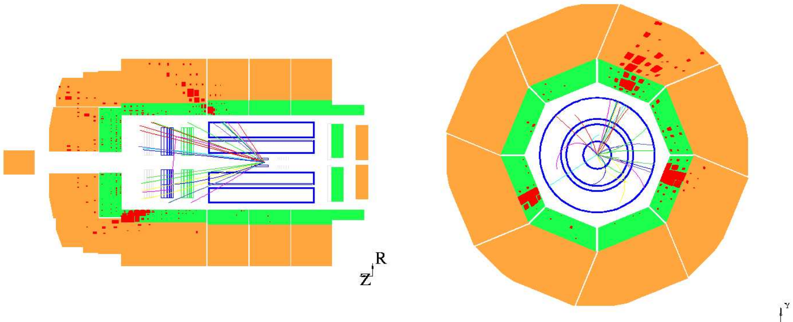

Figure 5.8: Example of an e^* Monte Carlo event for the $e^* \to eZ_{\hookrightarrow qq}$ decay channel, in the longitudinal (left) and transverse (right) plane.

The dominant SM backgrounds are:

- NC DIS processes: NC DIS events with two jets have a similar topology to $e^* \to eZ_{\hookrightarrow qq}$ events. It is the largest background in this decay channel.
- Photoproduction (γp) processes: γp events can be selected if one fake electron is mis-identified in a jet. Its contribution is much smaller than the background from NC DIS events.

Event Selection:

As discussed above, multi-jet NC DIS events are the main background from SM processes. In this decay channel candidate events are selected from an event sample of inclusive NC DIS with at least two high transverse momentum jets. Figure 5.9 shows some kinematic variables distributions of inclusive NC DIS events. The agreement between data and MC observed in those distributions indicates that inclusive NC DIS events are well under control. The requirements applied at each selection step in this decay channel are summarized in table 5.3.

We start by selecting candidate events satisfying the following conditions:

- at least one electromagnetic cluster has to be present in the final state,
- this electromagnetic cluster is required to have a transverse momentum P_T^e greater than 10 GeV and is detected in the polar angle range $5° < \theta^e < 145°$,
- At least two jets have to be present in the final state. The two jets must be detected in the polar angle range $5° < \theta^{jet1,jet2} < 130°$ with transverse momenta $P_T^{jet1,jet2}$ larger than 20 and 15 GeV, respectively.

Step		Selection criteria
1	Inclusive NC DIS	$P_T^e > 10$ GeV, $5^\circ < \theta_e < 145^\circ$
	NC DIS+2jets	$P_T^{jet1,jet2} > 20, 15$ GeV; $5^\circ < \theta^{jet1,jet2} < 130^\circ$
2	anti-NC DIS	$P_T^e > 20$ GeV, $\theta^e < 90^\circ$
3		$\xi^e > 23$ GeV or $P_T^e > 25$ GeV
	if $n^{isolated\ e.m.} > 1$	$P_T^{e1,e2} > 20, 10$ GeV and $P_T^{e1} + P_T^{e2} < 90$ GeV
4	Z mass window	$M_Z - 20$ GeV $< M_{jj}$
Final		$\theta^{jet1} < 80^\circ$ $\theta^{jet2} > 10^\circ$ if $P_T^{jet2} < 25$ GeV

Step	Data	MC	NC DIS	γp	Other SM
1	13303	12738 ± 2859	12488	216	34
2	2347	2403 ± 503	2346	45	12
3	2059	2058 ± 430	2010	39	9
4	409	365 ± 83	354	6.5	4.5
Final	286	277 ± 62	267	6	4

Table 5.3: In the first table, summary of the selection criteria of the $e^* \rightarrow eZ_{\hookrightarrow qq}$ decay channel. In the second table, observed and predicted event yields at each selection step of the $e^* \rightarrow eZ_{\hookrightarrow qq}$ decay channel. The errors on the prediction include model uncertainties and experimental systematic errors added in quadrature.

Looking at all jets in the events, a Z boson candidate is reconstructed from the combination of the two jets having an invariant mass M_{jj} closest to the Z boson mass ($M_Z = 91.2$ GeV). The method used for the reconstruction of the mass of the e^* candidate from the two jets and the electron is explained in section 4.4.5.

The main variables (P_T^e, θ^e and $P_T^{jet1,jet2}$, $\theta^{jet1,jet2}$) characterizing NC DIS events with at least two high P_T jets are shown in figure 5.10. The data events passing this first selection step are well described by SM expectation, is dominated by multi-jet NC DIS events (see table 5.3).

The large SM background from multi-jet NC DIS events should now be reduced, in order to enhance the sensitivity to a potential e^* signal. Figure 5.10 shows the distribution of the transverse momentum and polar angle of the electromagnetic cluster in NC DIS events. Due to the high e^* mass, the electron from the e^* decay is mainly boosted in the forward region of the detector. At the opposite, the electron in NC DIS events is scattered in the backward region. Therefore, at the second step, the selection is restricted to the forward region by requiring $\theta^e < 90^\circ$. The transverse momentum of the electromagnetic cluster is also required to be $P_T^e > 20$ GeV. The cut on the electron polar angle suppresses a large part of the multi-jet NC DIS background. Almost all γp background is suppressed by increasing the cut value on P_T^e from 10 GeV to 20 GeV (see table 5.3).

To further reduce the NC DIS background, the electron variable $\xi^e = E^e \cos^2(\theta^e/2)$ is used. Candidate events should verify $\xi^e > 23$ GeV or $P_T^e > 25$ GeV. The effect of this cut on both the e^* signal and the SM background is displayed in figure 5.11.

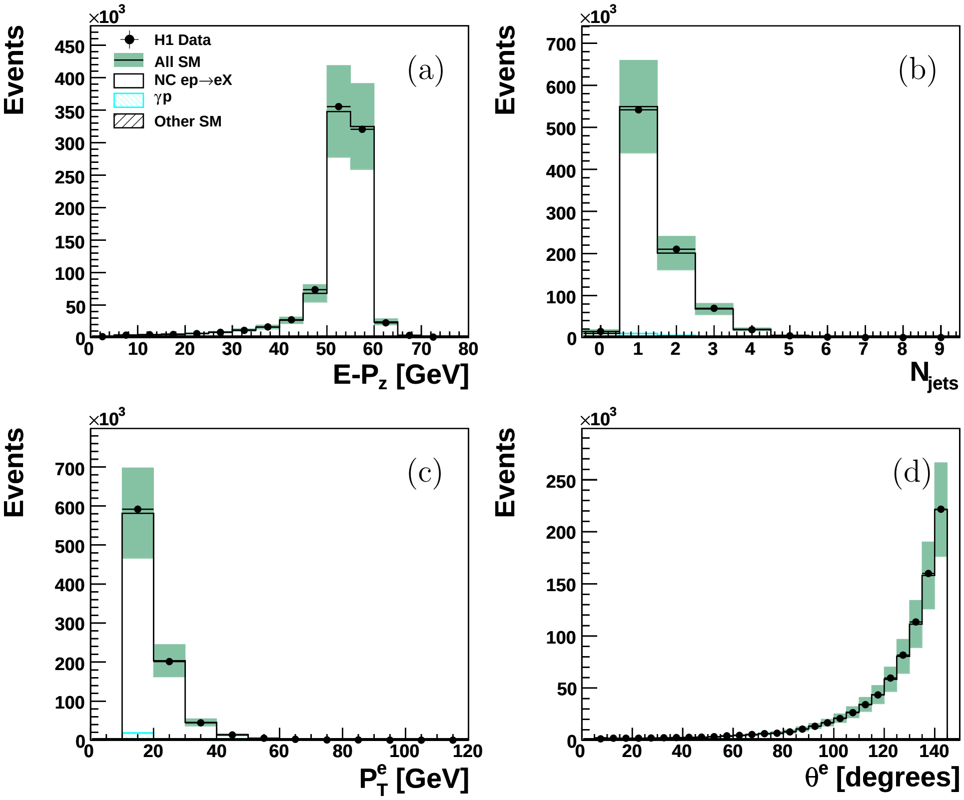

Figure 5.9: The longitudinal energy balance $E - P_z$ (a), the transverse momentum P_T^e (c) and the polar angle θ^e (d) of the electron in inclusive NC DIS events. The number of jets N_{jets} in those events is also shown (b).

In addition, to avoid possible double counting of events from the $e^*\to e\gamma$ radiative decay channel, events with two electrons of transverse momentum above 10 GeV and a total transverse momentum of these two electrons larger than 90 GeV are rejected.

In each candidate event, the two jets associated to a possible Z boson decay should have an invariant mass M_{jj} close to the nominal Z boson mass. Therefore only events with $M_{jj} > M_Z - 20$ GeV are selected. Figure 5.12 shows the distribution of the invariant mass of the two jets, associated to a possible Z boson decay, before applying this condition. This requirement on the invariant mass of the two jets removes a large part of the remaining NC DIS background.

To further reduce the NC DIS background, it is required that the polar angle of the jet with the highest transverse momentum (P_T^{jet1}) associated to the Z candidate be less than 80°. The distributions of polar angles of the two jets associated to a Z candidate are shown in figure 5.13. Finally, the polar angle of the second jet is required to be greater than 10° if $P_T^{jet2} < 25$ GeV. The effect on the signal and on the SM background of this cut is shown in figure 5.14.

After applying all selection cuts, 286 events are observed in the data, while 277 ± 62 are expected from the SM. The observed and expected event yields at each selection step of the $e^* \to eZ_{\hookrightarrow qq}$ selection are summarized in table 5.3. The

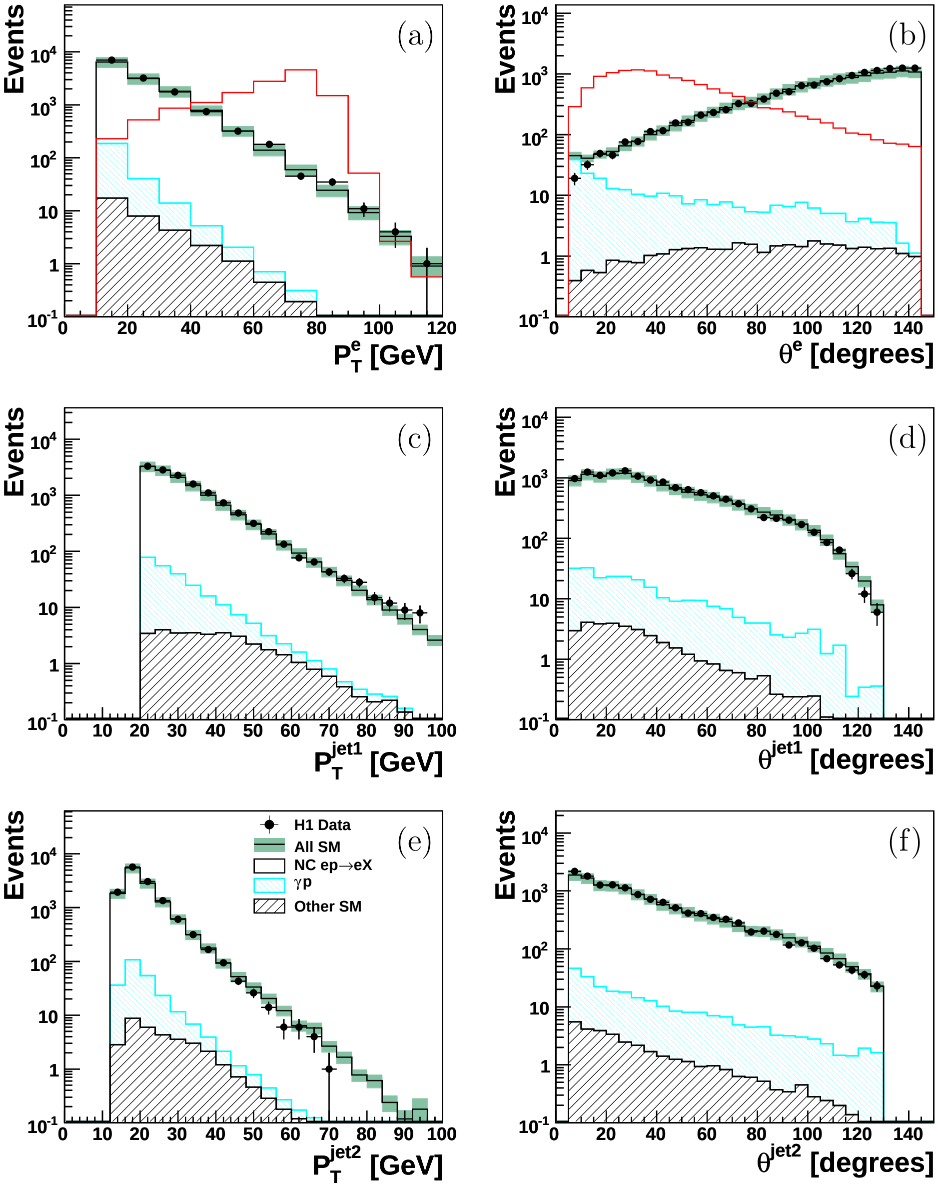

Figure 5.10: Transverse momentum (a) and polar angle (b) distributions of the electron in NC DIS events with at least two high P_T jets. Transverse momentum (c,e) and polar angle (d,f) distributions of the two jets associated to the decay of a Z candidate boson. The red line in (a,b) corresponds to the e^* signal at $M_{e^*} = 200$ GeV.

distribution of the reconstructed invariant mass of e^* and some kinematic variables of the electron and of the two jets in the final selection are presented in figure 5.15. The distribution of selected data events are in good agreement with the SM expectation. No significant excess of event is found in this channel. The selection efficiency in this channel is 20% for an e^* mass of 120 GeV, increasing to 55% for an e^* mass of 290 GeV. The experimental resolution on the recontructed e^* mass distribution varies between 2 GeV and 8 GeV for a generated e^* mass between 120 GeV and

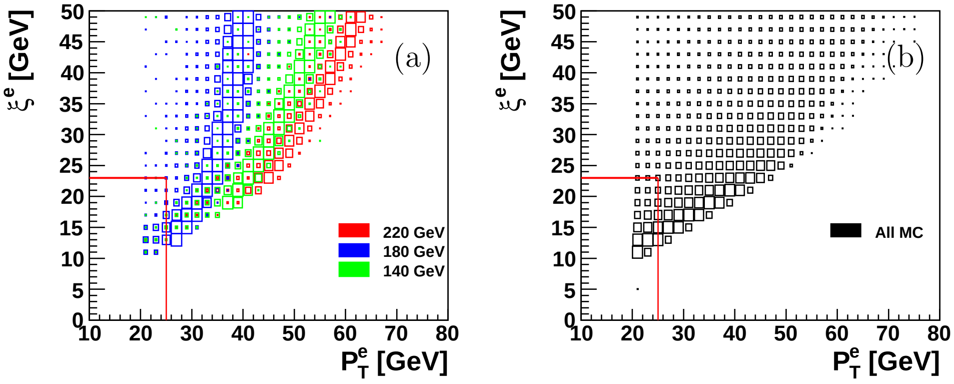

Figure 5.11: Distribution of the e^* signal for different masses (a) and of all SM background events (b) in the plane (P_T^e, ξ^e). The red lines present the rectangular selection cut: events with $P_T^e < 25$ GeV and $\xi^e < 23$ GeV are rejected.

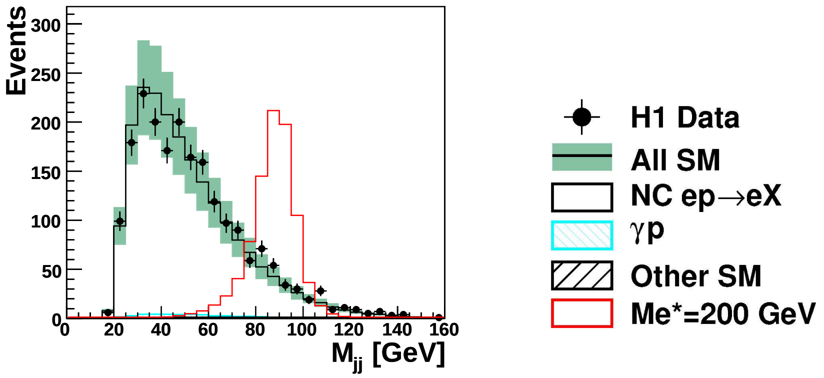

Figure 5.12: Invariant mass distribution of the two jets M_{jj} associated to a possible Z boson decay, before applying the condition $M_{jj} > M_Z - 20$ GeV. The red histogram corresponds to e^* events with $M_{e^*} = 220$ GeV.

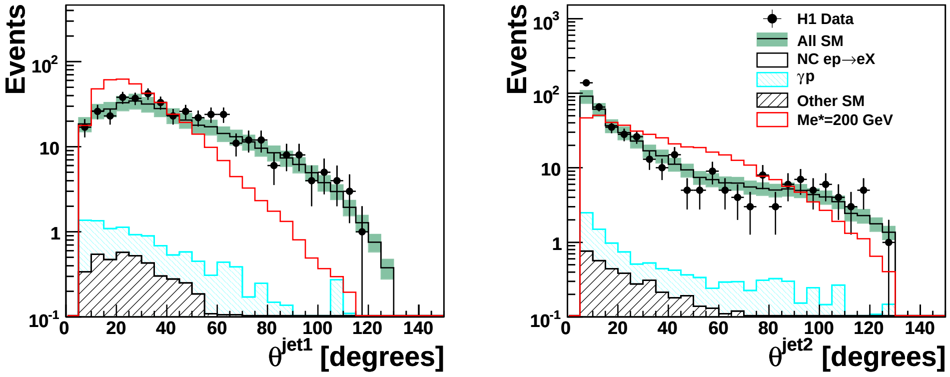

Figure 5.13: Distributions of the polar angle of the two jets associated to a possible Z boson decay, for events passing the step 4. The red histogram corresponds to e^* event with $M_{e^*} = 220$ GeV.

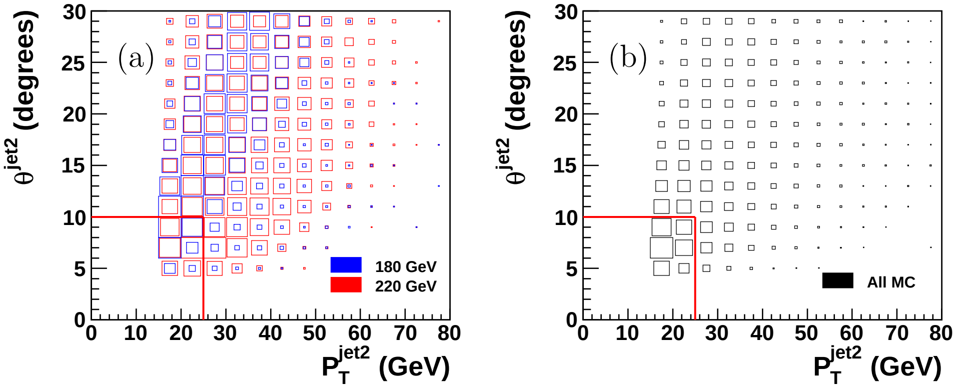

Figure 5.14: Distributions of e^* event for different masses (a) and of all SM background events (b) in the plane $(P_T^{jet2}, \theta^{jet2})$.

290 GeV.

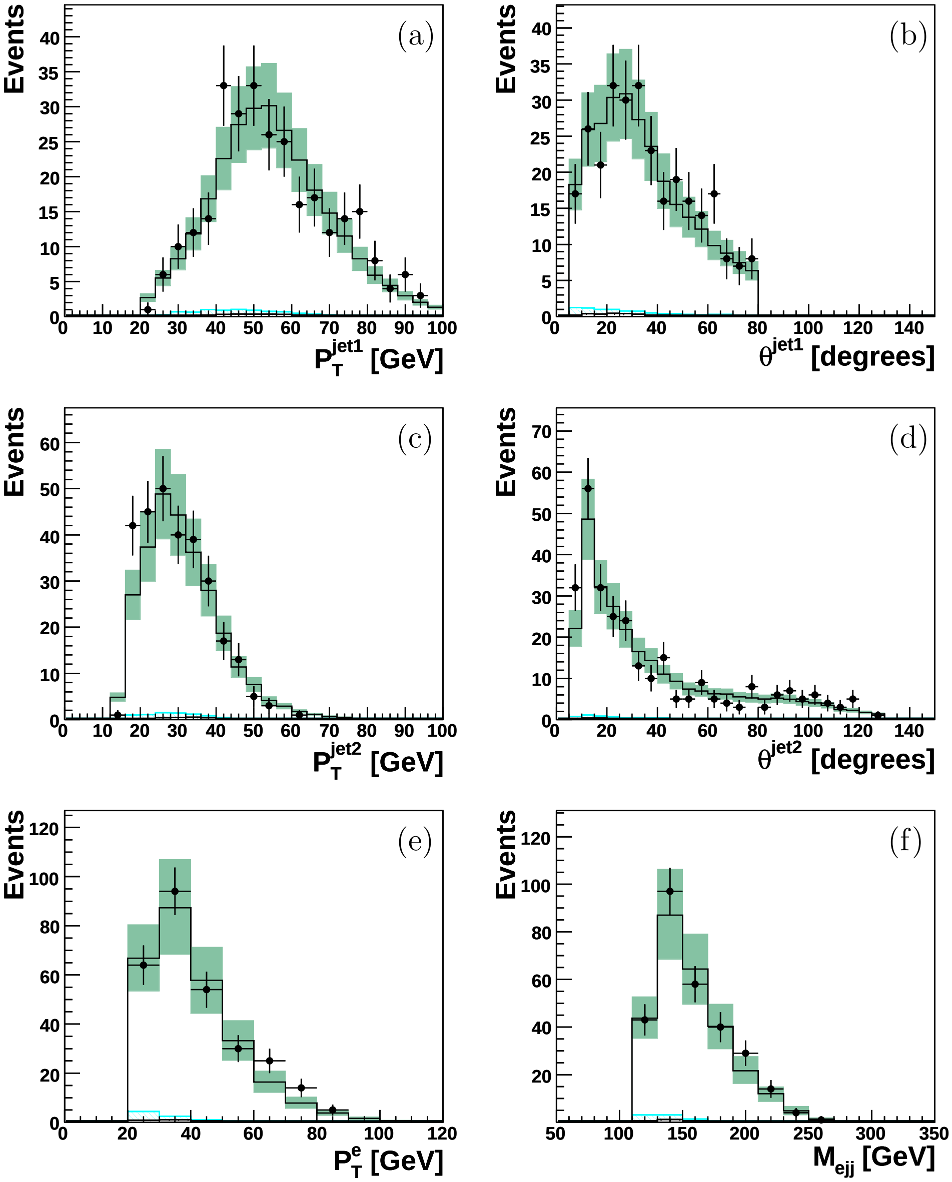

Figure 5.15: Distributions of the transverse momentum (a,b) and of the polar angles (b,c) of the two jets, the transverse momentum of the electron (e) and the e^* candidates invariant mass (f) in the final selection step of the $e^* \rightarrow eZ_{\hookrightarrow qq}$ decay channel.

5.3 The $e^* \rightarrow \nu W_{\hookrightarrow qq}$ decay channel

The $e^* \rightarrow \nu W_{\hookrightarrow qq}$ decay channel is characterized by a final state with at least two high transverse momentum jets and an undetected neutrino, leading to large missing transverse momentum P_T^{miss}. Figure 5.16 shows an example of an e^* MC event in this decay channel.

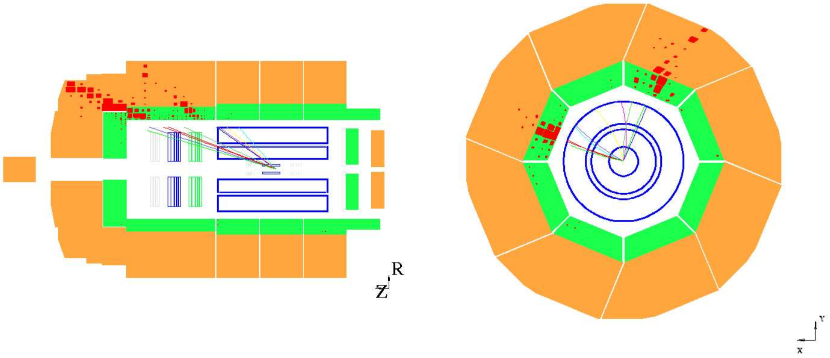

Figure 5.16: Example of an e^* Monte Carlo event for the $e^* \rightarrow \nu W_{\hookrightarrow qq}$ decay channel, in the longitudinal (left) and transverse (right) plane.

The main sources of SM background in the $e^* \rightarrow \nu W_{\hookrightarrow qq}$ channel come from CC DIS events with a moderate contribution from photoproduction events. NC DIS events may also have a similar final state if the electron is lost and if at least two jets are found in the final state. But NC DIS events will be suppressed by the requirement of a large P_T^{miss}.

	Inclusive CC DIS	$P_T^{miss} > 20$ GeV, $E - Pz < 65$ GeV no e.m. cluster with $P_T > 10$ GeV
1	CC DIS+2jets	$P_T^{jet1,jet2} > 20, 15$ GeV, $5^\circ < \theta^{jet1,jet2} < 130^\circ$
2	suppress γp	$V_{ap}/V_p < 0.3$
3	W mass window	$M_{jj} > M_W - 20$ GeV
Final		$M_X = M_{\text{Hadronic System}} - M_{jj} < 15$ GeV $x_h > 0.04$

Step	Data	MC	CC DIS	γp	Other SM
	13995	13728 ± 2595	12506	281	941
1	1183	1287 ± 231	938	240	109
2	700	870 ± 188	844	18	8
3	199	275 ± 67	266	6	3
Final	129	133 ± 32	129	1.5	2.5

Table 5.4: In the first table, summary of the selection criteria of the $e^* \rightarrow \nu W_{\hookrightarrow qq}$ decay channel. In the second table, observed and predicted event yields for each selection step. The errors on the prediction include model uncertainties and experimental systematic errors added in quadrature.

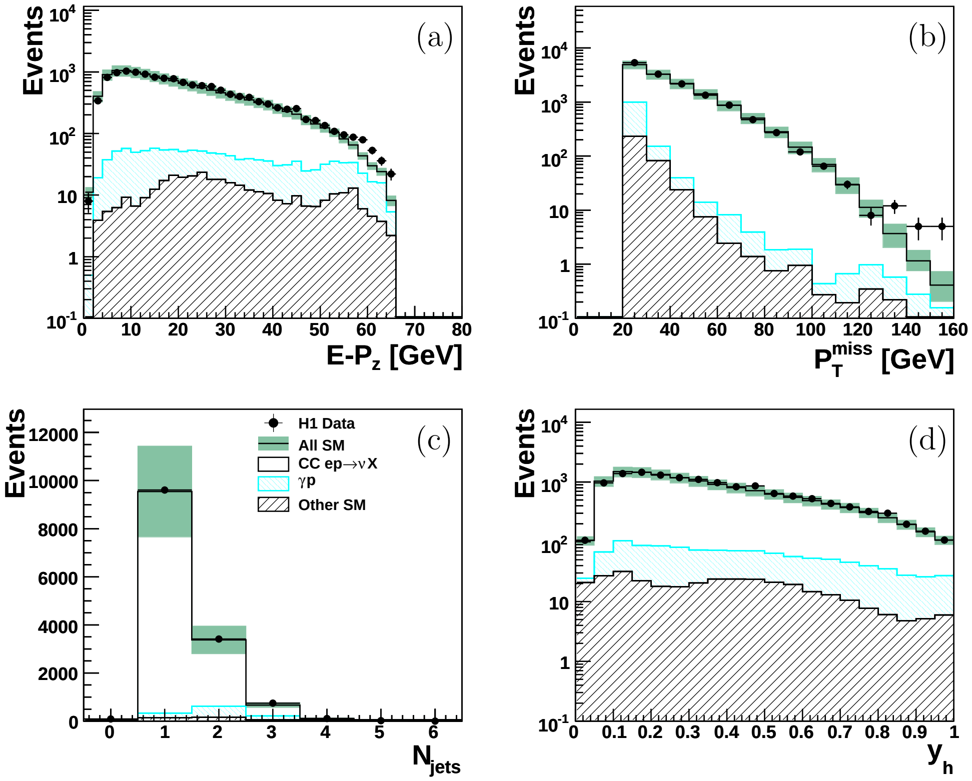

Figure 5.17: Longitudinal energy balance $E - P_z$ (a), missing transverse momentum P_T^{miss} (b), jet multiplicity (c) N_{jets} and y_h (d) distributions for the inclusive CC DIS event sample.

Event Selection:

As for the previous two decay channels, we will tighten, step by step, the selection criteria to reduce the SM background and to enhance the sensitivity to e^* signal events. The requirements at each selection step in this channel are summarized in table 5.4. The analysis starts from an event sample satisfying the following conditions:

- the presence of an un-observed neutrino is requested in the event by imposing the missing transverse momentum P_T^{miss} to be greater than 20 GeV,

- no isolated electromagnetic cluster with transverse momentum above 10 GeV should be present in the final state. This cut ensures that no candidate from the $e^* \rightarrow eZ_{\hookrightarrow qq}$ or $e^* \rightarrow e\gamma$ decay channels will enter in the $e^* \rightarrow \nu W_{\hookrightarrow qq}$ channel,

- two jets are required in the final state. The two jets are required to have transverse momenta $P_T^{jet1,jet2}$ greater than 20 and 15 GeV, and polar angles $\theta^{jet1,jet2}$ between 5° and 130°, respectively. Looking at all jets in the events, a W boson candidate is reconstructed from the combination of the two jets having an invariant mass M_{jj} closest to the W boson mass ($M_W = 80.4$ GeV).

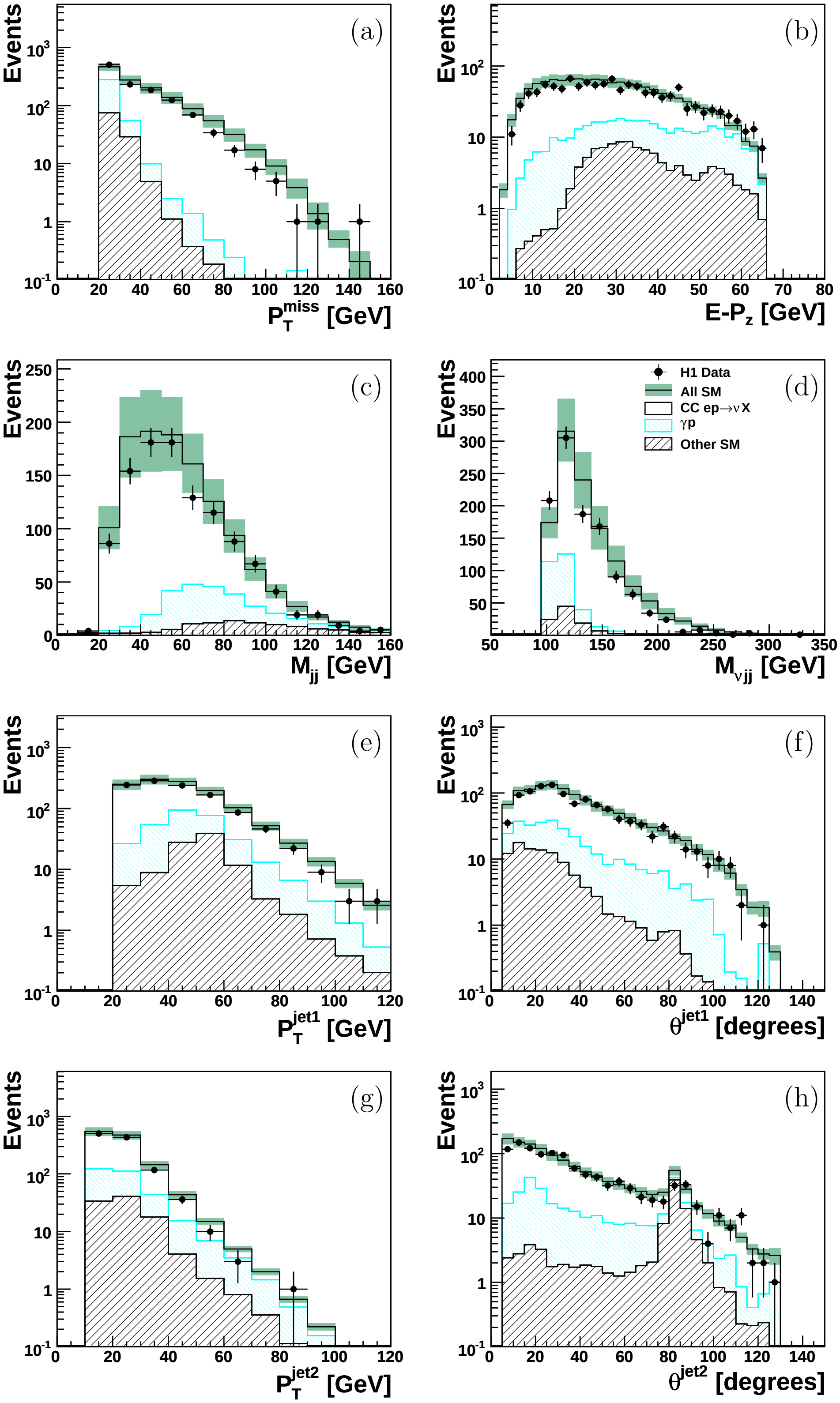

Figure 5.18: Distributions of the missing transverse momentum P_T^{miss} (a), of the longitudinal energy balance $E - P_z$ (b) and of the invariant mass of the excited electron candidate $M_{\nu jj}$ (d). Distributions of the transverse momentum (e,g) and of the polar angle (f,h) of the two jets associated to a possible W boson decay for multi-jet CC DIS events passing the first selection step.

Candidate events in this channel are selected from an event sample of CC DIS with at least two high transverse momentum jets. Distributions of kinematic variables, which characterize the inclusive CC DIS events are shown in figure 5.17. The agreement observed between data and SM MC simulations indicates that inclusive CC DIS events are well controled. Then, the main variables characterizing the sample of CC DIS events with at least two high P_T jets are presented in figure 5.18. After these requirements, the SM expectation is dominated by CC DIS events, with a small fraction of γp events (see table 5.4).

Figure 5.19 presents the distribution of the ratio V_{ap}/V_p of transverse energy flow anti-parallel and parallel to the hadronic final state (see section 4.4.4). This variable is used to reject background from γp events in which V_{ap}/V_p has a value closest to one, whereas for e^* event V_{ap}/V_p peaks to zero. Therefore, only events with $V_{ap}/V_p < 0.3$ are accepted. This cut almost suppress γp background events. The CC DIS background has now to be reduced, to isolate possible e^* events.

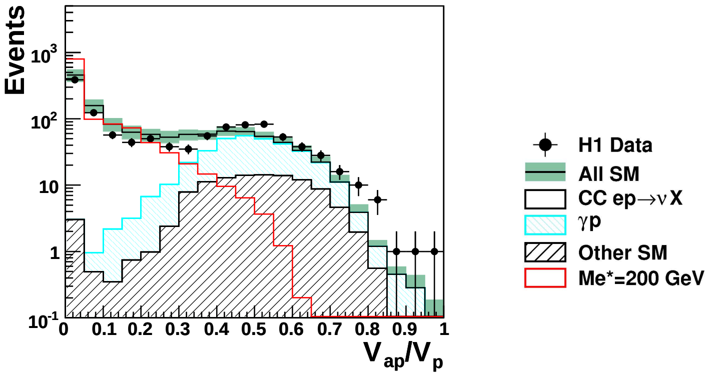

Figure 5.19: Distribution of the ratio V_{ap}/V_p. The red curve corresponds to an e^* signal with a mass of 200 GeV.

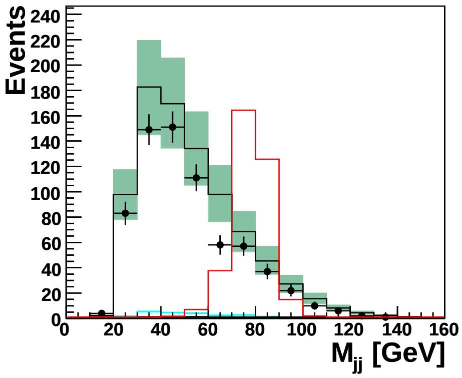

Figure 5.20: Invariant mass distribution of the two jets associated to a W candidate before requiring $M_{jj} > M_W - 20$ GeV.

At the third selection step, a cut on the reconstructed invariant mass of the two jets M_{jj} is applied. The invariant mass of the two jets associated to the possible decay of a W boson is required to be $M_{jj} > M_W - 20$ GeV. This cut is asymmetric to maximize the efficiency to e^* event for high M_{jj}, in a region where the CC DIS background is still small. Figure 5.20 presents the distribution M_{jj} before applying this cut. The same distribution for e^* events of mass 200 GeV is also shown.

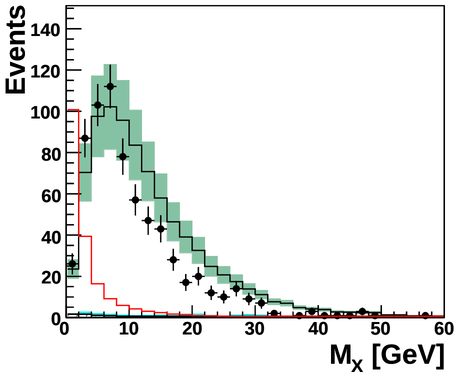

Figure 5.21: Distribution of the invariant mass of the spectator and scattered parton jets M_X after the third selection step. The distribution for e^* signal event (red line) peaks to zero.

At the last selection step, to further reduce the remaining background from multi-jet CC DIS events, as shown in figure 5.21, the invariant mass of the spectator and scattered parton jets, M_X, is used. e^* events which are elastic for a large fraction, have M_X values peaking at zero. At the opposite, CC DIS events have larger M_X values. Events with $M_X > 15$ GeV are thus rejected. Finally, an additional cut on x_h, the Bjorken scaling variable calculated from the hadronic system using the Jacquet-Blondel method, is applied to suppress the remaining background from γp and NC DIS events which typically contribute at low x_h, while e^* events have high x_h values. Events with $x_h < 0.04$ are rejected. The distribution of $\log_{10}(x_h)$ for signal events and SM background events is shown in figure 5.22.

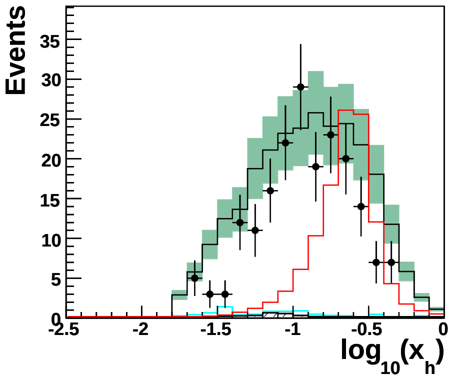

Figure 5.22: Distribution of $\log_{10}(x_h)$ for events passing the third selection step. Events with $\log_{10}(x_h) < -1.4$ are rejected.

After all selection cuts, 129 candidate events remain in the data, compared to an expected SM contribution of 133 ± 22 events. The observed and expected event yields at each selection step of the $e^* \to \nu W_{\hookrightarrow qq}$ decay channel are summarized in table 5.4. The distributions of the reconstructed e^* invariant mass, of P_T^{miss} and of kinematic variables of the two jets are presented in figure 5.23 for the final selection step. The distributions of data events are well described by the SM expectation which is dominated by CC DIS events. No significant excess of data events is found in this channel. The efficiency for selecting the signal is about 20% for an e^* mass of 120 GeV, increasing to 55% for an e^* mass of 290 GeV. The experimental resolution on the reconstructed e^* mass varies between 9 GeV and 20 GeV for a generated e^* mass between 120 GeV and 290 GeV.

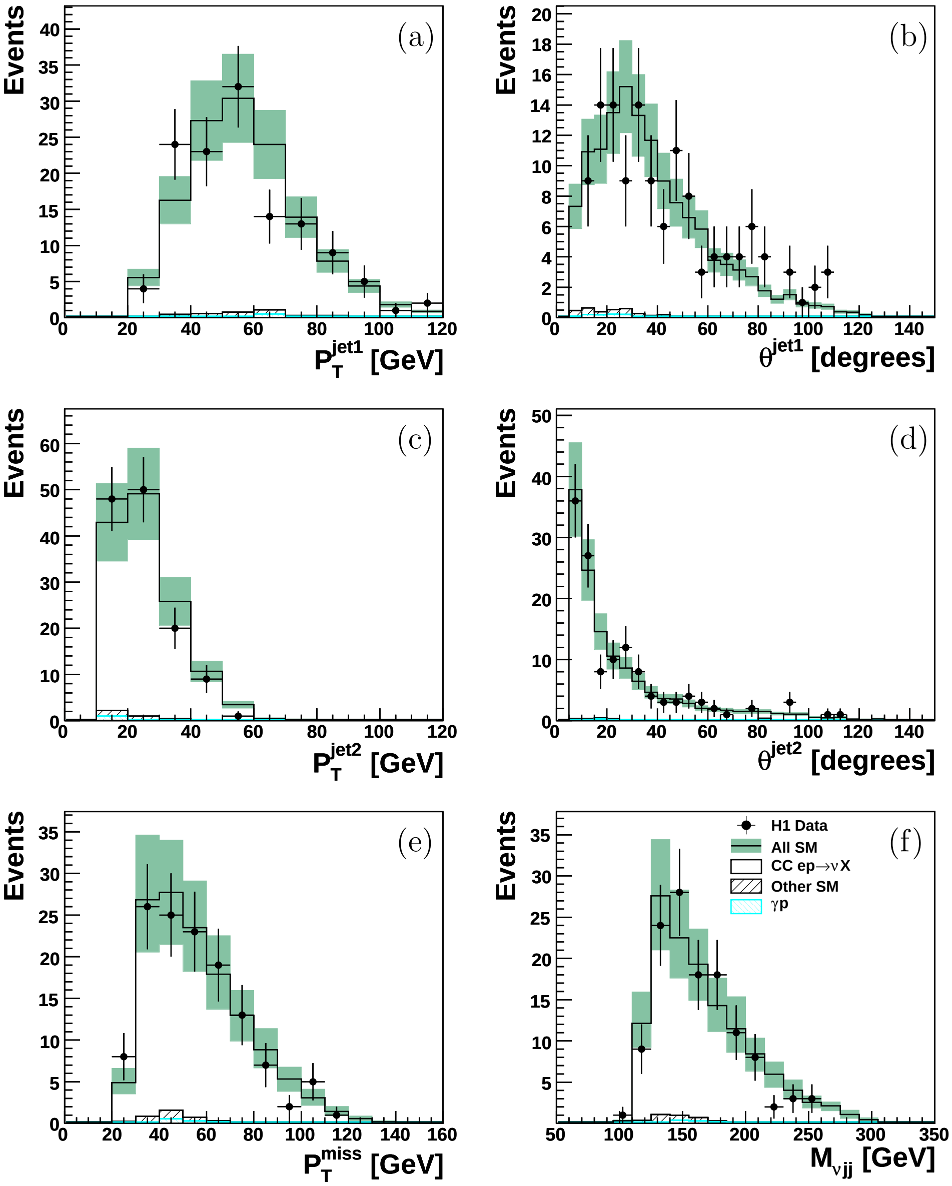

Figure 5.23: Distribution of the transverse momentum (a,c) and polar angles (b,d) of the $jet1$, $jet2$, and of the missing transverse momentum P_T^{miss} (e) in the final selection step of the $e^*\rightarrow\nu W_{\hookrightarrow qq}$ decay channel. The e^* candidate invariant mass $M_{\nu jj}$, reconstructed from the ν and the two jets is shown in (f).

5.4 Leptonic decay channels of Z and W bosons

The search for excited electrons has been performed in previous sections in the main three decay channels $e^*\rightarrow e\gamma$, $e^*\rightarrow eZ_{\hookrightarrow qq}$ and $e^*\rightarrow \nu W_{\hookrightarrow qq}$, in which the final states resulting from Z or W hadronic decays have been taken into account. To complement this search, possible final states resulting from the Z or W leptonic decays will be considered in this section.

5.4.1 The $e^*\rightarrow eZ_{\hookrightarrow \nu\bar{\nu}}$ and $e^*\rightarrow \nu W_{\hookrightarrow e\nu}$ channels

The signatures of the $e^*\rightarrow eZ_{\hookrightarrow \nu\bar{\nu}}$ and $e^*\rightarrow \nu W_{\hookrightarrow e\nu}$ decay channels are similar and consist of one high transverse momentum electron and two undetected neutrinos, leading to a large missing transverse momentum P_T^{miss}. As the two decay channels have the same final state, no distinction can be made between them. Therefore, they will be studied together, looking in the data to events with one high P_T electron and large P_T^{miss}.

The main sources of background in this channel arise from real W production and CC DIS processes:

- W production processes: the signature of these e^* decay channels is similar to W events, where an electron and a neutrino are coming from the W decay.
- CC DIS processes: background from CC DIS events may arise if one photon is radiated or if one electron is mis-identified in jets.

Step		
1	an electron and P_T^{miss}	$n_e\geq 1$, $P_T^e > 20$ GeV, $5° < \theta^e < 100°$, $D^e_{jet} > 1.0$ $P_T^{miss} > 25$ GeV, $V_{ap}/V_p < 0.1$
2		$N_{tracks} > 0$ if $\theta^e > 35°$ if $N_{e.m}\geq 2$ then $P_T^{e.m2} < 5$ GeV ; $D^e_{track} > 0.5$
3		$\gamma^h < 80°$
Final		$M_{e\nu\nu} > 90$ GeV, $P_T^h < 20$ GeV $E - Pz < 45$ GeV

Step	Data	MC	CC DIS	W	Other SM
1	61	59 ± 8	32	24	3
2	34	31 ± 3.8	8.3	20	2.7
3	19	24 ± 3	8	14	2
Final	4	4.6 ± 0.7	2.6	1.4	0.6

Table 5.5: In the first table, summary of the selection criteria in the $e^*\rightarrow eZ_{\hookrightarrow \nu\bar{\nu}}$ and $e^*\rightarrow \nu W_{\hookrightarrow e\nu}$ decay channels. In the second table, observed and predicted event yields for each selection step.

The requirements applied at each selection step for the searched topology are summarized in table 5.5. We start by selecting events satisfying the following conditions:

- at least one high transverse momentum electromagnetic cluster with $P_T^e >$ 20 GeV is required in the polar angle range $5^\circ < \theta^e < 100^\circ$. The polar angle of the electromagnetic cluster is restricted to the forward region of detector in order to suppress NC DIS events, in which the scattered electron is in the backward region,
- to reduce the rate of mis-identified electrons in jets, electron isolation criteria are tightened. The electromagnetic cluster is required to be isolated from jets by a minimum distance of $D^{jets} > 1$ in the $(\eta - \phi)$ plane,
- a missing transverse momentum larger than 25 GeV is required in the event. The cut value on P_T^{miss} has been increased from 15 to 25 GeV in this channel, to further suppress possible non ep background from cosmic rays and halo muons,
- the V_{ap}/V_p variable is used to distinguish the signal from SM backgrounds. Only events with $V_{ap}/V_p < 0.1$ are selected. Figure 5.24 shows the distribution of V_{ap}/V_p for events in those channels, where the e^* signal mainly peaks at low value of V_{ap}/V_p. This cut helps to reject the background from NC DIS events.

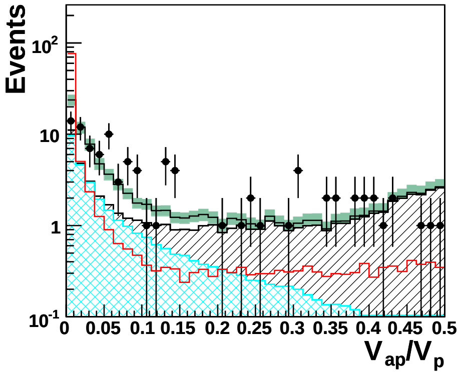

Figure 5.24: Distribution of V_{ap}/V_p before applying the criteria $V_{ap}/V_p < 0.1$. The e^* signal (red line) is peaked at very low values of V_{ap}/V_p.

After the first requirements, 61 events are found in the data, compared to a SM expectation of 59 ± 8 events, in which 32 and 24 events are expected from CC DIS and W production processes, respectively. Figure 5.25 shows the distribution of the missing transverse momentum P_T^{miss}, the electromagnetic cluster transverse momentum P_T^e and its polar angle θ^e of the candidate events passing the first selection step.

The goal of the second selection step is to reduce the SM background coming from CC DIS events where a photon can be radiated (radiative CC DIS events). Therefore, a track is required to be associated to the electron in the central region ($\theta^e > 35^\circ$). In addition, the electron is required to be isolated from any well measured track by a minimum distance of $D_{track} > 0.5$ in the $(\eta - \phi)$ plane. Furthermore, events with another electromagnetic cluster of energy larger than 5 GeV are rejected. After this second selection step, the SM expectation is dominated by W production events (see table 5.5).

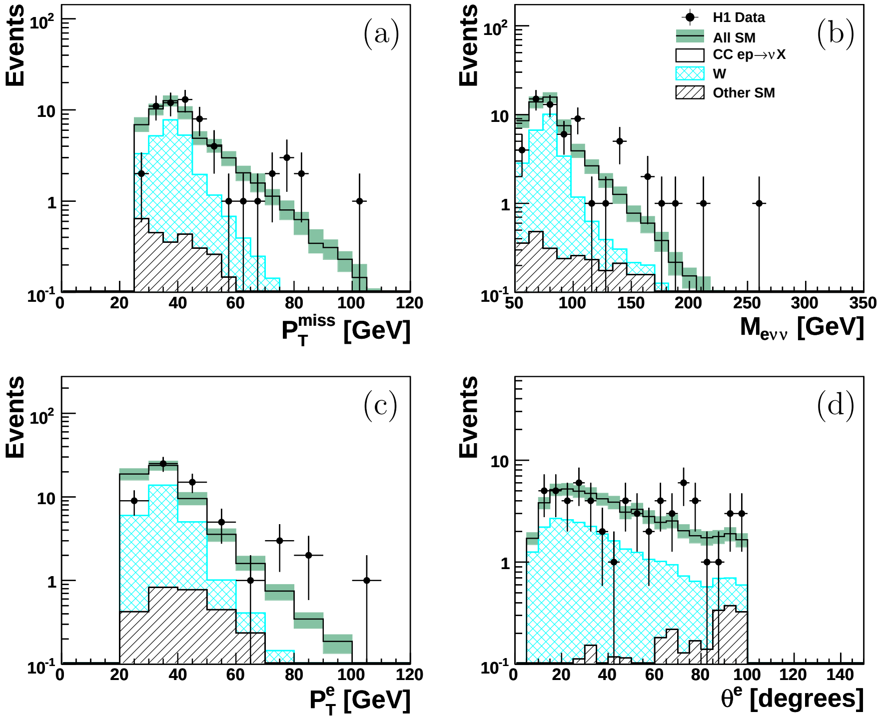

Figure 5.25: Distributions of the missing transverse momentum P_T^{miss} (a), of the electron transverse momentum P_T^e (c) and of the polar angle θ^e (d) for candidate events passing the first selection step, in the $e\nu\nu$ resonance search.

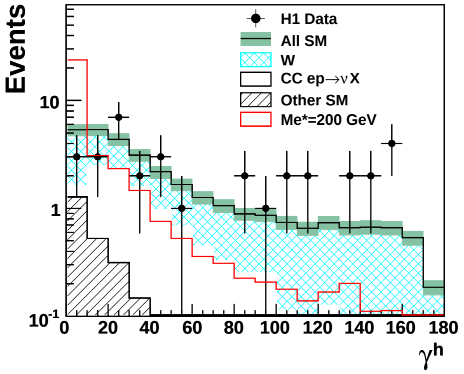

Figure 5.26: Distribution of the polar angle of the hadronic system γ^h for candidate events passing the first selection step of the $e\nu\nu$ resonance search.

Figure 5.26 shows the distribution of the polar angle of the hadronic system γ^h, where events from W production are distributed at all values of γ^h, while the e^* events peaks at lower γ^h values. The background from the W production is thus reduced by selecting only events with $\gamma_h < 80°$.

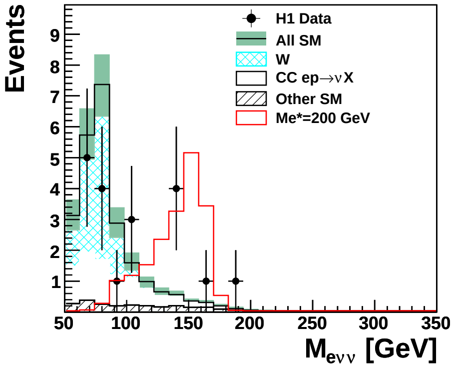

Figure 5.27: Distribution of the reconstructed invariant mass $M_{e\nu\nu}$ of e^* candidate events in the second selection step of the $e\nu\nu$ resonance search.

Figure 5.27 presents the distribution of the reconstructed invariant mass, $M_{e\nu\nu}$, for selected events. A large fraction of W events have a mass $M_{e\nu\nu}$ below 90 GeV. As we are interested only in e^* with masses above 90 GeV, only events with $M_{e\nu\nu} > \sim 90$ GeV are selected. This suppress the SM background from W production. Finally, remaining backgrounds from other sources such as NC DIS events are removed by requiring that the longitudinal energy balance be $E - P_z < 45$ GeV and that transverse momentum of the hadronic system be $P_T^h < 20$ GeV.

After all selection cuts, 4 events are observed in the data, while 4.65 ± 0.7 are expected from the SM. The yields of observed and expected events at each selection step are summarized in table 5.5. The efficiencies for selecting e^* events in both $e^* \rightarrow \nu W_{\hookrightarrow e\nu}$ and $e^* \rightarrow e Z_{\hookrightarrow \nu\bar{\nu}}$ channels are about 35% and 60%, respectively.

5.4.2 The $e^* \rightarrow e Z_{\hookrightarrow ee}$ channel

Step		Selection criteria
1	$N_e \geq 3$	$P_T^{e1,e2,e3} > 15, 10, 5$ GeV $5^\circ < \theta^{e1,e2,e3} < 150^\circ$ if $\theta^{e1,e2} < 35^\circ$ then $N_{tracks} > 0$
2		$P_T^{e1,2,3} > 20, 15, 10$ GeV
Final		$\lvert M_{ee} - M_Z \rvert < 7$ GeV

Step	Data	MC	NC	ee	Other SM
1	38	43 ± 3	4.8	38	0.2
2	4	2.5 ± 0.2	0.1	2.4	0
Final	0	0.72 ± 0.06	0.02	0.7	0

Table 5.6: In the first table, summary of the selection criterias of the $e^* \rightarrow e Z_{\hookrightarrow ee}$ decay channel. In the second table, observed and predicted event yields at each selection step.

The signature of the $e^* \rightarrow e Z_{\hookrightarrow ee}$ decay channel is very clear and consist of three high P_T electrons in the final state. The main source of background arises from lepton pair production, $\gamma\gamma \rightarrow e^+e^-$, where the scattered electron and the electron pair are reconstructed in the detector. In addition, a small background from NC DIS events may arise when in addition to the scattered electron, two electrons are mis-identified in jets. The selection for this channel starts from a sample of multi-electrons events. Three electromagnetic clusters ($e1$, $e2$, $e3$) are required in the polar angle range $5^\circ < \theta^{e1,e2,e3} < 150^\circ$ and with transverse momenta $P_T^{e1,e2,e3}$ larger than 15, 10 and 5 GeV. A track is required to be associated to the two highest P_T electromagnetic clusters, in the central region ($\theta^{e1,e2} > 35^\circ$). This tracking condition helps to remove the background from radiative QED Compton and NC DIS events. The distribution of the transverse momentum of the three electrons and of the invariant mass M_{eee} of e^* candidates, reconstructed from the combination of the three electrons, are shown in figure 5.28. The SM expectation is dominated by $\gamma\gamma \rightarrow e^+e^-$ events.

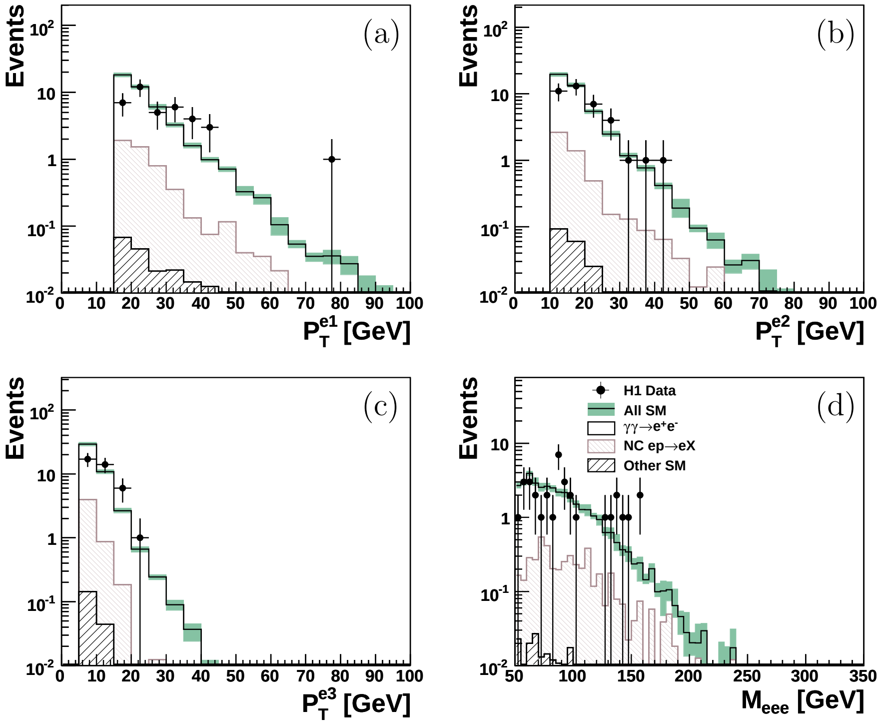

Figure 5.28: Distribution of the transverse momentum of the three electrons and of the reconstructed mass M_{eee} for candidate events passing the first selection step of the eee resonance search.

To reduce the SM background from electron pair production, only candidate events with high transverse momentum electrons $P_T^{e1,e2,e3} > 20, 15, 10$ GeV are selected. Only 4 events remain in the data, compared to a SM expectation of 2.5 ± 0.3 events. Because each e^* candidate event has two electrons coming from the Z boson decay, their invariant mass M_{ee} should be compatible with the Z boson mass. Therefore only events in which two of the three electrons have an invariant mass M_{ee} with $|M_{ee} - M_Z| < 7$ GeV are selected. Figure 5.29 shows the distribution of the invariant mass of the two electrons associated to a possible Z boson decay, before the last selection step.

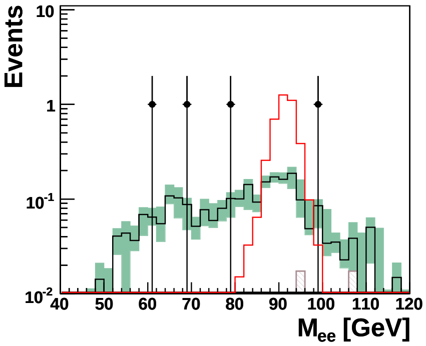

Figure 5.29: Invariant mass distribution of the two electrons associated to the possible decay of a Z boson, M_{ee}, before applying the condition $|M_{ee} - M_Z| < 7$ GeV. The red histogram corresponds to an e^* signal with a mass of 200 GeV.

After all selections, no candidate event is left, compared to a SM expectation of 0.72 ± 0.06. The observed and expected event yields at each selection step are summarized in table 5.6. The efficiency to select e^* events is about ~65% in this channel. The experimental resolution on the reconstructed e^* mass is ~2 GeV for generated e^* masses varying from 120 GeV to 290 GeV.

5.4.3 The $e^* \rightarrow eZ_{\hookrightarrow \mu\mu}$ channel

Step		Selection criteria
1	$N_\mu \geq 2$ $N_e \geq 1$	$P_T^{\mu1,\mu2} > 10, 5$ GeV, $10° < \theta^{\mu1,\mu2} < 160°$ $P_T^e > 15$ GeV, $5° < \theta^e < 150°$
2		$P_T^e > 20$ GeV, $P_T^{\mu1,\mu2} > 15, 10$ GeV
Final		$M_{\mu\mu} > 60$ GeV

Step	Data	MC	$\mu\mu$	$\tau\tau$
1	11	16.8 ± 1	16.7	0.1
2	2	2.2 ± 0.14	2.1	0.1
4	0	0.52 ± 0.05	0.52	0

Table 5.7: In the first table, summary of the selection criteria in the $e^* \rightarrow eZ_{\hookrightarrow \mu\mu}$ decay channel. In the second table, observed and predicted event yields at each selection step.

The signature of the $e^* \rightarrow eZ_{\hookrightarrow \mu\mu}$ decay channel consists of at least two high P_T muons and one high P_T electron. The transverse momentum of the two muons $P_T^{\mu1,\mu2}$ is required to be greater than 10 GeV and 5 GeV, respectively. They are detected in the polar angle range $10° < \theta^{\mu1,\ \mu2} < 160°$. One electromagnetic cluster is detected in the polar angle range $5° < \theta^e < 150°$ and its transverse momentum is required to be $P_T^e > 15$ GeV. The distributions of lepton transverse momenta, $P_T^e, P_T^{\mu1,\mu2}$, the invariant mass distribution of the two muons and of the reconstructed invariant mass distribution of the e^* candidate $M_{\mu1\mu2}$ are presented in figure 5.30. The only SM background arises from the $\gamma\gamma \rightarrow \mu^+\mu^-$ process.

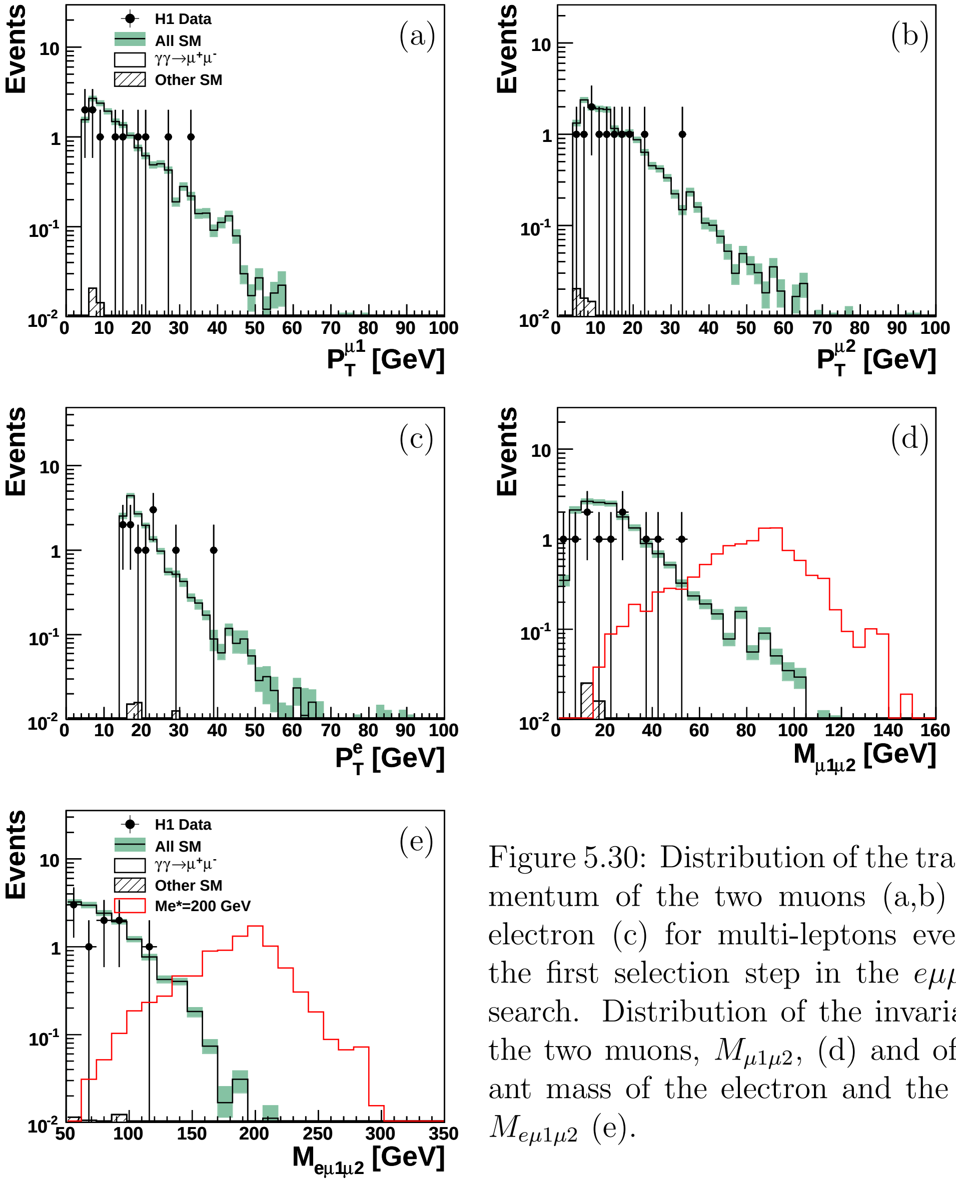

Figure 5.30: Distribution of the transverse momentum of the two muons (a,b) and of the electron (c) for multi-leptons events passing the first selection step in the $e\mu\mu$ resonance search. Distribution of the invariant mass of the two muons, $M_{\mu1\mu2}$, (d) and of the invariant mass of the electron and the two muons $M_{e\mu1\mu2}$ (e).

In a second step, to reduce the contribution from SM muon pair production, the transverse momenta of the leptons P_T^e, $P_T^{\mu1}$ and $P_T^{\mu2}$ are required to be larger than 20, 15 and 10 GeV, respectively. After this requirement, only 2 events remain in the data, compared to a SM background of 2.2 ± 0.14 events. Finally, because the two muons should come from the decay of a Z boson, their invariant mass should be close to the Z boson mass. Thus a cut on the di-muon invariant mass is applied $M_{\mu1\mu2} > 60$ GeV. After all selections, no event is observed, compared to a SM expectation of 0.52 ± 0.05, coming from the $\gamma\gamma\rightarrow\mu^+\mu^-$ process. The yields of observed and expected events at each selection step are summarized in table 5.7. The selection efficiency for e^* events in this channel is about $\sim$40% for an e^* mass of 140 GeV, decreasing to 15% for e^* mass of 260 GeV. The resolution on the e^* reconstructed mass is $\sim$20 GeV.

5.5 Results of the e^* search

Before coming to the summary of the e^* search, main sources of experimental and model uncertainties are summarized. In all plots presented in this chapter, model and experimental uncertainties were included in the total error band on the SM expectation.

5.5.1 Summary the systematic errors

- The uncertainty on the electromagnetic energy scale varies between 0.7% and 2% depending on the polar angle. The polar angle measurement uncertainty of electromagnetic clusters is 3 mrad.
- The scale uncertainty on the transverse momentum of high P_T muons amounts to 2.5%. The uncertainty on the reconstruction of the muon polar angle is 3 mrad.
- The hadronic energy scale is known is 2%. The uncertainty on the jet polar angle determination is 10 mrad.
- The uncertainty on the description of the V_{ap}/V_p variable is 10%.
- The uncertainty on the trigger efficiency is 3%.
- The uncertainty on the luminosity measurement is 3%.

The effect of the experimental systematic uncertainties on the SM expectation are determined by varying the experimental quantities by ± 1 standard deviation in the MC samples and propagating these variations through the whole analysis chain.

Additional model systematic uncertainties are attributed to the SM background MC generators described in section 2.7.1. The total error on the SM background prediction is determined by adding the effects of all model and experimental systematic uncertainties in quadrature.

5.5.2 Summary of results for the e^* search

The table 5.8 summarizes the data event yields compared to the total SM expectation for each analyzed decay channel of the excited electron search. The selection criteria used in the different channels prevent against double counting of candidate events between channels. The distributions of the invariant mass of the data events are in agreement with those of the expected SM background as shown in figure 5.31. Few or no data events are observed in channels corresponding to leptonic decays of the W or Z bosons, in agreement with the low SM expectations. No significant deviation to the SM prediction is found in the searches. The selection efficiencies for the different decay modes for masses M_{e^*} between 120 GeV and 300 GeV are also indicated and are shown in figure 5.32. The experimental resolution on the reconstructed e^* mass distribution for each decay channel is shown in figure 5.33.

Search for e^* at HERA (475 pb^{-1})			
Channel	Data	All SM	Signal Efficiency [%]
$e^*\!\to\! e\gamma$ (elastic)	42	48 ± 4	60–70
$e^*\!\to\! e\gamma$ (inelastic)	65	65 ± 8	60–70
$e^*\!\to\! \nu W_{\hookrightarrow q\bar{q}}$	129	133 ± 32	20–55
$e^*\!\to\! \nu W_{\hookrightarrow e\nu}$	4	4.5 ± 0.7	60
$e^*\!\to\! e Z_{\hookrightarrow \nu\nu}$			35
$e^*\!\to\! e Z_{\hookrightarrow q\bar{q}}$	286	277 ± 62	20–55
$e^*\!\to\! e Z_{\hookrightarrow ee}$	0	0.72 ± 0.06	60
$e^*\!\to\! e Z_{\hookrightarrow \mu\mu}$	0	0.52 ± 0.05	40–15

Table 5.8: Observed and predicted event yields for the studied e^* decay channels. The analyzed data sample corresponds to an integrated luminosity of 475 pb^{-1}. The errors on the SM predictions includes model and experimental systematic errors added in quadrature. Typical selection efficiencies for e^* masses ranging from 120 to 260 GeV are also indicated.

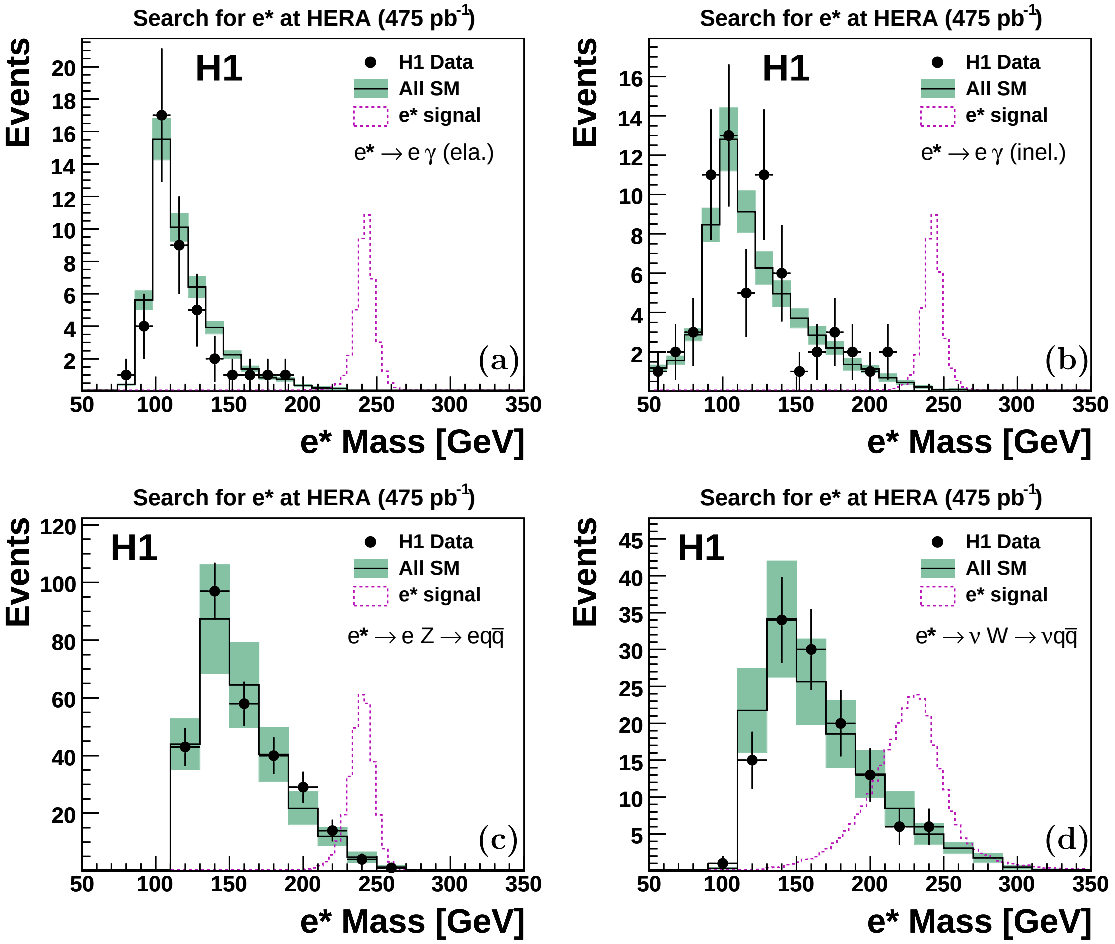

Figure 5.31: Invariant mass distribution of the e^* candidates for the elastic $e^*{\rightarrow}e\gamma$ (a), inelastic $e^*{\rightarrow}e\gamma$ (b), $e^*{\rightarrow}eZ_{\hookrightarrow q\bar{q}}$ (c) and $e^*{\rightarrow}\nu W_{\hookrightarrow q\bar{q}}$ (d) searches. The points correspond to the observed data events and the histogram to the SM expectation after the final selections. The error bands on the SM prediction include model uncertainties and experimental systematic errors added in quadrature.

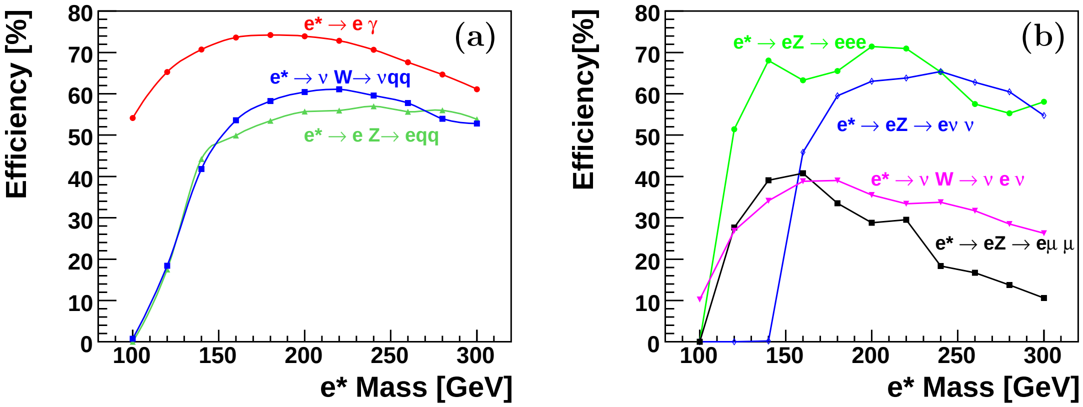

Figure 5.32: Efficiency to select e^* events in each decay channel: for three main decay channels (a): $e^* \to e\gamma$, $e^* \to \nu W_{\hookrightarrow qq}$ and $e^* \to eZ_{\hookrightarrow qq}$; for the leptonic decay channels of the Z or W boson (b): $e^* \to eZ_{\hookrightarrow \mu\mu}$, $e^* \to eZ_{\hookrightarrow ee}$ and $e^* \to \nu W_{\hookrightarrow e\nu}$ $e^* \to eZ_{\hookrightarrow \nu\nu}$.

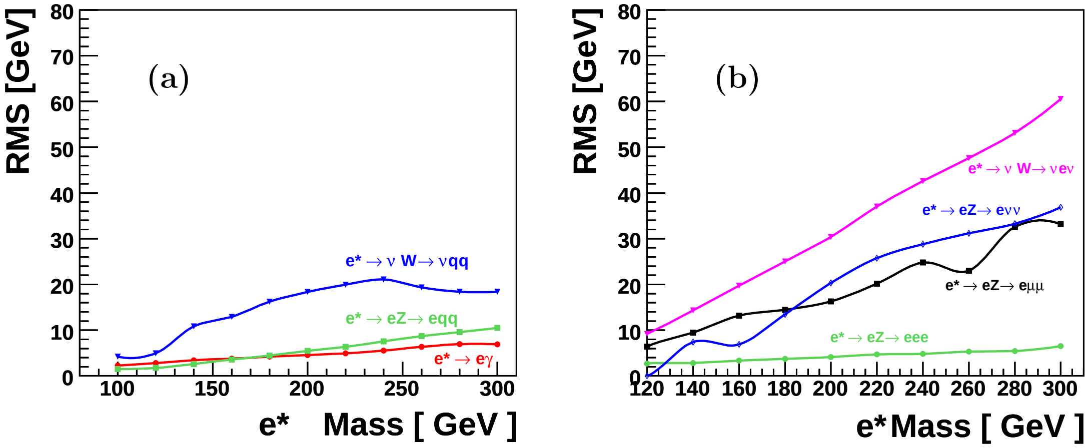

Figure 5.33: Resolution on the reconstructed e^* mass as a function of the excited electron mass for three main decay channels (a): $e^* \to e\gamma$, $e^* \to \nu W_{\hookrightarrow qq}$ and $e^* \to eZ_{\hookrightarrow qq}$ (red, blue, green curve); for the leptonic channels of the Z and W bosons: $e^* \to eZ_{\hookrightarrow \mu\mu}$, $e^* \to eZ_{\hookrightarrow ee}$ and $e^* \to \nu W_{\hookrightarrow e\nu}$ $e^* \to eZ_{\hookrightarrow \nu\nu}$.

Chapter 6

Search for excited neutrinos

As discussed in section 2.6, excited neutrinos could be produced in $e^{\pm}p$ collisions at HERA via $t-$channel W boson exchange. Details of the search for excited neutrino using H1 data are presented in this chapter. Excited neutrinos are searched for in the $\nu^* \to \nu\gamma$, $\nu^* \to \nu Z$, $\nu^* {\to} eW$ decay channels. Almost all final states resulting from hadronic and leptonic W and Z bosons decays are considered. All event final state topologies used in this analysis are summarized in table 6.1. The signatures we will search for as well as the main background sources from the SM are indicated for each channel. As explained in section 2.6, the ν^* production cross section is a factor of a hundred larger in e^-p collision than in e^+p collisions. Only e^-p data will therefore be used for the ν^* search. The e^-p data sample corresponds to an integrated luminosity of 184 pb^{-1}. Some of the topologies of the excited neutrino search are similar to those of the excited electron search. The decay channels $\nu^* \to \nu Z$ and $e^* {\to} \nu W$ as well as $\nu^* {\to} eW$ and $e^* \to eZ$, in which the Z or W bosons decay hadronically have the same final state composed of at least two jets and some missing transverse momentum or an electron. Therefore, the two analyses have many commun points, nevertheless, in the f/Λ domain probed, ν^* of high masses have larger decay width than e^*, leading to differences in the final state kinematic of signal events.

Channel	Signature	SM background
$\nu^* \to \nu\gamma$	$\gamma + P_T^{miss}$	Radiative CC DIS
$\nu^* \to \nu Z_{\hookrightarrow qq}$	P_T^{miss} + 2 jets	CC DIS + 2 jets
$\nu^* \to eW_{\hookrightarrow qq}$	electron + 2 jets	NC DIS + 2 jets
$\nu^* {\to} \nu Z_{\hookrightarrow ee}$	2 electrons + P_T^{miss}	NC DIS, W production
$\nu^* {\to} eW_{\hookrightarrow e\nu}$	2 electrons + P_T^{miss}	NC DIS, W production
$\nu^* {\to} eW_{\hookrightarrow \mu\nu}$	electron + muon + P_T^{miss}	$\gamma\gamma \to ll$

Table 6.1: Summary of event final states resulting from ν^* electroweak decays and used in this analysis. The associated signature and SM background sources are indicated.

6.1 The $\nu^* \rightarrow \nu\gamma$ decay channel

An example of a ν^* Monte Carlo event in the $\nu^* \rightarrow \nu\gamma$ decay channel is shown in figure 6.1. This decay channel corresponds to the electromagnetic de-excitation of an excited neutrino. Therefore, this channel is characterized by an undetected neutrino, leading to large missing transverse momentum P_T^{miss} and an electromagnetic cluster identified as a photon (see section 4.3.2). A photon from SM bacground is soft and colinear, on the opposite the photon coming from the de-excitation of ν^* is pure and non-colinear. This difference is important point to distinguish the signal from SM background in this channel. An additional recoil jet is also present in the final state.

We start by discussing the main sources of SM backgrounds in this channel. Background contributions may arise either from SM processes having the same final state as the $\nu^* \rightarrow \nu\gamma$ channel or by fake identification of final state particles.

- CC DIS processes: CC DIS events with an isolated π^0 or initial or final radiated photon (radiative CC DIS), have a topology similar to $\nu^* \rightarrow \nu\gamma$ events. This constitutes the main source of background in this decay channel. However, the energy of the photon resulting from radiative CC DIS events is lower than that of the photon resulting from the de-excitation of an excited neutrino.

- NC DIS processes: NC DIS events with a mis-measurement of the total hadronic energy, faking a missing transverse momentum, may be identified as $\nu\gamma$ events. But the electromagnetic cluster of the scattered electron should have a track associated and can thus be distinguished from a photon.

- Photoproduction (γp) processes: γp events where the energy of jets is wrongly measured, may contribute to the SM background.

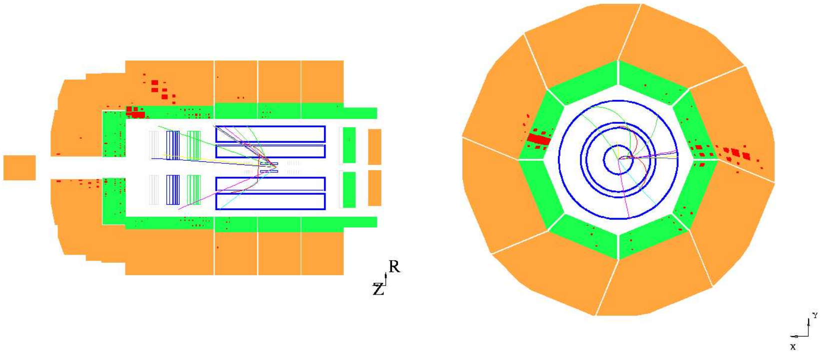

Figure 6.1: Example of a ν^* Monte Carlo event for the $\nu^* \rightarrow \nu\gamma$ decay channel, in the longitudinal (left) and transverse (right) plane.

Event Selection:

The search for excited neutrino will be performed using the same method as used for e^* searches: using discrimating conditions based on kinematic event variables, we will reduce the SM constribution step by step to try to single out a possible signal from ν^* events. The requirements at each selection step in this first $\nu^* \to \nu\gamma$ decay channel are summarized in table 6.2.

Candidate events in this decay channel are initially selected from a sample of CC DIS events with at least one electromagnetic cluster. Distributions of kinematic variables characterizing inclusive CC DIS events are shown in figure 6.2. The agreement between data and the SM MC simulations in those distributions indicates that inclusive CC DIS events are well controled. 11495 data events are found, compared to a SM expectation of 11859 ± 1894 events which mainly arise from inclusive CC DIS.

The analysis starts by selecting candidate events satisfying the following requirements:

- the presence of an undetected neutrino is verified by requiring a missing transverse momentum P_T^{miss} greater than 15 GeV in the event,
- at least one isolated electromagnetic cluster, defined as a photon, is required. The transverse momentum P_T^{γ} of the photon is required to be larger than 5 GeV and it should be detected in the polar angle range $5^\circ < \theta^e < 120^\circ$,
- the longitudinal energy balance is required to be $(E-P_z) < 55$ GeV to suppress a large part of NC DIS background events,
- the final state of signal events contains in most cases a recoil jet due to the ν^* production through t-channel W boson exchange. The presence of at least one jet with $P_T^{jet} > 5$ GeV is then required.

The main variables characterizing the CC DIS event sample with at least one electromagnetic cluster and one recoil jet are presented in figure 6.3. The number of good quality tracks pointing to the electron is also presented. The distribution of data events are also correctly described by the SM MC simulations. After the first selection step, the SM expectation is now dominated by NC DIS events.

To suppress the background arising from NC DIS events, it is necessary now to make the difference between an electron and a photon. In the central region ($\theta^\gamma > 20^\circ$) a photon candidate is defined only if no well measured track points to the electromagnetic cluster within a distance of closest approach (DCA) of 12 cm. In the forward region ($\theta^\gamma < 20^\circ$), the material density of the forward traker is too high and the conversion rate of photon is high. Therefore, to maximize the efficiency on the ν^* signal, no track veto is required in this region. The number of NC DIS events having the electron scattered in the forward region is also low (high Q^2 events). For events with P_T^{miss} below 50 GeV, tighter vetoes are applied on any central track pointing to the electron: no track should be present with a DCA to the cluster below 24 cm or within a distance $R < 0.5$ in the $(\eta - \phi)$ plane. The photon identification efficiency resulting from these conditions was presented in section 4.3.2.

After the application of track vetoes to the electron (second selection step), the SM expectation is now dominated by radiative CC DIS events (see table 6.2). Almost all background events coming from NC DIS processes are strongly suppressed. To

Step		Selection criteria
	Inclusive CC DIS	$P_T^{miss} > 15$ GeV, $E - P_z < 55$ GeV
1	$N_\gamma \geq 1$ $N_{jets} \geq 1$	$P_T^\gamma > 5$ GeV, $5° < \theta^\gamma < 120°$ $P_T^{jet} > 5$ GeV
2	No track associated if $P_T^{miss} < 50$ GeV	for $\theta^\gamma > 20°$: $DCA_{LW} > 12$ cm for $\theta^\gamma > 20°$: $DCA_{DTRA,DTNV} > 24$ cm
3	anti-CC DIS	$P_T^\gamma > 20$ GeV, $P_T^{miss} > 20$ GeV $P_T^{miss} > 30$ GeV or $\theta^\gamma < 60°$
Final	anti-CC DIS	$\xi^\gamma > 45$ GeV $E - P_z < 45$ GeV or $P_T^\gamma > 40$

Step	Data	MC	CC DIS	NC DIS	γp	Other SM
	11495	11859 ± 1894	8579	1195	2008	77
1	443	487 ± 83	86	374	7	20
2	65	90 ± 18	77	5	4.5	3.5
3	14	27 ± 6	22	1.7	0.7	2.6
Final	7	12.3 ± 2.4	8.5	1.2	0.3	2.3

Table 6.2: In the first table, summary of the selection criteria in the $\nu^* \rightarrow \nu\gamma$ decay channel. In the second table, observed and predicted event yields for each selection step of this decay channel. The errors on the prediction include model uncertainties and experimental systematic errors added in quadrature.

restrict further the selection to ν^* events with a high mass, only events with P_T^γ greater than 20 GeV and P_T^{miss} greater than 20 GeV will be accepted. The effect on the ν^* signal and on the SM background is displayed in figure 6.4. The cuts on P_T^{miss} and P_T^γ help to reject a large part of the background from radiative CC DIS events and also to suppress the remaining background from γp events. Since the photon comming from the ν^* decay is emitted in the forward region, the polar angle of the photon is restricted to $\theta^\gamma < 60°$ in events with P_T^{miss} below 30 GeV. The effect of this criteria on the ν^* signal and on the SM background is visible in figure 6.5.

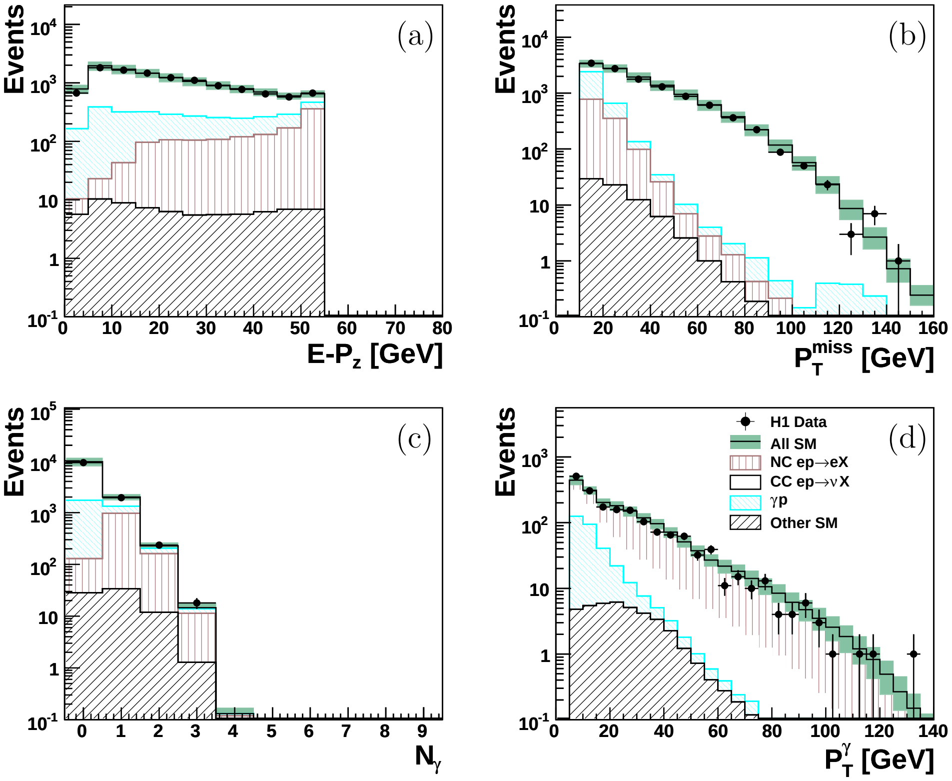

Figure 6.2: Distributions of the longitudinal energy balance $E - P_z$ (a), the missing transverse momentum P_T^{miss} (b), the number of isolated electromagnetic clusters and of the transverse momentum P_T^γ of the highest P_T electromagnetic cluster (c,d) for inclusive CC DIS events.

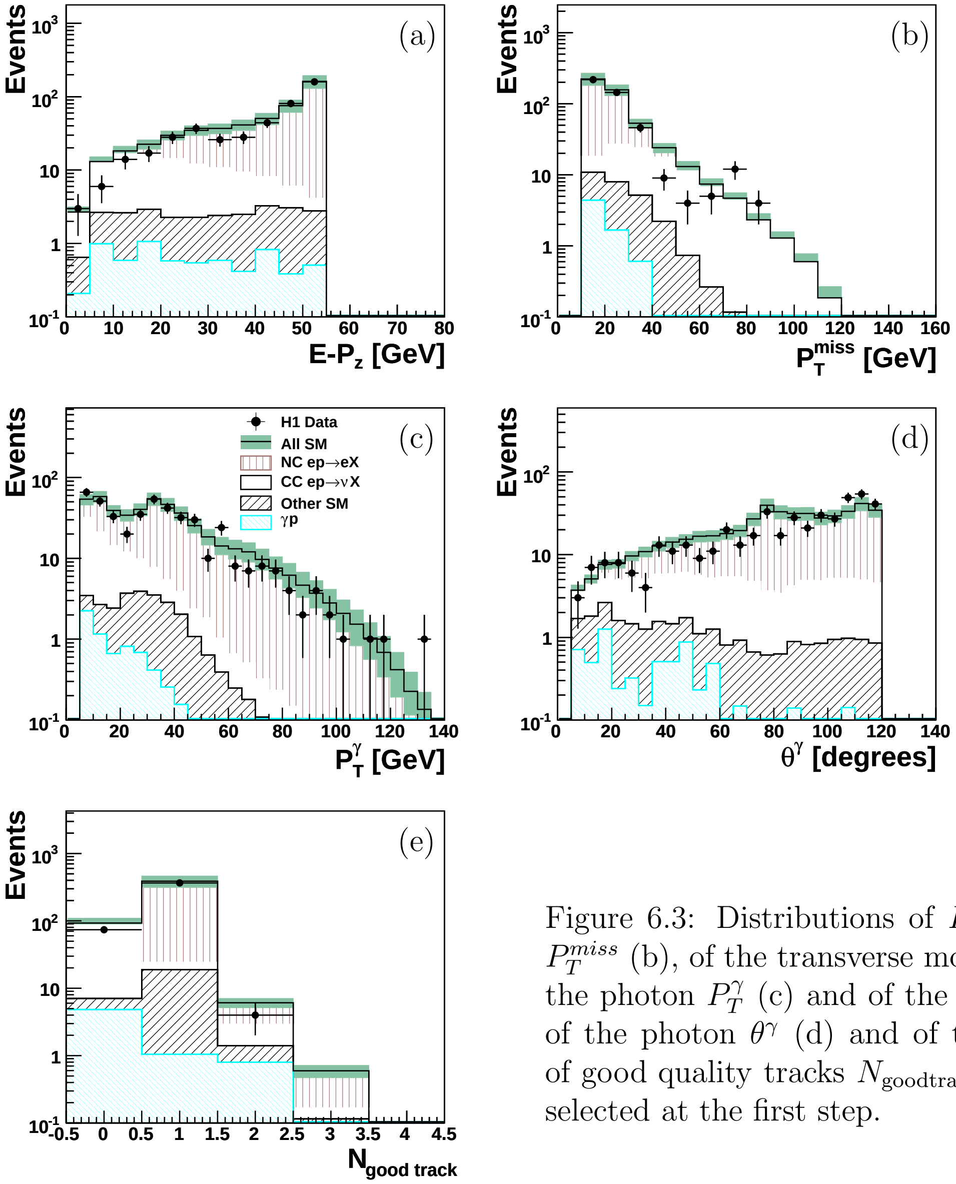

Figure 6.3: Distributions of $E - P_z$ (a), P_T^{miss} (b), of the transverse momentum of the photon P_T^{γ} (c) and of the polar angle of the photon θ^{γ} (d) and of the number of good quality tracks $N_{\mathrm{goodtrack}}$ for event selected at the first step.

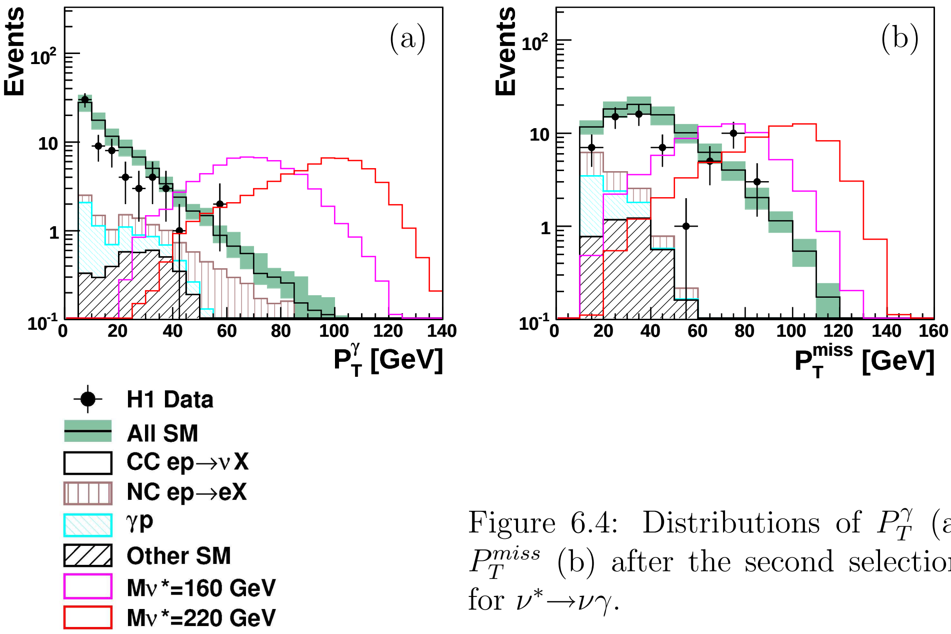

Figure 6.4: Distributions of P_T^γ (a) and P_T^{miss} (b) after the second selection step for $\nu^* \rightarrow \nu\gamma$.

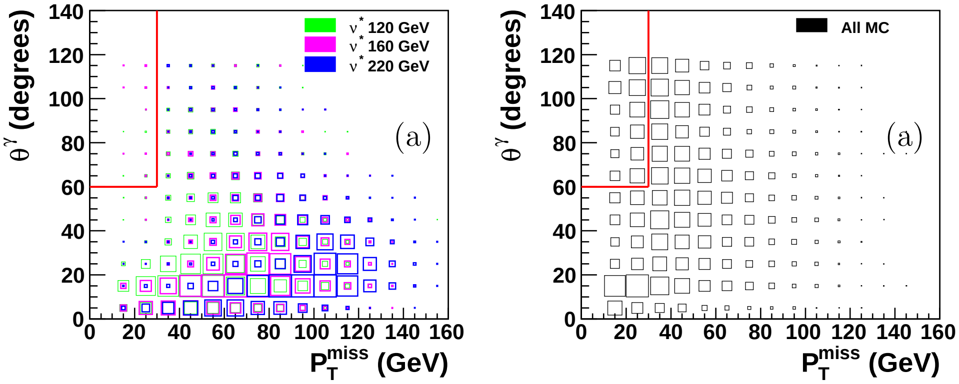

Figure 6.5: Distribution in ν^* events with different masses (a) and of all SM background events (b) in the (P_T^{miss}, θ_γ) plane. The red lines present the rectangular cut: events with $P_T^{miss} < 30$ GeV and $\theta^\gamma > 60°$ are removed.

Figure 6.6 shows the distribution of the variable ξ^γ for the photon candidate. High values of the variable ξ^γ are expected for ν^* events and a large part of the SM background from CC DIS process are reduced by selecting only events with $\xi^\gamma > 45$ GeV. In addition, the transverse momentum of the photon is required to be larger than 40 GeV in events where $E - P_z$ is larger than 45 GeV.

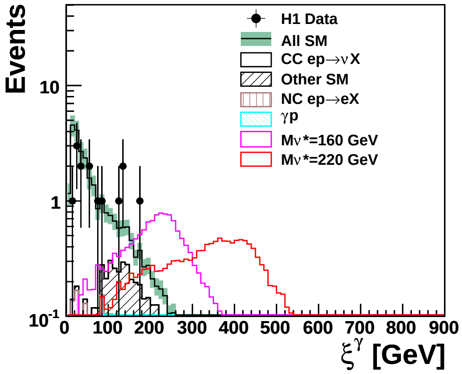

Figure 6.6: Distribution of the variable ξ^γ for events at the thrid selection step.

After all selection cuts, seven events are selected in the data, compared to a SM expectation of 12.3 ± 2.4 events, which are dominated by CC DIS events. No significant excess of event is found in this $\nu^* \rightarrow \nu\gamma$ channel. The distributions of the reconstructed invariant mass of the $\nu\gamma$ system of the missing transverse momentum and the kinematic variables of the photon candidate are shown in figure 6.7. The resulting selection efficiency varies from 50% to 55% for excited neutrinos with masses from 120 GeV to 300 GeV. The total width of the reconstructed ν^* mass distribution is 11 GeV for a generated ν^* mass of 120 GeV, increasing to 41 GeV for a ν^* mass of 260 GeV.

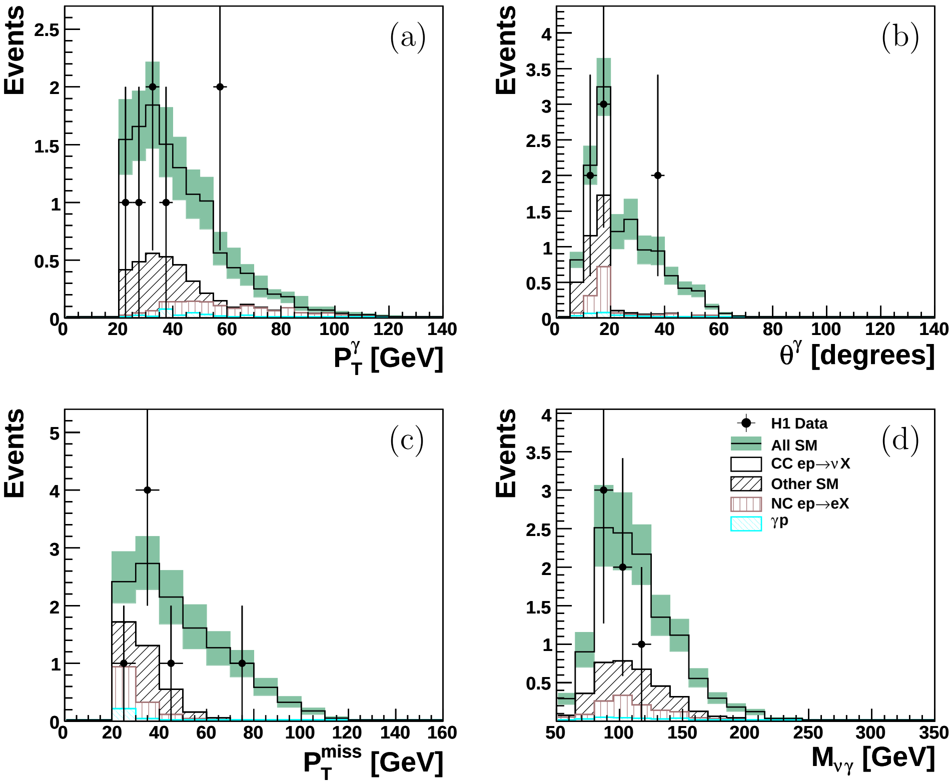

Figure 6.7: Distributions of the transverse momentum and polar angle of the photon (a,b), the missing transverse momentum (c) and the reconstructed invariant mass of the ν^* candidate in the final selection step of the $\nu^* \rightarrow \nu\gamma$ decay channel. One data event is observed with a reconstructed mass below 30 GeV and therefore does not appear in the figure (d).

6.2 The $\nu^* \to \nu Z_{\hookrightarrow qq}$ decay channel

The $\nu^* \to \nu Z_{\hookrightarrow qq}$ channel corresponds to the de-excitation of an excited neutrino by the emission of a Z boson which decays to hadrons. This leads to a final state containing at least two jets with an invariant mass equal to the Z boson mass and a large missing transverse momentum produced by the neutrino escaping from the detector. Figure 6.8 shows an example of a ν^* Monte Carlo event in this decay channel.

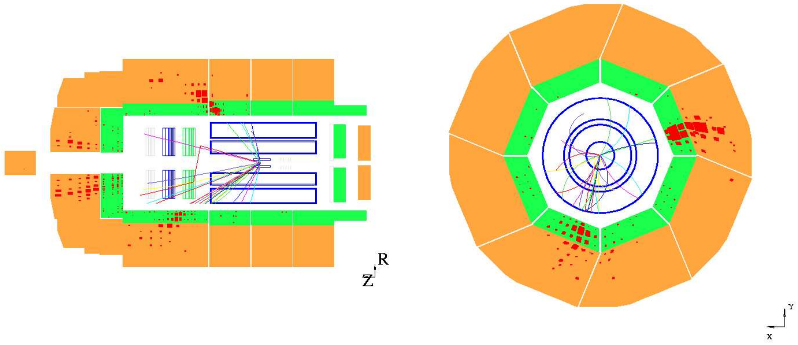

Figure 6.8: Example of a ν^* Monte Carlo event for the $\nu^* \to \nu Z_{\hookrightarrow qq}$ decay channel, in the longitudinal (left) and transverse (right) plane.

The topology of this channel is similar to the $e^* \to \nu W_{\hookrightarrow qq}$ channel in the e^* search. The main sources of SM background in this channel come from CC, NC DIS and γp processes.

- CC DIS processes: CC DIS events with two high P_T jets have a similar topology to $\nu^* \to \nu Z_{\hookrightarrow qq}$,
- NC DIS processes: fake missing transverse momentum can arise from mismeasurement of hadrons in NC DIS events with two jets. If the scattered electron is not found, these events may mimic ν^* signal events,
- photoproduction processes (γp): Photoproduction events with two jets and fake P_T^{miss} may also have a topology similar to ν^* events.

Event Selection:

The requirements at each selection step in the $\nu^* \to \nu Z_{\hookrightarrow qq}$ channel used to reduce the SM background and to select candidate events are summarized in table 6.3. Candidate events are first selected from a sample of inclusive CC DIS events with at least two high transverse momentum jets (multi-jet CC DIS events). These events are selected according to the following conditions:

- the presence of an undetected neutrino is required in the event by imposing a missing transverse momentum P_T^{miss} larger than 15 GeV,

Step		Selection criteria
	Inclusive CC DIS	$P_T^{miss} > 15$ GeV, $E - P_z < 55$ GeV
1	CC DIS + 2jets	$P_T^{jet1,jet2} > 20, 15$ GeV, $5° < \theta^{jet1,jet2} < 130°$
2	anti-γp	$P_T^{miss} > 20$ GeV
3	anti-CC DIS	$\gamma^h > 20°$, $E - P_z > 25$ GeV or $P_T^{miss} > 50$ GeV $V_{ap}/V_p > 0.1$ or $P_T^h > 30$ GeV
4	Z mass window	$M_{jj} > M_Z - 30$ GeV
5	if $P_T^{miss} < 50$ GeV	$N_{jets} \geq 3$, $N_{e.m.clusters} < 1$
Final		$x_h > 0.04$

Step	Data	MC	CC DIS	NC DIS	γp	Other SM
1	1220	1240 ± 186	647	221	362	10
2	713	837 ± 143	609	120	102	6
3	488	577 ± 100	401	111	61	4
4	278	279 ± 45	137	95	44	3
5	107	109 ± 22	87	6.4	15	0.6
Final	89	95 ± 21	84	4.2	6.3	0.4

Table 6.3: In the first table, summary of the selection criteria in the $\nu^* \rightarrow \nu Z_{\hookrightarrow qq}$ decay channel. In the second table, observed and predicted event yields for each selection step of this decay channel. The errors on the prediction include model uncertainties and experimental systematic errors added in quadrature.

- the longitudinal energy balance $E - P_z$ is required to be lower than 55 GeV to reduce a large part of the NC DIS background.
- at least two jets have to be present in the final state. The two jets are required to have transverse momenta $P_T^{jet1,jet2} > 20$, 15 GeV and are detected in the polar angle range $5° < \theta^{jet1,jet2} < 130°$, respectively. Looking to all jets in the event, a Z boson candidate is reconstructed form the combination of the two jets having an invariant mass M_{jj} closest to the Z boson mass,

Distributions of kinematic variables, characterizing inclusive CC DIS events, are shown in figure 6.9. Inclusive CC DIS events are also well described by the SM expectation. Distributions of the main kinematic variables characterizing candidate events passing the requirements of the first selection step, P_T^{miss}, V_{ap}/V_p, the transverse momentum and polar angle of the two jets, their invariant mass M_{jj} and the reconstructed invariant mass of ν^*, are presented in figure 6.10. After the first selection step, 1220 events are found in the data, compared to a SM expectation of 1240 ± 186 events, arising from both CC DIS and γp processes (see table 6.3).

The goal of the second selection step is to reject SM background coming from γp events. Here, we can not use the cut $V_{ap}/V_p < 0.3$ as in the e^* search in νqq resonance, because as shown in the figure 6.10(b), ν^* signal events can have large V_{ap}/V_p values. Therefore, a large part of the γp background has to be suppressed by

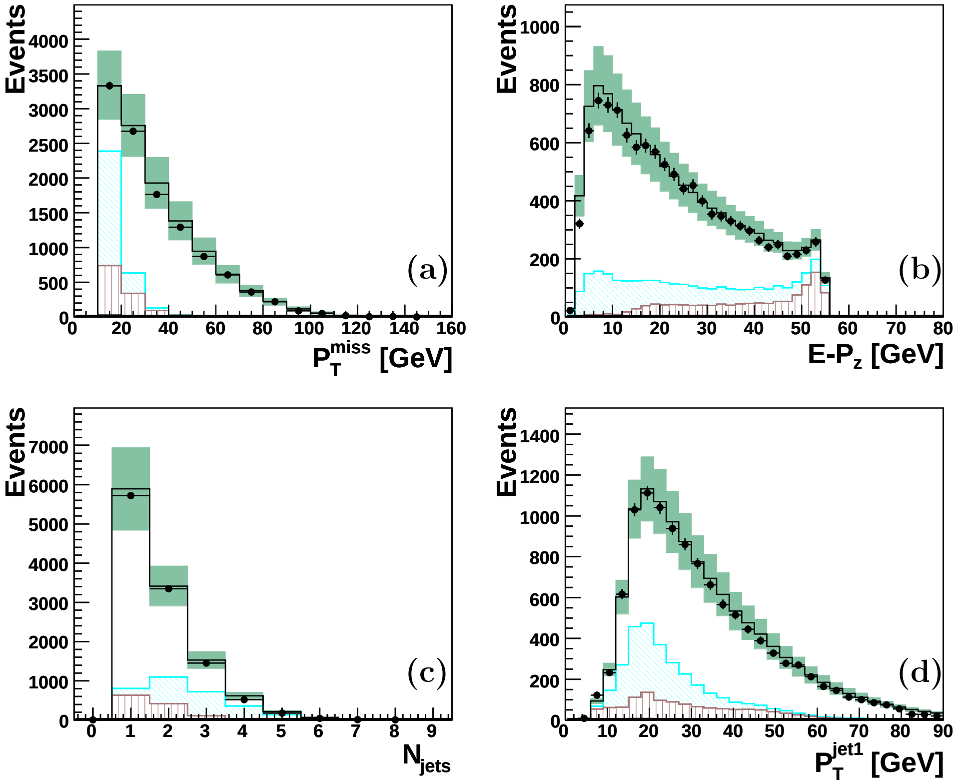

Figure 6.9: Distributions of the missing transverse momentum P_T^{miss} (a), longitudinal energy balance $E - P_z$ (b), jet multiplicity N_{jets} (c) and transverse momentum of the jet P_T^{jet1} (d) in inclusive CC DIS events.

requiring a high missing transverse momentum. Only events with $P_T^{miss} > 20$ GeV are accepted. The effect of this cut can be seen in the figure 6.10(a), where γp events contribute mainly at low P_T^{miss} while ν^* events have high P_T^{miss} value.

The third selection step aims to reduce the multi-jet CC DIS background. Only events with $P_T^{miss} > 50$ GeV or $E - P_z > 25$ GeV will be selected. The effect on the ν^* signal and on the SM expectation of this requirement is visible in figure 6.11. Additionally, the hadronic final state of selected events must exhibit a polar angle γ^h larger than 20°, in order to reduce the CC DIS background and also to remove the remaining background from γp events. The γ^h distribution is presented in figure 6.12. Furthermore, events with $P_T^{miss} < 30$ GeV are selected only if $V_{ap}/V_p \ > \ 0.1$.

In each candidate event, a Z boson candidate is reconstructed from the combination of the two jets with an invariant mass M_{jj} closest to the nominal Z boson mass. At the fourth selection step, a cut on the reconstructed invariant mass of the two jets $M_{jj} > M_Z - 30$ GeV is applied. Figure 6.13 shows the M_{jj} distribution before applying this requirement. The dominant background from multi-jet CC DIS events is strongly reduced by this cut on the invariant mass M_{jj} (see table 6.3).

As the ν^* is produced via the $t-$channel exchange of the W boson, a third jet from the struck quark is present in ν^* events. Hence, to further reduce the multi-jet

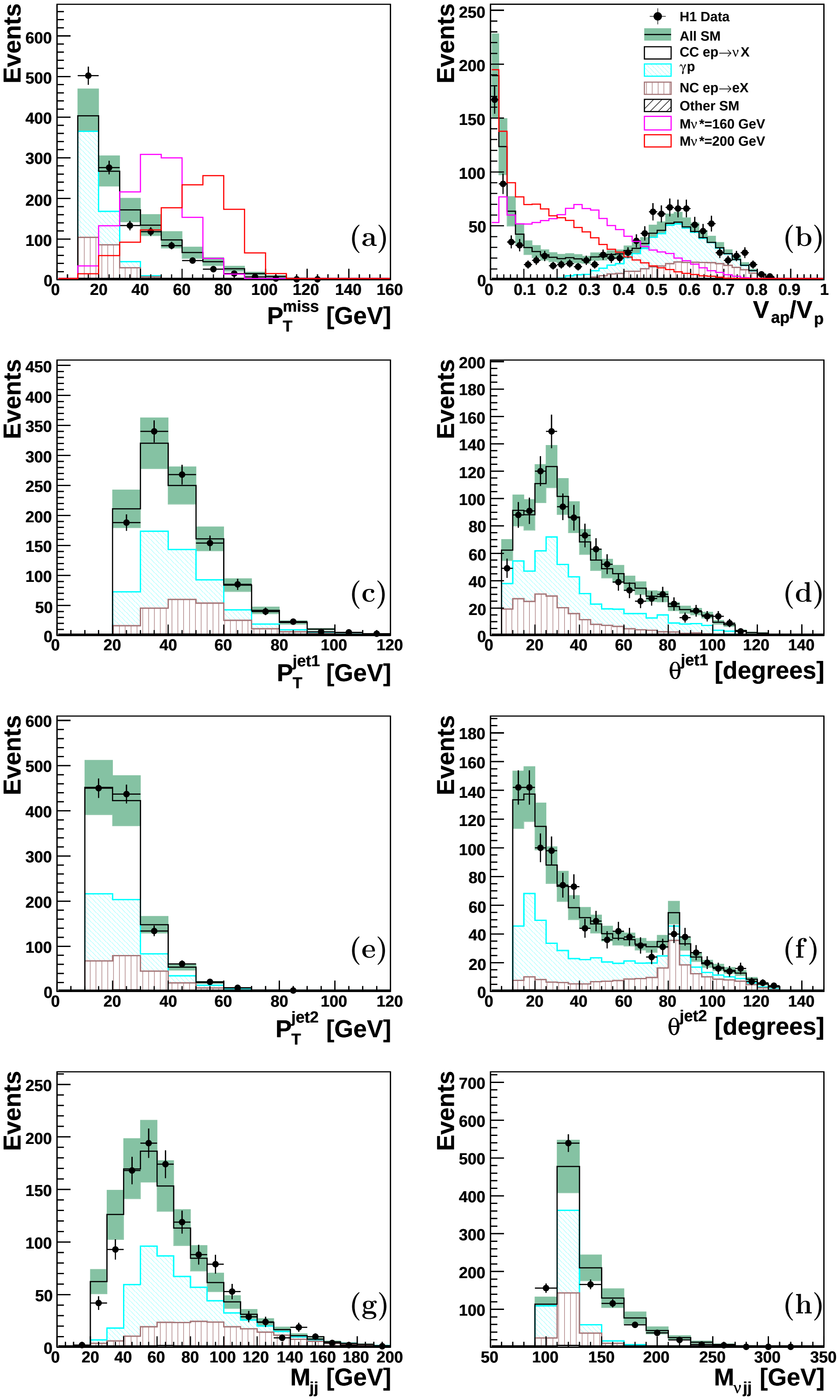

Figure 6.10: Distribution of the missing transverse momentum P_T^{miss} (a), the ratio V_{ap}/V_p (b), of the transverse momentum $P_T^{jet1,jet2}$ (c,e) and of the polar angle $\theta^{jet1,jet2}$ (d,f) of the two jets resulting from a possible Z boson decay, their invariant mass M_{jj} (g) and the reconstructed invariant mass of ν^*, $M_{\nu jj}$ (h) for multi-jet CC DIS events at the first selection step.

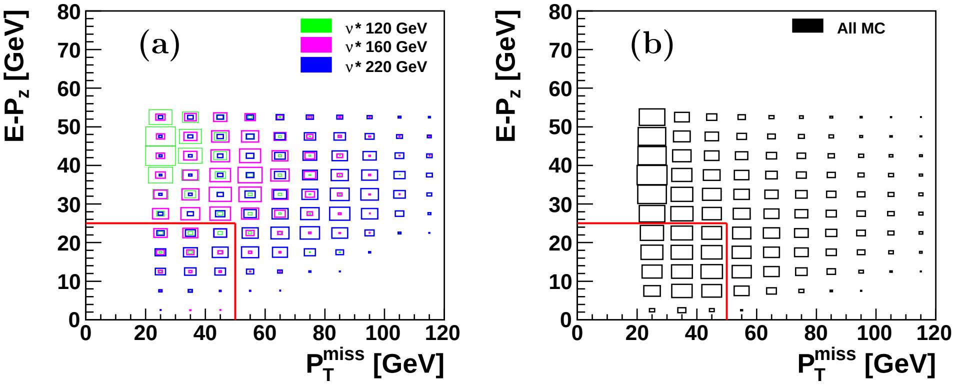

Figure 6.11: Distribution of ν^* events with different masses (a) and of all SM expectation (b) in the $(E - P_z,\ P_T^{miss})$ plane. The red lines present the rectangular selection cut: events with $E - P_z > 25$ GeV or $P_T^{miss} > 50$ GeV are selected.

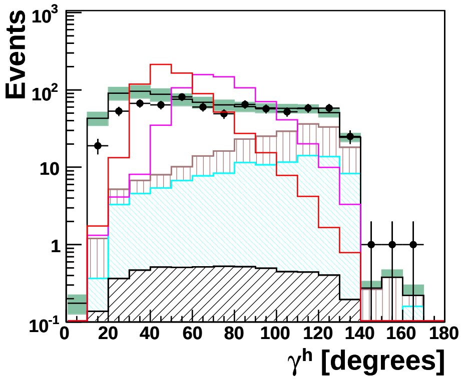

Figure 6.12: Distribution of the polar angle of the hadronic system γ^h for events selected at the second step of the νqq resonance search.

CC DIS background, a jet multiplicity greater or equal to three is required for events with a P_T^{miss} lower than 50 GeV. To suppress NC DIS events, where the scattered electron is often present, no electromagnetic cluster should be detected in events with $P_T^{miss} < 50$ GeV. Figure 6.14 presents the distributions of the jet multiciplity, of the electromagnetic cluster multiciplity and of the P_T^{miss} for selected events, before

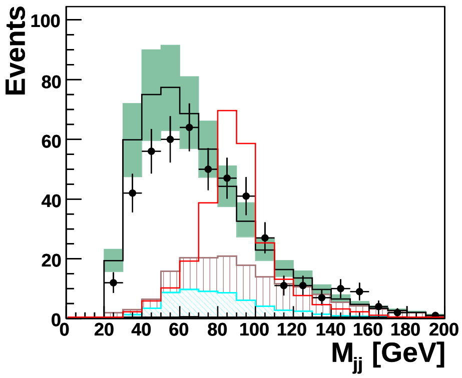

Figure 6.13: Distribution of the reconstructed invariant mass of the two jets M_{jj} associated to a Z boson candidate, before applying the condition $M_{jj} > M_Z - 30$ GeV.

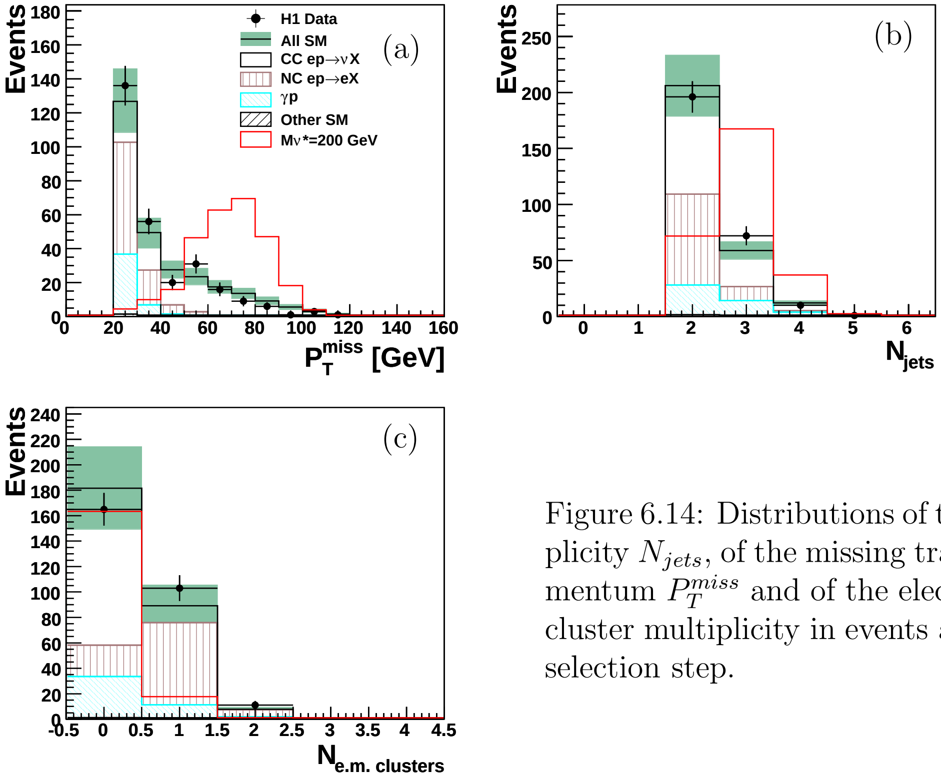

Figure 6.14: Distributions of the jet multiplicity N_{jets}, of the missing transverse momentum P_T^{miss} and of the electromagnetic cluster multiplicity in events at the fourth selection step.

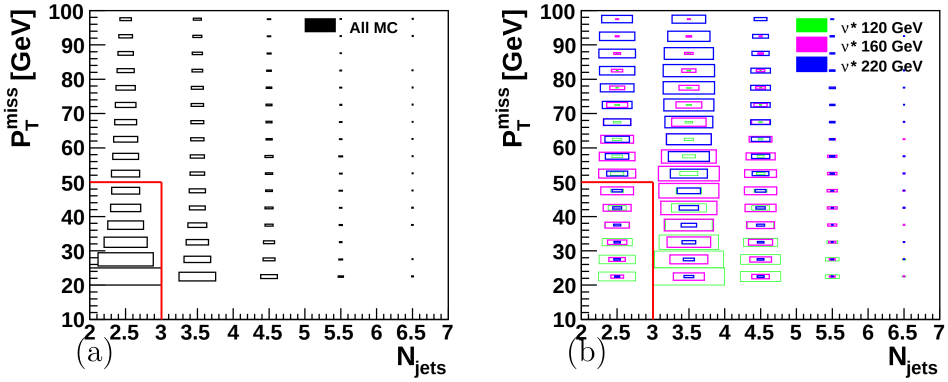

Figure 6.15: Distribution of ν^* evens with different masses (a) and of all SM expectation (b) in the (P_T^{miss}, N_{jets}) plane. The red line presents the rectangular cut: events with $P_T^{miss} < 50$ GeV and $N_{jets} < 3$ are rejected.

applying these criteria. The effect of these cuts on the ν^* signal and on the SM background are displayed in figures 6.16 and 6.15. With these additional cuts, CC DIS and γp events contribute now to the SM background. Finally, remaining background from γp events is suppressed by requiring $x_h > 0.04$, where x_h is the Bjorken scaling variable calculated from the hadronic system using the Jacquet-Blondel method. The distribution of $\log(x_h)$ before this final cut is presented in figure 6.17.

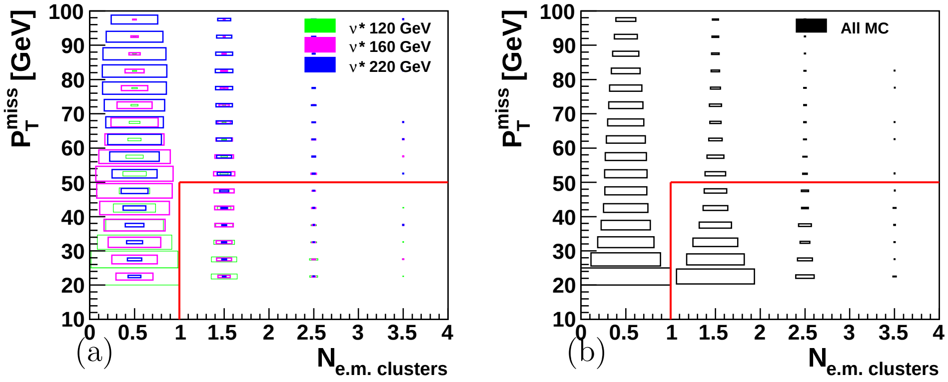

(a) (b)

Figure 6.16: Distribution of ν^* events with different masses (a) and of all SM expectation events (b) in the (P_T^{miss}, $N_{e.m.cluster}$) plane. The red line presents the rectangular cut: events with $P_T^{miss} > 50$ GeV or $N_{e.m.clusters} > 1$ are selected.

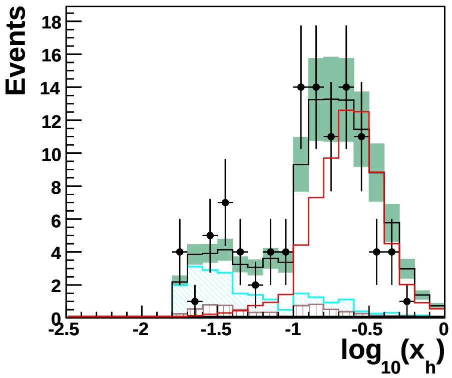

Figure 6.17: Distribution of $\log_{10}(x_h)$ for events passing the step 5. Events with $\log_{10}(x_h) < -1.4$ are rejected.

After all selection cuts, 89 candidate events are found in the data, compared to a SM expectation of 95 ± 21 events. The yields of observed and expected background events at each selection step are summarized in table 6.3. Distributions of the reconstructed invariant mass of ν^*, the missing transverse momentum and the kinematic variables of the two jets of candidate events passing all selection steps of the $\nu^* \to \nu Z_{\hookrightarrow qq}$ channel are presented in figure 5.15. Good overall agreement is observed between data and the SM background. No significant excess of event is found. The efficiency of selecting ν^* events is about 40% for ν^* masses varying from 120 GeV to 260 GeV. The total width of the reconstructed ν^* mass distribution is 31 GeV for a generated ν^* mass of 120 GeV, increasing to 41 GeV for a ν^* mass of 260 GeV.

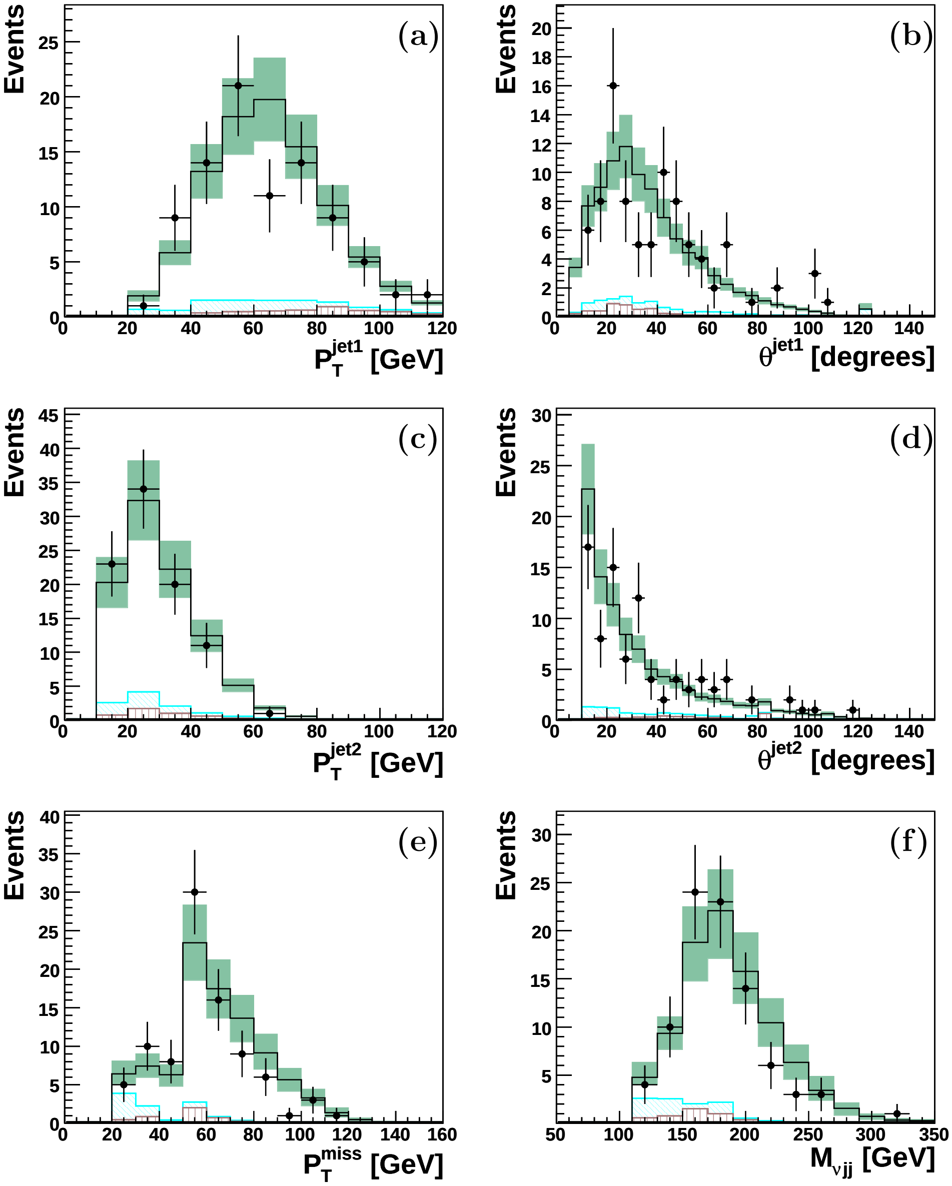

Figure 6.18: Distributions of the transverse momenta (a,c) and polar angle (b,d) of the two jets, the missing transverse momentum (e) and reconstructed invariant mass of ν^* (f) from the $(\nu, jet1, jet2)$ system for selected events at the final step in the $\nu^* \rightarrow \nu Z_{\hookrightarrow qq}$ channel.

6.3 The $\nu^*\rightarrow eW_{\hookrightarrow qq}$ decay channel

The de-excitation of an excited neutrino by emission of a W boson decaying into hadrons, leads to a final state containing two high P_T jets with an invariant mass equal to the W boson mass and an electron. An example of a ν^* Monte Carlo event in this channel is shown in figure 6.19.

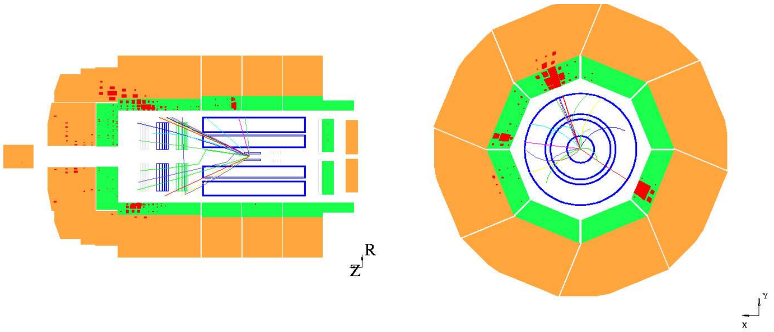

Figure 6.19: Example of a ν^* Monte Carlo event for the $\nu^* \rightarrow eW_{\hookrightarrow qq}$ decay channel, in the longitudinal (left) and transverse (right) plane.

The topology of this channel is similar to that of the $e^*\rightarrow eZ_{\hookrightarrow qq}$ channel studied in section 5.2. The main sources of SM background are also NC DIS processes with two jets.

Event Selection:

The selection criteria of this $\nu^*\rightarrow eW_{\hookrightarrow qq}$ channel are summarized in table 6.4. As for the $e^*\rightarrow eZ_{\hookrightarrow qq}$ search, we start by selecting a sample of inclusive NC DIS events with at least two high transverse momentum jets (multi-jet NC DIS events) using the following requirements:

- at least one electromagnetic cluster has to be present in the final state,
- this electromagnetic cluster is required to have a transverse momentum $P_T^e >$ 10 GeV and be detected in the polar angle range $5° < \theta^e < 145°$,
- at least two jets have to be present in the event. The two jets must be detected in the polar angle $5° < \theta^{jet1,jet2} < 130°$ with transverse momenta $P_T^{jet1,jet2} > 20, 15$ GeV. Looking at all jets in the events, a W boson candidate is reconstructed from the combination of the two jets having an invariant mass M_{jj} closest to the W boson mass.

As shown in section 5.2, both inclusive and multi-jet NC DIS events are well under control. Distributions of the kinematic variables of the electron (P_T^e, θ^e) and of two jets $(P_T^{jet1,jet2}, \theta^{jet1,jet2})$, the invariant mass of the two jets M_{jj} and the reconstructed invariant mass of the ν^*, M_{ejj} are shown in figure 6.20 for events passing the first selection step.

In the next two selection steps, the aim is to reduce the main background from NC DIS events. The selection requirements in those steps are the same as used in

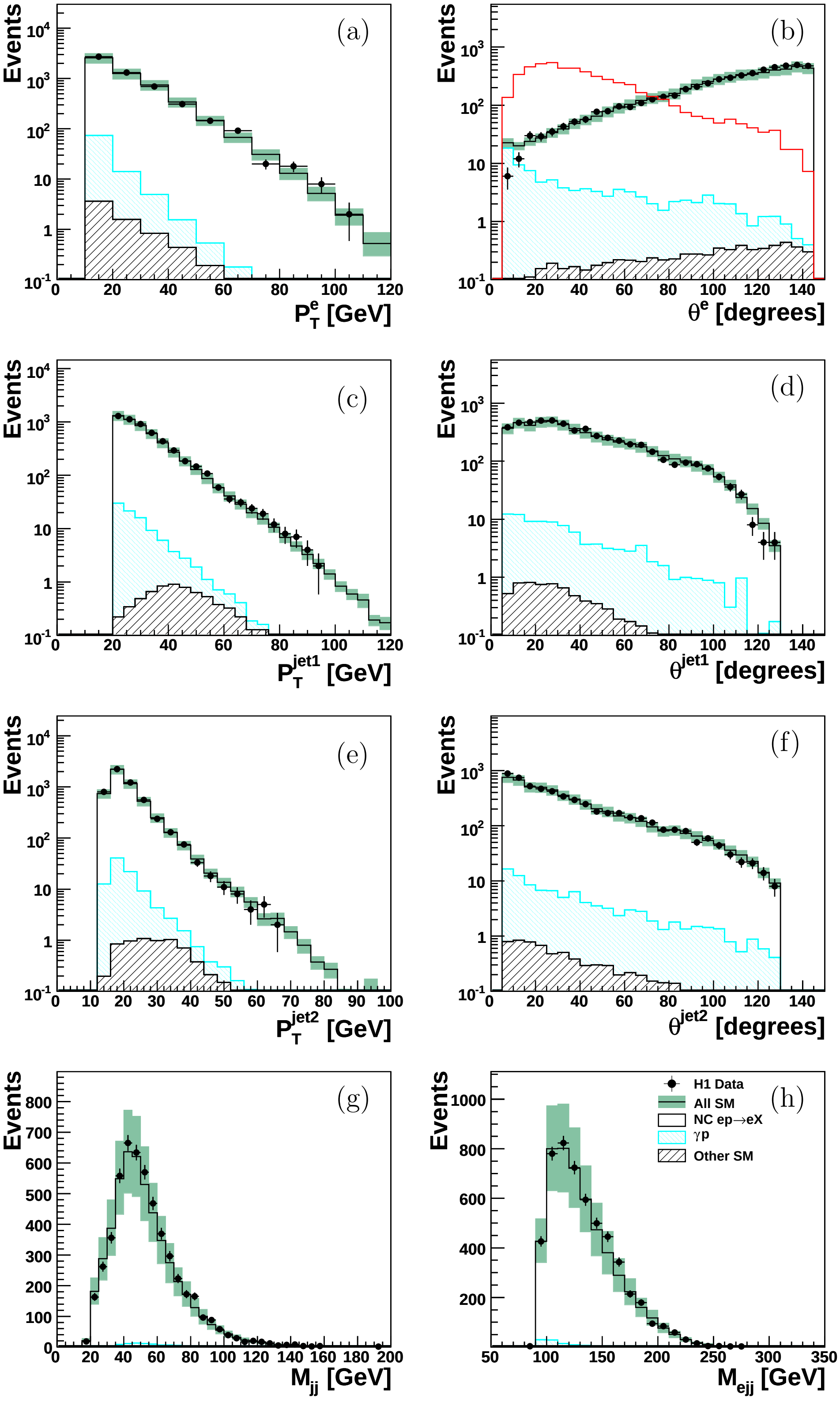

Figure 6.20: Distributions of the transverse momentum (a) and polar angle (b) of the electromagnetic cluster, of the transverse momntum (c, e) and polar angle (d, f) of the two jets coming from a W boson decay and their invariant mass M_{jj} and distribution of the reconstructed ν^* invariant mass M_{ejj} for events selected at the first step in the $\nu^* \rightarrow eW_{\hookrightarrow qq}$ channel.

Step		Selection criteria
	Inclusive NC DIS	$P_T^e > 10$ GeV, $5^\circ < \theta_e < 145^\circ$
1	NC DIS + 2jets	$P_T^{jet1,jet2} > 20(15)$ GeV,$5^\circ < \theta^{jet1,jet2} < 130^\circ$
2	anti-NC DIS	$\theta^e < 90^\circ$
3	anti-NC DIS	$\xi^e > 23$ GeV or $P_T^e > 25$ GeV
4	W mass window	$M_{jj} > M_W - 40$ GeV
Final		$\theta^{jet1} < 80^\circ$
	$N_{jets} \geq 3$	if $P_T^e < 65$ GeV

Step	Data	MC	NC DIS	γp	Other SM
1	5324	5194 ± 1164	5087	88	19
2	1318	1365 ± 275	1278	76	11
3	982	1031 ± 209	973	50	8
4	661	665 ± 137	619	40	6
Final	220	223 ± 47	208	13	2

Table 6.4: In the first table, summary of selection requirements in the $\nu^* \rightarrow eW_{\hookrightarrow qq}$ decay channel. In the second table, observed and predicted event yields for each step selection of this decay channel. The errors on the prediction include model uncertainties and experimental systematic errors added in quadrature.

the e^* search. Only events with an electromagnetic cluster polar angle θ^e lower than 90° are selected. To further reduce the NC DIS background, the electron variable is required to be $\xi^e > 23$ GeV in events with $P_T^e < 25$ GeV. The effect of this cut on the ν^* signal and on all SM backgrounds is displayed in figure 6.21.

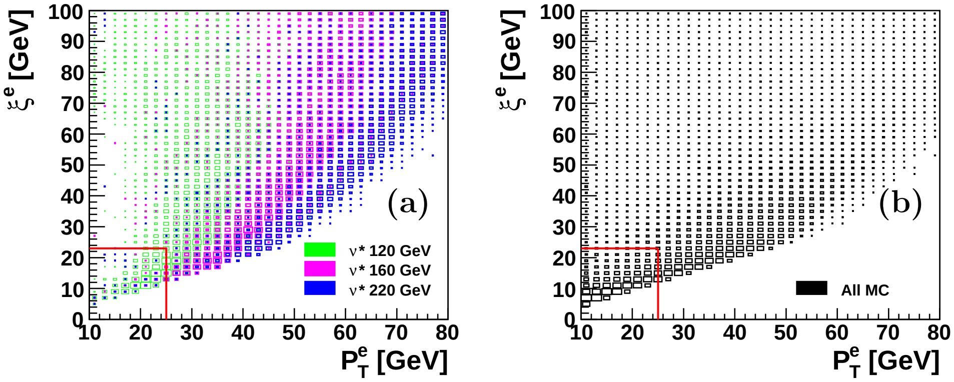

Figure 6.21: Distribution of ν^* events with different masses (a) and of all SM expectation (b) in the $(P_T^e,\ \xi^e)$ plane. The boxes are proportional to the number of events obtained in this plane. The red line presents the rectangular cut: events with $P_T^e > 25$ GeV or $\xi^e > 23$ GeV are selected.

In each candidate event, the two jets associated to a possible W boson decay should have an invariant mass M_{jj} close to the nominal W boson mass. Therefore, only events with $M_{jj} > M_W - 40$ GeV are accepted. Distribution of M_{jj} before applying any cut on it is shown in figure 6.22. As it can be seen in this figure, the cut on M_{jj} allows to remove a large part of the NC DIS background. At the selection step 4, 661 candidate events are selected in the data, compared to a SM expectation of 665 ± 137 events, still dominated by NC DIS events.

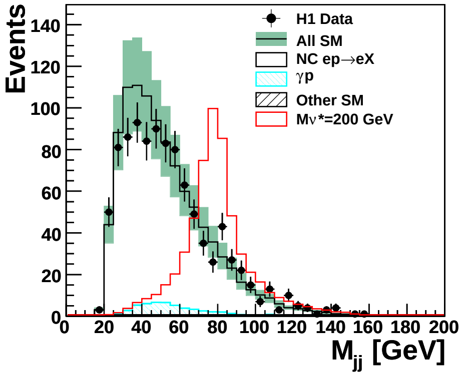

Figure 6.22: Distribution of the reconstructed invariant mass M_{jj} of the two jets associated to a possible W boson decay, before applying any requirement on it.

Finally, in ν^* events, the jet of highest P_T $(jet1)$ is mostly in the forward direction, as shown in the figure 6.23(c). An additional cut on its polar angle $\theta^{jet1} < 80°$ is then applied to increase the separation power between NC DIS events and a ν^* signal. Figure 6.23 presents also the distributions of the transverse momenta and polar angle of the two jets of events selected after applying the criteria on M_{jj}. Because ν^* are produced via the $t-$channel exchange of the W boson, a third jet is often present in the final state. Therefore, in events with a low transverse momentum electromagnetic cluster $P_T^e < 65$ GeV, a third jet with $P_T^{jet3} > 5$ GeV is required. The effect of this last requirement on the ν^* signal and on all background events is displayed in figure 6.24.

After all selection cuts, 220 candidate events are found in the data, compared to a SM expectation of 223 ± 47 events, which is dominated by 208 NC DIS events. No significant excess of event is found in the $\nu^* \rightarrow eW_{\hookrightarrow qq}$ channel. The observed and expected events at each selection step are summarized in table 6.4. The distributions of the reconstructed ν^* invariant mass M_{ejj} and of the kinematic variables of the electron and of the two jets are presented in figure 6.25. The selection efficiency for the ν^* events varies from 40% for a ν^* mass of 120 GeV to 65% for a ν^* mass of 300 GeV. The total width of the reconstructed ν^* mass distribution is 15 GeV for a generated ν^* mass of 120 GeV, increasing to 38 GeV for a ν^* mass of 260 GeV.

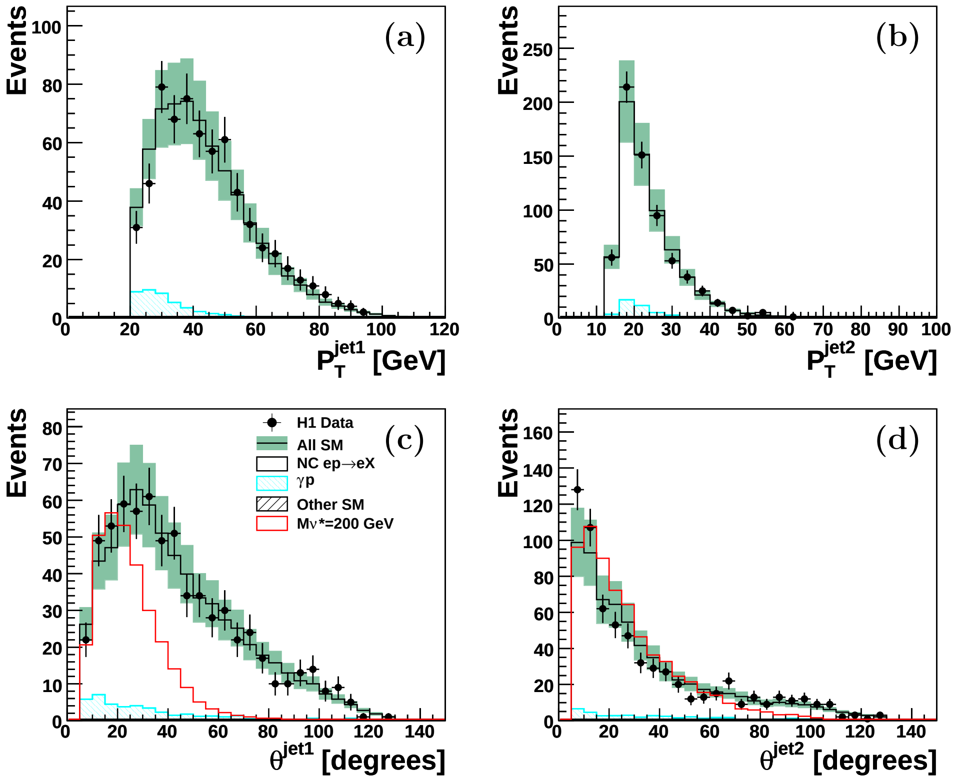

Figure 6.23: Distributions of the transverse momentum $P_T^{jet1,jet2}$ (a,b) and polar angle $\theta^{jet1,jet2}$ (c,d) of the two jets associated to a possible W boson decay, after the cut $M_{jj} > M_W - 40$ GeV, at the fourth selection step.

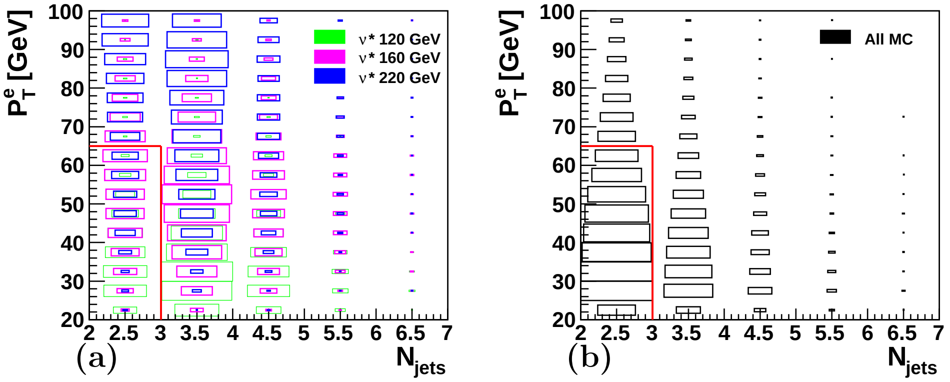

Figure 6.24: Distribution of e^* events with different masses (a) and of all SM expectation (b) in the (N_{jets}, P_T^e) plane, where N_{jets} is the number of jets in each event. The boxes are proportional to the number of events obtained in this plane (N_{jets}, P_T^e). The red lines show the rectangular cut: events with $P_T^e > 65$ GeV or $N_{jets} \geq 3$ are selected.

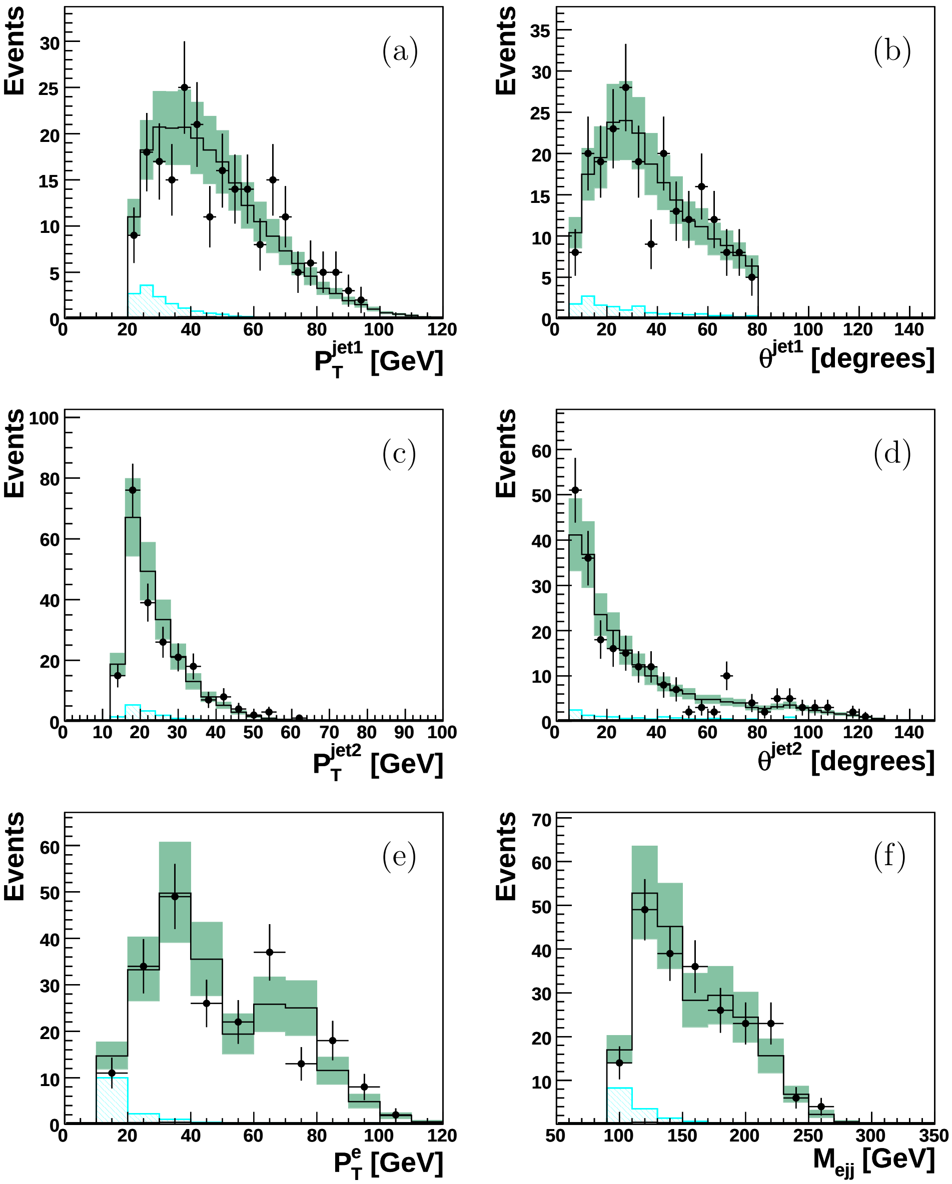

Figure 6.25: Distributions of the transverse momenta (a,c), of the polar angle (b,d) of the two jets, of the transverse momentum of the electron (e) and of the reconstructed ν^* invariant mass M_{ejj} (f), in the final selection step of the $\nu^* \to eW_{\hookrightarrow qq}$ decay channel.

6.4 Leptonic decay channels of Z and W bosons

To complete the previous ν^* searches in hadronic W or Z decay channels, possible final states resulting from the Z or W bosons leptonic decays will be considered in this section.

6.4.1 The $\nu^* \to \nu Z_{\hookrightarrow ee}$ and $\nu^* \to eW_{\hookrightarrow e\nu}$ channels

The signatures of the $\nu^* \to \nu Z_{\hookrightarrow ee}$ and $\nu^* \to eW_{\hookrightarrow e\nu}$ channels are similar. They consist of at least two electrons $e1, e2$ and an undetected neutrino ν, leading to large missing transverse momentum.

The main sources of background in these channels are:

- NC DIS processes: background from NC DIS events may arise if the hadronic energy is wrongly measured in the detector, creating fake P_T^{miss}.
- W production processes: the topology of ν^* decays is similar to events from W production, where an electron and a neutrino are coming from the W boson decay.
- Elastic QED Compton and $\gamma\gamma \to l^+ l^-$ processes: elastic QED Compton events can be selected if wrong energy measurement of the two electromagnetic clusters creates fake P_T^{miss}.

The selection cuts of the $\nu^* \to \nu Z_{\hookrightarrow ee}$ and $\nu^* \to eW_{\hookrightarrow e\nu}$ channels are summarized in tables 6.5 and 6.6, respectively. These analyses start from a sample of di-electrons events:

- the two electromagnetic clusters are detected in the polar angle range: $5° < \theta^{e1,e2} < 150°$, their transverse momentum $P_T^{e1,e2}$ is required to be larger than 10 GeV and 5 GeV, respectively.
- the longitudinal momentum balance $E - P_z$ should be lower than 55 GeV to reduce the background from NC DIS events.

With these requirements, 4969 candidate events are found in the data, compared to a SM expectation of 4967 ± 1033 events, which mainly arise from NC DIS and elastic QED Compton processes. The data events are well described by the SM expectation. Figure 6.26 shows the distributions of the transverse momentum and of the polar angle of these two electrons. The reconstructed invariant mass of the two electromagnetic clusters associated to a possible Z boson decay for the $\nu^* \to \nu Z_{\hookrightarrow ee}$ decay is presented in figure 6.27 (a), and that of the neutrino and of one of the electromagnetic cluster associated to a possible W boson decay for the $\nu^* \to eW_{\hookrightarrow e\nu}$ are presented in figure 6.27 (b).

Step		Selection criteria
1	$N_e \geq 2$	$E - P_z < 55$ GeV $P_T^{e1,e2} > 10, 5$ GeV, $5° < \theta^{e1,e2} < 150°$
2	if $\theta^{e1,e2} > 35°$	$P_T^{e1,e2} > 20, 15$ GeV, $5° < \theta^{e1,e2} < 100, 120°$ $N_{DTNV\|\|DTRA\|\|LW} > 0$
3		$P_T^{miss} > 20$ GeV
Final		$\|M_{ee} - M_Z\| \leq 10$ GeV

Step	Data	MC	NC DIS	W	$e\gamma$	$\gamma\gamma \rightarrow l^+l^-$	Other SM
1	4969	4967 ± 1033	3487	2	1061	392	25
2	51	58 ± 9	29	0.44	4	24	0.57
3	1	1.03 ± 0.14	0.42	0.4	0.05	0.2	0.03
Final	0	0.19 ± 0.05	0.09	0.07	0.01	0.02	0

Table 6.5: Summary of the selection criteria, and observed and predicted event yields for the $\nu^* \rightarrow \nu Z_{\hookrightarrow ee}$ decay channel. The errors on the prediction include model uncertainties and experimental systematic errors added in quadrature.

Step		Selection criteria
1	$N_e \geq 2$	$E - P_z < 55$ GeV $P_T^{e1,e2} > 10, 5$ GeV; $5° < \theta^{e1,e2} < 150°$
2	if $\theta^{e1,e2} > 35°$	$P_T^{e1,e2} > 20, 15$ GeV; $5° < \theta^{e1,e2} < 100, 120°$ $N_{DTNV\|\|DTRA\|\|LW} > 0$
3		$P_T^{miss} > 20$ GeV, $\xi^e > 29$ GeV
Final		$M_{e\nu} \geq M_W - 20$ GeV

Step	Data	MC	NC DIS	W	$e\gamma$	$\gamma\gamma \rightarrow l^+l^-$	Other SM
1	4969	4967 ± 1033	3487	2	1061	392	25
2	51	58 ± 9	29	0.44	4	24	0.56
3	1	0.92 ± 0.1	0.36	0.34	0.04	0.15	0.03
Final	0	0.7 ± 0.11	0.32	0.26	0.04	0.06	0.02

Table 6.6: Summary of the selection criteria, and observed and predicted event yields for the $\nu^* \rightarrow eW_{\hookrightarrow e\nu}$ decay channel. The errors on the prediction include model uncertainties and experimental systematic errors added in quadrature.

Only events with high transverse momenta electromagnetic clusters ($P_T^{e1,e2} > 20, 15$ GeV) and detected in the polar angle ranges $5° < \theta^{e1,e2} < 100°, 120°$ are selected. The effects on the ν^* signal and on the SM background of the cuts on $\theta^{e1,e2}$ are displayed in figures 6.26 (b,d). The restriction to the forward region for the detection of the highest P_T electromagnetic cluster allows to reduce the NC DIS background. In addition, to suppress the background from QED Compton processes, a track has to be associated to each electromagnetic cluster in the central region

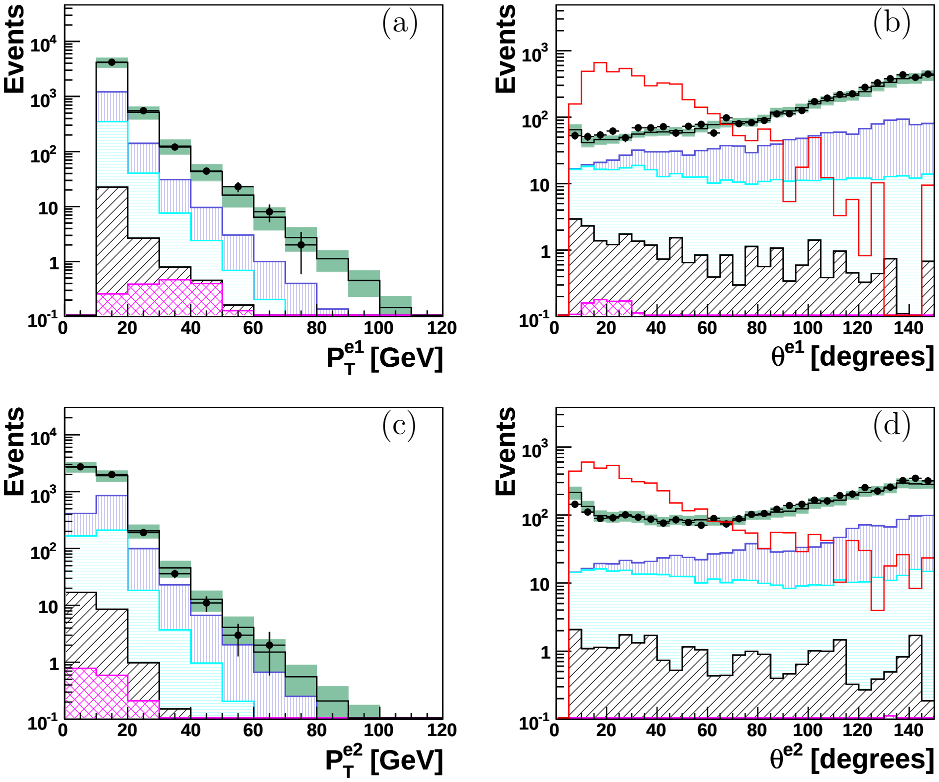

Figure 6.26: Distributions of the transverse momentum (a,c), polar angle (b,d) of the two electrons at the first selection step in both $\nu^*\!\rightarrow\!\nu Z_{\hookrightarrow ee}$ and $\nu^*\!\rightarrow\!eW_{\hookrightarrow e\nu}$ channels.

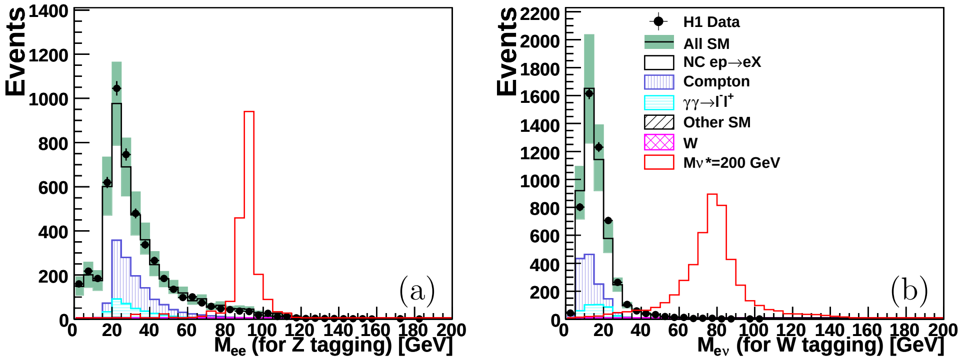

Figure 6.27: Distributions of the di-electrons invariant mass for Z tagging for the $\nu^*\!\rightarrow\!\nu Z_{\hookrightarrow ee}$ channel (a) and for W tagging for the $\nu^*\!\rightarrow\!eW_{\hookrightarrow e\nu}$ channel (b), for candidate events passing the first selection step.

($\theta^{e1,e2} > 35°$). To ensure the presence of an undetected neutrino in the final state, a missing transverse momentum P_T^{miss} greater than 20 GeV is required. The effect on the ν^* signal and on the SM background of this cut is displayed in figure 6.28. Only one candidate event is found in the data after these requirements. The expectation from SM processes is 1.03 ± 0.14 events.

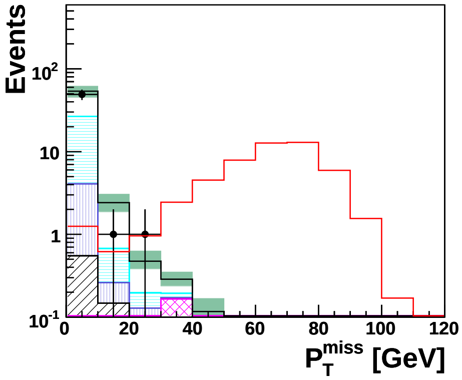

Figure 6.28: Distribution of the missing transverse momentum P_T^{miss} for the event sample of the two high transverse momentum electrons detected in the polar angle in range $5° < \theta^{e1,e2} < 100°, 120°$ and having a track associated to each of them in the central region of the detector.

The separation between $\nu^* \to \nu Z_{\hookrightarrow ee}$ and $\nu^* \to e W_{\hookrightarrow e\nu}$ is now done using the invariant mass of the two electrons M_{ee} or the invariant mass of the neutrino four-vector and one of the electrons $M_{\nu e}$. Events with $|M_Z - M_{ee}| < 10$ GeV are associated to the $\nu^* \to \nu Z_{\hookrightarrow ee}$ channel and other events are associated to the $\nu^* \to e W_{\hookrightarrow e\nu}$ channel, if $M_{e\nu} > M_W - 20$ GeV. Additionally, in the $\nu^* \to e W_{\hookrightarrow e\nu}$ channel the variable ξ^e defined from the highest P_T electron is required to be above 29 GeV.

Finally, no data candidate is found in both channels, compared to SM expectations of 0.19 ± 0.05 and of 0.7 ± 0.1 in the Z and W leptonic decay channels, respectively. Tables 6.5 and 6.6 summarize the observed and expected event yields at each selection step for the Z and W bosons leptonic decay channels, respectively. The selection efficiency for ν^* events is ~45% for masses ν^* ranging from 100 to 300 GeV in both channels.

6.4.2 The $\nu^* \to e W_{\hookrightarrow \mu\nu}$ channel

The signature of the $\nu^* \to e W_{\hookrightarrow \mu\nu}$ channel consists of at least one electron, one muon and an undetected neutrino, leading to a large missing transverse momentum P_T^{miss}. The main sources of background in this channel come from $\gamma\gamma \to l^+ l^-$, NC DIS and W production processes.

The selection cuts are summarized in table 6.7. The analysis starts from a sample of multi-lepton events containing at least one electromagnetic cluster and one muon and satisfying the following conditions:

- the electromagnetic cluster is detected in the polar angle range $5° < \theta^e < 150°$. Its transverse momentum P_T^e is required to be larger than 10 GeV.
- the muon is detected in the polar angle range $10° < \theta^\mu < 160°$. Its transverse momentum P_T^μ is required to be larger than 5 GeV. In addition, this muon must be isolated from the nearest good track by $D^\mu_{track} > 0.5$ in the $(\eta - \phi)$ plane.

With these requirements, 190 candidate events are found in the data, compared to a SM expectation of 163 ± 24 events which is dominated by NC DIS and $\gamma\gamma\rightarrow\mu^+\mu^-$ processes. Figure 6.29 shows the distributions of the transverse momentum and of the polar angle of the electromagnetic cluster and muon for events selected at the first step. A good agreement between data and MC is observed in these distributions.

Step		Selection criterias
1		$E - P_z < 55$ GeV
	$N_e \geq 1$	$P_T^e > 10$ GeV, $\theta^e > 5°$
	$N_\mu \geq 1$	$P_T^\mu > 5$, $5° < \theta^\mu < 160°$; $D_{jet}^\mu > 1$,$D_{track}^\mu > 0.5$
2		$P_T^e > 20$ GeV, $P_T^\mu > 10$; $\xi^e > 9$ GeV
		$5°, 10° < \theta^{e,\mu} < 100°, 160°$
Final		$P_T^{miss} > 15$ GeV

Step	Data	MC	NC DIS	W	$\gamma\gamma$	Other SM
1	190	163 ± 24	95	0.64	66	1.1
2	2	2.29 ± 0.18	0.194	0.16	1.9	0
Final	0	0.4 ± 0.04	0.03	0.15	0.22	0

Table 6.7: In the first table, summary of selection criteria in the $\nu^*\rightarrow eW_{\hookrightarrow\mu\nu}$ decay channel. In the second table, observed and predicted event yields for this decay channel. The errors on the prediction include model uncertainties and experimental systematic errors added in quadrature.

Since we are looking for electron and muon resulting from the de-excitation of an excited neutrino, only events with high transverse momenta leptons ($P_T^{e,\mu} > 20, 10$ GeV) are selected. The electromagnetic cluster and the muon have to be detected in the polar angle ranges $5° < \theta^e < 100°$ and $10° < \theta^\mu < 160°$, respectively. The NC DIS background contribution is reduced by requiring $\xi^e > 9$ GeV. After the second selection step, 2 events are found in the data, compared to a SM expectation of 2.29 ± 0.18 dominated by $\gamma\gamma\rightarrow\mu^+\mu^-$ events.

Finally, as ν^* events must contain an undetected neutrino, a missing transverse momentum P_T^{miss} larger than 15 GeV is required. Figure 6.30 shows the P_T^{miss} distribution before applying a cut on its. After this selection, no candidate event is left, compared to a SM expectection of 0.401 ± 0.04 event. The number of observed and expected events at each selection step are summarized in table 6.7. The selection efficiency for ν^* events is about ∼35% for masses ranging from 100 GeV to 300 GeV

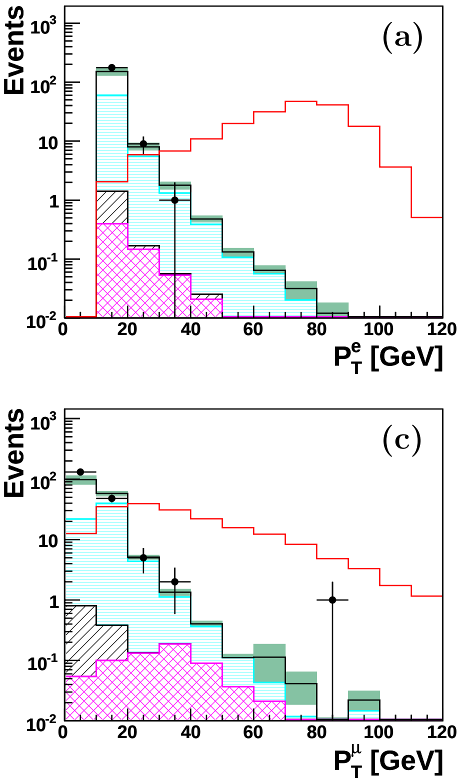

Figure 6.29: Distributions of the transverse momentum and polar angle of the electromagnetic cluster (a,b) and muon (c,d) for the sample of multi-lepton events after the first selection step in the $\nu^* \to eW_{\hookrightarrow \mu\nu}$ channel.

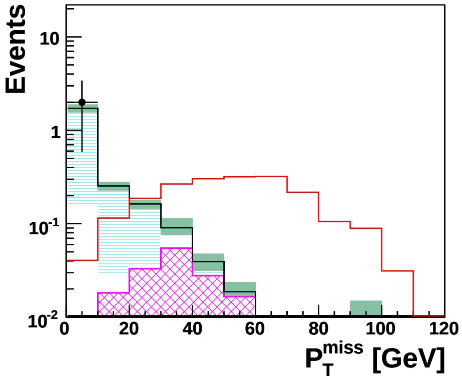

Figure 6.30: Distribution of the missing transverse momentum P_T^{miss} of multi-lepton events with high $P_T^{e,\mu}$ (step 2).

6.5 Result of the ν^* search

6.5.1 Summary of systematic uncertainties

In all plots presented in this chapter the error bands on the SM expectation include model and experimental uncertainties added in quadrature. The sources of systematical errors relevant for the search for excited neutrino are summarized in section 5.5.1. In addition, a systematic uncertainty on the photon identification of 10% is taken into account. The theoretical uncertainty on the ν^* production cross section is dominated by the uncertainty on the scale at which the proton parton densities are evaluated. It was estimated by varying this scale from $\sqrt{Q^2}/2$ to $2\sqrt{Q^2}$. The resulting uncertainty is 10% at $M_{\nu^*} = 100$ GeV, increasing to 30% at $M_{\nu^*} = 300$ GeV.

6.5.2 Summary of results for the ν^* search

The table 6.8 summarizes the data event yields compared to the total SM expectation for each analyzed decay channel of the excited electron search. The selection criteria used in the different channels prevent against double counting of candidate events between channels. The selection efficiencies for the different decay modes for masses M_{ν^*} between 120 and 300 GeV are also indicated. The distribution of the invariant mass of the data events are in agreement with those of the expected SM background as shown in figure 6.31. In each analyzed decay channel, a good agreement between data event yields and SM expectations is observed. No data events are observed in the channels corresponding to leptonic decays of the W or Z bosons, in agreement with the low SM expectations. No significant deviation from the SM prediction is found in the searches. The selection efficiencies for the different decay modes for masses M_{ν^*} between 120 GeV and 300 GeV are shown in figure 6.32. The total reconstructed width of ν^* mass distribution for the three decay channel, $\nu^* \to \nu\gamma$, $\nu^* \to \nu Z$ and $\nu^* \to eW$ are shown in figure 6.33 as a function of the ν^* mass.

Search for ν^* at HERA (e^-p, 184 pb^{-1})			
Channel	Data	All SM	Signal Efficiency [%]
$\nu^* \to \nu\gamma$	7	12.3 ± 3	50 − 55
$\nu^* \to \nu Z_{\hookrightarrow qq}$	89	95 ± 21	25 − 55
$\nu^* \to eW_{\hookrightarrow qq}$	220	223 ± 47	40 − 65
$\nu^* \to \nu Z_{\hookrightarrow ee}$	0	0.19 ± 0.05	45
$\nu^* \to eW_{\hookrightarrow e\nu}$	0	0.70 ± 0.1	45
$\nu^* \to eW_{\hookrightarrow e\mu}$	0	0.40 ± 0.05	35

Table 6.8: Observed and predicted event yields for the analyzed decay channels. The analyzed data sample corresponds to an integrated luminosity of 184 pb^{-1}. The errors on the prediction include model uncertainties and experimental systematic errors added in quadrature. The selection efficiencies for the different ν^* decay modes for masses M_{ν^*} between 100 and 300 GeV are also indicated.

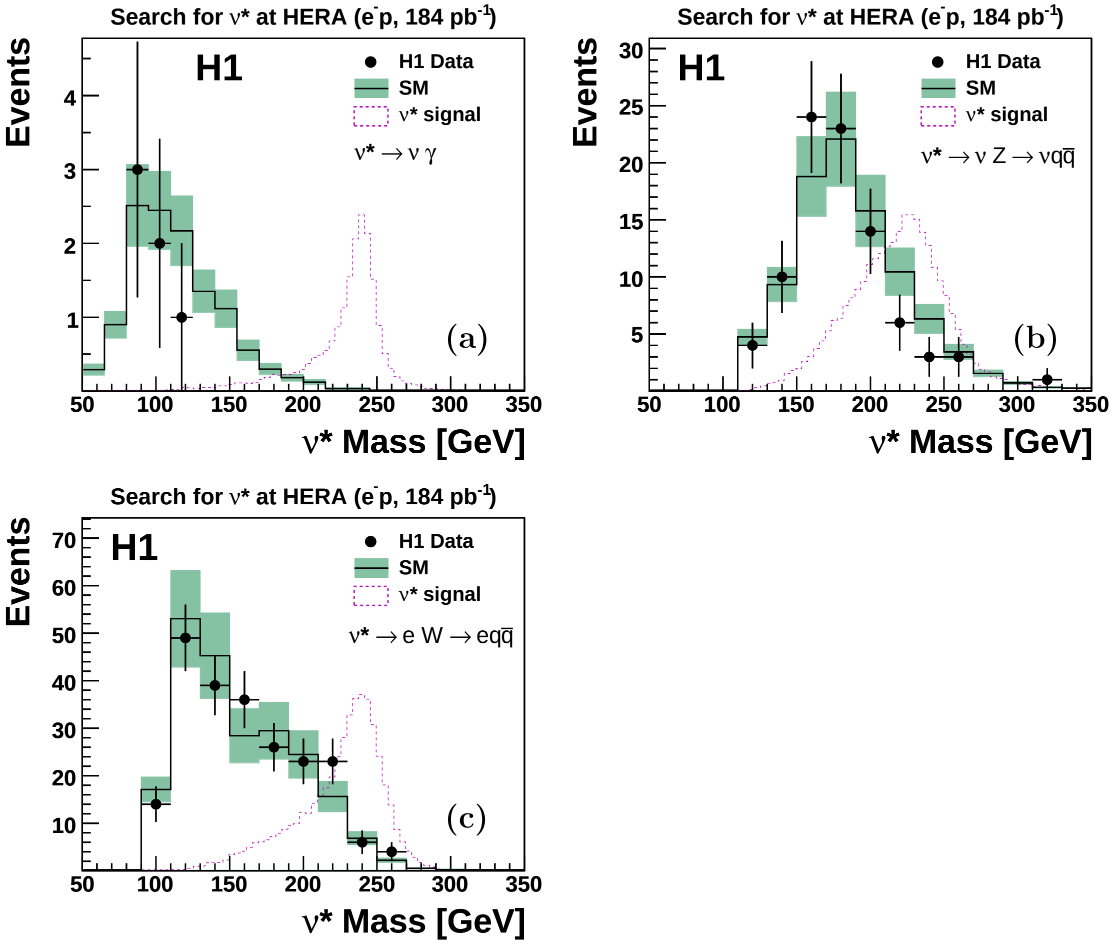

Figure 6.31: Invariant mass distribution of the ν^* candidates for the $\nu^*\!\to\!\nu\gamma$ (a), $\nu^*\!\to\!\nu Z_{\hookrightarrow q\bar{q}}$ (b) and $\nu^*\!\to\!eW_{\hookrightarrow q\bar{q}}$ (c) searches. The points correspond to the observed data events and the histogram to the SM expectation after the final selections. The error bands on the SM prediction include model uncertainties and experimental systematic errors added in quadrature. One data event is observed with a reconstructed mass below 30 GeV and therefore does not appear in the figure (a).

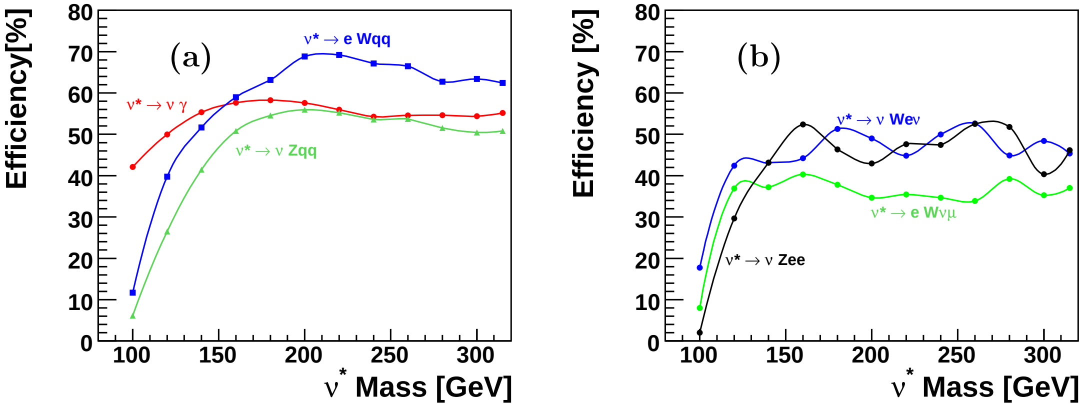

Figure 6.32: Efficiency to select ν^* events in each decay channel for the three main decay channel in (a): $\nu^* \to \nu\gamma$, $\nu^* \to eW_{\hookrightarrow qq}$ and $\nu^* \to \nu Z_{\hookrightarrow qq}$ decay channel; for the leptonic decay channels of the Z or W bosons in (b): $\nu^* \to \nu Z_{\hookrightarrow ee}$, $\nu^* \to eW_{\hookrightarrow e\nu}$ and $\nu^* \to eW_{\hookrightarrow \mu\nu}$.

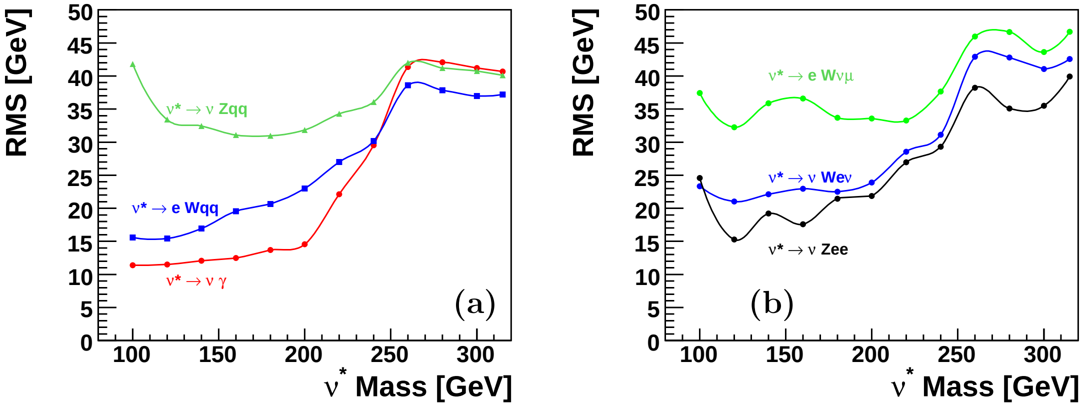

Figure 6.33: Width of the reconstructed ν^* masses as a function of the excited neutrino generated mass: for the three main decay channels (a): $\nu^* \to \nu\gamma$, $\nu^* \to eW_{\hookrightarrow qq}$, $\nu^* \to \nu Z_{\hookrightarrow qq}$ (red, blue and green curves); for the leptonic decay channels of the Z and W boson: $\nu^* \to \nu Z_{\hookrightarrow ee}$, $\nu^* \to eW_{\hookrightarrow e\nu}$ and $\nu^* \to eW_{\hookrightarrow \mu\nu}$.

Chapter 7

Interpretation of Results

Searches for excited electron and neutrino in almost all decay channels have been performed using the full *ep* data sample collected by the H1 experiment. Total number of predicted background events have been compared to the number of candidate events observed in the data. They are in good agreement for each searched topology and no evidence for the production of excited electrons or excited neutrinos is observed. This result does not allow to absolutely exclude the existence of excited lepton but only to say that they are not where we were looking for. We must therefore extract upper limits on the e^* or ν^* production cross sections and on model parameters used to perform our search.

In this chapter, the limit calculation method used will be first summarized. Then upper limits on the model parameters will be derived for both excited electron and excited neutrino searches. The limits obtained for e^* and ν^* production will be compared to existing constraints from other colliders.

7.1 Limit calculation

From the level of agreement between data and MC which is observed in our final selections, we can determine the maximum number of excited lepton (l^*) events N_{lim} which may be hidden in the data if we assume that our data contain both l^* and SM background events. This number N_{lim} depends on the number of observed data events, the total number of background events expected from MC simulations and the selection efficiency to l^* events.

In order to maximize the visible branching ratio of potential e^* or ν^* signals, results from all investigated decay channels need to be combined. For this limit calculation, the Modified Frequentist Method, as implemented in [74], is used. It provides a robust way of combining individual channels while incorporating also systematics uncertainties. Basic concepts of the Modified Frequentist Method will be first introduced. Then the technical implementation used for this analysis will be presented.

7.1.1 The Likelihood ratio

To discriminate signal-like outcomes from background-like outcomes of a search with n independent channels we have to define a test statistic X. The Likelihood ratio is a good choice for such a test statistic [75]. The Likelihood ratio is defined for each channel as the ratio of the probabilities of observing exactly that outcome, assuming a signal and background ($s + b$) hypothesis and a background only (b) hypothesis. If N is the total number of signal events, the expected number of signal events in the selection channel i is given by $s_i = N.(\epsilon\beta)_i$, where $(\epsilon\beta)_i$ is the total visible branching ratio of this selection channel.

The Likelihood ratio of the selection channel i can be written as the ratio of Poisson probabilities

$$X_i = \frac{e^{-(s_i+b_i)}(s_i + b_i)^{d_i}}{d_i!} / \frac{e^{-b_i} b_i^{d_i}}{d_i!}\,, \tag{7.1}$$

where b_i and d_i are the number of expected background events and the number of observed data candidates of this channel i, respectively.

For a set of n channels, the Likelihood ratio is given by the product of the ratios of the independent channels:

$$X = \prod_{i=1}^{n} X_i\,. \tag{7.2}$$

This choice of a test statistic can be used to determine a confidence level (CL).

7.1.2 Confidence Level

By definition, the confidence level for excluding the possibility of the simultaneous presence of a signal (new particle production or interaction) and background is the probability that the test statistic X be less than or equal to the one observed in the data, X_{obs}. This probability is given by a sum of Poisson probabilities:

$$CL_{s+b} = P_{s+b}\ (X \le X_{obs}) = \sum_{X(\{d'_i\}) \le X(\{d_i\})} \prod^{n} \frac{e^{-(s_i+b_i)}(s_i + b_i)^{d'_i}}{d'_i!}\,, \tag{7.3}$$

where $X(\{d_i\})$ is the test statistic for the observed set of candidates in each channel $\{d_i\}$. The sum runs over all possible final outcomes $\{d'_i\}$ which lead to a test statistic less or equal to the one observed in the data. The signal+background hypothesis can then be excluded at the 95% CL if $CL_{s+b} = 0.05$, and at more than 95% CL if $CL_{s+b} < 0.05$.

This way, the quantity $(1 - CL_{s+b})$ can be used to set exclusion limits but it has the property that a search with downward fluctuating background will set strong exclusion limits, simply because the observed outcome was determined to be unlikely in any case. To correct for this effect, the confidence level for the background alone hypothesis must be calculated by:

$$CL_b = P_b\ (X \le X_{obs}), \tag{7.4}$$

where the probability sum assumes the presence of background only.

Then the quantity:

$$CL_s = \frac{CL_{s+b}}{CL_b} = \frac{P_{s+b}\ (X \leq X_{obs})}{P_b\ (X \leq X_{obs})}\ , \tag{7.5}$$

is defined as the modified frequentist confidence level [74]. An upper limit N_{lim} on the number of signal events is set such that $CL_s \leq 0.05$ for $N \geq N_{lim}$.

Systematic errors are treated as uncertainties on the expected numbers of signal and background events. A generalization of the method proposed by Cousins and Highland [76] is used. During the limit calculation, s_i and b_i are chosen randomly within their uncertainties which are assumed to follow Gaussian distributions, leading to a smearing of probabilities and test statistics.

7.1.3 Technical implementation

For final limit calculations, we want to calculate the evolution of the number N_{lim} as a function of the mass l^* of a potential excited lepton. For this purpose, signal events of excited leptons are generated with high statistic for different generated masses M_{l^*}, spaced by 20 GeV. From these signal samples, the evolution of the signal efficiency selection ϵ can be calculated for each M_{l^*} (as shown in figures 5.34, 5.35 and 6.33, 6.34 for e^* and ν^* decay channels, respectively).

By a linear interpolation between the reconstructed mass distributions of each generated sample [77], we can also deduce the reconstructed mass distribution of the signal, for any generated M_{l^*} mass. This complete mass spectra is used for the limit calculation.

For each bin i of the reconstructed mass distributions, s_i, b_i and d_i values are calculated. For a given M_{l^*} mass, the limit number N_{lim} is then calculated by combining together all bin i from all decay channels using formula (7.3). The calculation is done for M_{l^*} varying from 100 GeV to 300 GeV in 1 GeV steps.

This procedure allows to take into account the complete spectra of the reconstructed mass distribution of the signal. This is especially important for excited neutrinos where very broad reconstructed mass distributions can be observed for high ν^* masses.

7.2 Limits on e^* production

In the following, upper limits on cross section of excited electron production and on the coupling constant f/Λ will be derived under the assumption of a pure gauge mediated production and decay. The limits obtained will be compared to existing constraints from other colliders. In the second part, an upper limit on $1/\Lambda$ will also be derived assuming for the first time possible e^* production by both gauge and contact interactions together.

7.2.1 Limits on cross section

The upper limit N_{lim} on the number of events coming from an excited lepton decay can be calculated at a given CL using the modified frequentist approach. In summary, the following quantities enter in the limit calculation:

- the number of events observed in the data,
- the corresponding number of events expected from SM background processes,
- the signal efficiencies for the different excited lepton masses,
- the uncertainties on the signal efficiencies and on the number of background events.

The values of N_{lim} obtained as a function of the excited lepton mass (M_{l^*}) is then translated into on upper limit on the excited lepton production cross section times their branching ratio $(\sigma\times BR)_{lim}$ which is given by:

$$(\sigma\times BR)_{lim} = \frac{N_{lim}}{\mathcal{L}}, \tag{7.6}$$

where $\mathcal{L}$ is the integrated luminosity of the analyzed data sample.

In the search for excited electron, all HERA data from 1994 up to mid-2007 with different center-of-mass energy ($\sqrt{s} = 301$ GeV and $\sqrt{s} = 319$ GeV) and also with different collision modes (e^-p and e^+p) have been used. Therefore, the combination of all data periods, has a mean center-of-mass energy of $\sqrt{s} = \sim 318$ GeV, very close to $\sqrt{s} = 319$ GeV. The derived upper limit on the product of the excited electron cross section and of the branching ratio $(\sigma\times BR)$ corresponds to this mean center-of-mass energy $\sqrt{s} = 318$ GeV.

The upper limits on $(\sigma\times BR)$ obtained for each gauge decay channel are presented in figure 7.1. The separate decay channels of the W and Z bosons are combined.

7.2.2 Limits on the gauge coupling parameter f/Λ

The upper limits on the product of the cross section σ and of the branching ratio of excited leptons production are used to constrain values of the ratio of the coupling constant to the compositeness scale, f/Λ. As discussed in section 2.6.1, fixed numerical relations between f and f' can be assumed. Here, the conventional assumption $f = +f'$ is used. The cross section then only depends on f/Λ and the mass of the excited lepton. Therefore, the limit on f/Λ can be calculated as:

$$\left(\frac{f}{\Lambda}\right)_{lim} = \sqrt{\frac{(\sigma\times BR)_{lim}}{(\sigma_{th}\times BR)_{fixed}}}\left(\frac{f}{\Lambda}\right)_{fixed}, \tag{7.7}$$

where $(\sigma\times BR)_{lim}$ is the upper limit on the product of the cross section and of the branching ratio calculated in the previous section. $(\sigma_{th}\times BR)_{fixed}$ is the theoretical

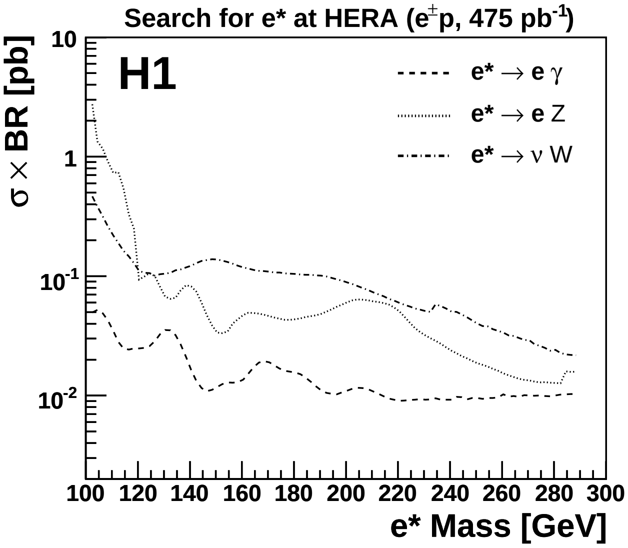

Figure 7.1: Upper limits at 95% CL on the product of the e^* production cross section σ and of the decay branching ratio BR for the excited electron at $\sqrt{s} = 318$ GeV in the different electroweak decay channel $e^*\rightarrow e\gamma$, $e^*\rightarrow eZ$ and $e^*\rightarrow\nu W$ as a function of the e^* mass. The separate decay channels of the W and Z bosons are combined. Areas above the curves are excluded.

cross section calculated using a fixed coupling $\left(\frac{f}{\Lambda}\right)_{fixed}$. Values of $f = 1$ and $\Lambda =$ 1 TeV have been used.

In the case of the e^* search, to combine the different data sets with different center-of-mass energies and collision modes, an effective e^* cross section σ_{th} is calculated as:

$$\sigma_{th} = \frac{\sigma_{301}^{e^+p}\mathcal{L}_{301}^{e^+p} + \sigma_{319}^{e^-p}\mathcal{L}_{319}^{e^-p} + \sigma_{319}^{e^+p}\mathcal{L}_{319}^{e^+p}}{\mathcal{L}_{301}^{e^+p} + \mathcal{L}_{319}^{e^+p} + \mathcal{L}_{319}^{e^-p}} \tag{7.8}$$

where $\sigma_{301}^{e^+p}$, $\sigma_{319}^{e^-p}$, $\sigma_{319}^{e^+p}$ are the e^* production cross section in e^+p at $\sqrt{s} = 301$ GeV, in e^-p at $\sqrt{s} = 319$ GeV and in e^+p at $\sqrt{s} = 319$ GeV, respectively. $\mathcal{L}_{319}^{e^+p}$, $\mathcal{L}_{319}^{e^-p}$ are the total integrated luminosities of the data collected at center-of-mass energies of 319 GeV for different collision modes e^+p, e^-p, respectively. $\mathcal{L}_{301}^{e+p}$ is the total integrated luminosity of the sample recorded at $\sqrt{s} = 301$ GeV.

The resulting upper limits on f/Λ for each separate decay channel and after the combination of all decay channels are displayed in figure 7.2, where the dotted curves correspond to the expected limits and the dashed curves correspond to the observed limits. The agreement between the expected and observed limits is satisfactory. The limit on f/Λ after combination of all decay channels is dominated by the $e^*\rightarrow e\gamma$ radiative decay at low e^* mass, while the $e^*\rightarrow\nu W$ channel starts to contribute to the limit for e^* masses above 220 GeV. For this result, the limit calculation is stopped at $M_{e^*} = 290$ GeV, as for higher e^* masses the decay width of the e^* resonance is larger than the experimental resolution (typically $10-20$ GeV). Figure 7.3 presents the evolution of the e^* decay width for f/Λ values along the final limit.

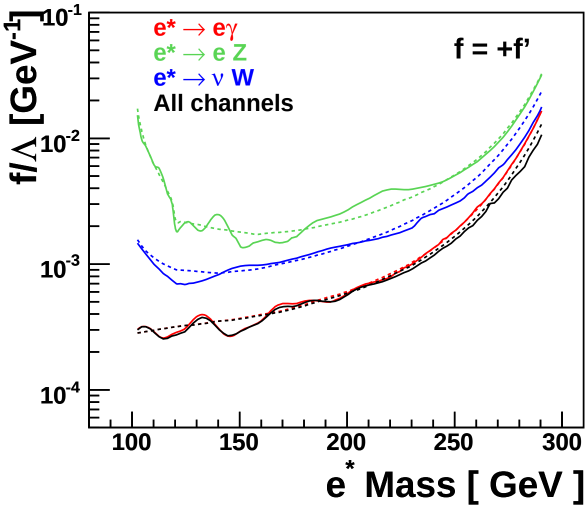

Figure 7.2: Exclusion limits on the coupling f/Λ at 95% CL as a function of the mass of the excited electron with the assumption $f = +f'$. The upper limits on f/Λ are displayed separately for each decay channel and after the combination of all decay channels. The dashed curves correspond to the expected upper limits and the plain curves to the observed upper limits. Areas avobe the curves are excluded.

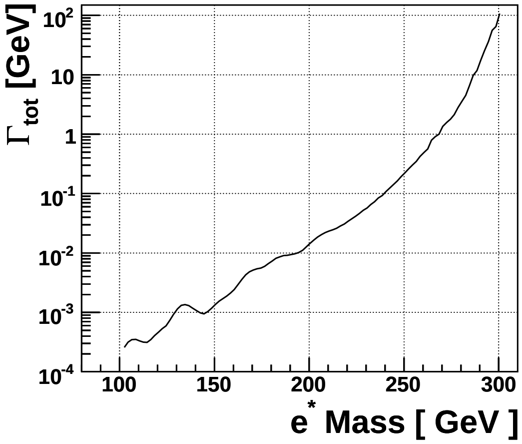

Figure 7.3: Evolution of the e^* width for f/Λ values along the final limit.

7.2.3 Comparison with existing constraints

Constraints on f/Λ obtained in other e^* searches performed at different colliders are reviewed here and compared to our present result.

Previous e^* searches have been performed by the H1 Collaboration [78] and the ZEUS Collaboration [79] using HERA-I data. In the case of e^* production via gauge interactions only, using the assumptions $f/\Lambda = 1/M_{e^*}$ and $f = +f'$, e^* with masses up to 250 GeV and 228 GeV have been excluded in previous H1 and ZEUS analyses, respectively. The limit obtained by H1 with HERA-I data is displayed in figure 7.4. The present result extends nearly up to the HERA kinematic limit and improves by more than a factor of two the bounds previously obtained by H1 and ZEUS using only HERA-I data. Considering the assumption $f/\Lambda = 1/M_{e^*}$ and $f = +f'$, excited electrons with masses up to 272 GeV are now excluded.

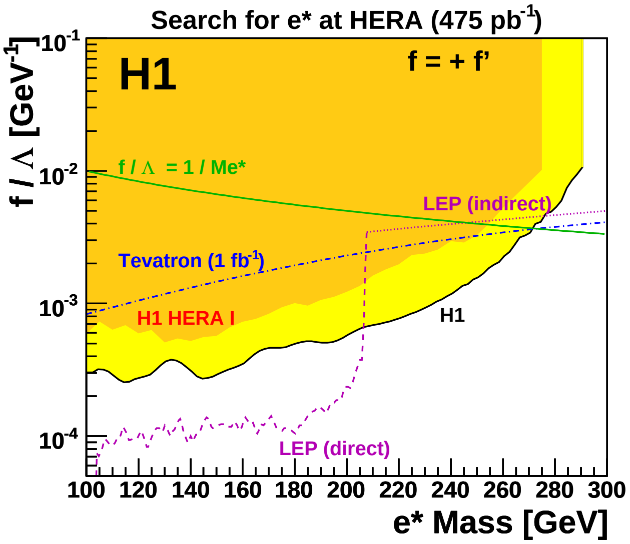

Figure 7.4: Exclusion limits on the coupling f/Λ at 95% CL as a function of the mass of the excited electron with the assumption $f = +f'$. The observed limits from this analysis is represented by the yellow area. Values of the couplings above the curves are excluded. The orange-dark area corresponds to the domain excluded by previous H1 result [78], using HERA-I data. The most stringent exclusion limit from LEP experiments is presented by the violet line, for direct search by the OPAL collaboration [81] and for indirect search by the DELPHI collaboration [82]. The recent result from the D0 experiment [84] is also shown (blue dotted line).

Excited electrons have also been searched in electron-positron collisions at LEP. In e^+e^- collisions, e^* could be singly produced or pair produced. Searches for pair-produced e^* are independent of the coupling f/Λ but are limited to masses lower than $\sqrt{s}/2$. Excited electrons with masses below ∼103.2 GeV have been excluded at LEP [81]. Only results obtained in searches for e^* single productions can extend to higher e^* masses. Only these results are thus compared with the present results. Figure 7.5 (a) shows the production mechanism for single excited electron in electron-positron collisions. In addition to the direct search for e^* via pair and single production at LEP, the existence of e^* could be looked for indirectly via deviations from the SM differential cross section of events containing two photons ($e^+e^- \rightarrow \gamma\gamma$). The existence of e^* may alter this cross section via a $e^*e\gamma$ chiral magnetic coupling and creates a deviation from the SM expectation [80]. The strongest direct and indirect limits from LEP have been obtained by the OPAL [81] and DELPHI Collaborations [82], respectively. They are compared to our present limit in figure 7.4. The limit from the present analysis extends at high mass beyond the kinematic reach of LEP searches.

Searches for the existence of excited electrons have been done in $p\bar{p}$ collisions at TEVATRON by both CDF [83] and D0 Collaborations [84]. Figure 7.6 presents the diagram for excited electron production in $p\bar{p}$ collisions. In figure 7.4, the recent

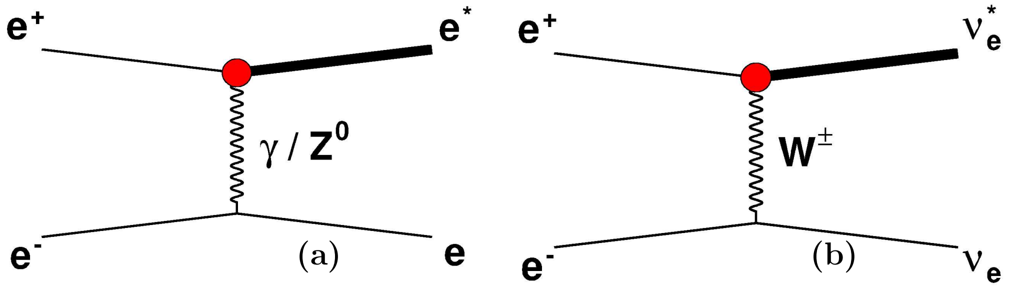

Figure 7.5: Feynman diagrams for the single e^* (a) and ν^* (b) production in e^+e^- collisions, via $t-$channel γ or Z and W bosons exchanges, respectively.

result obtained by the D0 Collaboration using Run-II data corresponding to 1 fb^{-1} is shown. The new H1 limit obtained in this thesis extends to lower f/Λ values than TEVATRON searches.

The limit obtained in this thesis on the search for excited electron production via gauge mediated interactions is currently the most stringent for masses between 203 and 272 GeV.

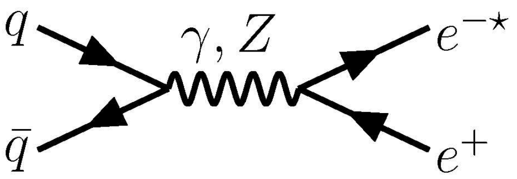

Figure 7.6: Feynman diagram for the excited electron production via $s-$channel γ, Z boson exchange in $p\bar{p}$ collisions at TEVATRON.

7.2.4 Limit on contact interaction

For the first time at HERA, possible e^* production via contact interactions, in addition to the gauge mediated production discussed earlier, have been studied. The production mechanism via contact interaction and the interference with gauge mediated production was discussed in section 2.6.2. Both gauge and contact interaction are considered together for e^* production as well as for e^* decays. The same analysis as used for e^* search considering pure gauge models (see chapter 5) is used here. This analysis only looks for specific GM e^* decays and we will therefore conservatively assume that the efficiency of the analysis to e^* decays via CI is zero.

The selection efficiencies of the analysis to e^* produced via GM only and via CI+GM are compared in figure 7.7, for the two main gauge decay channels $e^* \rightarrow e\gamma$ and $e^* \rightarrow eW_{\hookrightarrow qq}$. We observe that the efficiency for e^* events produced with CI+GM is lower than the efficiency of pure GM events by $\sim 10-15\%$. In fact, e^* events from CI+GM are more inelastic than pure GM events, due to the additional inelastic contribution of contact interaction production. An upper limit on $1/\Lambda$ is derived, under the assumption $f = +f' = 1$, $\eta_L = \eta"_L = 1$ and $\eta_R = 0$. Figure 7.8 presents this limit on $1/\Lambda$ as a function of the e^* mass, compared to the limit on $1/\Lambda$ obtained considering only gauge interactions. For e^* masses below 250 GeV, the additional contribution of CI to e^* production change the limit on Λ by a factor from 1.15 to 1.2. The limit calculated by using both GM and CI models is stopped at $M_{e^*} = 260$ GeV, as after this value, the width of e^* decaying via CI reaches ∼15 GeV.

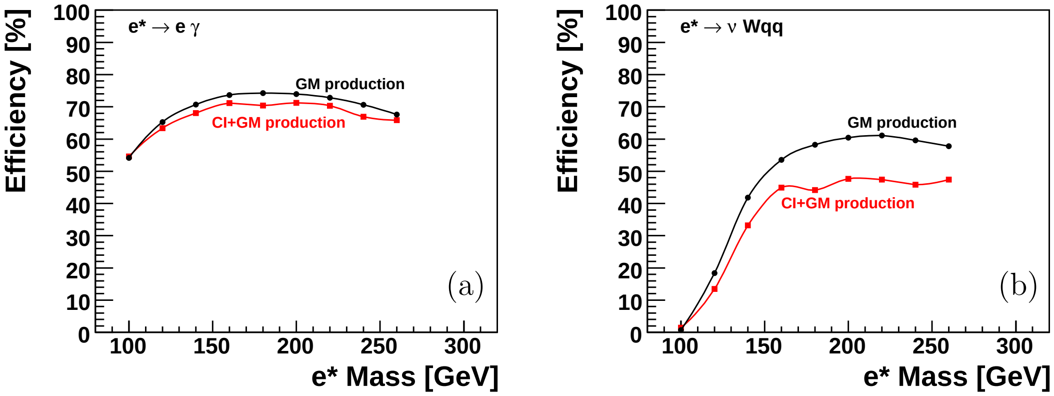

Figure 7.7: Efficiency to select e^* events produced by GM only (black lines) and by CI+GM (red lines) in the two decay channels $e^* \to e\gamma$ (a) and $e^* \to eW_{\hookrightarrow qq}$ (b).

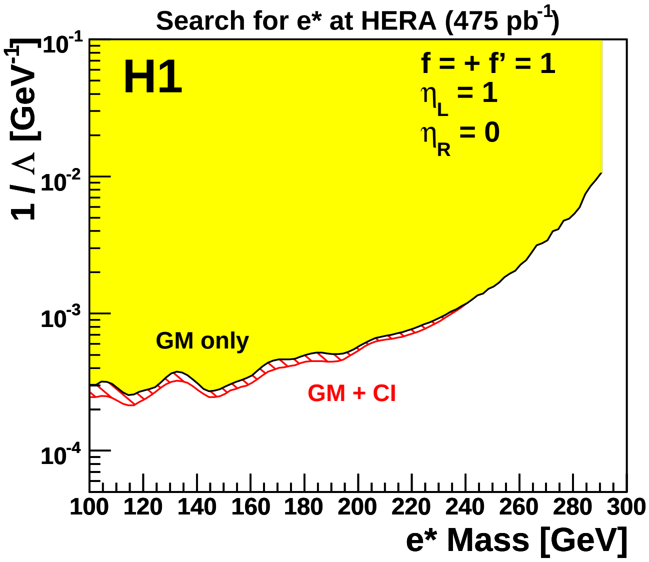

Figure 7.8: Exclusion limits at 95% CL on the inverse of the compositeness scale $1/\Lambda$ as a function of the mass of the excited electron. The excluded domain obtained by considering an e^* production via gauge mediated interactions only and under the assumption $f = +f' = 1$ is represented by the shaded area. The hatched area corresponds to the additional domain excluded if gauge and contact interactions are considered together for e^* production. Areas above the curves are excluded.

The limit on $1/\Lambda$ obtained in this analysis assumes a production via contact and gauge interactions together. At TEVATRON, searches for e^* production via contact and gauge interactions have also been performed by the CDF Collaboration [83] and the D0 Collaboration [84]. In these analyses, a production via CI only was assumed, while both gauge and contact interaction decays were allowed. The possible interference between gauge and contact interactions was therefore neglected at the production in these analyses. Therefore, it is not completely correct to compare our result to those of D0 or CDF.

7.3 Limits on ν^* production

7.3.1 Limit on cross section

The upper limits obtained on the product of the ν^* production cross section and of the ν^* decay branching ratio ($\sigma \times BR$) are presented in figure 7.9 for the three ν^* gauge decay channels. The leptonic and hadronic decay channels of the W and Z bosons are combined.

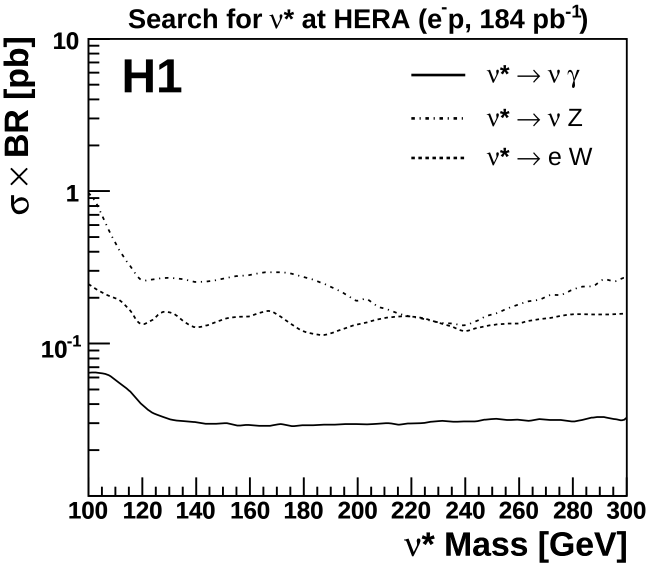

Figure 7.9: Upper limits at 95% CL on the product of the cross section σ and of the decay branching ratio BR in the three decay channels as a function of the excited neutrino mass. The leptonic and hadronic decay channels of the W and Z bosons are combined. Areas above the curves are excluded.

7.3.2 Limits on the coupling parameter f/Λ

For a coupling constant $\frac{f}{\Lambda} = 10^{-3}$ GeV^{-1}, an excited neutrino with a mass around 200 GeV has a width of about 10 GeV (see section 2.6.1). However, for $f/\Lambda = 10^{-3}$ GeV and a ν^* mass larger than 230 GeV, the ν^* width can reach up to a few hundred GeV (see section 2.6.1). Therefore, the narrow width approximation can not be applied for the calculation of the ν^* production cross section and the limit calculation procedure becomes different, as the ν^* production cross section depends also on the ν^* width in this case.

Therefore, for the whole range of ν^* masses the limit calculation is performed using an iterative method. A first limit on f/Λ is calculated and the corresponding ν^* width is calculated. These width and f/Λ values give a new ν^* cross section. From this new cross section, a new limit on f/Λ is derived. The procedure is iterated until the convergence to a certain f/Λ value. The final value gives the limit on f/Λ corresponding to the considered ν^* mass. In addition, for a correct determination of signal efficiencies, ν^* events are generated with f/Λ values corresponding for each ν^* mass to the expected limit in the plane defined by M_{ν^*} and f/Λ.

Figure 7.10 presents the upper limits obtained for each separate ν^* decay channel and the results of the combination of all decay channels, under the two different assumptions $f = -f'$ and $f = +f'$. The expected and observed upper limits are compared and they are in good agreement. The evolution of the ν^* decay width for f/Λ along the expected limit is also presented in figure 7.11. In the case $f = -f'$, the limit on f/Λ is dominated at low ν^* mass by the $\nu^* \to \nu\gamma$ channel, while the $\nu^* \to eW$ channel starts to contribute to the combined limit for ν^* masses above 200 GeV. Under the assumption $f = +f'$, the limit on f/Λ is driven mainly by the $\nu^* \to eW$ channel, as the $\nu^* \to \nu\gamma$ decay mode is forbidden in that case.

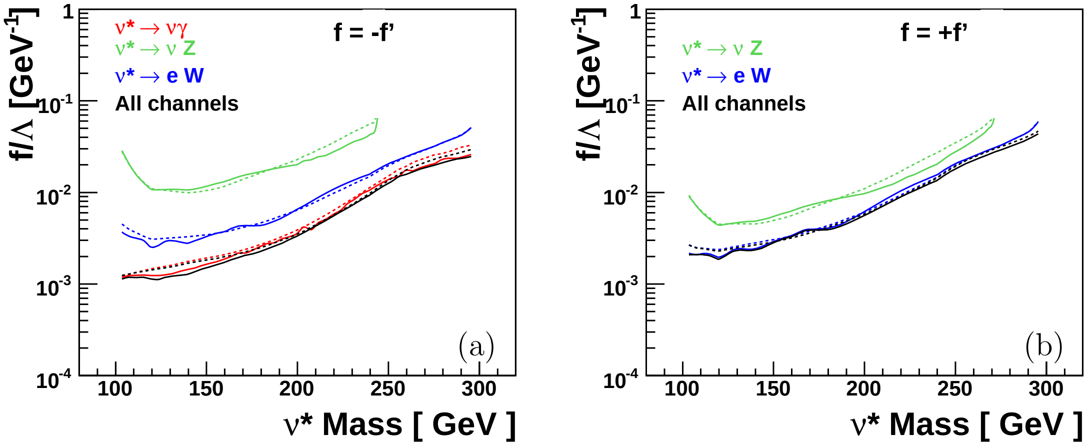

Figure 7.10: Exclusion limits on the coupling f/Λ at 95% CL as a function of the mass of the excited neutrino with two assumptions: $f = -f'$ (a) and $f = +f'$ (b). The upper limits on f/Λ are displayed for each separate decay channel and for the combination of all decay channels. The dashed curves correspond to the expected upper limits and the plain curves to the observed upper limits. Areas above the curves are excluded.

Upper limits obtained previously on ν^* production have been calculated assuming fixed relations between f and f'. However, it is also possible to calculate limits as a function of the ratio f/f', which are therefore less model-dependent. Figure 7.12(a) illustrates how the limits depend on the f/f' ratio as a function of the ν^* mass. At

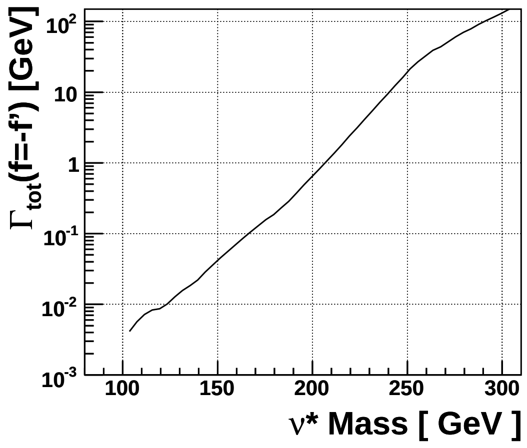

Figure 7.11: Evolution of ν^* width for f/Λ values along the final limit.

HERA the cross section of the excited leptons production depends on the coupling c_{We^*e} or $c_{W\nu^*e}$ which are independent on f'. Therefore, a very large absolute value of ratio f/f' can not really be achieved and this study is then limited to values of the f/f' between -5 and $+5$. Limits which are independent of f/f' can be derived in the range $f/f' = [-5, +5]$ by choosing from the figure 7.12(a) the weakest limit for each mass hypothesis. The limit obtained is presented in figure 7.12(b). This limit is very close to the limit obtained under the assumption $f = +f'$. The present limit for $f/f' = [-5, +5]$ is compared to the same limit, previously obtained by H1 using HERA-I data.

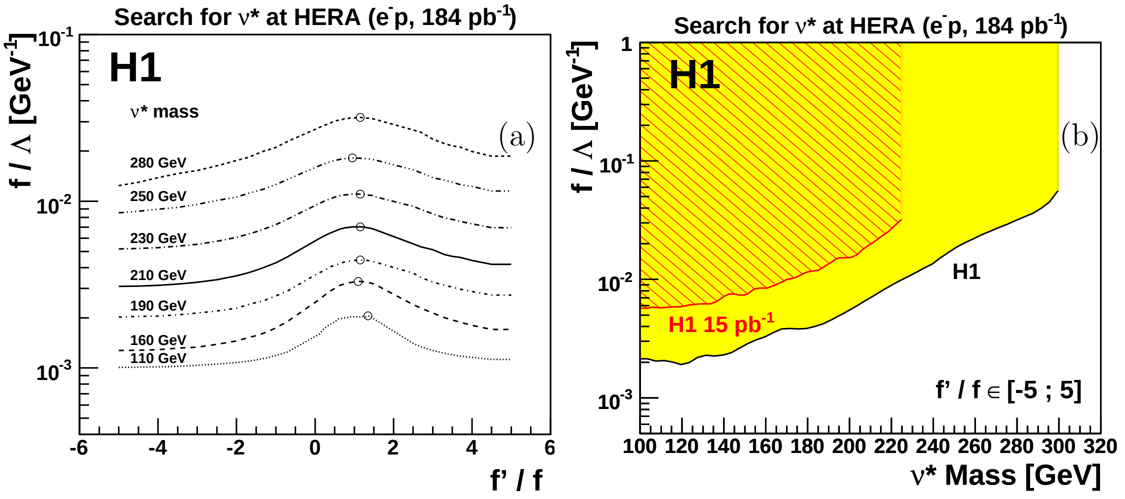

Figure 7.12: Exclusion limits for excited neutrino on the coupling f/Λ at 95% CL as a function of the ratio f/f' (a). Each curve corresponds to a different ν^* mass. The circle indicates the weakest limit for each mass. Exclusion limit at 95% CL on the coupling f/Λ as a function of the mass of the excited neutrino (shaded area) (b). This limit corresponds to the weakest limit on f/Λ for f'/f values in the interval $[-5; +5]$. The hatched area corresponds to the exclusion domain obtained by H1 in a previous analysis [86]. The regions above the lines are excluded.

7.3.3 Comparison with existing constraints

Previous searches for ν^* have been performed by H1 [86] and ZEUS Collaborations [79] using data from the HERA-I running period. Lower limits on the ν^* mass obtained by H1 using only HERA I data, under the assumption $f/\Lambda = 1/M_{\nu^*}$, was 150 GeV (140 GeV) for $f = -f'$ ($f = +f'$). Under the same assumptions, ZEUS excluded ν^* masses up to 158 GeV (135 GeV) for $f = -f'$ ($f = +f'$) using HERA-I data. The limits obtained by H1 with HERA-I data are displayed in figure 7.13. The present results improve significantly the previously published H1 and ZEUS limits. With the assumption $\frac{f}{\Lambda} = 1/M_{\nu^*}$, excited neutrinos with masses up to 213 GeV (196 GeV) are now excluded for $f = -f'$ ($f = +f'$).

Excited neutrinos have also been looked for in electron-positron collisions at LEP. In e^+e^- collisions, ν^* could be singly produced or pair produced. Only results obtained in the case of single production are compared with the present results. Figure 7.5 (b) shows the mechanism of single excited lepton production in electron-positron collisions. The most stringent limits for ν^* searches in e^+e^- collisions at LEP for the two cases $f = -f'$ and $f = +f'$, have been obtained by the L3 [87] and DELPHI Collaborations [88], respectively. These limits are also shown in figure 7.13.

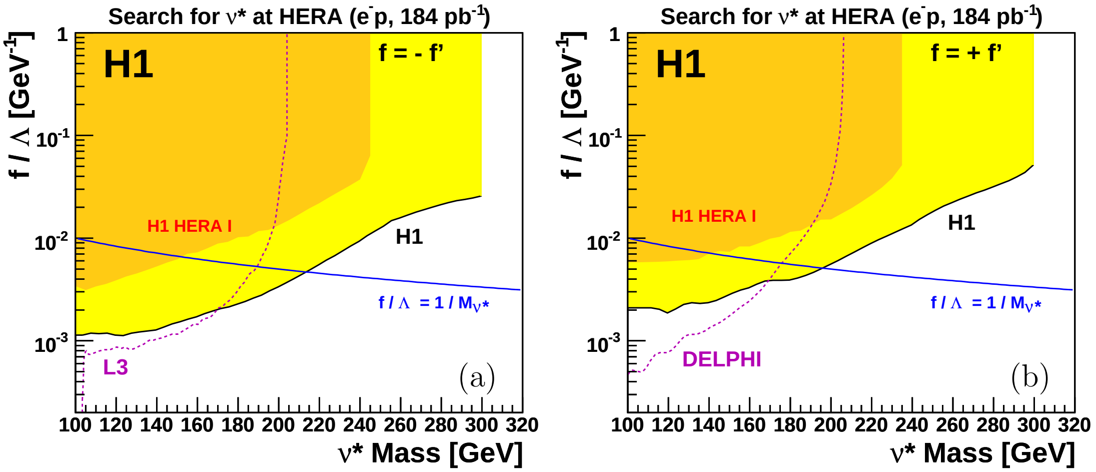

Figure 7.13: Exclusion limits on the coupling f/Λ at 95% CL as a function of the mass of the excited neutrino with the assumptions $f = -f'$ (a) and $f = +f'$ (b). The observed limits from this analysis is presented by the yellow area. Values of the couplings above curves are excluded. The orange-dark area corresponds to the exclusion domain previously excluded by H1 [86]. The dashed line corresponds to the exclusion limit obtained at LEP by the L3 Collaboration [87] in (a) and by the DELPHI Collaboration [88] in (b).

Conclusion and Perspectives

The work presented in this Ph.D. thesis is a search for excited leptons using the full data sample collected by the H1 detector located on the electron(positron)-proton collider HERA. This study is motivated by theoretical approaches which extend the Standard Model by assuming the existence of lepton compositeness. The whole e^-p and e^+p collisions data collected by H1 from 1994 to 2007 have been used for this analysis.

We started with the search for excited electron states (e^*). All data have been analyzed corresponding to an integrated luminosity of 475 pb^{-1}. First, the production and the main topologies resulting from the potential de-excitation of an electron via gauge interaction have been studied. In each channel, the numbers of candidate events found in the data are in agreement with the SM expectations. Therefore, no evidence for excited electrons production was observed. This result was translated into an exclusion limit on the coupling constant f/Λ as a function of the e^* mass. The limit obtained in this analysis on the search for excited electron production via gauge interactions extends nearly up to the HERA kinematic limit. It improves by more than a factor of two the bounds previously obtained by H1 and ZEUS and extends at high mass beyond the kinematic reach of LEP searches. Furthermore, for $M_{e^*} < 270$ GeV, the present limit extends to lower f/Λ values than TEVATRON searches using 1 fb^{-1} of data. For the first time at HERA, possible e^* production via contact interactions has been studied. The possible e^* production via contact and gauge productions together was considered. Different contrary to TEVATRON, in ep collisions, the additional contribution of contact interaction to e^* production changes only slightly the total production cross section. The upper limit obtained on the coupling parameter $1/\Lambda$, if gauge and contact interactions are considered together, improves only by a factor of 1.15 compared to gauge interactions alone.

Then a search for excited neutrinos, whose production is favoured by electron-proton interactions, was performed. Only e^-p data have been used for the ν^* search, corresponding to an integrated luminosity of 184 pb^{-1} which represents a ten-fold increase compared to previous HERA searches. The six main topologies resulting from the potential de-excitation of a ν^* have been studied. Gauge mediated ν^* production and decays were assumed. For this analysis, a new Monte Carlo generator has been developed to simulate ν^* events. Its main innovation is to account for the natural decay width of the excited neutrino. It therefore allows to generate events with masses up to the kinematic limit. The number of candidate events obtained in the data is in agreement with the SM expectaction and no indication of an excited neutrino production was found. In absence of observation of ν^*, this result allowed to determine upper constraints on the coupling constant f/Λ as a function of the ν^* mass. The limits obtained in this analysis greatly extend previously excluded domains and demonstrate the unique sensitivity of HERA to excited neutrinos with masses beyond the LEP reach.

The results of the excited neutrinos search have been published in Phys. Lett. B [89] and the results of the excited electrons search have been submitted to Phys. Lett. B [90].

The operation of the HERA collider ended beginning of July 2007. The present searches use all data collected by H1 at HERA. Therefore, those results on excited electrons and neutrinos searches will be the last H1 results on this subject. Other searches for excited leptons have also been performed at other large colliders, LEP and TEVATRON, but no evidence of the existence of such particles was found so far.

At HERA, the present search for excited leptons of first generation will be completed by a search for excited quarks using also all data recorded by H1. Research of 2^{nd} or 3^{rd} generation excited leptons could also be undertaken. But these last could be produced at HERA only by higher order diagrams and their production cross sections would be very low. Therefore, it will not be possible at HERA to probe values of f/Λ not already excluded by present LEP limits.

The Large Hadron Collider (LHC), under completion at CERN, is expected to start colliding protons at the end of the year 2008 with a center-of-mass energy of $\sqrt{s} = 14$ TeV. Single production of excited spin electrons and neutrinos at the LHC may happen via the reactions $pp{\rightarrow}e^{\pm}e^{*}{\rightarrow}e^{+}e^{-}V$ and $pp{\rightarrow}\nu e^{*} + \nu^{*}e^{\pm}{\rightarrow}e^{\pm}\nu V$. Experimental signatures expected from the production of excited leptons in pp collisions will be diffcult to separate from the large background of strong interaction processes. However, the LHC would be able to tighten considerably the current constraints on these possible new states and to probe excited lepton masses up to 1 TeV [91]. In particular, preons exchange may lead to contact interactions between quarks and leptons and may be an important source for the production of excited lepton at the LHC.

A new Linear Collider (ILC) machine, with different e^+e^-, $e\gamma$ and $\gamma\gamma$ collisions modes and a center-of-mass energy of $\sqrt{s} \geq 500$ GeV, would be an ideal instrument to search also for fermion excited states. With the same production mechanisms as studied in this thesis, excited leptons could be singly on resonance produced in $e\gamma$ collisions. A sensibility similar to the LHC could be reached at the ILC [92].

Conclusion et Perspectives

Le travail de cette thèse a été consacré à la recherche de leptons excités dans les données enregistrées par l'expérience H1 auprès du collisionneur électron(positron)-proton HERA. Cette recherche est motivée par les approches théoriques qui étendent le modèle standard en supposant l'existence de sous-structures composites aux leptons. L'ensemble des données de collisions e^+p et e^-p accumulées par H1 entre 1994 et 2007 ont été utilisées pour cette recherche.

Nous avons commencé par la recherche d'états excités de l'électron (e^*). L'ensemble des données analysées correspond à une luminosité intégrée de 475 pb^{-1}. Tout d'abord, la production et les topologies principales résultant de la désexcitation potentielle d'un e^* via interaction de gauge ont été étudiées. Dans chaque canal, le nombre de candidats trouvés dans les données est en accord avec les prédictions du modèle standard, ce qui signifie qu'aucune preuve de la production d'électrons excités n'a été observée. Nous en avons donc déduit des limites d'exclusion sur le couplage f/Λ en fonction de la masse des électrons excités, dans le cadre d'une production par interaction de gauge. Les limites obtenues dans ce cadre améliorent les résultats de recherches menées précédement à HERA et au LEP. De plus, pour des masses $M_{e^*} < 270$ GeV, ces résultats permettent d'étendre le domaine d'exclusion à de plus faible couplage f/Λ que ceux accessibles dans les analyses récentes du TEVATRON qui utilisent 1 fb^{-1} de données. Pour la première fois à HERA, la production possible de e^* par interaction de contact a également été étudiée. Les deux modes conjoints de production par interaction de jauge et par interaction de contact, ainsi que l'interférence possible entre les deux processus, ont été considérés. Contrairement au TEVATRON, en collisions ep, la possibilité d'une production additionelle de e^* par interaction de contact change peu la section efficace totale de production. La limite supérieure obtenue sur l'échelle de sous-structure Λ change seulement d'un facteur 1.15, selon que l'on considère une production de e^* par interactions de jauges pures ou bien aussi par interactions de contact.

Nous nous sommes ensuite intéressés à la recherche de neutrinos excités (ν^*), dont la production est favorisée par les interactions électron-proton. Seules les données de collisions électron-proton ont été utilisées pour cette recherche, ce qui représente une luminosité intégrée de 184 pb^{-1}, soit dix fois plus que les précédentes recherches menée à HERA. Les six topologies principales résultant de la désexcitation potentielle d'un ν^* ont été étudiées. Le modèle considéré suppose que la production et la déexcitation d'un neutrino excité peuvent avoir lieux par l'intermédiaire d'un couplage entre les bosons de gauge, les fermions standards et les fermions excités (interaction de gauge). Pour cette analyse, un nouveau générateur Monte Carlo servant à simuler les événements ν^* a été developpé. La principale innovation de ce générateur vient de la prise en compte de la largeur de désintégration naturelle du neutrino excité, permettant une simulation complète des événements de signal jusqu'à l'énergie maximum disponible dans le centre de masse. Le nombre de candidats trouvés dans les données est en bon accord avec les prédictions du modèle standard et rien n'indique une production de neutrino excité. En l'absence d'observation de ν^*, ce résultat a permis de déterminer des contraintes supérieures sur le couplage f/Λ des neutrinos excités aux leptons standards, en fonction de la masse du neutrino excité. Les limites obtenues dans cette analyse étendent le domaine précédement exclu et démontrent la sensibilité unique de HERA à des neutrinos excités de masses supérieures à la limite cinématique du LEP.

Les résultats sur les neutrinos excités présentés dans cette thèse ont été publiés dans Phys. Lett. B [89] et ceux sur la recherche d'électrons excités ont été soumis à Phys. Lett. B [90].

Le collisioneur HERA a été arreté définitivement début juillet 2007. Les recherches présentées dans cette thèse utilisent toutes les données accumulées par H1 à HERA. Ces résultats sur les recherches d'électrons et neutrinos excités seront donc les derniers résultats de H1 sur ce sujet. D'autres recherches de leptons excités ont été également réalisées auprès d'autres grand collisioneurs, le LEP et le TEVATRON, mais l'existence de telles particules n'a pas été mise en évidence.

À HERA, cette recherche de leptons excités de première génération va être complétée par une recherche de quarks excités utilisant également l'ensemble des données de H1. La recherche de lepton excités de seconde ou troisième génération pourrait également être entreprise. Mais ces derniers ne pouvant être produit à HERA que par des diagrammes d'ordre supérieurs, les sections efficaces de production seraient très faible. Ceci ne permettrait donc pas de sonder des valeurs de f/Λ qui ne soient pas déja exclues par les limites actuelles du LEP.

Le Grand Collisioneur de Hadrons (LHC), dont l'installation se termine au CERN, devrait délivrer des collisions proton-proton à la fin de l'année 2008 avec une énergie disponible dans le centre-de-masse de $\sqrt{s} = 14$ TeV. La production d'électrons et de neutrinos excités au LHC pourrait se faire par les réactions $pp \rightarrow e^{\pm}e^* \rightarrow e^+e^-V$ et $pp \rightarrow \nu e^* + \nu^* e^{\pm} \rightarrow e^{\pm}\nu V$. Bien que les signatures expérimentales de la production de lepton excités attendues dans les collisions pp soient plus difficiles à distinger du grand bruit de fond due aux processus d'interaction forte, le LHC devrait être capable d'étendre considérablement les contraintes actuelles, en sondant des masses de leptons excités jusqu'à 1 TeV [91]. En particulier, l'échange de préons peut induire une interaction de contact entre les quarks et les leptons, pouvant être une source importante de production de leptons excités au LHC.

Un Collisioneur Linéaire (ILC) disposant d'une énergie dans le centre-de-masse $\sqrt{s} \geq 500$ GeV serait un instrument idéal pour la recherche de fermions excités. Avec les mêmes mécanismes de production que ceux étudiés dans cette thèse, des leptons excités pourraient être produit en resonance dans des collisions $e\gamma$. Une sensibilité comparable au LHC pourrait être atteinte à l'ILC [92].

Bibliography

[1] S. L. Glashow, Nucl. Phys. **22** (1961) 579.
S. Weinberg, Phys. Rev. Lett. **19** (1967) 1264.

[2] S. M. Bilenky, C. Giunti, J. A. Grifols and E. Massó Phys. Rep. **379** (2003) 69.

[3] H. P. Nilles, Phys. Rep. **110** (1984) 1.

[4] H. E. Haber and G. L. Kane, Phys. Rep. **117** (1985) 75.

[5] S. R. Coleman and J. Mandula, Phys. Rev. **159** (1967) 1251.

[6] P. Langacker and M. X Luo, Phys. Rev. **44** (1991) 817.

[7] N. Arkani-Hamed, S. Dimopoulos and G. R. Dvali, Phys. Lett. **B 429** (1998) 263, [hep-ph/9803315].

[8] H. Georgi and S. L. Glashow, Phys. Rev. Lett. **32** (1974) 438.

[9] C. Berger *et al.* [Frejus Collaboration], Z. Phys. **C 50** (1991) 385.

[10] K. S. Hirata *et al.* [KAMIOKANDE-II Collaboration], Phys. Lett. B **220** (1989) 308.

[11] I. A. D'Souza and C. S. Kalman, *Preons: Models of leptons, quarks and gauge bosons as composite objects*, World Scientific, Singapore (1992).

[12] S. Weinberg, Phys. Rev. **D 13** (1976) 974.

[13] L. Susskind, Phys. Rev. **D 20** (1970) 2619.

[14] M. Suzuki, Phys. Rev. **D 37** (1988) 210.

[15] H. Fritzsch and G. Mandelbaum, Phys. Lett. **B 102** (1981) 319.

[16] H. Harari, Phys. Lett. **B 86** (1979) 83.

[17] M. A. Shupe, Phys. Lett. **B 86** (1979) 87.

[18] J. Kühn and P. M. Zerwas, Phys. Lett. **B 147** (1984) 189.

[19] K. Hagiwara, S. Komamiya, and D. Zeppenfeld, Z. Phys. **C 29** (1985) 115.

[20] F. M. Renard, Phys. Lett. **B 116** (1982) 264.

[21] F. del Aguila, A. Mendez, and R. Pascual, Phys. Lett. **B 140** (1984) 431.

[22] U. Baur, M. Spira and P. M. Zerwas, Phys. Rev. **D 42** (1990) 815.

[23] C. Adloff *et al.*, Phys. Lett. **B 479** (2000) 358, [hep-ex/003002];
C. Adloff *et al.*, Phys. Lett. **B 568** (2003) 35, [hep-ex/0305015].

[24] K. Hagiwara and S. Matsumoto, Phys. Lett. **B 424** (1998) 362.

[25] A. Adloff *et al.*, Eur. Phys. J. **C 30** (2003).

[26] A. Nikiforov, *Measurements of the Neutral Current e±p Cross Sections Using Longitudinally Polarised Lepton Beams at HERA II*, Ph.D. thesis, München, 2007.

[27] M. Kein and T. Riemann, Z. Phys. **C 24**, (1984) 1551.

[28] *High Q^2 Charged Current in polarised ep collisions*, H1Prelimary results, Contibuted paper to ICHEP06, 23rd International Conference on High Energy Physics.

[29] F. Boudjema, A. Djouadi, and J. L. Kneur, Z. Phys. **C 29** (1992) 425.

[30] M. Spira, private communication.

[31] R. Y. Rubinstein, *Simulation and the Monte Carlo Method*, Wiley (1981).

[32] H. Jung, Comput. Phys. Commun. **86** (1995) 147.

[33] J. Pumlin *et al.*, JHEP **0207** (2002) 012, [hep-ph/0201195].

[34] A. Kwiatkowski, H. Spiesberger and H.-J. Möhring, Comput. Phys. Commun. **69** (1992) 155.

[35] C. Adloff et *al.*, [H1 Collaboration], Eur. Phys. J. **C 25** (2002) 13, [hep-ex/0201006]

[36] G. Ingelman, A. Edin and J. Rathsman, Comput. Phys. Commun. **101** (1997) 108.

[37] K. Charchula, G. A. Schuler and H. Spiesberger, Comput. Phys. Commun. **81** (1994) 381.

[38] C. Adloff *et al.*, Eur. Phys. J. **C 30** (2003).

[39] Y. Azimov et *al.*, Phys. Lett. **B 165** (1985) 147.
G. Gustafson, **B 175**, (1986) 453.
G. Gustafson and U. Pettersson, Nucl. Phys. **B 306** (1988) 746.
B. Andersson et *al.*, Z. Phys. **C 43** (1989) 625.

[40] L. Lönnblad, Comput. Phys. Commun. **71** (1992) 15.
L. Lönnblad, Z.Phys. **C 65** (1995) 285.

[41] T. Helbig and H. Spiesberger, Nucl. Phys. **B 373** (1992) 73.

[42] T. Sjostrand, P. Eden, C. Friberg, L. Lomblad, G. Mui, S. Mrenna and E. Norrbin, Comput. Phys. Commun. **135** (2001) 238, [hep-ph/0010017].

[43] C. Berger and P. Kandel, Prepared for Workshop on Monte Carlo Generators for HERA Physics Hamburg, Germany, 27-30 Apr 1998.

[44] T. Abe, Comput. Phys. Commun. **136** (2001) 126, [hep-ph/0012029].

[45] U. Baur, J. A. Vermaseren and D. Zeppenfeld, Nucl. Phys. **B 375** (1992) 3.

[46] A. Aktas *al.*, [H1 Collaboration], Phys. Lett. **B 583** (2004) 28-40.

[47] D. Waters, *A first estimate of* $\sigma(e^- p \rightarrow e^- X^{\pm} X)$, Ph.D. thesis, University of Oxford, (1998).

[48] T. Köhler, Proceeding of *Physics at HERA*, Hamburg 1991, vol. 3, 1526.

[49] G. P. Lepage, Journal of Computational Physics **27** (1987) 192.

[50] Ch. Berger, W. Wagner, Phys. Rep. **146** (1987).

[51] B. Andersson et *al.*, Phys. Rep. **97** (1983) 31.

[52] E. Boos *et al.*, [CompHEP Collaboration], Nucl. Instrum. Meth. **A 534** (2004) 250, [hep-ph0403113].

[53] S. Aid *et al.*, [H1 Collaboration], *Guide to Simulation Program, H1SIM*, H1 Internal Report (1995).

[54] R. Brun *et al.*, *GEANT3 User's Guide*, **CERN-DD/EE-84-1**.

[55] I. Abt *et al.*, [H1 Collaboration], Nucl. Instrum. Meth. **A 386** (1997) 310.

[56] B. Andrieu *et al.*, [H1 Calorimeter group], Nucl. Instrum. Meth. **A 336** (1993) 460.

[57] R.-D. Appuhn *et al.*, [H1 Spacal group], Nucl. Instrum. Meth. **A 386** (1993) 397.

[58] C. Kiesling *et al.*, *The H1 Neural Network Trigger*, Preprints submitted to Elsevier Preprint, AIHENP **99**, Crete, Greece.

[59] C. Beigbeder *et al.*, *Level 2 Topological Trigger (L2TT) Hardware*, H1 internal note H1-10/96-499, 1996.

[60] K. Müller, R. Beyer, *1996 L4 Filter Farm Selection Algorithm*, H1 internal note H1-07/98-547, 1996.

[61] E. Chabert *et al.*, *QBGFMAR: An update PHAN package for cosmic and halo muon topological rejection in high p_T physics analysis*, H1 internal note H1-11/98-556, 1998.

[62] I. Négri *et al.*, *A minimal comprehensive set of muon background topological finders for high P_T physics analysis*, H1 internal note H1-10/96-498.

[63] M. Peez, B. Portheault and E. Sauvan, *An Energy Flow Algorithm for Hadronic Reconstruction in OO: Hadroo2*, H1 internal note H1-01/05-616, 2005.

[64] The H1OO group, *The H1OO physics analysis project*, H1 internal note.

[65] QHQTRK manual, (Heavy Flavor Working Group track selection code by Lee West).

[66] P. Bruel, *Recherche d'interaction au-delà du modèle standard à HERA*, Ph.D. thesis, Université Paris Orsay, May 1998.

[67] C. Adloff et *al.*, [H1 Collaboration], Phys. Lett. **B 583** (2004) 40.

[68] S. D. Ellis and D. E. Soper, Phys. Rev. **D 48** (1993) 3160, [hep-ph/9305266].

[69] S. Catani, Y. L. Dokshitzer, M. H. Seymour and B. R. Webber, Nucl. Phys. **B 406** (1993) 187.

[70] J. Dingfelder, *Search for Anomalous Top Production of Single Top Quarks with the H1 Experiment at HERA*, Ph.D. thesis, University of Heidelberg, 2003.

[71] S. Bentvelsen *et al.*, *Reconstruction of (x, Q^2) and extraction of structure function in neutral current scattering at HERA*. In W. Buchmüller and G. Ingelmann, Proceedings of the Workshop: Physics at HERA, volume 1, **DESY** (1992) 23-40 .

[72] A. Blondel and F. Jacquet, In U. Amaldi, Proceeding of the Study of an ep Facility for Europe,

[73] O. M. Henshaw, *A First Measurement of the Neutral Current Cross Section at High Q^2 in Longitudinally Polarised* e^+p *Scattering with the H1 Detector*, Ph.D. thesis, University of Birmingham.

[74] T. Junk, Nucl. Instrum. Meth. **A 434** (1999) 435, [hep-ex/9902006].

[75] A. L. Read, *Optimal Statistical Analysis of Search Results based on the Likelihood Ratio and its Application to the Search for the MSM Higgs Boson at* $\sqrt{s} = 161$ *and* 171 *GeV*, 1997, DELPHI note 97-158 PHYS 737.

[76] R. D. Cousins and V. L. Highland, Nucl. Instrum. Meth. **A 320** (1992) 331.

[77] A. L. Read, Nucl. Instrum. Meth. **A 425** (1999) 357.

[78] C. Adloff *et al.*, [H1 Collaboration] Phys. Lett. **B 548** (2002) 35, [hep-ex/0207038].

[79] S. Chekanov *et al.*, [ZEUS Collaboration], Phys. Lett. **B 549** (2002) 32, [hep-ex/0109018].

[80] B. Vachon *Excited electron contribution to the* $e^+e^-\rightarrow\gamma\gamma$ *cross-section*, [hep-ph/0103132].

[81] G. Abbiendi *et al.*, [OPAL Collaboration], Phys. Lett. **B 544** (2002) 405, [hep-ex/0206061].

[82] J. Abdallah *et al.*, [DELPHI Collaboration], Eur. Phys. J **C 37** (2004) 405, [hep-ex/0409058].

[83] D. Acosta *et al.*, [CDF Collaboration], Phys. Rev. Lett **94** (2005) 101802, [hep-ex/0410013].

[84] V.M. Abazov *et al.*, [D0 Collaboration], *Search for Excited Electrons in the* $ee\gamma$ *Channel*, [hep-ex/0801.0877v1].

[85] P. J. Johr and B. N. Taylor, Rev. Mod. Phys. **72** (2000) 351.

[86] C. Adloff *et al.*, [H1 Collaboration], Phys. Lett. **B 525** (2002) 9, [hep-ex/0110037].

[87] P. Achard *et al.*, [L3 Collaboration], Phys. Lett. **B 568** (2003) 23, [hep-ex/0306016].

[88] J. Abdallah *et al.*, [DELPHI Collaboration], Eur. Phys. J **C 46** (2006) 277, [hep-ex/0603045].

[89] A. Aktas *et al.*, [H1 Collaboration], *Search for Excited Neutrinos in* e^-p *Collisions at HERA*, Phys. Lett. **B 663** (2008) 382, [hep-ex/0802.1858].

[90] A. Aktas *et al.*, [H1 Collaboration], *Search for Excited Electrons in ep Collisions at HERA*, [**DESY**-08-052], [hep-ex/0805.4530].

[91] O. J. Eboli, S. M. Lietti and P. Mathews, Phys. Rev. **D 65** (2002) 075003.

[92] E. M. Gregores, M. C. Gonzalez-Garcia, and S. F. Novaes, Phys. Rev. **D 56** (1997) 2920.

RÉSUMÉ

Recherche de leptons excités sur le collisionneur HERA avec le détecteur H1

Le travail de cette thèse est consacré à la recherche de leptons excités de première génération dans les données enregistrées par l'expérience H1 auprès du collisionneur électron (positron)-proton HERA.

Cette recherche est motivée par les approches théoriques qui étendent le modèle standard en supposant l'existence de sous-structures composites aux leptons. L'ensemble des données de collisions e^+p et e^-p accumulées par H1 entre 1994 et 2007, correspondant à une luminosité intégrée de 475 pb^{-1}, ont été utilisées pour cette recherche. Les analyses effectuées concernent treize topologies différentes, ce qui couvre la totalité des rapports de branchement de déexcitation de l'électron (e^*) et du neutrino (ν^*) excités. Aucune preuve de la production de ces leptons excités de première génération n'a été observée. Des limites d'exclusions sur la section efficace de la production de leptons excités et sur le couplage f/Λ en fonction de la masse des leptons excités sont déduites dans le cadre d'une production par interaction de gauge. Les limites obtenues dans ce cadre étendent les résultats de recherches menées précédement.

Pour la première fois à HERA, la production possible de e^* par interaction de contact a également été étudiée. Les deux modes conjoints de production par interaction de gauge et par interaction de contact, ainsi que l'interférence possible entre les deux processus, ont été considérés.

Mots-clefs: *Modèles composites, Préons, HERA, H1, Leptons excités, Electron excité, Neutrino excité, Interactions de Contact.*

ABSTRACT

Search for excited leptons at the HERA collider with the H1 detector

The work presented in this Ph.D. thesis is a search for first generation excited leptons using the full data sample collected by the H1 detector installed on the HERA electron(positron)-proton collider.

This study is motivated by theoretical approaches which extend the Standard Model by assuming the existence of lepton compositeness. The whole e^-p and e^+p collisions data collected by H1 from 1994 to 2007 and corresponding to a total integrated luminosity of 475 pb^{-1} have been used for this analysis. The analysis of 13 different topologies was done, covering all the decay branching ratio of excited electrons (e^*) and neutrinos (ν^*). No evidence of the production of first generation excited leptons was observed. Exclusion limits on e^* and ν^* production cross section and on the coupling constant f/Λ as a function of the excited leptons mass are derived within gauge mediated models. The limit obtained extend the excluded region compared to previous excited lepton searches.

For the first time at HERA, possible e^* production via contact interactions is also studied. The e^* production via contact and gauge productions together, including the interference between the two production modes, was considered.

Keywords: *Composite Model, Preons, HERA, H1, Excited Lepton, Excited electron, Excited neutrino, Contact Interactions.*